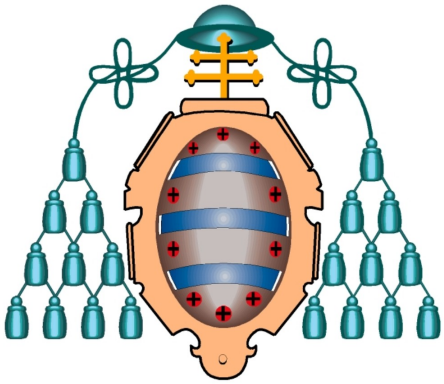

UNIVERSIDAD DE OVIEDO

Departamento de Ciencia de los Materiales e Ingeniería Metalúrgica

Doctoral Thesis

Magnetocaloric and magnetovolume effects in Fe-based alloys

Pablo Alvarez Alonso

July 2011

Resumen

En esta memoria de Tesis Doctoral se presentan los resultados del estudio del efecto magnetocalórico y magnetovolúmico que se ha llevado a cabo en dos familias de compuestos ricos en Fe: aleaciones R_2Fe_{17}, sintetizadas en forma policristalina, y cintas amorfas de composición FeZrBCu. Estas aleaciones presentan transiciones magnéticas de segundo orden con temperaturas críticas en torno a temperatura ambiente.

La serie de aleaciones R_2Fe_{17} (con R = Y, Ce, Pr,...) ha sido sintetizada mediante la fusión de los diferentes elementos por horno de arco. Se ha determinado la estructura cristalina de estos compuestos mediante difracción de rayos x y de neutrones de alta resolución. Los compuestos de esta familia pueden cristalizar en dos tipos de estructuras cristalinas dependiendo de la tierra rara que se emplee: para las tierras raras ligeras (Ce, Pr, Nd, Sm, Gd, Tb y Dy) los compuestos que se han sintetizado son romboédricos tipo Th_2Zn_{17}, para las pesadas (Ho, Er, Tm y Lu) son hexagonales tipo Th_2Ni_{17}, mientras que el compuesto Y_2Fe_{17} presenta ambas estructuras cristalinas. A partir de la termodifracción de neutrones se ha determinado la dependencia con la temperatura (T) tanto de los parámetros de malla como de los momentos magnéticos de cada sitio cristalográfico. Existe una magnetostricción espontánea anisótropa, más pronunciada a lo largo del eje uniáxico, con independencia de la estructura cristalina que presente el compuesto. Más aún, se ha observado que la magnetostricción de volumen depende cuadráticamente con el momento total de la subred del Fe hasta temperaturas cercanas a la de Curie, T_C. Experimentos de rayos x bajo alta presión han mostrado que existe una pequeña anisotropía en los compuestos romboédricos al comprimir la celda cristalográfica, puesto que es más fácil comprimirla en la direccion uniáxica. Ajustando la dependencia del volumen con la presión con una ecuación de estado de Birch-Murnaghan se han estimado los módulos de compresibilidad.

También se ha estudiado el efecto magnetocalórico a partir de la dependencia de la imanación con el campo magnético a diferentes temperaturas, obteniéndose la variación de la entropía magnética (ΔS_M) con T y el campo magnético aplicado (H). En los compuestos ferrimagnéticos $\Delta S_M\,(T, H)$ presenta un máximo a bajas temperaturas, asociado con un efecto magnetocalórico inverso, y un mínimo, asociado con un efecto directo, el cuál ocurre a $T \approx T_C$. En cambio, en los ferromagnéticos sólo existe el efecto directo. Para el caso especial del Ce_2Fe_{17} aparecen dos mínimos, estando el de más alta temperatura asociado a la transición de segundo orden del estado ferromagnético al paramagnético, mientras que el de más baja temperatura es debido a una transición metamagnética.

Se ha investigado la influencia que tiene la molienda mecánica en la microestructura de las aleaciones Pr_2Fe_{17} y Nd_2Fe_{17}, así como los efectos de estas modificaciones en sus propiedades magnéticas. Mediante técnicas de difracción se ha determinado su estructura cristalina, la cuál no se ve modificada tras el proceso de molienda. Sin embargo, sí se produce un cambio drástico en la microestructura debido a la rotura progresiva de granos cristalinos y la formación de partículas de tamaño nanoscópico, lo cual ha sido corroborado mediante la microscopía electrónica de barrido y de transmisión conjuntamente con la difracción. Conforme se incrementa el tiempo de molienda se produce una disminución del tamaño de partícula, y los granos presentan una dispersión de tamaños menor. Estas modificaciones en la microestructura tienen como resultado la aparición de una distribución de temperaturas de Curie, con el consiguiente ensanchamiento de la curva $\Delta S_M(T)$, así como una disminución del valor máximo del cambio en la entropía magnética.

Asimismo se han sintetizado diferentes compuestos pseudobinarios tipo $A_xB_{2-x}Fe_{17}$ (siendo A y B tierras raras y/o Itrio). En este caso, mezclando diversas tierras raras se puede controlar el valor de la temperatura de orden magnético alrededor de la temperatura ambiente. Dependiendo de las tierras raras empleadas, estos compuestos pueden presentar cualquiera de las dos estructuras cristalinas en las que cristaliza la familia R_2Fe_{17}. En los compuestos sintetizados la estructura cristalina es romboédrica ($R\bar{3}m$), no habiéndose detectado la existencia de fase hexagonal mediante la difracción de neutrones ni de rayos x, dentro de los límites de detección.

En el caso de las aleaciones amorfas tipo Nanoperm, FeZrBCu, las muestras se han obtenido en forma de cinta mediante la técnica de enfriamiento ultrarrápido. En estos compuestos, T_C depende de la cantidad de Fe, por lo que se puede seleccionar la temperatura a la que se obtiene el máximo de $|\Delta S_M\,(T,H)|$. Además, presentan una transición ferro-paramagnética que se extiende en un amplio rango de temperaturas, lo cual lleva asociado una curva $\Delta S_M(T)$ muy ancha. Definiendo la capacidad relativa de refrigeración de un material magnético como el producto de la anchura a mitad de altura de $|\Delta S_M\,(T,H)\,|$ por el valor máximo de $|\Delta S_M(T)|$, se obtiene un valor alto, aún cuando el valor de $|\Delta S_M^{peak}|$ es moderado, en comparación con los materiales que presentan una transición magnética de primer orden. Asimismo, se ha determinado ΔS_M en diferentes aleaciones de FeZrBCu para campos magnéticos entre 0 y 8 T, lo que permite discutir la existencia de un comportamiento común de la variación de la entropía magnética para los elementos esta familia. Por último, se han estudiado las propiedades magnetocalóricas resultantes de la combinación de dos cintas de distintas composiciones. El resultado más destacado es que se puede producir un incremento de la capacidad de refrigeración y, además, la aparición de un aplanamiento de la curva $\Delta S_M(T)$ en un amplio rango de temperaturas.

Abstract

THIS thesis reports the results of the study of the magnetocaloric and magnetovolume effects that have been investigated in two families of Fe-rich compounds: R_2Fe_{17} alloys, which have been synthesized in polycrystalline form, and FeZrBCu amorphous ribbons. These alloys exhibit second order magnetic phase transitions close to room temperature.

The R_2Fe_{17} alloys series (with R = Y, Ce, Pr, ...) has been synthesized by arc melting. We have determined the crystal structure of these compounds by means of high-resolution x-ray and neutron powder diffraction. The alloys of this family can crystallize in two types of crystal structures depending on which rare-earth is used: for light rare-earths (Ce, Pr, Nd, Sm, Gd, Tb and Dy) the compounds have been synthesized into the rhombohedral Th_2Zn_{17}-type structure, whereas for the heavy rare-earths (Ho, Er, Tm and Lu) the structure is the hexagonal Th_2Ni_{17}-type. From neutron thermo-diffraction experiments, the variation of both lattice parameters and the magnetic moments at each crystallographic site with the temperature (T) has been determined. There is an anisotropic spontaneous magnetostriction more pronounced along the uniaxial axis regardless of the crystal structure. Furthermore, it has been shown that the volume magnetostriction depends quadratically on the total magnetic moment of the Fe-sublattice up to temperatures near the Curie temperature, T_C. X-ray diffraction experiments under high pressure have shown that exists an anisotropy in rhombohedral compounds when compressing the unit cell, as it is easier to compress along the uniaxial direction. Bulk modulus have been estimated fitting the pressure dependence of the cell volume to a Birch-Murnaghan equation of state.

We have also studied the magnetocaloric effect from the dependence of the magnetization with the applied magnetic field at different temperatures, obtaining the magnetic entropy change (ΔS_M) as a function of T and the applied magnetic field (H). In the ferrimagnetic compounds, $-\Delta S_M\,(T, H)$ has a minimum associated with an inverse magnetocaloric effect at low temperature, and a maximum associated with a direct effect, which occurs at $T \approx T_C$. In contrast, only the direct effect is observed in the ferromagnetic compounds. For the special case of Ce_2Fe_{17} there are two maxima, being the high temperature maximum associated with the second order ferromagnetic to paramagnetic phase transition, while the low temperature one is associated with a metamagnetic phase transition.

Moreover, we have studied the influence of mechanical milling on the microstructure of the Pr_2Fe_{17} and Nd_2Fe_{17} alloys, and the effect of these changes in their magnetic properties. Powder diffraction experiments have evidenced that the crystal structure is maintained after the milling process. Nevertheless, drastic changes in the microstructure, such as grain breakage and nano-sized particles formation, appear. This has been observed by scanning and transmission electron microscopy, and confirmed by diffraction experiments. With increasing milling time, a decrease of nanoparticle size is observed, and the size distribution becomes narrower. These changes in the microstructure are linked with a distribution of Curie temperatures, giving rise to a broadening of the magnetic entropy peak. In contrast, this temperature distribution produces a decrease of the value of the peak of the magnetic entropy change.

Likewise different $A_xB_{2-x}Fe_{17}$ (with A and B rare-earth or yttrium) pseudobinary compounds have been synthesized. In this case, it is possible to tune the value of the ordering temperature by mixing different rare-earths. These compounds can have any of the two crystal structures in which the family R_2Fe_{17} crystallizes, depending on the rare-earths employed. In the synthesized

compounds, the crystal structure is rhombohedral ($R\bar{3}m$), and no traces of hexagonal phase have been detected within the limits of detection of neutron and x-ray powder diffraction.

In the case of FeZrBCu amorphous alloys, the samples were obtained in ribbon shape by means of the melt-spinning technique. In these compounds, T_C depends on the relative amount of Fe and B, thus the temperature at which the maximum of $|\Delta S_M(T,H)|$ takes place, can be selected. Furthermore, those compounds shown a broad ferromagnetic-paramagnetic transition, giving rise to a broad $\Delta S_M(T)$ curve. If the relative cooling power of a magnetic material is defined as the product of the full width at half maximum of $|\Delta S_M(T,H)|$ times the value of the peak, it yields a large value, even though the peak value is moderate compared with those of materials exhibiting a first order magnetic transition. We have determined $\Delta S_M(T,H)$ in different FeZrBCu alloys with the applied magnetic ranging from 0 to 8 T, which allows us to discuss the existence of a common behavior of the magnetic entropy change for the alloys of this family. Finally, we have studied the magnetocaloric properties resulting from the combination of two ribbons of different compositions. The main result is that the relative cooling power can be increased, and, furthermore, an almost flat $\Delta S_M(T)$ curve is observed for a large temperature range, if the combination of alloys is optimized.

To my parents.

Acknowledgements

This thesis is the final part of a long and hard work, which could not be performed without the help of several persons and institutions. Therefore I would like to thank:

My supervisors Blanca Hernando Grande and Pedro Gorria Korres, who have invested plenty of time and effort to lead this project to a successful end.

My colleague and buddy Jose Luis Sánchez Llamazares, whose teachings, support and advices helped me to find my way for finishing this thesis.

Jesús Blanco, who has perpetually encouraged me and help me with some aspects of the theory.

Jesús Rodriguez, Luis Fernández Barquín, Victorino Franco, Javier Campo, Rastislav Varga and Marian Reiffers, for accepting me in their laboratories and helping me to clarify ideas.

Jesús Daniel and Maria José, for their help in our laboratory.

The FICYT, which has funded my fellowship, the University of Oviedo, where the main part of my research has done, and the Spanish Education and Science Department for supporting the research projects in which I have participated. Also the Institut Laue-Langevin and the European Synchrotron Research Facility, where an important part of my experiments has been carried out.

Gabriel, Gastón, Inés, Teresa, Alberto, Jorge and Sergio for their help during my experiments at the ILL and the ESRF.

Tatiana, Chus, Javier, Wagner, Lorena, Maida, Mari Paz, Ángel, Lucas, Rebeca and Paola, my colleagues, but also my friends, at lab and office.

My friends, especially Bea, Roberto, Borja, Lorena, María, Irene and Zara, for all this good years. Also, I would like to thank my flatmates, Rosalía, Lurdes, María, Raúl and Gonzalo, for doing me laugh and enjoy our dinners.

My fiancée, Paula, for her support and understanding (I love you).

And last but not least, I would like to thank my parents, brother, grandparents and the rest of my family.

Preface

MAGNETISM is a fascinating topic in which this Thesis has been developed. It is well known that the history of the Magnetism starts with the magnetite, an iron oxide, in the town of Magnesia, in Greece. The earliest reported observations of macroscopic magnetic effects on magnets were done by the Greek philosopher Thales around 600 B.C. One of the first applications of Magnetism was the magnetic compass, which had a great importance for navigation (and is still in use). The use of magnets and the study of magnetic materials has been a continuous source of progress. Nowadays, the Magnetism is essential in our common live. There are magnetic materials present in a great variety of devices: media storage, power supply transformers, motors, loudspeakers, mobiles, computers, ... Any conventional house contains more than fifty of such devices.
A milestone in the history of magnetism was William Gilbert's *De Magnete, Magneticisque Corporibus, et de Magno Magnete Tellur* work (1600), which summarized all the available knowledge of magnetism until that time. Major qualitative steps in the knowledge of the basics of Magnetism were done in the nineteenth century, when Øersted found that a magnetic field could be generated with an electric current, Ampère established quantitative laws of the magnetic force between electric currents, and Faraday discovered the magnetic induction and introduced the concept of the magnetic field like an independent physical entity. In the twentieth century, Curie introduced the idea of how an external magnetic field orients the magnetic dipoles, being counteracted by the thermal agitation, whereas Weiss postulated the existence of an internal magnetic field in ferromagnets, resulting in a spontaneous magnetization even in the absence of an external field. The properties of the magnetic domain walls, proposed by Weiss, were studied in detail by Bloch, Landau and Néel, leading to the explanation of ferrimagnetism and antiferromagnetism.

The magnetic behavior of a material depends on its crystal structure, and changes with the temperature. In the case of crystalline materials, the magnetic properties are governed by the crystal symmetry. Thereby the possible magnetic structures are defined by the magnetic space groups. In the case of collinear arrangements of magnetic moments, this would lead to ferromagnetism, antiferromagnetism or ferrimagnetism, and, in the case of non-collinear structures, fan, helimagnetism or canted spin structures are possible. For amorphous alloys, both chemical and structural disorder lead to a distribution in magnitude of magnetic moments and exchange interactions, giving rise to different non-collinear magnetic structures like speromagnetism, asperomagnetism and sperimagnetism.

The structure of matter, indeed the interatomic distances between the magnetic atoms, describes the sign and the intensity of the magnetic coupling, such is the case of both direct and RKKY exchange interactions. Not in vain, the magnetovolume anomalies like the Invar phenomena, found in 1897 by Guillaume in ferromagnetic fcc FeNi alloys, consisting in a very low or even negative thermal expansion in a wide range of temperatures, highlights the dependence of magnetic interactions with interatomic distances. For these reasons, the knowledge of the structure of the magnetic material is a key point.

Investigation of magneto-thermal phenomena is of great importance to solve fundamental problems of magnetism and solid state physics, as well as for technological applications. These phenomena have a strong influence on several physical properties like entropy. Among them, there

is the magnetocaloric effect (MCE), discovered by Warburg in 1881 heating iron by means of the application of a magnetic field and cooled again when removed out. Soon after, Edison (1887) and Tesla (1890) suggested their thermomagnetic generators of electrical power using materials with a sharp temperature dependence of magnetization. Nevertheless, nowadays the main application of this effect is in the magnetic refrigeration, which has been applied since the 1930s to cool down samples from a hundred Kelvin down to a few miliKelvin. Materials used for magnetic refrigeration at low temperatures mainly concentrate on paramagnetic salts, and the needed magnetic fields are about 1 T. However, this effect has been not used in room temperature magnetic refrigeration systems yet, because the requirements for the spreading of such systems are determined by the strength of the magnetic fields obtained by current magnets, and the magnetocaloric properties around room temperature shown by the magnetic materials. Commercially viable applications for magnetocaloric cooling are only possible if there is an abundant supply of magnetic materials with a marked MCE at low applied magnetic field and close to room temperature. Therefore, research on new magnetic materials with improved magnetocaloric properties is currently a trend topic of Materials Science.

This Thesis work adds to the efforts in this direction, and is divided into six chapters and two appendices:

In ***Chap. 1*** an introduction to some important terms on magnetocaloric and magnetovolume effects is done, and the state of the art of the knowledge collected until now on crystalline R_2Fe_{17} (R = Y, Ce, Pr, Nd, ...) and FeZrBCu amorphous alloys is shown. Motivation and objectives that have driven this work are also included in this chapter.

Chap. 2 is devoted to explain the experimental techniques employed in fabricating the samples and in their characterization. It is worth noting that the use of different complementary techniques allows to improve the information obtained from both structural and magnetic characterization.

Experimental results in the R_2Fe_{17} compounds are presented and discussed in the ***Chap. 3***. Crystal and magnetic structures are determined together with the temperature dependence of the lattice parameters and the magnetic moments at each crystallographic site. The magnetic entropy change is obtained from the applied magnetic field and the temperature dependence of the magnetization. Modification of the microstructure by effect of mechanical milling, and its influence on the magnetic properties, are largely studied in Pr_2Fe_{17} and Nd_2Fe_{17} alloys.

The effects on both crystal structure and magnetic properties and on MCE of binary compounds by mixing two different rare-earths are summarized in ***Chap. 4***.

In order to complete the study of the magnetocaloric effect in Fe-based alloys, amorphous FeZrBCu alloys have been selected because they present second-order magnetic transition around room temperature. In ***Chap. 5*** the results in a series of FeZrBCu ribbons are reported.

Chap. 6 outlines the most important conclusions which can be drawn from this work.

In the ***Appendices*** the basic scripts used to obtain the main magnetocaloric properties and a list of publications are listed.

Contents

List of Figures

List of Tables

Chapter 1

Introduction

Material Science is an interdisciplinary field focused on the relationship between the structure of substances at atomic or molecular scales and their macroscopic properties, so that new materials with controlled physical-chemical behavior can be designed and fabricated. The major determinants of a material structure are its constituents and the way in which it has been processed, which, in combination with the laws of Thermodynamics, controls the properties of such substance. The study of metallic alloys is one of the main fields of research in Material Science. In this case, Fe-based alloys attract a great interest because of the number of applications in which they can be used, and its commercial value. Concerning to the applications, nowadays Fe-based alloys (e.g. MnFe(P,As), $La(Fe,Si)_{13}$ and Finemet-type amorphous ribbons [1–4]) are being widely studied due to their potential application in room temperature magnetic refrigeration systems. Such systems use the magnetization-demagnetization processes of a magnetic substance to substitute the expansion-compression processes of the conventional refrigerant systems. Magnetic refrigeration is a well-established cryogenic-range cooling technology to cool down to 100 mK, but it is still in an incipient stage for refrigeration systems at ambient temperature. However, due to its environmental and energetic advantages over the conventional cooling systems, the interest on magnetic refrigeration in the room temperature range has been renewed. In fact, the search for magnetic substances which exhibit suitable magnetocaloric properties is a growing research area [5].

1.1 Magnetocaloric effect (MCE)

The magnetocaloric effect (MCE) was discovered by Warburg in 1881 [6]. It can be understood as either the magnetic entropy or the temperature change in a magnetic material when an external magnetic field is varied isothermally or adiabatically respectively [7]. This is the result of the variation of the internal energy of the material when changing the applied magnetic field, due to the thermal coupling between the lattice and the magnetic degrees of freedom [8]. Thereby, the MCE is an intrinsic property of all magnetic substances. Furthermore, as the entropy is linked to the disorder of a system, the magnetic entropy will be reduced when the magnetic moments

become partly ordered, which in the case of ferromagnetic materials can be achieved mainly in two ways: increasing the magnetic field or lowering the temperature [9].

1.1.1 Thermodynamics of the magnetocaloric effect

As this thesis focus on the study of second order magnetic phase transitions, a theoretical description in this section is done for the Thermodynamics of MCE for such kind of magnetic phase transitions [10–14].

Let's consider that the total entropy of any magnetic system with a second order magnetic phase transition is always a continuous function of temperature, regardless of magnetic field. It is also assumed that hysteresis, coercive fields, anisotropy and remanence are all negligible and, hence, they have no effect on the magnetocaloric effect. Furthermore, it is supposed that the magnetic systems are in a static equilibrium. Finally, all processes in the magnetic systems are assumed to be reversible.

We consider a magnetic system in a thermodynamic equilibrium state with no changes in composition (i.e., $dN = 0$). For such a system, the first law of the thermodynamics states that its internal energy is a function of the extensive properties (also called generalized displacement) of the system, entropy (S), volume (V) and the magnetic extensive variable (M):

$$U = TS - PV + HM, \tag{1.1}$$

where T (temperature), P (pressure) and H (magnetic field) are the intensive variables (also called generalized forces or fields) conjugated of S, V and M respectively. M is the component of the total magnetic dipole moment in the direction of the applied field. The internal energy can be written in a differentiable form:

$$dU = \left(\frac{\partial U}{\partial S}\right)_{V,M} dS + \left(\frac{\partial U}{\partial V}\right)_{S,M} dV + \left(\frac{\partial U}{\partial M}\right)_{S,V} dM, \tag{1.2}$$

with

$$\begin{aligned} \left(\frac{\partial U}{\partial S}\right)_{V,M} &= T(S,V,M) \\ \left(\frac{\partial U}{\partial V}\right)_{S,M} &= -P(S,V,M) \\ \left(\frac{\partial U}{\partial M}\right)_{S,V} &= H(S,V,M). \end{aligned} \tag{1.3}$$

From 1.3 it is clear that a given generalized displacement can be modified by more than one generalized force. It should be noticed here that the tensorial product of an intensive variable times the corresponding extensible variable is a scalar that quantifies the (reversible) work associated with changes of the intensive properties induced by the corresponding generalized field.

The Legendre transformation of $U\,(S,V,M)$ with respect to S, V and M,

$$A = U - TS + PV - MH, \tag{1.4}$$

gives the free energy of the system in terms of the intensive parameters T, P and H. Its differential form is

$$dA = \left(\frac{\partial A}{\partial T}\right)_{P,H} dT + \left(\frac{\partial A}{\partial P}\right)_{T,H} dP + \left(\frac{\partial A}{\partial H}\right)_{T,P} dH. \tag{1.5}$$

The extensive parameters are given by

$$\begin{aligned} S(T,P,H) &= -\left(\frac{\partial A}{\partial T}\right)_{P,H} \\ V(T,P,H) &= \left(\frac{\partial A}{\partial P}\right)_{T,H} \\ M(T,P,H) &= -\left(\frac{\partial A}{\partial H}\right)_{T,P} \end{aligned} \tag{1.6}$$

From an elementary theorem of calculus, two mixed second partial derivatives of A with respect to T and H are equal. Thus, using 1.6, the following Maxwell relation

$$\left(\frac{\partial S}{\partial H}\right)_{P,T} = \left(\frac{\partial M}{\partial T}\right)_{P,H} \tag{1.7}$$

results. Integrating eq. 1.7 for an isothermal (and isobaric, $dP = 0$) process, with the magnetic field changing from H_1 to H_2 ($\Delta H = H_2 - H_1$):

$$\Delta S\left(T, H_2\right)_{P,\Delta H} = \int_{H_1}^{H_2} \left(\frac{\partial M}{\partial T}\right)_{P,H} dH \tag{1.8}$$

At a constant pressure P, the total entropy of a magnetic solid is a function of both the applied magnetic field, H, and the temperature, T. As a solid magnetic material refrigerant contains two energy reservoirs, the usual phonon excitations and the magnetic excitations, generally well coupled by the spin lattice coupling [15], the total entropy for rare-earth compounds is assumed to be the combination of the lattice (S_L), electronic (S_e) and magnetic (S_M) contributions:

$$S_{Total}\left(T, H\right) = S_L\left(T\right) + S_e\left(T\right) + S_M\left(T, H\right), \tag{1.9}$$

where, in a first approach, only S_M varies with H. It must be pointed out that in the case of $3d$ materials, separation of electronic and lattice contributions is not straightforward [8].
In a isothermal process, if the magnetic field varies ΔH the magnetic entropy of the material changes (it can be reduced or increased), whereas both S_L and S_e remain unchanged in a first approximation. Therefore, the value of $\Delta S_M\left(T, H_2\right)_{P,\Delta H}$ at a constant temperature T is given by:

$$\begin{aligned} \Delta S_M\left(T, H_2\right)_{P,\Delta H} &= \left[S_M\left(T\right)_{H_2} - S_M\left(T\right)_{H_1}\right]_{T,P} \\ &= \left[S\left(T\right)_{H_2} - S\left(T\right)_{H_1}\right]_{T,P} = \Delta S\left(T, H_2\right)_{P,\Delta H}. \end{aligned} \tag{1.10}$$

Nevertheless, when the magnetic field is changed adiabatically by ΔH, the combined lattice and electronic entropies change by $\Delta\left(S_L + S_e\right) = -\Delta S_M$. Such change in the lattice entropy results in a measurable variation of temperature, the so-called adiabatic temperature change, ΔT_{ad}, of

the magnetic material, which is also used to describe the MCE. ΔT_{ad} is also a function of the temperature, and is given by

$$\Delta T_{ad}\left(T, H_2\right)_{P,\Delta H} = \left[T\left(S\right)_{H_2} - T\left(S\right)_{H_1}\right]_{S,P} \tag{1.11}$$

for a fixed ΔH and arbitrary T. Let's now obtain a formula which describes the adiabatic temperature change of a magnetic substance.

The differential of the total entropy of the magnetic system, expressed as a function of T, P and H, is

$$dS = \left(\frac{\partial S}{\partial T}\right)_{P,H} dT + \left(\frac{\partial S}{\partial P}\right)_{T,H} dP + \left(\frac{\partial S}{\partial H}\right)_{T,P} dH. \tag{1.12}$$

Under an adiabatic and isobaric ($dS = dP = 0$) process

$$\left(\frac{\partial S}{\partial T}\right)_{P,H} dT = -\left(\frac{\partial S}{\partial H}\right)_{T,P} dH. \tag{1.13}$$

Taking into account the definition of the heat capacity for a set of constant parameters x

$$C_x = T\left(\frac{\partial S}{\partial T}\right)_x, \tag{1.14}$$

and eq. 1.7, the variation of temperature due to a infinitesimal change of the applied magnetic field is given by:

$$dT = -\frac{T}{C_{P,H}}\left(\frac{\partial M}{\partial T}\right)_{P,H} dH. \tag{1.15}$$

Integrating eq. 1.15,

$$\Delta T_{ad}\left(T, H_2\right)_{P,\Delta H} = -\int_{H_1}^{H_2} \left(\frac{T}{C_P\left(T, H\right)}\right)\left(\frac{\partial M}{\partial T}\right)_{P,H} dH, \tag{1.16}$$

gives the adiabatic temperature change.

It is also possible to determine the magnetic entropy change through the definition of the heat capacity. According to the second law of thermodynamics, an infinitesimal change of entropy, at constant magnetic field and pressure, can be written down as

$$dS = \frac{C_{P,H}\left(T, H\right)}{T} dT. \tag{1.17}$$

Integrating eq. 1.17, and taking into account that, according to the third law of thermodynamics, the entropy at $T = 0$ is assumed to be zero,

$$\Delta S_M\left(T, H_2\right)_{P,\Delta H} = \Delta S\left(T, H_2\right)_{T,P,\Delta H} = \int_0^T \frac{C_{P,H_2}\left(T\right) - C_{P,H_1}\left(T\right)}{T} dT. \tag{1.18}$$

MCE is determined by both $\Delta S_M(T, H)$ and $\Delta T_{ad}(T, H)$. Thus, eqs. 1.11 and 1.18 completely define the MCE in magnetic solids. Eq. 1.11 is often employed in direct measurements of ΔT_{ad}: the temperature of the magnetic material is measured in both H_1 and H_2, and the difference between the two temperatures yields the intensive MCE value [16, 17]. On the other hand, isofield measurements of the heat transfer and, therefore, measurements of ΔS_M using eq. 1.18, are seldom performed in practice, because the numerical integration involved in evaluating the total entropy function may result in the accumulation of errors that can reach 20-30 % [18, 19]; also the heat capacity measurements must be carried out starting as close to the absolute zero as possible.

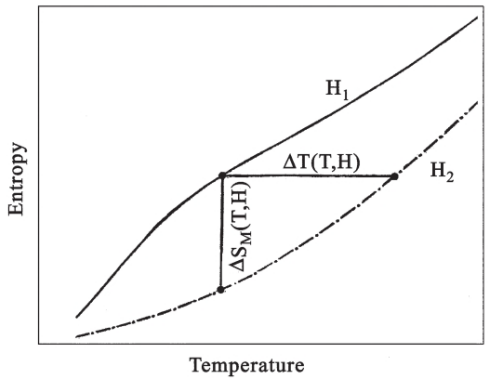

Figure 1.1: Temperature dependence of the total entropy for H_1 and H_2 applied fields. Both the isothermal magnetic entropy change, $\Delta S_M\,(T)_{\Delta H}$, and the adiabatic temperature change, $\Delta T_{ad}\,(T)_{\Delta H}$, for the given temperature T, are shown as thick vertical and horizontal bars respectively [12].

For this reason, indirect measurement of ΔS_M, which involve measuring the magnetization isotherms as functions of H (eq. 1.8) for different temperatures, is the usual way to determine this extensive variable of the MCE [19].

An indirect method to determine ΔT_{ad} is based on eq. 1.16, which needs to express the heat capacity as a function of T and H, and the magnetization isotherms as well. However, using the ΔS_M data it is also possible to calculate the ΔT_{ad} if the heat capacity at constant field is available: the ΔT_{ad} values can be extracted as the isentropic distance between the two isofield curves for H_1 and H_2 on the entropy-temperature (ST) diagram (see fig. 1.1) [16, 20].

It is worth noting that changing the pressure and the applied magnetic field simultaneously, it is produced the so-called magneto-barocaloric effect [21]. However, there are not many studies concerning this phenomena, so, commonly, pressure changes are avoided in magnetic refrigeration to avoid the barocaloric effect.

Taking into account that samples are under vacuum during the measurements, hereafter we assume that the absolute pressure of the system is constant, so P is not taken into account. Also, we will estimate the magnetic entropy change using as starting applied magnetic field, $H_1 = 0\,\mathrm{T}$. Therefore, we will refer $\Delta S_M\,(T, H_2)_{P,\Delta H}$ like $\Delta S_M\,(T, H_2)$.

Analyzing eqs. 1.8 and 1.16, some general features of the MCE in solids with a second order magnetic phase transition can be derived:

- ⋆ As the MCE depends on $\partial M/\partial T$ and ΔH, those materials whose total entropy is strongly influenced by a magnetic field, and whose magnetization varies rapidly with temperature, are expected to exhibit a large MCE.
- ⋆ For ferromagnetic materials, the magnetization decreases with temperature ($(\partial M/\partial T)_{P,H} \leq 0$). Thus, for positive field changes, ΔT_{ad} is positive, while ΔS_M is negative.
- ⋆ As $|(\partial M/\partial T)_{P,H}|$ is maximum at T_C, $|\Delta S_M|$ peaks at $T = T_C$. The MCE is gradually lowered both below and above the T_C.
- ⋆ ΔT_{ad} will be larger at higher T and lower heat capacity.
- ⋆ Paramagnetic solids, since $(\partial M/\partial T)_{P,H}$ is small, can only show a relevant ΔT_{ad} value when the heat capacity is also very small.

1.1.2 Magnetic refrigeration

The MCE has been successfully used to achieve ultra low temperatures, since Debye (1926) [22] and Giauque (1927) [23] proposed the idea of utilizing reversible temperature changes in $Gd_2(SO_4)_3 8H_2O$ paramagnetic salts, and Giauque and MacDougall (1933) reached 0.25 K by means of the so-called "adiabatic demagnetization" [24]. Before, Langevin (1905) had demon-

strated that the change of a paramagnet magnetization would result in a reversible temperature change. Since these years, magnetic refrigeration has been used for attaining ultra low temperatures and for gas liquefaction, like hydrogen, helium and nitrogen.
However, the first magnetic refrigerator operating around room temperature was reported in 1976 by Brown [25]. This prototype was unnoticed until Zimm developed a magnetic refrigerator in 1996, which used approximately 3 kg of Gd as working material and generated up to 500-600 W cooling power in a 5 T magnetic field [26]. Later on, an increase of the research efforts has been produced. Research on the MCE has experienced a nearly exponential growth [27], appearing several families of materials which were found to be interesting from the point of view of magnetic refrigeration. In fact, in 1997 the discovery of the "giant" MCE in the $Gd_5Si_2Ge_2$ compound by Pecharsky and Gschneidner marked a new milestone [28], that led to the development of different magnetic refrigeration systems for room temperature applications [5]. After that, more than 25 prototype of magnetic refrigerators operating at room temperature have been successfully built and tested.

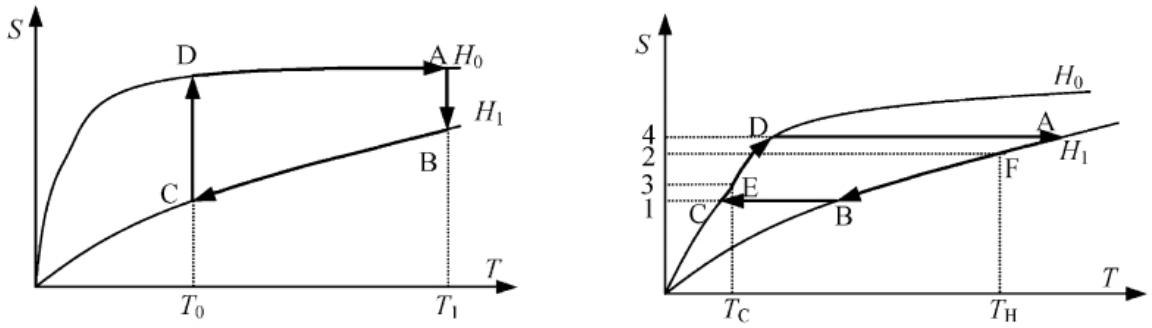

(a) Ericcsson cycle.

(b) Bryton cycle.

Figure 1.2: Main thermodynamic cycles used in magnetic refrigeration at room temperature [5].

At low temperatures, the thermodynamic cycle used on magnetic refrigeration is the Carnot cycle. This cycle consists of two adiabatic and two isotherm processes. When the operation temperature of a magnetic refrigerator is shifted over 20 K, the heat capacity of a magnetic working substance becomes larger, and the adiabatic temperature change occurring due to magnetic field change becomes smaller. Therefore, the Carnot thermodynamic cycle cannot be used in room temperature refrigeration systems [29]. Instead, the used thermodynamic cycles for magnetic refrigeration at room temperature are regenerative cycles, which can operate at higher temperatures and with larger temperature spans [30]. Those cycles are Ericsson, Brayton (see fig. 1.2) and active magnetic regenerator (AMR) [5, 31] cycles.

Ericsson's cycle consists of two isothermal processes, represented by $A \rightarrow B$ and $C \rightarrow D$ in fig. 1.2(a), and two isofield steps (corresponding to H_0 and H_1, with $H_0 < H_1$ in fig. 1.2(a)), labeled by $B \rightarrow C$ and $D \rightarrow A$. Brayton's cycle consists also of two isofield stages ($A \rightarrow B$ and $C \rightarrow D$ in fig. 1.2(b)), but changing the two isothermal for adiabatic processes ($B \rightarrow C$ and $D \rightarrow A$). In both cases, the maximum refrigeration efficiency is attained with constant magnetic entropy change ΔS_M curves. Deviation causes irreversibility and the generation of entropy in the system. In most cases it is better for the material to have wide $\Delta S_M(T)$ and $\Delta T(T)$ dependences [7]. In order to obtain a constant $\Delta S_M\,(T)$, several authors have suggested using a complex magnetic refrigerant composed of several ferromagnetic nanocomposites or layers of magnetic materials with different transition temperatures [32–34].

AMR thermodynamic and Brayton cycles are closely related, because in an ideal AMR cycle each element of the magnetic material is carried through a Brayton cycle [30]. The main difference between them is that in the latter case the regenerator (a thermal device which returns the heat expelled by the magnetic material in one step to it in another point of the magnetic cycle) is filled with a magnetocaloric material, so a heat transfer fluid can flow through the bed [5, 32, 35].

It is interesting to note that, in the conventional refrigeration, the gas refrigerant interchanges heat directly with the environment and the load. In magnetic refrigeration, the refrigerant is a solid which cannot be pumped through the heat exchanger. Instead, a fluid is used to transfer heat between the load and the magnetic refrigerant.

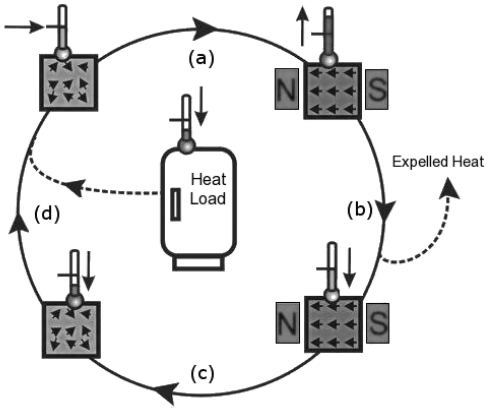

Figure 1.3: Scheme of a Brayton cycle [36].

The main steps of a passive magnetic refrigerator based on the magnetic Brayton cycle (see fig. 1.3) going from the cold source to the hot sink are: a) Disordered magnetic moments are aligned by the action of a magnetic field in an adiabatic way, thus the magnetic entropy decreases. Following eq. 1.9, the magnetic material is heated because the entropy of the lattice is increased. b) Heat is then removed from the material by a heat-transfer medium. This heat amounts the area AB14 in fig. 1.2(b). c) The field is then removed adiabatically, and as a consequence, the magnetic moments randomize. The magnetic entropy increases, thus the refrigerant is cooled below the temperature at which the magnetic field was previously applied. d) Heat from the load is extracted using again a heat-transfer medium. The amount of heat to be absorbed is the area DC14.

A basic AMR thermodynamic cycle can be divided also into four steps [35, 37] (see fig. 1.4): a) The bed is in a demagnetized state. Fluid flows through the regenerator from the hot to the cold end entering the bed at a temperature T_H. As the fluid flows through the bed it is cooled by the solid refrigerant, and exits the bed at T_C, where can absorb a heat load through a heat exchanger. b) A high magnetic field is applied, thus the temperature of the refrigerant increases by the local MCE value. c) The fluid flows through the magnetized regenerator from the cold to the hot end, absorbs heat from the bed, and delivers a heat load to the warm sink through a heat exchanger at the hot side of the bed. The fluid enters the cold end of the regenerator, absorbs heat from the bed, and exits the AMR bed at a tempera-

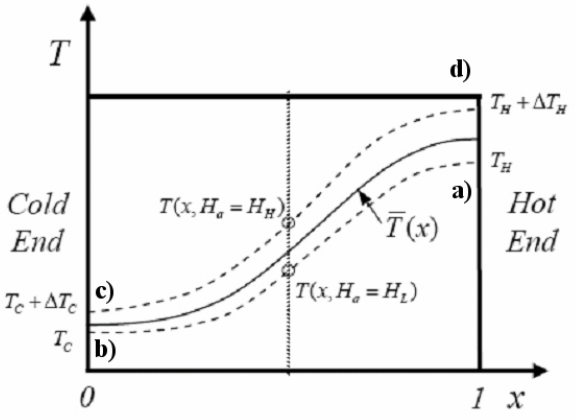

Figure 1.4: Scheme of an active magnetic regenerator. The solid curve shows the average temperature through the length of the bed. The dashed lines show the temperature of the refrigerant just after magnetization and demagnetization processes [37].

ture $T + \Delta T_H$. d) The AMR is now demagnetized, and its temperature decreases due to the local MCE.

Unique features of an AMR cycle are that at each section the refrigerant undergoes its own refrigeration cycle, as the matrix of magnetic materials is subjected to a spatially and temporally varying magnetic field and fluid flow rate, which allows multiple bed configurations [38, 39]. Since the temperature gradient in the packed bed becomes steeper with each repetition of the cycle, the temperature difference between the hot and cold ends increases gradually.

The properties that a magnetic substance must fulfill for its applicability in magnetic refrigeration are not only the magnitude of the MCE, but also the magnetic cooling power and the temperature range within the magnetic material is useful. The relative cooling power (RCP) of a substance indicates how much heat can be transferred between this material and its environment, from the cold end to the hot end of a thermodynamic cycle. There are several attempts, in the literature, to quantify the RCP for a magnetic material to be potentially used in a magnetic refrigeration system [13, 40, 41]; the simplest and most used is the so-called RCP_1, which consists of the calculus of the area of a rectangle whose base equals the full width at half maximum of the $\Delta S_M(T)$ curve (δT_{FWHM}), and height equals $|\Delta S_M^{Peak}|$:

$$RCP_1(H) = |\Delta S_M^{Peak}(H)| \times \delta T_{FWHM}. \tag{1.19}$$

The RCP_2 results from the area under the $\Delta S_M(T)$ curve between those temperatures corresponding with its full width at half maximum:

$$RCP_2(H) = \int_{T_C}^{T_H} |\Delta S_M(H,T)| \; dT. \tag{1.20}$$

Wood and Potter proposed another criterion of efficiency of the working material, referred as RCP_3; it is obtained maximizing the rectangle $|\Delta S_M| \times \delta T_{Cyc}$, where $\delta T_{Cyc} = T_{hot} - T_{cold}$ is the operating temperature range of a cycle. ΔS_M is supposed to be constant over the cycle. This value also determines T_{hot} and T_{cold} for which the material is more efficient. It must be pointed out that these definitions are useful when the magnetic entropy change has well-resolved peaks, and, thus, those definitions can be used in each peak.

An optimum material for application in room temperature magnetic refrigeration must fulfill several features [1, 5, 42]:

- ⋆ Low cost of the magnetic solids and their processing.
- ⋆ Harmless.
- ⋆ Molding and processing of the magnetic materials appropriate for the magnetic refrigeration.
- ⋆ Small specific heat and large thermal conductivity, which ensures a remarkable temperature change with the fastest heat exchange.
- ⋆ Large electric resistance to avoid the eddy current loss.
- ⋆ Curie temperature in the vicinity of working temperature, guaranteeing that the magnetic entropy change can be gained in the whole temperature range of the cycle.
- ⋆ Essentially zero magnetic hysteresis, which avoids magnetic-work losses each refrigeration cycle.
- ⋆ Large spontaneous magnetization with a sharp drop at its critical temperature.
- ⋆ Large relative cooling power.

These two last conditions are fulfilled in materials with a large magnetic entropy change and a broad $\Delta S_M(T)$ peak. Due to their high magnetic moments, heavy rare-earth elements and their compounds are considered the best candidate materials to obtain a large MCE. Not in vain the highest MCE involving a second-order phase transition known so far is produced by the rare-earth metal Gd [43].
Other interesting compounds suitable for magnetic refrigeration are the amorphous magnetic materials, which may have a large $\Delta S_M\,(T)$ width, which can be broader than those of the crystalline magnetic refrigerants. Furthermore, their high electrical resistivity, tailorable nature associated with their disordered structure, outstanding mechanical properties, and high thermally stability, make them good candidates as magnetic refrigeration materials [42].

The advantages of the magnetic refrigeration compared to their household analogues are [2, 13, 15, 43, 44]:

- ⋆ Less energy consumption: the work done by a compressor in a conventional refrigerant system can be done by a permanent magnet in several magnetic systems.
- ⋆ High cooling efficiency: magnetic refrigerators working with gadolinium reached 60% of the theoretical limit, compared with only about 40% in the best gas-compression refrigerators.
- ⋆ The cooling power can be varied by scaling from milliwatt to a few hundred watts or even kilowatts.
- ⋆ It is an environmental friendly technology, as it does not use ozone depleting chemicals (CFCs), hazardous chemicals (NH_3) or greenhouse gases (HCFCs, HFCs, PFCs,...). Moreover, CO_2 emissions are also reduced.
- ⋆ Simple design of machines, e.g. rotary porous heat exchanger refrigerator.
- ⋆ Low maintenance costs.
- ⋆ Large durability and stability.
- ⋆ Disappearance of mechanical vibrations and noise.
- ⋆ Low pressure (this is an advantage in certain applications such as in air-conditioning and refrigeration units in automobiles).

1.2 Magnetovolume anomalies

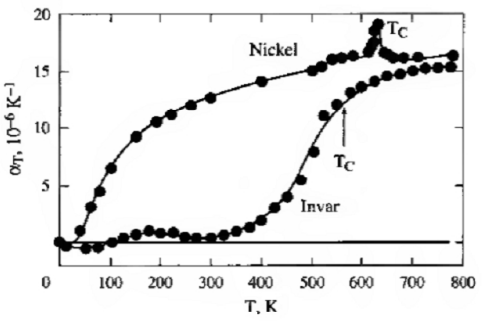

Figure 1.5: Temperature dependence of the linear thermal expansion coefficient of Invar®$Fe_{64}Ni_{36}$ and nickel [45].

The Invar effect was the first reported magnetovolume anomaly (Guillaume, 1897), consisting in an almost constant thermal expansion in a wide range below the Curie temperature [46]. Materials exhibiting this kind of behavior are used where high stability is required, such as precision instruments, clocks, seismic creep gauges, valves in motors, ...

As in chapter 3 some results are related with magnetovolume anomalies, outstanding theoretical aspects are presented here.

Experimental relative volume change, $\omega_{exp} = (\Delta V/V)_{exp}$, has two main components, the lattice vol-

ume, ω_{latt}, and the magnetic contribution, represented by the spontaneous volume magnetostriction ω_s [46, 47]. ω_s is the responsible of the magnetovolume effects, and is related with α_m, the magnetic contribution to the thermal expansion coefficient (see fig. 1.6) by the following equation [46]:

$$\omega_s(T) = 3\int_{T_1}^{T} \alpha_m(T')\,dT', \tag{1.21}$$

where T_1 is a reference temperature for which ω_s vanishes. It must be noted that eq. 1.21 is a simplification, because the thermal expansion coefficient is a second rank symmetric tensor [48].

Let's calculate ω_s. Assuming that $\alpha_{exp}(T) = \alpha_{nm}(T) + \alpha_m(T)$, where α_{exp} is the experimental thermal expansion coefficient, and $\alpha_{nm}(T)$ denotes the non-magnetic term of the thermal expansion (which takes into account the phonon and the electron contribution), it is firstly necessary to separate the magnetic contributions to the thermal expansion from the lattice contribution.

This is usually done by extrapolating the temperature variation of the lattice parameters from the paramagnetic range. For this reason, $\alpha_{exp}(T)$ is fitted in the paramagnetic region for temperatures well above T_C, thus $\alpha_{nm}(T)$ is estimated in this region. This is doing assuming a quasiharmonic approximation, a simple Debye model for the phonons, and a classical specific heat contribution, by means of the Grüneisen relation,

$$\alpha_{nm}(T) = \frac{\kappa\Gamma C_p(T)}{3V}, \tag{1.22}$$

with κ being the isothermal compressibility, Γ the Grüneisen parameter, V the molar volume and C_p the specific heat [49, 50]. The Grüneisen parameter is a measure of the anharmonic interactions (higher than quadratic terms in the inter-atomic displacements), which play an important role in describing properties like thermal expansion, thermal conductivity and decay of elastic waves [51]. Commonly, the electronic and phonon contributions to the total thermal expansion α_{exp} are taken into account [52], being the electric term

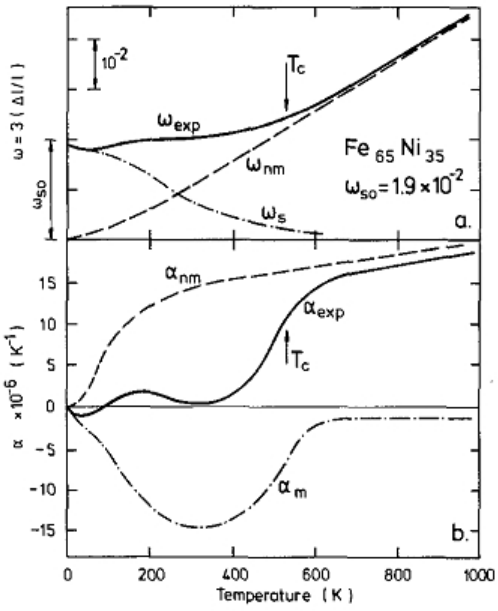

Figure 1.6: a) Temperature dependence of the experimental thermal expansion (full line), together with the magnetic α_m (dashed line) and extrapolated non-magnetic α_{nm} (dashed-dotted line) contributions for $Fe_{65}Ni_{35}$ Invar® alloy. Extrapolated non-magnetic part represents the phonon contribution to the thermal expansion. b) Temperature dependence of the experimental thermal expansion (continuous line) for $Fe_{65}Ni_{35}$ Invar® alloy. The dashed line gives the temperature dependence of the non-magnetic term determined using the Grüneisen relation. The magnetic part α_m (dashed-dotted line) results from the difference $\alpha_{exp} - \alpha_{nm}$. The Curie temperature is marked by an arrow [46].

$$C_e(T) = \gamma_e T, \tag{1.23}$$

and using the Debye theory to evaluate the phononic part of C_p

$$C_{ph}(T) = 9NK_B \left(\frac{T}{\theta_D}\right)^3 \int_0^{\theta_D/T} \frac{x^4 e^x}{(e^x - 1)^2} dx, \tag{1.24}$$

Usually, κ and γ coefficients are estimated fitting eq. 1.22 to the slope of the experimentally determined relative volume change curve in the paramagnetic range well above T_C (see fig. 1.6). Extrapolating this non-magnetic term to low temperature and subtracting it to the experimental data, the spontaneous magnetostriction is obtained by means of eq. 1.21.

The volume magnetostriction has been discussed in terms of the localized-moment or itinerant-electron models. ω_s in the localized-moment model is related to the two-spin correlation function $m_i \times m_j$ as

$$\omega_s = \sum_{i,j} \kappa C_{int}(m_i \times m_j), \tag{1.25}$$

where κ is the compressibility, C_{int} the magnetovolume coupling constant for the localized-moment mechanism, and i, j are the neighboring lattice sites. On the other hand, ω_s is related to the mean-square amplitude of the local magnetic moment:

$$\omega_s = \kappa C_{band} \left\langle M_{loc}^2 \right\rangle, \tag{1.26}$$

where C_{band} is the magnetovolume coupling constant from the band contribution.

In general, the magnetic system belongs to an intermediate regime between these two limits, and both localized-moment and itinerant-electron pictures contribute to the volume magnetostriction [53]. In the case of R-T intermetallics, ω_s can be phenomenologically described by:

$$\omega_s = n_{RR}\mu_R^2 + n_{RT}\mu_R\mu_T + n_{TT}\mu_T^2 \tag{1.27}$$

where μ_R and μ_T are the magnetic moments of R and T atom, respectively, n_{RR} and n_{TT} are the magnetoelastic-coupling coefficients in the R and T sublattices, and n_{RT} is the intersublattice magnetoelastic-coupling coefficient [54]. However, for the R_2Fe_{17} alloys, n_{RR} and n_{RT} coefficients are negligible.

1.3 R_2Fe_{17} alloys

A wide family of magnetic intermetallic compounds arises from the alloy of rare-earth (R) and 3d transition metals (M). In fact, the number of such compounds amounts over a thousand. [55]. Localized magnetism of rare-earth sublattice combined with an itinerant magnetism of 3d sublattice, makes these magnetic intermetallics very attractive from bot fundamental Solid State Physics and commercial applications.

In the case of 3d transition metals, stable R-M compounds have been obtained only for M = Mn, Fe, Co or Ni, where the unpaired 3d electrons of the transition metal component give rise to a net magnetic moment in most cases. The magnetic interactions in R-M compounds comprise, therefore, three different types: the R-R interaction, the R-M interaction and the M-M interaction. The R-R interaction is the weakest due to the localized character of the electrons.

The high Fe-content R_2Fe_{17} intermetallics present polymorphism, crystallizing into two kind of structures depending on the atomic weight of the rare-earth. From Ce to Sm the crystal structure is rhombohedral Th_2Zn_{17}-type ($R\bar{3}m$ space group), with the rare-earth occupying an unique crystallographic site, $6c$ (labeling for the R element and Fe atomic coordinates is the same as that used in the International Tables for Crystallography, i.e., Wychoff notation [56]), whereas the Fe atoms occupy four inequivalent positions: $6c$, $9d$, $18f$, $18h$ [57]. The crystal symmetry is hexagonal Th_2Ni_{17}-type ($P6_3/mmc$ space group) for Dy to Lu, with the rare-earth occupying two different sites: $2b$ and $2d$, characterized by a quite similar local atomic arrangement of Fe next-neighbors and by a slight different arrangement of the rare-earth atoms. The Fe atoms also occupy four positions: $4f$, $6g$, $12j$ and $12e$ [58]. In fig. 1.7 a sketch of the unity cell for each crystal structure are depicted. In the case of Ho, Tm and Lu several authors have pointed out the existence of disordered crystal structures [59–62], in which extra positions, not fully occupied, for the rare-earth ($2c$) and the Fe ($4e$) are considered. Furthermore, R_2Fe_{17} alloys with R = Y, Gd and Tb can exhibit both crystal structures depending on the annealing temperature [63].

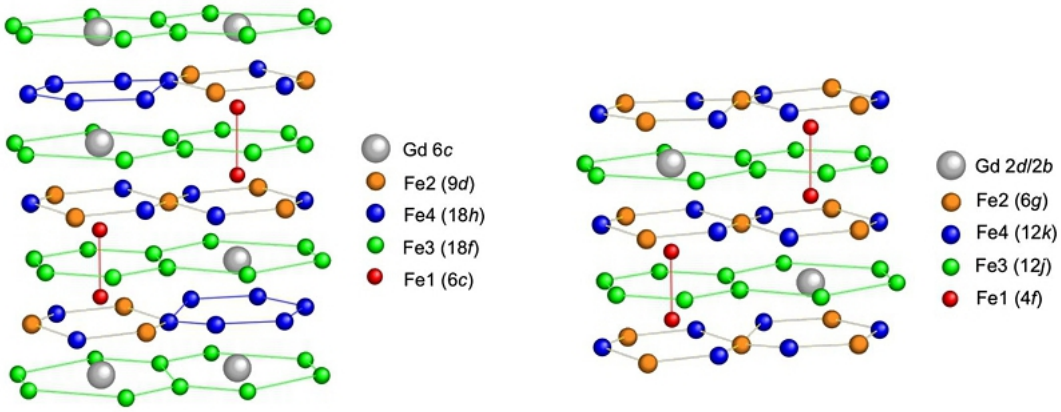

Figure 1.7: Left plot: Sketch of the rhombohedral crystallographic unit cells of the R_2Fe_{17} alloys. Right plot: Sketch of the hexagonal crystallographic unit cells of the R_2Fe_{17} alloys [64].

Both rhombohedral and hexagonal structures are derived from a hexagonal $CaCu_5$-type structure by the ordered substitution of one-third of rare-earth atoms in the basal plane by a pair (dumb-bell) of Fe atoms. In the rhombohedral Th_2Zn_{17}-type form, these substituted layers are stacked in the sequence $ABCABC\ldots$ along the c axis on the $CaCu_5$-type structure, and each unit cell contains three formula units. In the hexagonal Th_2Ni_{17}-type form, the ordering is, instead, $ABAB\ldots$ along the same direction, and the unit cell contains two formula units [59, 65, 66]. It is worth noting that, as a consequence, the cell volume of rhombohedral-type over cell volume of hexagonal-type is almost 3/2.

In this family of compounds, the magnetic behavior is determined mainly by the Fe sublattice. The magnetic coupling of the Fe magnetic moments depends on the Fe-Fe interatomic distance. For distances lower than 2.45 Å, the exchange coupling favors an antiparallel alignment of the magnetic moments, whereas for longer distances they are parallel [63]. Moreover, these alloys can exhibit different magnetic behavior: ferromagnetism (e.g. Pr_2Fe_{17}), ferrimagnetism (e.g. Tb_2Fe_{17}), helimagnetism (e.g. Ce_2Fe_{17}),... The majority of the alloys of this family present a magnetic ordering temperature close to room temperature. Furthermore, T_C is well below to that

of pure Fe (1073 K), even though the values of the magnetic moments of the Fe atoms in these compounds are almost the same as that of pure Fe (2.2 μ_B) [67]. It is believed that this variety of behaviors is due to a competing ferro- and antiferromagnetic interactions between some Fe atoms, mainly those at the $6c$ and $4e$ positions, the so-called dumb-bell sites, in the rhombohedral and hexagonal crystal structures respectively. The strong dependence of the magnetic interactions with interatomic distances causes a decrease of the Curie temperatures magnetovolume effects, where the anomalous thermal expansion below the ordering temperature or the negative pressure dependence of the ordering temperature are the most representative features [68, 69].

1.4 FeZrBCu amorphous ribbons

Amorphous alloys, called metallic glasses when are obtained by rapidly quenching from the melt, are characterized by a structural disorder, which leads to different behavior with respect to their properties when are compared to their crystalline counterparts. The first explicit reported ferromagnetic amorphous alloy was the sputter-deposited thin-film Co-Au, following the earlier theoretical prediction of amorphous ferromagnetic materials [70–72]. In a glassy metal the symmetry is absent and each atom constitutes a structural unit. For this reason, they are in a metastable state and, accordingly, tends to transform towards the stable crystalline phase through structural relaxation phenomena. Those materials exhibit lower electric conductivity than crystalline ones, which reduces the losses for eddy currents [73]. Nevertheless, their mass density, magnitude of magnetic moments, and other properties are similar to those of crystalline compounds, suggesting that there exhists a short-range order similar to that in crystalline materials of the same composition [65, 74, 75].

Magnetic properties of amorphous alloys are strongly affected by bond and chemical disorder, because they have a distribution of both magnetic moments and exchange interactions. Common ferromagnetic and ferrimagnetic behaviors are observed in many amorphous materials, but new magnetic structures arise from the structural disorder [76, 77]: non-collinear speromagnetic, asperomagnetic and sperimagnetic order, which occur due to a competing random anisotropy and exchange interaction, and spin-glass behavior, which comes from the existence of competing positive and negative exchange coupling. Spin-glass materials exhibits a typical spin-freezing temperature, defined experimentally by a sharp peak in the low-field susceptibility.

Some ferromagnetic glassy metals have large values of saturation magnetization (M_S), permeability and Curie temperatures. Fe-rich amorphous alloys with general formula Fe_xM_{100-x} ($x \geq 80$), being M an early transition metal (Zr, Hf,...) or a metalloid (B, Si,...), can be considered as amorphous iron stabilized by small amounts of impurities [78]. Metalloid addition decreases the melting temperature and increases the glass transition temperature, T_g (which is the critical temperature at which the material changes from being hard and brittle to elastic and flexible), thus favoring the formation of the amorphous alloys. Also the magnetic properties can be modified by the transfer of electrons from the metalloid to the 3d Fe atom [79]. These glassy metals are formed by cooling the melt below T_g. The cooling rate required to avoid the development of the long-range order in these Fe-based alloys is on the order of $10^5\,\mathrm{Ks}^{-1}$ [80].

Within this family of Fe-based amorphous metals, Fe-Zr-B alloys, or commercially known as "Nanoperm" alloys when the nanocrystalline phase that is gained after a heat treatment, present

an atomic configuration which consists of triangle prisms connected with each other through glue atoms, mainly some Zr. Such a structure favors the stabilization of the supercooled liquid in the Fe-Zr-B type glassy alloys [80]. These alloys can exhibit "spin-glass-like" reentrant behavior, exceptional magneto-volume effects, as well as a reduction of T_C with increasing Fe content, due to the strong competition between Fe-Fe magnetic interactions [78, 81, 82].

1.5 Motivation

Our interest in studying Fe-based magnetic materials was motivated by the fact that the magnetic entropy change spreads into a wide temperature range when it is associated to second order magnetic phase transitions. Because of that (and the absence of thermal hysteresis), the relative cooling power of these materials are comparable to those of the Gd-based materials displaying first order phase transitions, even though Fe-based magnetic materials exhibit relatively low values of the $\left|\Delta S_M^{Peak}\right|$. Furthermore, most of the selected compounds have transition temperatures in the range 200-380 K, which are appropriate for room temperature applications in magnetic refrigeration. Even more, Fe-rich compounds are cheap and it is relatively easy to prepare several grams of each Fe-based alloy.

In the case of R_2Fe_{17} alloys, some works [83, 84] had shown that, in these alloys, $\left|\Delta S_M^{Peak}\right|$ has a full width at half maximum of the order of 100 K for applied magnetic field changes of 5 T, but not so much effort in this direction has been done. Moreover, the magnetovolume anomalies present near room temperature make them more suitable for magnetic refrigeration, as it prevents the deterioration of the properties of these material with the refrigeration cycles (no large volume changes, as in normal metals, are involved, which avoids the material fatigue). Hence, an extensive study of the crystal and magnetic structure, as well as magnetic properties, has been carried out in this Thesis work.

A severe mechanical processing usually gives rise to drastic changes in the physical-chemical behavior of a material by generating structural disorder and/or modifying its microstructure. In this sense, we are interested in the effects on the magnetic entropy change of the disorder induced by the mechanical milling in the Pr_2Fe_{17} and Nd_2Fe_{17} ball-milled alloys. Moreover, this powder morphology is interesting from the point of view of possible applications because implies a large electric resistance, which avoid the eddy current losses produced in a cycle.

For magnetic refrigeration, the Curie temperature must be in the vicinity of the working temperature to guarantee that the MCE is present in the whole temperature range of the cycle. The Curie temperature of R_2Fe_{17} compounds can be easily tuned by mixing two different rare-earths. For this reason, we have investigated the magnetocaloric properties of several pseudobinary $A_xB_{2-x}Fe_{17}$ alloys, with A and B being two different rare-earths.

We have studied the MCE in FeZrBCu amorphous ribbons series because they are Fe-rich magnetic materials with a Curie temperature close to room temperature. Even more, they have a high electric resistivity and are not easily oxidized. It should be noted that our group has a vast experience in those amorphous materials [85–89]. We have also investigated the magnetocaloric properties of combinations of two alloys with different compositions, with the aim of optimizing the MCE response.

In several amorphous materials the $\Delta S_M(T)$ curves for different applied magnetic fields collapse in a single curve [90, 91]. These studies had been previously done at low field range, so we have extended them to high steady magnetic fields, in order to check the feasibility of the so-called master curve at these fields.

1.6 Aims

The main objectives of the work presented in this thesis are:

I) Determination of the magnetovolume anomalies present in the bulk R_2Fe_{17} alloys. This goal is divided into several tasks:

   (a) Realization of a complete structural characterization of the alloys by means of both x-ray and neutron powder diffraction. Once the crystal parameters are determined, the cell parameters variation, with either temperature or high pressure, will be investigated.

   (b) Analysis of the temperature dependence of the magnetic moment at each crystallographic site.

   (c) A further study of temperature and applied magnetic field dependence of the magnetization under different values of the external pressure (up to 1 GPa) is carried out to determine the effect of pressure on the transition temperature of these alloys.

II) To study the MCE in polycrystalline and amorphous Fe-rich materials with the aim of determine mainly the role of the Fe atoms, and how it can be changed with rare-earths, metalloids and early transition metal. To accomplish this objective, four main points are carried out.

   (a) Estimation of the MCE in Fe-rich R_2Fe_{17} and $A_xB_{2-x}Fe_{17}$ systems, in terms of the variation of the magnetic entropy change with the temperature and the applied magnetic field.

   (b) Fabrication of nanostructured R_2Fe_{17} alloys to investigate the effect of the changes in their microstructure with the duration of ball-milling process in the MCE.

   (c) Magnetic characterization under high steady applied magnetic fields of a series of FeZrBCu ribbons. Estimation and comparison of the magnetic entropy change in these amorphous alloys.

   (d) Characterization of the MCE properties in combined systems of two FeZrBCu ribbons of different composition.

Chapter 2

Experimental

In this work, a several experimental techniques and devices have been used to characterize both structurally and magnetically the families of Fe-based intermetallics, which were synthesized in either amorphous ribbons after quenching or polycrystalline form. Here, these techniques are briefly exposed.

2.1 Fabrication

The studied Fe-based alloys were either in polycrystalline or amorphous form. The fabrication procedures have been different for each type.

2.1.1 Arc-furnace

Figure 2.1: Arc melting furnace.

To synthesize the alloys the conventional arc-melting technique was utilized. As-cast pellets were melted in a MAM-1 arc furnace (Edmund Bühler GmßH), in which the built-in power supply may supply up to 200 A, allowing specimens melt up to 3500 °C, in an argon protection atmosphere, by discharging an electrical arc. The anode is a watter-cooled copper crucible, and the cathode consists in a freely movable sharp rod of tungsten, which is also watter-cooled. The atmosphere of the furnace chamber is controlled by a vacuum-pump and flowing high-purity Ar, which evacuates oxygen, and acts as ionizing gas. A number of meltings with the sample being turned over each time is done in order to ensure a good homogeneity of the alloys, which can be hard to achieve because of the different cooling speed at the bottom (which is in contact with the water-cooled Cu crucible) and the top of the specimen. The specimen is weighted after each melting to control possible weight losses and compensate it with

the rare-earth to obtain the desired stoichiometry. This fabrication procedure presents a drawback when synthesizing R_2Fe_{17}, and is that a residual phase may appear due to Fe segregation in an α phase (usually c.a. 5 %). For this reason, an extra amount of rare-earth was usually added. The purity of elements was, at least, 99.9%.

2.1.2 Heat treatment

In order to both facilitate the homogeneity of the compounds and keep as low as possible the Fe segregation, heat treatments were carried out. As-cooled pellets were wrapped in a tantalum foil and sealed under vacuum or Ar atmosphere in a quartz ampule to avoid oxidation. Then, each ampule was annealed at a fixed temperature between 1200 and 1400 K in a conventional furnace. Annealing was followed by water-quenching.

As it has been already said in the introduction, Y_2Fe_{17}, Gd_2Fe_{17} and Tb_2Fe_{17} intermetallics present polymorphism depending on the annealing temperature. For that reason selected annealing temperatures were chosen to obtain rhombohedral Gd_2Fe_{17} and Tb_2Fe_{17} compounds. In the case of Y_2Fe_{17} alloy, not a single-phase but a two-phase compound was obtained, which will help to study the temperature dependence of both rhombohedral and hexagonal Fe-sublattice moments, because Y has not magnetic moment.

2.1.3 Ball-milling (BM)

Figure 2.2: Planetary ball-mill.

Nanocrystalline Pr_2Fe_{17} and Nd_2Fe_{17} powders were obtained by means of high-energy dry-ball milling. The alloys pearls were manually pulverized by means of an agate mortar. Resulting powders were sieved using a 106 μm pore size metallic sieve. Then, they were sealed together with stainless steel balls in a stainless steel vial under an Ar atmosphere, for minimizing oxidation. Balls were chosen with 10 mm in diameter, and selected ball-to-powder weight ratio was 8:1. Milling process was carried out using a high-energy planetary ball mill (Retsch PM/400) in rotations of 5 min clockwise, followed by 5 min anticlockwise with a break of 5 min in between, which ensured that the temperature was sufficiently low during the milling process to avoid possible recrystallization of samples. This procedure was followed during 10, 20 or 40 h.

2.1.4 Melt-spinning

Ribbons of FeZrBCu intermetallics were prepared by the melt-spinning technique, a method based on the fast quenching of a liquid by means of a moving cooled metallic block that extracts heat from the liquid. The procedure is as follows: mixed elements in powder form were compressed into tablet form and sintered at 700 °C. After that, pill was molten in an induction furnace at temperatures of the order of 1600 °C, and subsequently cast on the outer surface of a wheel, in our case made of stain steel, which rotates at high speed (usually the tangential speed at the

surface of the wheel is around $50\,\mathrm{m{\cdot}s^{-1}}$), forcing the liquid to cool down to room temperature. It forms a ribbon of a few tens of microns thick due to the solidification of the melt when the melt enters in contact with the wheel. Cooling velocities of this technique are of the order of $10^6\,\mathrm{K{\cdot}s^{-1}}$. Ribbons produced in such a way have thickness around $20\,\mu$m, and width of typically $1-2\,$mm.

2.2 Structural characterization

Concerning the structural characterization both the microstructure and the crystalline phases of R_2Fe_{17} were studied. X-ray (XRD) and neutron powder diffraction (ND) are relevant techniques to investigate the crystal structure, and the pressure and temperature dependence of both the lattice parameters and cell volume. Moreover, the mean crystalline size of the nanoparticles, as in the case of the Pr_2Fe_{17} and Nd_2Fe_{17} nanostructured alloys, can be also estimated from powder diffraction patterns. Additionally, grain morphology of ball-milled specimens was directly observed by transmission and scanning electron microscopies.

2.2.1 X-ray and neutron powder diffraction

Both x-ray and neutron powder diffraction are widely used to characterize crystalline phases [92, 93]. In addition, from the angle dependence of the peak width it is possible to estimate the average particle size and the microstrain [94]. As neutron have magnetic moment, it is scattered by atomic magnetic moments, making neutrons particularly suited to investigate magnetic structures and excitations. Indeed, neutron thermo-diffraction (NTD) is commonly used to investigate the temperature induced magnetic and structural transformations in a material [87].

XRD under high pressure is one of the most important experimental methods for measuring the pressure dependence of cell parameters. The main advantage of the x-ray diffraction method lies in the direct measurement of the lattice parameters, allowing the determination of anisotropic effects also in polycrystalline specimens. Especially, distortions of the crystal symmetry can easily be detected by this method.

Information from diffraction patterns was obtained by peak fitting by means of Le Bail (useful to determinate the profile and cell parameters) and Rietveld's methods (refinement of the atomic positions, magnetic moments, and peak width parameters from which mean grain size and microstrain values can be estimated) [95], which are implemented in the *FullProf* suite [96]. Also simulation of neutron diffraction patterns with different magnetic moment configurations and/or crystal structure were done using this software, in order to optimize the neutron and x-ray powder diffraction experiments.

Conventional x-ray powder diffraction

Diffraction patterns at room temperature were collected in two powder diffractometers at the University of Oviedo:

Philips X' PERT Pro: diffractometer working in reflexion mode with Cu $K\alpha$ radiation ($\lambda_1 =$ 1.541 Å and $\lambda_2 =$ 1.544 Å). An angle step of $\Delta\theta = 0.02°$, and counting times of 20 s per point were used.

Seifert XRD 3000 T/T: diffractometer working in Bragg-Brentano geometry mode with Mo $K\alpha$ radiation ($\lambda_1 = 0.7093$ Å and $\lambda_2 = 0.7136$ Å). An angle step of $\Delta\theta = 0.01°$, and counting times of 40 s per point were used.

Synchrotron x-ray powder diffraction with pressure

Synchrotron powder diffraction (SPD) experiments under high pressure were carried out in the instrument ID27 at the ESRF (Grenoble, France). Powders were pressurized in a diamond anvil cell at room temperature. The selected pressure-transmitting medium was Neon. A small ruby chip was also loaded in the sample chamber for pressure calibration. SPD patterns were recorded using a high-brilliance rotating anode generator. The collecting time for each pattern was 1 min. The full Debye ring patterns were processed and reduced to intensity versus 2θ patterns using Fit2D software [97].

Neutron powder diffraction

In the case of neutron powder diffraction, experiments were carried out at the Institut Laue-Langevin, placed in Grenoble, France, in four different two-axis powder diffractometers: D1A, D2B, D1B and D4. A schematic view of a two-axis diffraction pattern is shown in fig. 2.3.

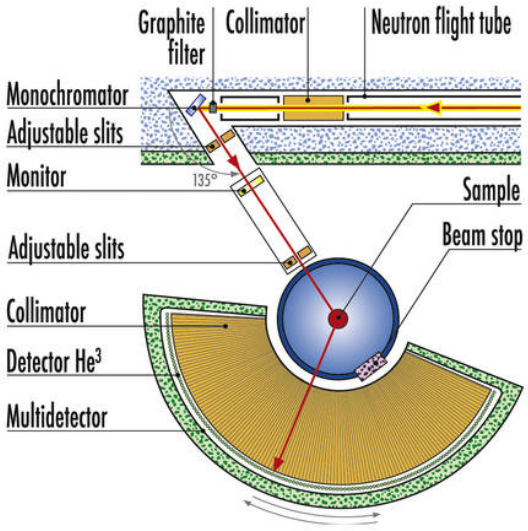

Figure 2.3: D2B, a high-resolution neutron powder diffractometer at the ILL.

D1A and D2B: they are high resolution diffractometers, which were used for determining accurately the crystallographic parameters.

Measurements in D1A were done in a cryo-furnace in the temperature range (250 ,450 K) with wavelength $\lambda = 1.91$ Å.

The wavelength of D2B was selected to $\lambda = 1.60$ Å using the Ge[335] direction. Experiments were done in the temperature range (2 , 400 K) using a cryostat and a furnace.

D1B: this is a high flux diffractometer suited for investigating phase transitions by means of thermo-diffraction experiments, and for determining the magnetic structure. Experiments were carried out in the temperature range between 5 and 850 K combining a conventional orange cryostat and a vanadium furnace. The wavelength $\lambda = 2.52$ Å is selected with a pyrolytic graphite (002) monochromator. The angular range in 2θ is (20°, 100°) with a $\Delta 2\theta = 0.2°$.

D4: uses short-wavelength ($\lambda = 0.50$ Å) neutrons from the hot source. As neutron absorption cross section depends on the wavelength [93], this instrument allows to study the magnetic structure of very absorbent systems, as those containing Gd. The angular range in 2θ is (0°, 140°) with a $\Delta 2\theta = 0.125°$. Diffraction patterns were taken in the temperature range from 2 to 500 K.

2.2.2 Scanning and transmission electron microscopy

Electron microscopy produces an electronically-magnified image of a specimen by means of an electron beam. Because it uses accelerated electrons with energies up to 400 keV, it has a great resolving power, attaining 0.5 Å for high-resolution transmission electron microscopy [98]. When a beam of accelerated electrons comes into contact with a material, different interaction processes takes place (e.g. transmitted electrons, secondary electrons, back-scattered electrons, characteristic x-rays,...). The main electron microscope advantages over diffraction techniques are that the specimen do not need to be neither a single crystal nor a polycrystalline powder, and also that the image of the sample is in the real space [99]. However, three-dimensional crystal structures are determined exclusively from diffraction data [95].

Scanning (SEM) and Transmission (TEM) Electron Microscopy were utilized to study the microstructure, and the size and shape of grains of the ball-milled samples at the micrometer and nano-length scales.

Scanning electron microscopy

In an inelastic collision between a beam of electrons and an electron belonging to an atom in a material, some amount of energy is transferred to the bonded electron. If the transferred energy exceeds the work function of the material, such electron would exit the solid. Those released electrons are used in the SEM technique to obtain the image of the specimen surface. High topological contrast is achieved because the efficiency of generating those secondary electrons strongly depends on the angle at which the probe beam strikes the surface. Nevertheless, if the energy transfered is very small, the emitted electron will probably not have enough energy to exit the material, and x-rays can be produced when decaying to its ground state. The x-ray emission signals, sorted by energy in an energy dispersive x-ray detector (EDS), are characteristic of the elements that produced them. EDS technique is useful to determine the different elements which

are present in a material. Information about the spatial distribution of different elements in the specimen is obtained using the back-scattered electrons (those electrons elastically scattered by the nucleus of an atom) because the generation of those electrons depends on the atomic number Z [92, 99].

SEM images were recorded using a JEOL JSM-6100 SEM at the University of Oviedo. As the ball-milled Pr_2Fe_{17} and Nd_2Fe_{17} compounds are metallic, it was not necessary to cover them with a coating of electrically-conducting material, and the powders were directly sticked on a conductive tape.

Transmission electron microscopy

In TEM, the electron beam is firstly diffracted by the sample, and then the electron microscope lenses re-focus the beam into a Fourier-transformed image of the diffraction pattern. The high lateral spatial resolution in a TEM instrument is a consequence of both the highly focused electron beam, often a μm in diameter, and the highly-coherent beam of monoenergetic emitted electrons of small wavelength ($\lambda = 0.04$ Å for 100 keV electrons). However, high lateral spatial resolution is achieved only in ultra-thin specimens. By contrast with SEM, no depth information is obtained [92, 99]. Also it is possible to perform an analysis of spatial distribution of the scattered electrons, known as electron diffraction pattern, from which information about the arrangement of the atoms in the specimen can be obtained.

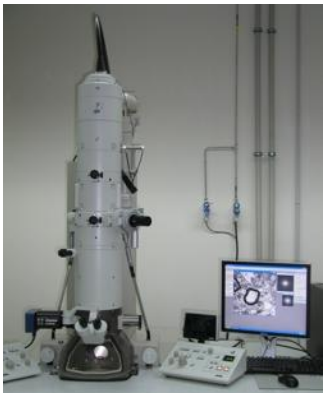

Figure 2.4: Transmission Electron Microscope at the University of Oviedo.

TEM images were taken using a JEOL 2000 EX-II, located at the University of Oviedo. Sample preparation is critical, since the specimen thickness must be less than 200 nm. Hence, powder was dispersed in ethanol and manually homogenized with an agate mortar. Then, several drops of the solution were placed on a membrane with a Cu grid. After the ethanol was dried, the specimen was inserted into the stage and all the components of the TEM column were sealed in vacuum.

2.3 Magnetic characterization

The study of magnetization as a function of temperature and applied magnetic field was done using three different types of magnetometers: Faraday susceptometer, Vibrating sample magne-

tometer (VSM) and Magnetic Property Measurement System (MPMS). Detalils of the program developed to calculate the main magnetic and magnetocaloric properties from the magnetization measurements are shown in the Scilab Functions appendix of this thesis.

2.3.1 Faraday susceptometer

A Faraday's susceptometer, placed in our laboratory at the University of Oviedo, was used for determining the magnetic transition temperature for samples in the range of temperatures from 250 to 500 K. It measures the force exerted on a magnetic specimen by placing it within a nonuniform magnetic field. That force is proportional to the magnetization of the sample [100].
An electromagnet with specially designed pole pieces applies a magnetic field along the horizontal plane with a gradient in the vertical direction. Specimens are located in a position with constant gradient and maximum field. A precision balance determines the force on the sample [101].

2.3.2 Vibrating sample magnetometer

The VSM technique is based in the Faraday induction law. A specimen is placed inside a uniform magnetic field to magnetize it. Then the sample is forced to oscillate sinusoidally, and the induced voltage in the pickup-coil is proportional to the sample's magnetic moment, but does not depend on the strength of the applied magnetic field. Two different VSM architectures were used:

- ⋆ Lakeshore VSM 7407, with a maximum applied magnetic field of 1.5 T generated by an electromagnet, and a measuring range of the magnetization from 1×10^{-7} to 100 emu. The range of available temperatures is (85 −630) K. This VSM is located in the University of Sevilla, Spain.

Figure 2.5: Vibrating Sample Magnetometer system at the University of Sevilla.

- ⋆ VSM option of Quantum Design Physical Properties Measurement System (PPMS), in which the applied magnetic field is generated by a superconducting magnet coil. In this work, two types of PPMS were utilized, one with a maximum applied magnetic field of 9 T (for this kind of PPMS, two devices were used, located at the University of Cantabria, Spain, and the Instituto Potosino de Investigación Científica y Tecnológica, Mexico), and other with a maximum applied magnetic field of 14 T (located at the University of Oviedo). The a measuring range of the magnetization is from 2.5×10^{-5} to 5 emu. The range of temperatures is (1.9 −400) K.

Figure 2.6: Physic Property Measurement System-14T system at the University of Oviedo.

2.3.3 Superconducting quantum interference device magnetometer system

A MPMS uses a superconducting quantum interference device (SQUID) for measuring the magnetization. A Quantum Design MPMS XL-5 was used, which produces a maximum applied magnetic field of 5 T by a superconducting magnet. The absolute sensitivity of the magnetization is 1×10^{-8} emu. The range of temperatures is (1.9 −400) K. The used instrument belongs to the Institute of experimental physics of the Slovak Academy of Science.

Figure 2.7: Magnetic Property Measurement System XL-5 system at the Institute of experimental physics of the Slovak Academy of Science.

Chapter 3

Magnetovolume anomalies and magnetocaloric effect of R_2Fe_{17} compounds

3.1 Summary

We investigated the magnetovolume anomalies and the magnetocaloric properties exhibited by the R_2Fe_{17} alloys, with R = Y, Ce, Pr, Nd, Dy, Ho, Er, Tm and Lu, which have transition temperatures around room temperature. Moreover, this family of alloys present magnetovolume anomalies. With the aim of undertaking a complete study of these magnetovolume effects, we also synthesized other alloys of this series: Tb_2Fe_{17} and Gd_2Fe_{17}, which have the highest transition temperatures of the R_2Fe_{17} series (410 K and 478 K respectively). However, due to fact that the ordering temperatures are above the temperature range of the used magnetometers, no magnetization measurements were done in these alloys.

Crystal structures of these alloys were determined by means of XRD, and confirmed by ND experiments. Fig. 3.1 shows two high-resolution ND patterns collected in D1A, obtained from both rhombohedral Tb_2Fe_{17} and hexagonal Er_2Fe_{17} alloys in the magnetically ordered state, but close to T_C. The observed peaks in the Tb_2Fe_{17} alloy pattern can be indexed as Bragg reflections belonging to two different phases, with $R\bar{3}m$ space group and $Im\bar{3}m$ body-centered cubic crystal structures. The former is a Tb_2Fe_{17} phase (Th_2Zn_{17}-type crystal structure), while the latter is an α-Fe impurity phase. For the rhombohedral R_2Fe_{17} alloys this impurity is present in amounts circa 4 % wt. The lack of phase purity is due to the peritectic nature of the solidification in these alloys [102].
On the contrary, hexagonal R_2Fe_{17} alloys were shown to be single phase, as it is shown in the pattern corresponding to the Er_2Fe_{17} alloy, where the Bragg reflexions belong to the $P6_3/mmc$ space group. It must be said that several authors [60, 103] have pointed out that those compounds can exhibit a disordered Th_2Ni_{17}-type structure, in which R($2b$) atoms are partially replaced by R($2c$), and Fe($4f$) atoms are partially substituted by Fe($4e$). However, refinements using this disordered crystal structure do not lead to better results in our case. For this reason, data shown here does not take into account such model.

An interesting result is that we obtained the Dy_2Fe_{17} compound in the rhombohedral Th_2Zn_{17}-type crystal structure (see fig. 3.2). As far as we know, this is the first time that Dy_2Fe_{17} alloy

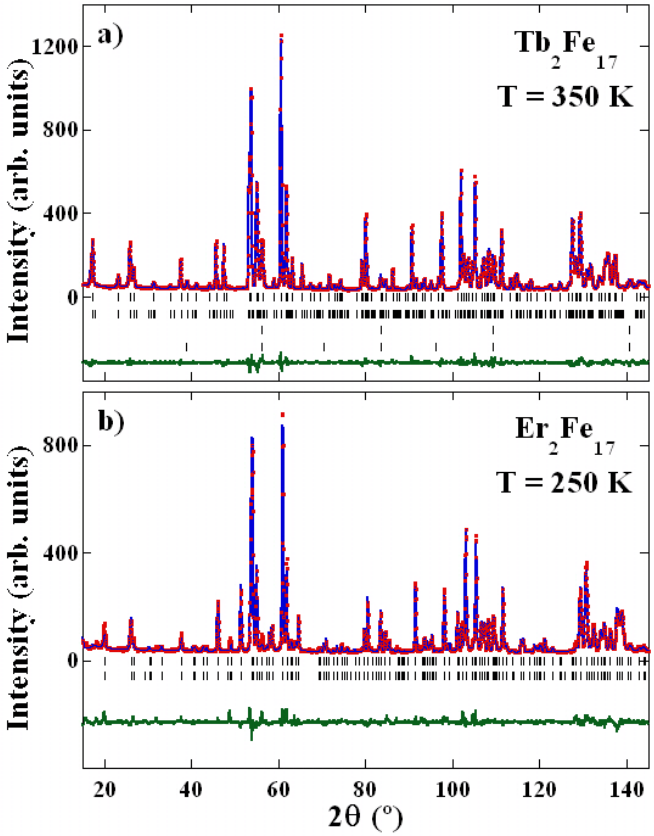

Figure 3.1: Comparative of the neutron powder diffraction patterns belonging to a) the rhombohedral and b) hexagonal R_2Fe_{17} alloys. The observed (dots) and calculated (solid line) patterns from D1A of the ordered state of a) Tb_2Fe_{17} and b) Er_2Fe_{17} alloys are depicted. Position of the Bragg reflections are represented by vertical bars; the first row corresponds, in each figure, to a) the Th_2Zn_{17} and b) the Th_2Ni_{17}; the second row corresponds with the magnetic phase. In the case of fig. a), the third and fourth rows corresponds with the nuclear and magnetic contributions of the α-Fe impurity phase respectively. Observed-calculated difference is depicted at the bottom of each figure.

is synthesized with this crystal structure. This compound, as in its hexagonal counterpartner, exhibits ferrimagnetic behavior, with magnetic structure composed by two ferromagnetic sublattices: one, formed the the Dy magnetic moments, and the other, by the Fe magnetic moments [104].

Atomic positions of all samples, except those of Gd_2Fe_{17}, were determined from the Rietveld refinement of the ND pattern in the paramagnetic state of each alloy, in order to reduce the number of free parameters. Atomic coordinates of Gd_2Fe_{17} were determined by means of XRD because the large Gd neutron absorption cross section and the low resolution of the D4 diffractometer. Results are summarized in table 3.1 for rhombohedral compounds, and, for those with hexagonal-type crystal structure, in table 3.2.

Table 3.1: Atomic coordinates of the rhombohedral bulk R_2Fe_{17} intermetallics obtained from the high-resolution neutron powder diffraction patterns in the paramagnetic state.

Compounds	Y_2Fe_{17}	Ce_2Fe_{17}	Pr_2Fe_{17}	Nd_2Fe_{17}	Gd_2Fe_{17}	Tb_2Fe_{17}	Dy_2Fe_{17}
R-z	0.3391	0.3428	0.3443	0.3448	0.3440	0.3417	0.3427
Fe1-z	0.0954	0.0969	0.0967	0.0941	0.0946	0.0969	0.0964
Fe3-x	0.29532	0.2900	0.2877	0.2866	0.2941	0.2936	0.2921
Fe4-x	0.16676	0.1684	0.1690	0.1699	0.1679	0.1680	0.1678
Fe4-z	0.49344	0.4883	0.4896	0.4899	0.48573	0.4898	0.4883

Table 3.2: Atomic coordinates of the hexagonal bulk R_2Fe_{17} intermetallics obtained from the high-resolution neutron powder diffraction patterns in the paramagnetic state.

Compounds	Y_2Fe_{17}	Ho_2Fe_{17}	Er_2Fe_{17}	Tm_2Fe_{17}	Lu_2Fe_{17}
Fe1-z	0.1064	0.1056	0.1073	0.1038	0.1058
Fe3-x	0.3273	0.3315	0.3271	0.3325	0.3283
Fe3-y	0.9621	0.9633	0.9577	0.9628	0.9615
Fe4-x	0.1661	0.1695	0.1663	0.1656	0.1658
Fe4-z	0.9854	0.9868	0.9831	0.9840	0.9832

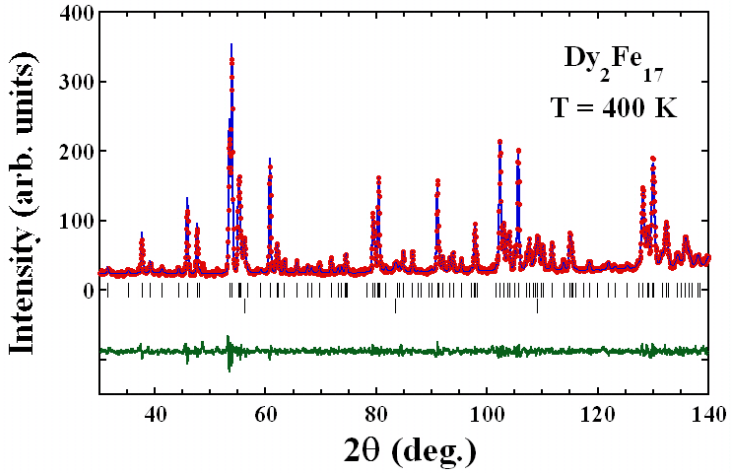

Figure 3.2: Fit of the Dy_2Fe_{17} diffraction pattern obtained on the high resolution D1A diffractometer at 400 K. Fit was done using the Le Bail method [95]. Positions of the Bragg reflections are represented by vertical bars. The first row corresponds to the Dy_2Fe_{17} phase. The second row is associated with an α-Fe impurity. The observed-calculated difference is depicted at the bottom of the figure.

From NTD patterns it was possible to estimate the temperature dependence of the magnetic moment for several compounds. It is worth to note that the Fe-sublattice magnetic moments were refined, where possible, using the values obtained for the Y_2Fe_{17} compound as initial parameters. In fig. 3.3(a), the magnetic moment at each atomic site of the Tb_2Fe_{17} are shown. Such temperature dependencies for Fe-sites are congruent with a Heisenberg exchange Hamiltonian within the mean field approximation, considering a spin angular momentum $S = 1$. On the other hand, temperature dependence of Tb moment can be modeled by combining Heisenberg exchange Hamiltonian with crystal electric field effects.
For Gd_2Fe_{17} alloy, due to the poor resolution of the D4 diffractometer, the peaks corresponding to Bragg reflections belonging mainly to Fe magnetic reflexions cannot be resolved. However, this condition is met for several peaks corresponding to the Gd sublattice, allowing to determine the Gd magnetic moment as a function of the temperature (see fig. 3.3(b)). The observed magnetic moment for Gd agrees with the obtained using the Heisenberg Hamiltonian describing the 3d-4f exchange coupling (the 4f-4f exchange interaction is expected to be negligible compared to the 3d-4f one).

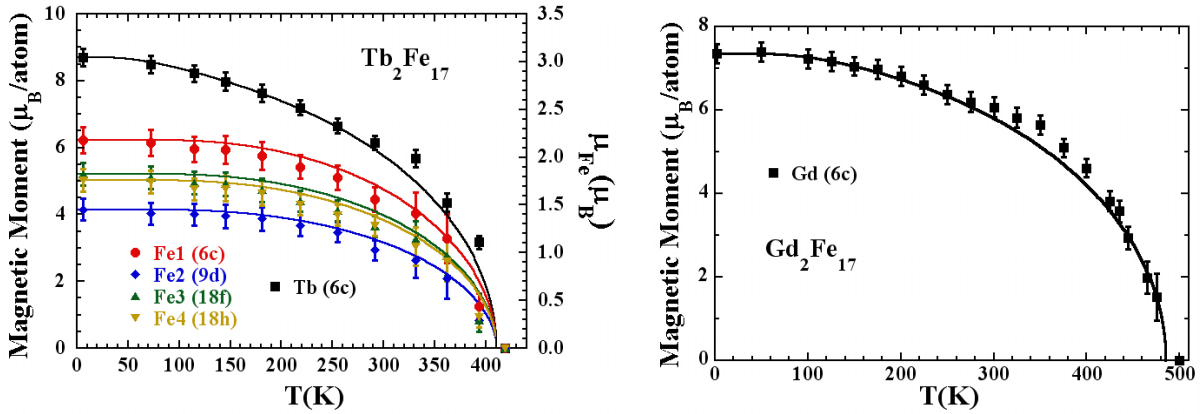

Figure 3.3: Left plot: Temperature dependence of the magnetic moments of each crystal site for the Tb_2Fe_{17} compound obtained from neutron thermo-diffraction (NTD) data. Full lines represent the calculation of the magnetic moments from the mean field approximation, scaled using the experimental values at 6 K. Right plot: Estimation of the temperature dependence of the magnetic moments of Gd atom for the Gd_2Fe_{17} compound obtained from NTD patterns. Full line represents the temperature dependence of the normalized magnetic moment of Gd atom calculated from Heisenberg Hamiltonian.

The parameters and the volume of the crystallographic cell as functions of temperature were obtained from NTD. The rescaled cell volume as a function of the reduced T/T_C is plotted in fig. 3.4. In the case of Ce_2Fe_{17} alloy (see fig. 3.4(a)), the two different magnetic phase transitions [105, 106], have associated two minimums for the normalized $V(T)$. For the other R_2Fe_{17} compounds, only the minimum associated with the ferro-(ferri-) paramagnetic phase transition is present.

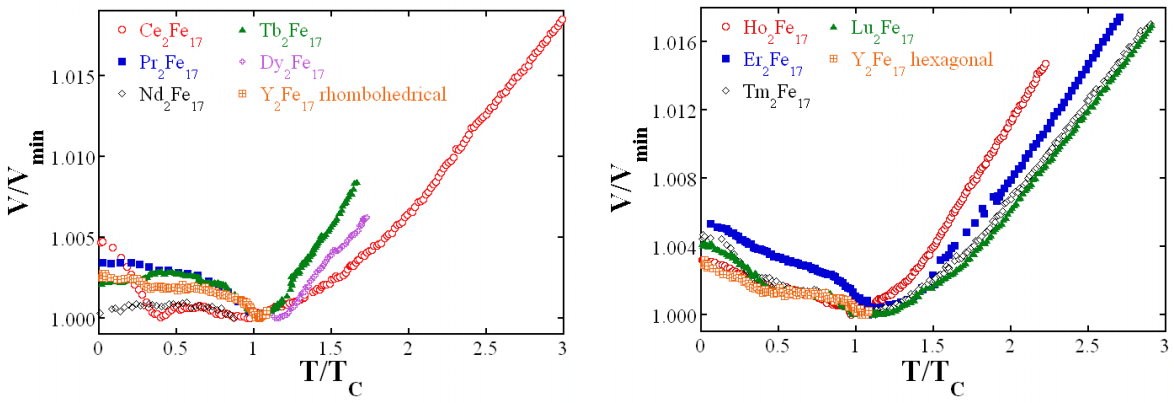

Figure 3.4: Left plot: Temperature dependence cell volume for the rhombohedral R_2Fe_{17} alloys. Right plot: Temperature dependence cell volume for the hexagonal R_2Fe_{17} alloys.

We defined the magnetostriction as the change of the lattice parameters and volume cell normalized to those values expected for a non-magnetic system, i.e.,

$$\begin{aligned} \lambda_a &= (a - a_0)/a_0 \\ \lambda_c &= (c - c_0)/c_0 \\ \omega_S &= (V - V_0)/V_0 \end{aligned} \tag{3.1}$$

were a_0, c_0 and V_0 are the values extrapolated from the paramagnetic state using the Debye theory (see section 1.2). In Fig.3.5(a) we compare λ_a and λ_c for each compound. Clearly, the magnetostriction is larger along the c direction, regardless of the crystal structure. This is related with the fact that the dumb-bell sites are oriented along this direction, which are believed to be responsible of the magnetovolume anomalies exhibited by these alloys [68, 69].

It should be noticed that the λ_a of the Ce_2Fe_{17} alloy has a local minimum around 0.4 T_C (see Fig. 3.5(b)). However, no such behavior can be seen along the uniaxial direction, which has a temperature dependence similar to the other R_2Fe_{17} alloys. This indicates that the influence of the two magnetic transitions in the magnetovolume effects for the Ce_2Fe_{17} alloy is mainly focused in the basal plane. Moreover, comparing λ_a and λ_c for all the alloys, it can be observed that λ_a has an almost constant temperature dependence up to 0.5 T_C (except for the Ce_2Fe_{17} alloy), whereas the constant dependence of λ_c with temperature goes up to 0.1 T_C. For higher temperatures, the decrease of λ_c is almost linear, whereas for λ_a it is more abrupt.

The spontaneous volume magnetostriction was calculated for different compounds as the difference between the volume corresponding to the non-magnetic extrapolation and experimental volume using the procedure explained in sec. 1.2. The results for the non-magnetic contribution to the cell volume for the Tb_2Fe_{17} alloy is shown in fig. 3.6(a). The experimental cell volume at low temperatures is higher than it could be expected if the system were non-magnetic. As the temperature is increased, the Fe magnetic moments decrease and the magnetovolume coupling losses strength progressively, giving rise to a lattice contraction. Thus the volume goes down to the corresponding equilibrium value in the absence of magnetic order, which is reached above the critical temperature.

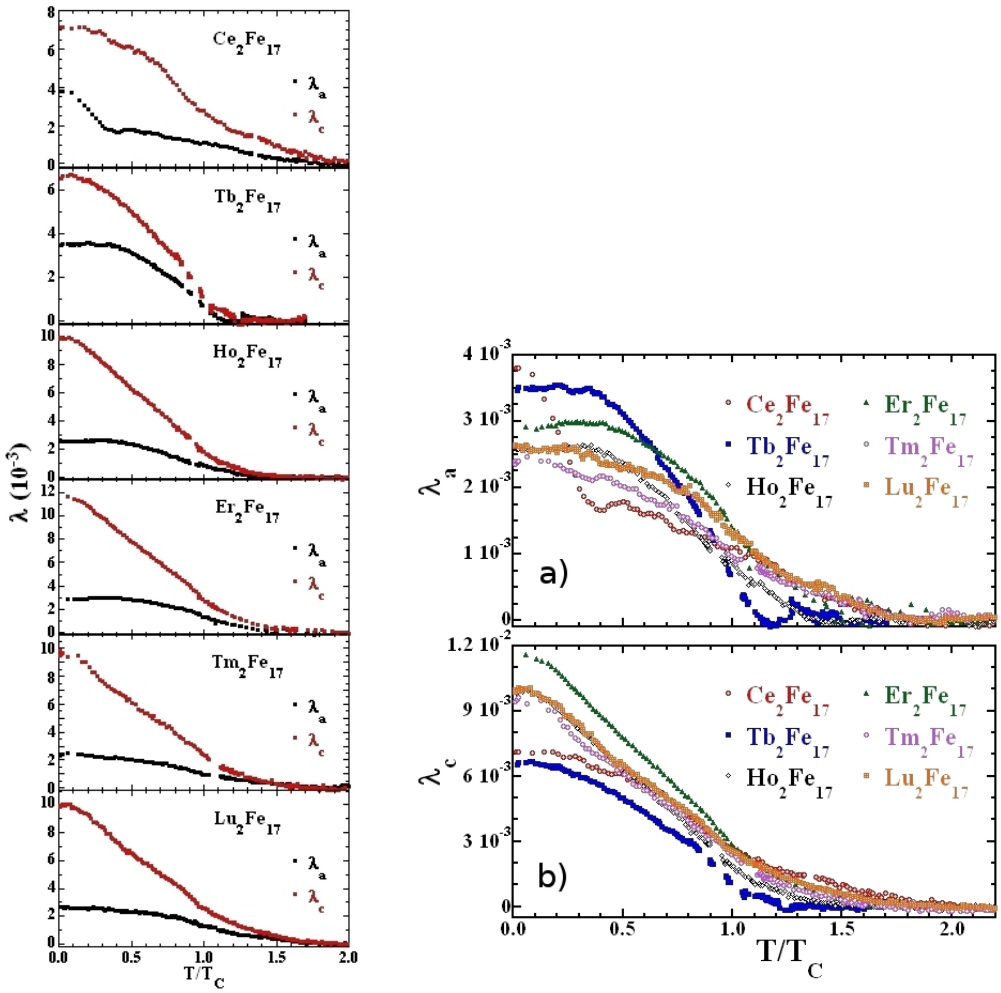

Figure 3.5: Left plot: Comparison of the temperature dependence of both λ_a and λ_c for each compound. Right plot: a) Comparison of λ_a for all compounds. b) Comparison of λ_c for all compounds.

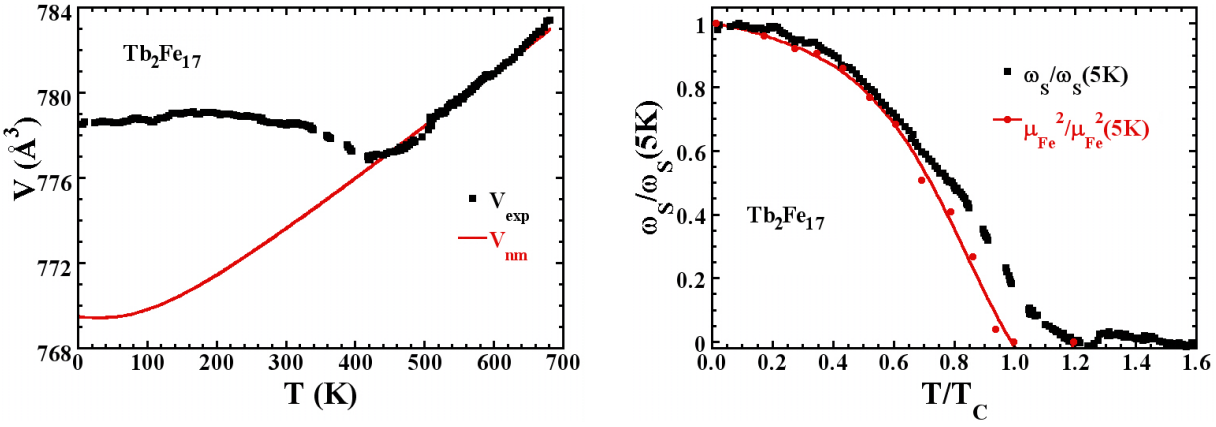

Figure 3.6: Left plot: Temperature dependence of experimental and non-magnetic cell volume of Tb_2Fe_{17}. Right plot: Comparison between the spontaneous volume magnetostriction and the Fe-sublattice total magnetic moment for Tb_2Fe_{17}. The full line is a guide for the eyes.

Plotting the normalized volume magnetostriction, ω_s, and the normalized Fe-sublattice total magnetic moment, μ_{Fe}^2, to their values at 5 K, it is shown that for Tb_2Fe_{17} alloy the spontaneous magnetostriction has the same temperature dependence as the magnetic moment up to $T \approx 0.8\,T_C$. At higher temperatures, $\omega_s(T)$ deviates from μ_{Fe}^2, and, at T_C, about 20 % of $\omega_s(5\,\mathrm{K})$ still remains, which reflects certain short-range order that disappears around 80 K above T_C [47, 107]. In the case of Er_2Fe_{17}, such short-range order remains up to 120 K over T_C.

We measured the pressure dependence of the cell parameters for Gd_2Fe_{17}, Dy_2Fe_{17} and Er_2Fe_{17} alloys (see fig. 3.7). A small anisotropy of the compression of the cell in the Dy_2Fe_{17} and Gd_2Fe_{17} alloys is found, being easier to compress the cell in the uniaxial direction that in a direction within the basal plane. The Er_2Fe_{17} alloy is almost isotropic, as c dependence with pressure is almost the same than for the a direction.

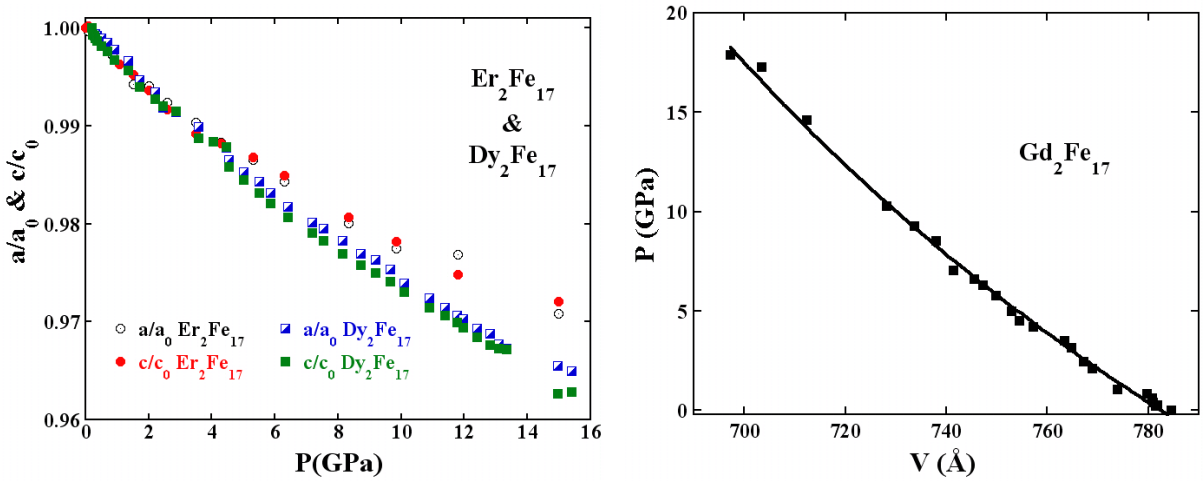

Figure 3.7: Left plot: Pressure dependence of the normalized cell parameters for the rhombohedral Dy_2Fe_{17} and hexagonal Er_2Fe_{17} alloys. Right plot: Pressure as a function of cell volume of Gd_2Fe_{17} alloy, fitted with eq. 3.2.

We fitted the pressure dependence of the cell volume to a first-order Birch-Murnaghan equation of state [108, 109]:

$$P = \frac{3}{2} B_0 \left[\left(\frac{V}{V_0} \right)^{-7/3} - \left(\frac{V}{V_0} \right)^{-5/3} \right] \tag{3.2}$$

where P is the pressure, B_0 is the bulk modulus, and V_0 is the cell volume at zero pressure. From these fits we estimated the bulk modulus of the alloys, being 125, 110 and 143 GPa^{-1} for the Gd_2Fe_{17}, Dy_2Fe_{17} and Er_2Fe_{17} alloys respectively. Indeed, in the case of Er_2Fe_{17}, such value was compared with the obtained by fitting the experimental volume cell in the paramagnetic range

We obtained the field dependence of magnetization at different temperatures (see fig. 3.8) of those R_2Fe_{17}, with critical temperatures lower than 370 K, with the aim of obtaining at least the full width at half maximum of the $\Delta S_M(T)$ curve.

The magnetic entropy change for the rhombohedral and hexagonal R_2Fe_{17} alloys are depicted for a magnetic field change of 5 T in Fig. 3.9. Several remarkable features are shown:

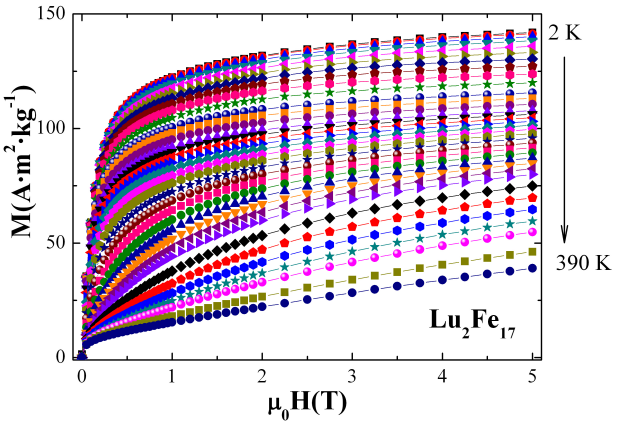

Figure 3.8: Field dependence of the magnetization for the Lu_2Fe_{17} alloy at different temperatures.

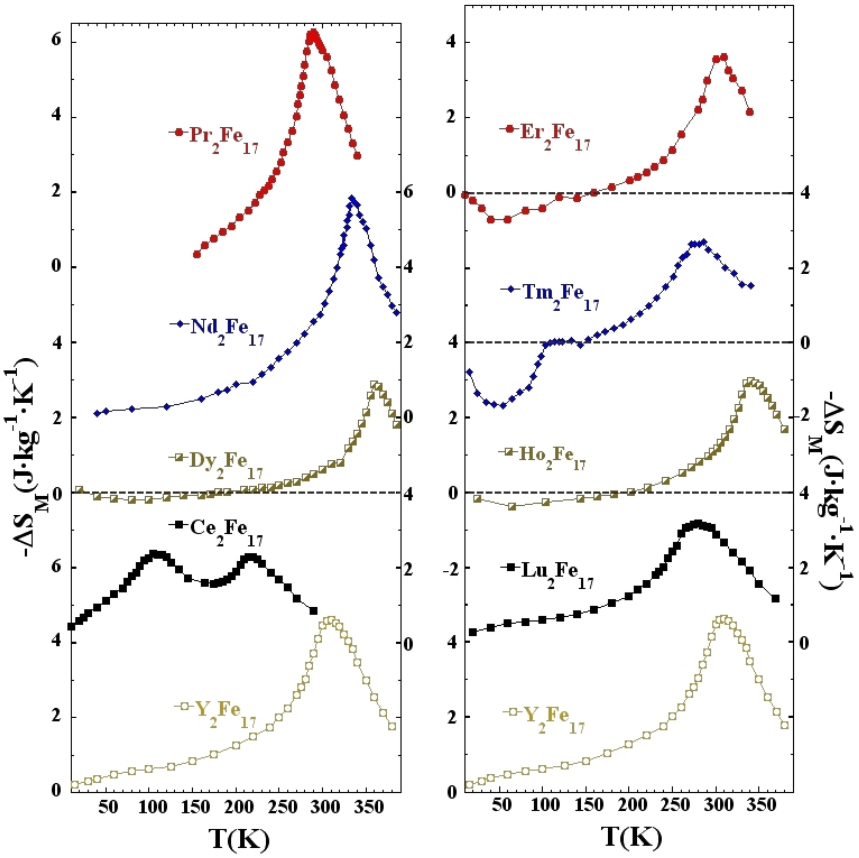

Figure 3.9: Left plot: Magnetic entropy change of the rhombohedral R_2Fe_{17} alloys for a maximum applied field of 5 T. Right plot: Magnetic entropy change of the hexagonal R_2Fe_{17} alloys for a maximum applied field of 5 T.

- ⋆ Ce_2Fe_{17} has a double peak with the same sign. The peak at lower temperature is associated with a metamagnetic phase transition from to the antiferromagnetic to a forced-ferromagnetic state [106, 110]. For this reason, the temperature at which the magnetic magnetic entropy change peaks, increases. However, the peak at higher temperature is associated with the order-disorder phase transition, hence no change in the temperature of the peak is observed within the experimental limit.
- ⋆ Pr_2Fe_{17} and Nd_2Fe_{17} have the largest $(-\Delta S_M)^{Peak}$ values, even though Pr and Nd magnetic moments are lower than those of the Ho and Dy atoms. This occurs due to the ferromagnetic behavior of Pr_2Fe_{17} and Nd_2Fe_{17} alloys.
- ⋆ In the case of ferrimagnetic hexagonal R_2Fe_{17} alloys, a double peak is also observed, but instead of having the same sign as in Ce_2Fe_{17} alloy, here they have opposite sign. In the case of Tm_2Fe_{17}, this should be due to a spin reorientation [111, 112]. For Ho_2Fe_{17} and Er_2Fe_{17}, it can been attached to differences in the temperature dependencies of the two sublattices on the ferrimagnetic configuration [113]. On the other hand, this behavior has been also obtained considering the crystal effect fields effects on other cubic rare-earth intermetallic compounds [114].

In tables 3.3 and 3.4 the main magnetic and magnetocaloric properties of the R_2Fe_{17} alloys are summarized, respectively. Saturation magnetization values were obtained from the magnetization vs applied magnetic field at 5 K by means of the approach-to-saturation law [115]:

$$M = M_S\left(1 - b/H^2\right) + \chi_0 H \tag{3.3}$$

Table 3.3: Main magnetic characteristics of bulk R_2Fe_{17} intermetallic compounds. M_S values were estimated from the isotherms at $T = 5$ K.

Composition	T_{Order} (K)	M_S (Am^2kg^{-1})
Y_2Fe_{17}	303	157
Ce_2Fe_{17}	225	124
Pr_2Fe_{17}	285	148
Nd_2Fe_{17}	335	143
Gd_2Fe_{17}	478	-
Tb_2Fe_{17}	410	-
Dy_2Fe_{17}	363	62
Ho_2Fe_{17}	334	71
Er_2Fe_{17}	303	31
Tm_2Fe_{17}	265	87
Lu_2Fe_{17}	265	135

It is worth noting that the Dy_2Fe_{17} alloy has a Curie temperature slightly lower than that of the rhombohedral one, which is 371 K [104, 116].

For Tm_2Fe_{17} and Er_2Fe_{17} alloys their heat capacities as a function of temperature were measured, and then utilized to obtain $S(T)$ by means of eq. 1.17. Fig. 3.10(a) plots $C_P(T)$ and $S(T)$

Table 3.4: Main magnetocaloric features of bulk R_2Fe_{17} intermetallic compounds. Magnetocaloric data corresponds with a magnetic field change $\mu_0\Delta H = 5\,\mathrm{T}$.
– Experimental temperature range not available.

Composition	Direct Indirect	$\lvert\Delta S_M^{Peak}\rvert$ ($\mathrm{Jkg^{-1}K^{-1}}$)	δT_{FWHM} (K)	RCP_1 ($\mathrm{Jkg^{-1}}$)	RCP_2 ($\mathrm{Jkg^{-1}}$)	RCP_3 ($\mathrm{Jkg^{-1}}$)
Y_2Fe_{17}	Direct	4.6	103	477	367	249
Ce_2Fe_{17}	Direct	2.4	99	225	180	168
Pr_2Fe_{17}	Direct	6.3	80	506	385	256
Nd_2Fe_{17}	Direct	5.8	79	464	339	233
Dy_2Fe_{17}	Indirect	0.2	132	17	14	9
Dy_2Fe_{17}	Direct	2.9	-	-	-	74
Ho_2Fe_{17}	Indirect	0.4	101	38	28	19
Ho_2Fe_{17}	Direct	3.0	93	-	-	-
Er_2Fe_{17}	Indirect	0.7	80	56	44	28
Er_2Fe_{17}	Direct	3.6	-	-	-	-
Tm_2Fe_{17}	Indirect	1.7	75	125	107	76
Tm_2Fe_{17}	Direct	2.7	-	-	-	-
Lu_2Fe_{17}	Direct	3.2	128	406	317	205

for Tm_2Fe_{17} alloy. ΔT_{ad} was obtained from the distance between the isofield curves without any applied magnetic field and the desired one of the entropy−temperature (ST) diagram (see sec. 1.1.1). Results for Er_2Fe_{17} and Tm_2Fe_{17} for $\mu_0 H = 2\,\mathrm{T}$ are depicted in fig. 3.10(b). As the magnetic entropy changes exhibit a double peak behavior, the adiabatic temperature changes also does. It is worth noting that in the interval (100, 160) K the adiabatic temperature change of Tm_2Fe_{17} alloy is almost zero (which also occurs for $\Delta S_M(T)$).

We measured the temperature dependence of magnetization of Pr_2Fe_{17} and Tm_2Fe_{17} alloys under different pressures, ranging from ambient pressure up to 1 GPa (see fig. 3.11(a)). In the case of Pr_2Fe_{17}, the Curie temperature decreases almost linearly with pressure, with a slope $\frac{dT_C}{dP} = -40\,\mathrm{K{\cdot}GPa^{-1}}$. For the Tm_2Fe_{17} alloy, we observed that the such decrease of the ferrimagnetic-paramagnetic transition with pressure is also linear, but the absolute value of the slope is much larger, $\frac{dT_C}{dP} = -100\,\mathrm{K{\cdot}GPa^{-1}}$. Moreover, this is not the only effect of pressure on Tm_2Fe_{17}, it was shown that the temperature of the spin reorientation (T_{SR}) increases with pressure. Modifications of the spin reorientation with pressure in Tm_2Fe_{17} alloy have been previously studied by means of susceptibility [117], but under lower pressure. Indeed, as the pressure increases, T_{SR} and T_C become closer. Therefore, it is expected that both transitions would overlap at higher pressures.

Studies of the evolution of the microstructure with milling time were carried out for Pr_2Fe_{17} and Nd_2Fe_{17} alloys, and the interplay with the magnetic and magnetocaloric properties. we have selected those alloys because they exhibit the largest direct magnetocaloric effect (see table 3.3).

The powder morphology of both Pr_2Fe_{17} and Nd_2Fe_{17} ball-milled during 10 h is shown in fig. 3.12. SEM micrographs [fig. a) and c)] suggest that the powders consist of agglomerated macroscopic grains with irregular shapes, rounded borders and sizes mostly between 0.5 and 10 μm. Higher magnification micrographs revealed that the grains are close-packed assemblies of

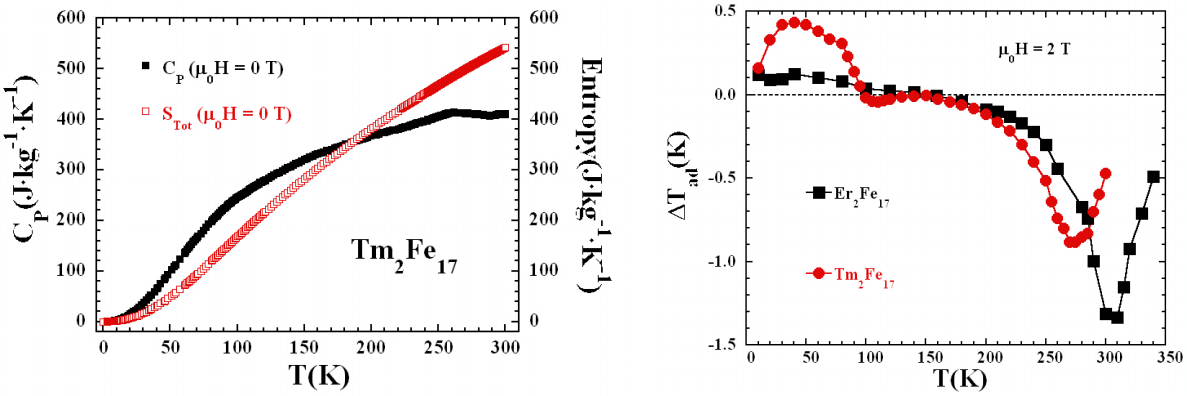

Figure 3.10: Left plot: Temperature dependence of the total entropy and heat capacity of the Tm_2Fe_{17} at $\mu_0 H = 0\,\mathrm{T}$. Right plot: Temperature dependence of the ΔT_{ad} at a maximum applied field of 2 T for the Er_2Fe_{17} and Tm_2Fe_{17} compounds.

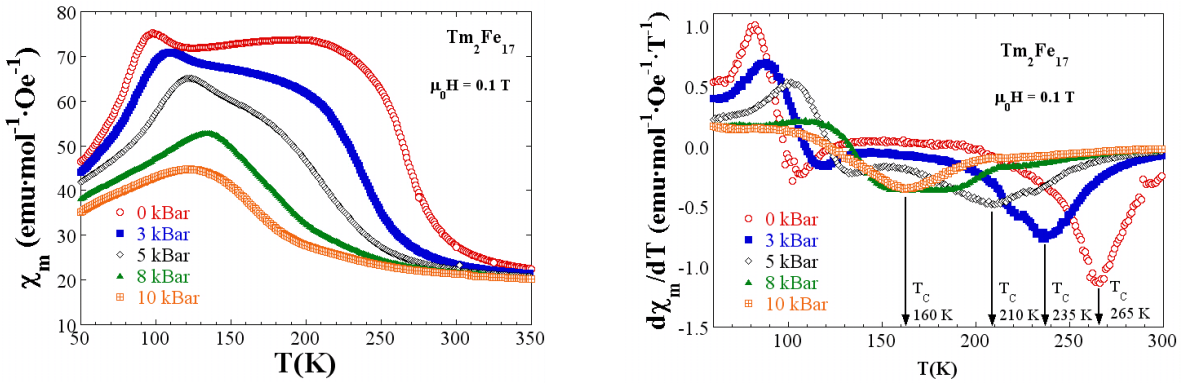

Figure 3.11: Left plot: Temperature dependence of the magnetization of the alloy Tm_2Fe_{17} for different pressures under a applied magnetic field of $\mu_0 H = 0.1\,\mathrm{T}$. Right plot: Temperature derivative of the magnetic susceptibility for different pressures of Tm_2Fe_{17} alloy. Curie temperatures were marked by the arrows. For $P = 8\,\mathrm{kBar}$ it is not possible to define an unique T_C, because the $M(T)$ decreases linearly for temperatures over 150 K.

smaller, flaky or laminar-like entities. TEM study of the microstructure of these grains at the nanometer length-scale (fig. 3.12 b) and d)) showed that the nanoparticle size of a large number of individual particles (over 500 in each compound) follows a log-normal distribution, giving an average size, $\langle\tau\rangle_{TEM}$, of 23 (1) nm for Pr_2Fe_{17} BM-10h alloy, and 17 (1) nm for Nd_2Fe_{17} BM-10h alloy.

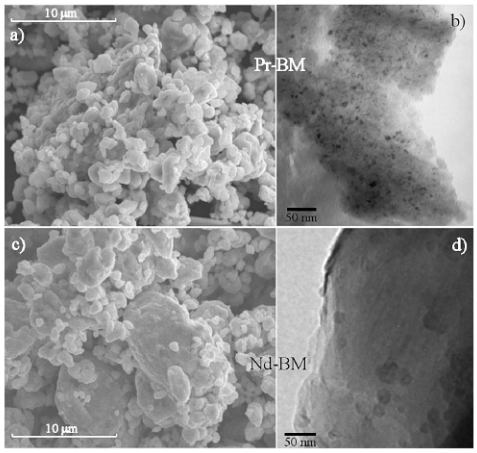

Figure 3.12: Scanning [a) and c)] and transmission [b) and d)] electron microscopy images obtained for the 10 hours ball-milled Pr_2Fe_{17} and Nd_2Fe_{17} alloys.

The increase of the milling time gives rise to a further grain fracturing and nanocrystallite size reduction. The histogram gives an average size of the crystallites $\langle\tau\rangle_{TEM} = 8(1)$ nm and 17(1) nm are for the Nd_2Fe_{17} and Pr_2Fe_{17} BM-20h samples, respectively. However, for BM-40h samples the nanostructure is less defined, mainly due to the structural disorder induced by the severe mechanical treatment. In fact, no nanocrystals were observed in the BM-40h alloys.

ND and XRD shown that the position of the Bragg reflections in the diffraction patterns corresponding to ball-milled samples remain almost unaltered, thus indicating that the Th_2Zn_{17}-type crystal structure is maintained (see fig. 3.13). Peak broadening shows a drastic reduction of the grain size and, therefore, the emergence of a considerable amount of disorder, mainly located at the increasing intergranular regions and/or grain boundaries [94]. From the peak profile analysis, a mean crystalline size of $\langle\tau\rangle_{DIFF} = 24\,(3)$ and $14\,(5)$ nm for BM-10h and BM-20h Nd_2Fe_{17} samples respectively were estimated, in reasonable agreement with those found from TEM images. However, the mechanically-induced microstrain is very low ($\epsilon \approx 0.04(2)$ %). Thus the milling process mainly produces a progressive breaking of the Nd_2Fe_{17} crystals down to the nanometer length scale. The same conclusions can be extracted for Pr_2Fe_{17} samples.

The main change in the magnetic behavior at low magnetic field of the $Pr_2Fe_{17}$and Nd_2Fe_{17} compound after milling is that, while the ferromagnetic to paramagnetic phase transition is abrupt in the Bulk samples, it becomes broader as the milling time increases. The value of the Curie temperature of each alloys was estimated as the minimum of the dM/dT vs. T curve. Bulk sample exhibits a sharp and well-defined minimum at $T_C = 285 \pm 2\,K$ and $T_C = 339 \pm 2\,K$ for Pr_2Fe_{17} and Nd_2Fe_{17} bulk alloys, respectively. After milling, a slight shift towards higher temperatures is accompanied by an increase of the temperature range in which the phase transition occurs. Because the dM/dT vs. T curves display broad and asymmetric minimum, instead of a unique and

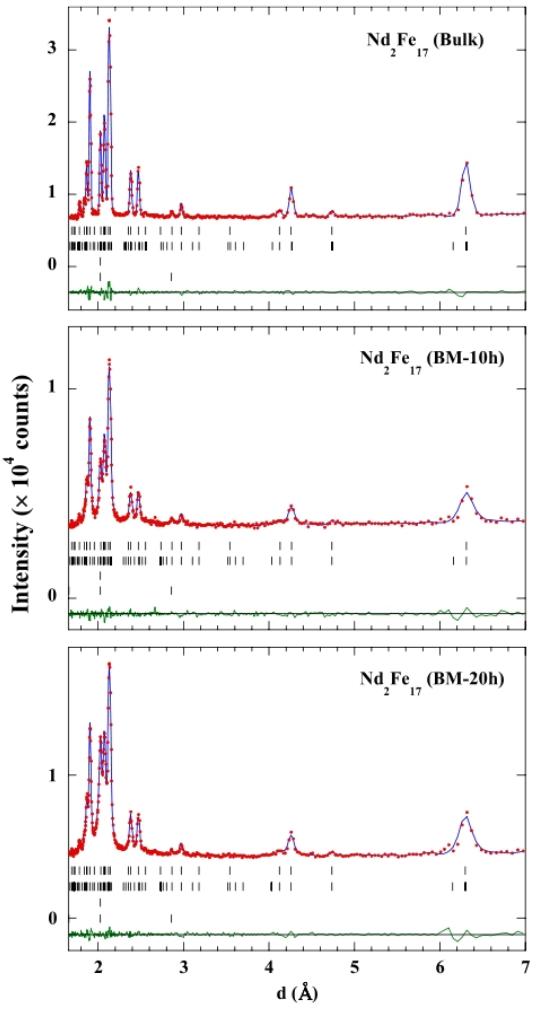

Figure 3.13: Observed (dots) and calculated (solid line) patterns for bulk, BM-10h and BM-20h Nd_2Fe_{17} alloys at T = 300 K. Positions of the Bragg reflections (in terms of the interplanar distance, d) are represented by vertical bars; the first row corresponds to the Nd_2Fe_{17} phase while the second one is associated with an α-Fe impurity. The observed-calculated difference is depicted at the bottom of each figure.

well-defined T_C for the milled samples, a distribution of Curie temperatures should be considered. This fact can be a direct consequence of the induced structural disorder and the slightly different local environments of the atoms at the grain boundaries, giving rise to modification in their magnetic behavior [118].

In Fig. 3.14 the temperature dependence of the magnetic entropy change at $\mu_0 H = 1.5\,T$ in the bulk, BM-10h, BM-20h and BM-40h Nd_2Fe_{17} samples is depicted. The abrupt decrease of the magnetization near T_C in the Bulk alloy (see Fig. 1.8), gives rise to a remarkable change in its magnetic entropy, reaching a maximum value of $|\Delta S_M| \approx 2.6\,J\,kg^{-1}K^{-1}$ at $15\,kOe$. For the milled samples $|\Delta S_M|(T)$ the maximum values of $|\Delta S_M|$ are 1.9, 1.6 and $J\,kg^{-1}K^{-1}$ for BM-10h, BM-20h and BM-40h, respectively. The temperatures at which the maximum are reached are nearly the same for the four samples ($\approx T_C$).
Inset in Fig. 3.14 shows the applied magnetic field dependence of the RCP_1. The fact that the full width at half maximum of $|\Delta S_M|(T)$ increases with the milling time counteracts the decrease in the peak value of $|\Delta S_M|$ for the BM-10h and BM-20h samples, showing values of RCP_1 quite similar but higher than that of the Bulk. Nevertheless, that broadening is not enough for the BM-40h, whose RCP_1 value is the lowest of the present study.

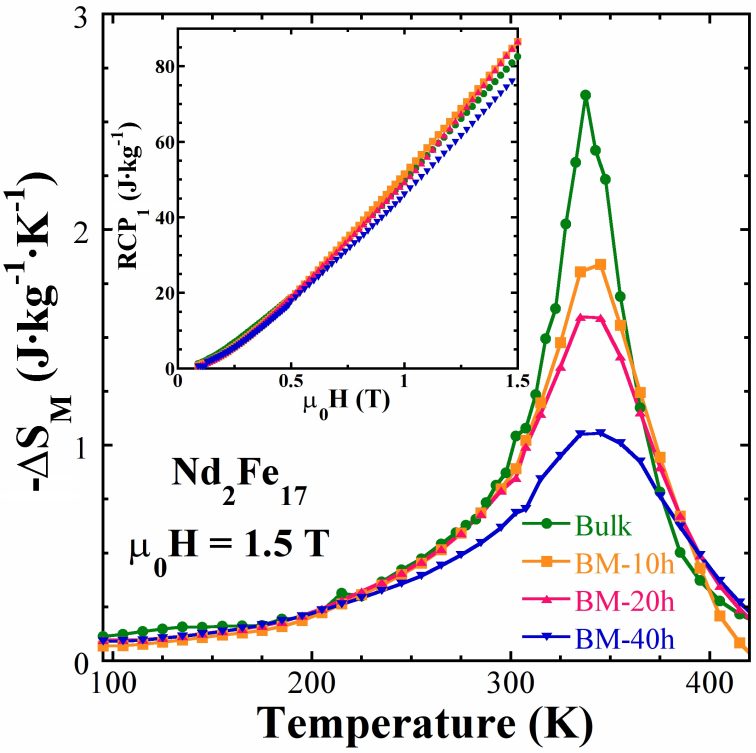

Figure 3.14: Magnetic entropy change at $\mu_0 H = 1.5\,\mathrm{T}$ for the bulk and ball-milled Nd_2Fe_{17} alloys. Inset depicts the magnetic field dependence of the RCP_1 for the studied samples.

Available online at www.sciencedirect.com
ScienceDirect
Acta Materialia 57 (2009) 1724–1733
Acta MATERIALIA
www.elsevier.com/locate/actamat

Crystal structure, magnetocaloric effect and magnetovolume anomalies in nanostructured Pr_2Fe_{17}

Pedro Gorria [a,*], Pablo Álvarez [a], Jorge Sánchez Marcos [b,c], José L. Sánchez Llamazares [a], María J. Pérez [a], Jesús A. Blanco [a]

[a] Departamento de Física, Universidad de Oviedo, Calvo Sotelo, s/n, 33007 Oviedo, Spain
[b] Institute Laue-Langevin, BP 156, 6 rue Jules Horowitz, 38042 Grenoble Cedex 9, France
[c] Instituto de Ciencia de Materiales de Madrid, CSIC, Cantoblanco, 28049 Madrid, Spain

Received 22 August 2008; received in revised form 7 December 2008; accepted 9 December 2008
Available online 13 January 2009

Abstract

Using high-energy ball milling, nanostructured Pr_2Fe_{17} powders can be obtained from their arc-melted bulk alloys. High-resolution X-ray and neutron powder diffraction experiments reveal that the Th_2Zn_{17}-type rhombohedral crystal structure is maintained, after milling for 10 h, with almost unchanged values for both crystalline lattice parameters (Δa; $\Delta c < 0.05\%$) and vanishing mechanically induced microstrain (<0.1%). Although the mean crystalline size decreases down to 20 ± 3 nm, magnetovolume anomalies observed in pure Pr_2Fe_{17} are still present with a significant volume decrease on heating from 5 up to 320 K. After the milling, a significant increase in the magnetic anisotropy, due to the drastic reduction in crystalline size, is observed, while the value of the magnetic moment seems to be increased slightly (5%). In addition, the magnetocaloric effect of bulk and nanostructured Pr_2Fe_{17} has been investigated. The magnetic entropy change, $|\Delta S_M|$, decreases from 6.3 to 4.5 J kg^{-1} K^{-1} under an applied magnetic field $\mu_0 H = 5$ T after the milling process. However, the width of the $|\Delta S_M|(T)$ curve is substantially enlarged and hence the refrigerant capacity is enhanced. These findings make the iron-based nanostructured Pr_2Fe_{17} powders interesting for applications in magnetic refrigeration at around room temperature.

Keywords: Nanostructured materials; Magnetocaloric effect; Magnetovolume anomalies; Mechanical milling; Neutron powder diffraction

1. Introduction

Recent years have witnessed significant progress in the preparation, characterization and industrial exploitation of new magnetic systems with transition metals (TM) and/or rare earth metals (R) with reduced size scales [1–3]. This change of scale may imply both the modification of the magnetic properties with respect to those of the corresponding bulk compositions and the emergence of new physical and chemical phenomena [4,5]. In particular, an intense research effort has been devoted to binary R–Fe alloys, and these are still considered as very attractive systems for studying competing 3*d*–4*f* magnetic interactions [6,7]. The diverse magnetic scenarios displayed by these compounds give rise to a great variety of functional materials for technological applications, from hard and soft magnets [3,8] to magnetic refrigeration [9,10].

Among these intermetallic compounds, Fe-rich R_2Fe_{17} alloys crystallize in the Th_2Zn_{17}-type rhombohedral crystal structure when R is one of the rare earths with the largest atomic radii (from Ce to Sm), and exhibit ferromagnetic order with high values for the Fe magnetic moment (close to that of pure Fe, $\sim 2\ \mu_B$/Fe atom, and independent of the rare earth element), and Curie temperatures, T_C, around room temperature in the case of Pr or Nd [11,12]. In both Pr_2Fe_{17} and Nd_2Fe_{17}, Fe atoms occupy four different crystallographic sites (in Wyckoff notation, 6c, 9d, 18f and 18h,

* Corresponding author. Tel.: +34 985102899; fax: +34 985103324.
E-mail address: pgorria@uniovi.es (P. Gorria).

1359-6454/$36.00 © 2008 Acta Materialia Inc. Published by Elsevier Ltd. All rights reserved.
doi:10.1016/j.actamat.2008.12.014

respectively) [13,14], and the ferromagnetic character of these alloys is intimately related to the local environment of these Fe atoms, i.e., the sign and the magnitude of the magnetic interactions depends on the number of Fe nearest neighbors and especially on the Fe–Fe interatomic distances [15]. Previous works on the whole R_2Fe_{17} series have clearly shown that in these compounds the Fe–Fe interatomic distances, d_i, control the magnetic coupling between the Fe magnetic moments: for $d_i < 2.45$ Å these magnetic moments are antiparallel, while for $d_i > 2.45$ they are parallel [16,17]. In particular, if the distance between 6c and 6c Fe atoms (located along the *c*-axis), the so-called "dumbbell site", is lower than 2.45 Å [18,19], the local magnetic interaction being negative, and the direct exchange then gives rise to an antiferromagnetic coupling which depends strongly on the lattice strain. The rest of the Fe–Fe interactions are positive, leading to parallel magnetic moments, and hence magnetic energy is stored next to the Fe1(6c)–Fe1(6c) shortest interatomic distances, where negative interactions prevail. For this reason, a compensation between magnetic and elastic energies results in a large and negative thermal expansion along the *c*-axis. Consequently, a slight increase in such distances, i.e., through the introduction of interstitial light elements (N, Al, Ga) [16,17,20], could lead to a decrease in the antiferromagnetic interaction, thus favouring ferromagnetism in this alloy. The strong dependence of the magnetic interactions on the distances leads to large magnetovolume effects, where anomalous thermal expansion below the ordering temperature or a large and negative pressure dependence of T_C are the most representative signatures [16,17,21,22].

Moreover, these binary R_2Fe_{17} intermetallic compounds exhibit a moderate magnetocaloric effect (MCE) [23], showing values of the magnetic entropy change, $|\Delta S_M| \sim 6$ J kg^{-1} K^{-1} (for $\mu_0 H = 5$ T) at about room temperature (for R = Nd, Pr) [24,25]. These values are lower than those measured in other well-known families of magnetocaloric materials, such as $Gd_5(Si_{1-x}Ge_x)_4$ [26–28] or $La(Fe_xSi_{1-x})_{13}$ [29]. However, Pr_2Fe_{17} and Nd_2Fe_{17} compounds have some advantages, such as a maximum of $|\Delta S_M|$ around room temperature and broader $|\Delta S_M|$ peaks, thus making them potential candidates for use in magnetic refrigeration, provided that they can be adequately processed [22,23,30].

High-energy ball milling (HEBM) is a widely used technique for either alloying and/or mechanical processing of materials [31]. On the one hand, HEBM allows the synthesis of alloys which are not miscible by other fabrication routes, such as nanostructured Fe–Cu solid solutions [32] or disordered Fe–Zr metallic glasses [33], thus giving rise to new metastable compounds with interesting physical–chemical properties [34,35]. On the other hand, mechanical processing by means of HEBM is used to alter the microstructure of materials (decreasing the mean crystalline size down to the nanometer scale, and/or introducing mechanical microstrain through the generation of a large number of defects, which leads to changes in the atomic environments), and therefore to modify the physical properties [36]. Recently, moderate MCE has been observed in disordered and/or metastable compounds, such as milled GdNiAl compounds [37], melt-spun Y_2Fe_{17} [38] and GdSiGeSn [39] alloys or in GdAlMn [40] and Fe-rich metallic glasses [41]. However, the production of nanostructured R_2Fe_{17} alloys with rhombohedral crystal structure has not yet been reported, and we present in this paper a fabrication route, via mechanical processing from the starting Pr_2Fe_{17} bulk alloy by means of HEBM, which gives rise to such a peculiar microstructural configuration. A detailed study of the correlation between crystal structure, microstructure and magnetic properties, including magnetovolume anomalies and magnetocaloric effect, in these compounds will be shown.

2. Materials and methods

2.1. Synthesis of materials and processing

Pieces of commercially pure elements Fe 99.9% and Pr 99.98% (relative to the rare earth metal content [42]), from Goodfellow, were used as starting materials for preparing Pr_2Fe_{17} as-cast pellets by means of an arc melter (MAM-1, Edmund Bühler GmßH) under a controlled Ar atmosphere. The pellets (wrapped in a tantalum foil and sealed under vacuum in quartz ampoules) were furnace annealed for 1 week at 1373 K in order to homogenize the Th_2Zn_{17}-type phase and to minimize the amount of other possible impurity phases. The thermal treatment was finished by direct water quenching of the pellets from the furnace. The samples were subsequently manually pulverized by means of an agate mortar to prepare powders for the measurements and also for the milling process. The powders were sieved using a 106 μm pore size metallic sieve and were then sealed together with stainless steel balls (10 mm in diameter; ball-to-powder weight ratio of 8:1) in a stainless steel vial under an Ar atmosphere. The milling process was carried out using a high-energy planetary ball mill (Retsch PM/400) for 10 h, following successive rotations of 5 min clockwise followed by 5 min anticlockwise with a break of 5 min in between. This procedure ensures that the temperature is sufficiently low during the milling process, favouring the progressive diminution of the average grain size of the crystals and avoiding possible recrystallization of samples. In the following the samples will be named "Bulk" and "BM-10 h" Pr_2Fe_{17} for the as-cast and the 10 h ball milled (or mechanically stressed) materials, respectively.

2.2. Sample morphology and structural characterization

The morphology of the milled powders was evaluated by means of scanning electron microscopy (SEM) using a JEOL JSM-6100. Additionally, several transmission electron microscopy (TEM) images were collected (JEOL 2000-EXII) in order to obtain a statistical distribution of the mean nanocrystalline sizes. The crystal structures of

both bulk and BM-10 h Pr_2Fe_{17} samples were checked by high-resolution X-ray powder diffraction (Seifert XRD3000) using graphite-monochromated Cu K_α radiation ($\lambda = 1.5418$ Å). Scans of 2θ between 2° and 160° with $\Delta\theta = 0.02°$ steps and counting times of 20 s per point were measured at room temperature. Neutron diffraction experiments were carried out at the Institute Laue-Langevin (ILL), Grenoble, France. Two powder diffraction patterns of the as-cast and milled samples were collected at $T = 300$ K on the D2B two-axis diffractometer, in a d-space range between 0.8 and 10 Å, operating in "high-resolution" mode with a neutron wavelength of $\lambda = 1.594$ Å selected with a Ge(335) monochromator. For each sample, approximately 4 g was introduced in a cylindrical vanadium sample-holder. In addition, neutron powder thermodiffraction experiments were carried out on the "high-flux" D1B two-axis neutron diffractometer in the temperature range between 5 and 550 K combining a conventional orange cryostat and a vanadium furnace [43]. The aim of these low-temperature experiments was to monitor the temperature dependence of the crystal lattice parameters in both Bulk and BM-10 h Pr_2Fe_{17} powder samples. The diffraction patterns were collected in a d-space range between 1.6 and 7 Å using a neutron wavelength of $\lambda = 2.52$ Å selected with a pyrolytic graphite (002) monochromator. The refinement of the patterns was performed using the Fullprof package, based on the Rietveld method [44].

2.3. Magnetic characterization

A Faraday balance was used to measure the temperature dependence of the magnetization curves, $M(T)$, in the temperature range 250–380 K and under an applied magnetic field $\mu_0 H = 20$ mT, in order to accurately determine the Curie temperature, T_C, of the samples. The measurements of the magnetic field dependence of the magnetization curves, $M(H)$, were performed using the vibrating sample magnetometer (VSM) option of a Quantum Design PPMS-14 T platform. If an accurate estimate of the MCE is sought, precise experimental data is needed, hence 40 isothermal $M(H)$ curves have been collected for each sample over a broad temperature range in order to achieve this. The temperature steps between consecutive isothermal $M(H)$ curves were 2 K near T_C, and 5 or 10 K far from the magnetic ordering temperature. At each temperature the data were collected under constant DC applied magnetic field steps of $\mu_0 \Delta H = 0.1$ T in the magnetic field range between 0 and 5 T. The MCE was determined as a function of the temperature and the applied magnetic field through numerical integration of the isothermally measured $M(H)$ curves. Taking into account that 50 field values were measured for each $M(H)$ curve, experimental errors have been largely minimized. In addition, another three $M(H)$ curves from $\mu_0 H = 0$ up to 14 T were measured for each of the two samples, with steps of 0.1 T (140 points), one at $T = 4$ K, in order to estimate the value of the magnetic moment at low temperature, and the other two at $T_C - 2$ K and $T_C + 2$ K, with the aim of obtaining the field dependence of the maximum of the magnetic entropy change, $|\Delta S_M|^{max}(H)$.

3. Results and discussion

3.1. Powder morphology and microstructure

The SEM images in Fig. 1a show the morphology of the milled powders at mesoscopic scale. The powders are composed of irregularly shaped microscale grains with a broad size distribution, in the range of 0.5–5.0 μm, with a tendency to agglomeration. The higher-magnification micrograph reveals that the grains are in fact close-packed assemblies of smaller, flaky, or laminar-like, entities. The actual size of these is difficult to establish due to the poor definition of grain boundaries, but can be roughly estimated as 100–400 nm. Accordingly, the representation of a particle-size distribution in this case is not a simple task. Thus, a further study of the internal structure of these microscale grains was carried out by TEM. In the inset of Fig. 1b we show a typical TEM image where individual nanoscale particles can be resolved. The histogram showing the mean crystalline size distribution over a large number of individual particles (>500) follows a log-normal function, giving an average size of the crystallites, $\langle\tau\rangle_{TEM}$, of 23(1) nm, with a standard deviation of 6(1) nm.

3.2. Crystal structure and microstructural evolution

Fig. 2 shows high-resolution neutron powder diffraction patterns obtained at $T = 300$ K for both Bulk and BM-10 h Pr_2Fe_{17} samples. The peaks observed in the pattern corresponding to the starting bulk alloy can be indexed as Bragg reflections belonging to two different phases with $R\bar{3}m$ (#166) rhombohedral and $Im\bar{3}m$ (#229) body-centered cubic crystal structures. The former is a Pr_2Fe_{17} phase (Th_2Zn_{17}-type crystal structure), while the latter is an α-Fe impurity phase (<8%). From the Rietveld refinement of the pattern we have obtained accurate values for the most important structural parameters associated with the atoms in the unit cell, i.e., crystal unit cell parameters, atomic positions in this unit cell and Debye–Waller temperature factors; these are in good agreement with previously reported single-crystal data [13] and are summarized in Table 1. The labeling for the Pr and Fe atomic coordinates is the same as that used in the International Tables for Crystallography [45] for the hexagonal setting of space group $R\bar{3}m$ (#166).

If we now focus our attention in the pattern corresponding to the milled sample (Fig. 2, bottom panel), the most noticeable findings are an overall decrease in the peak intensities and a considerable line-broadening of the Bragg reflections. However, the Th_2Zn_{17}-type crystal structure is maintained, and the amount of impurity phase does not change within experimental error. The peak profile analysis (see Ref. [46] for more details) gives two important results: (i) a mean crystalline size of $\langle\tau\rangle_{Diff} = 20(2)$ nm, which

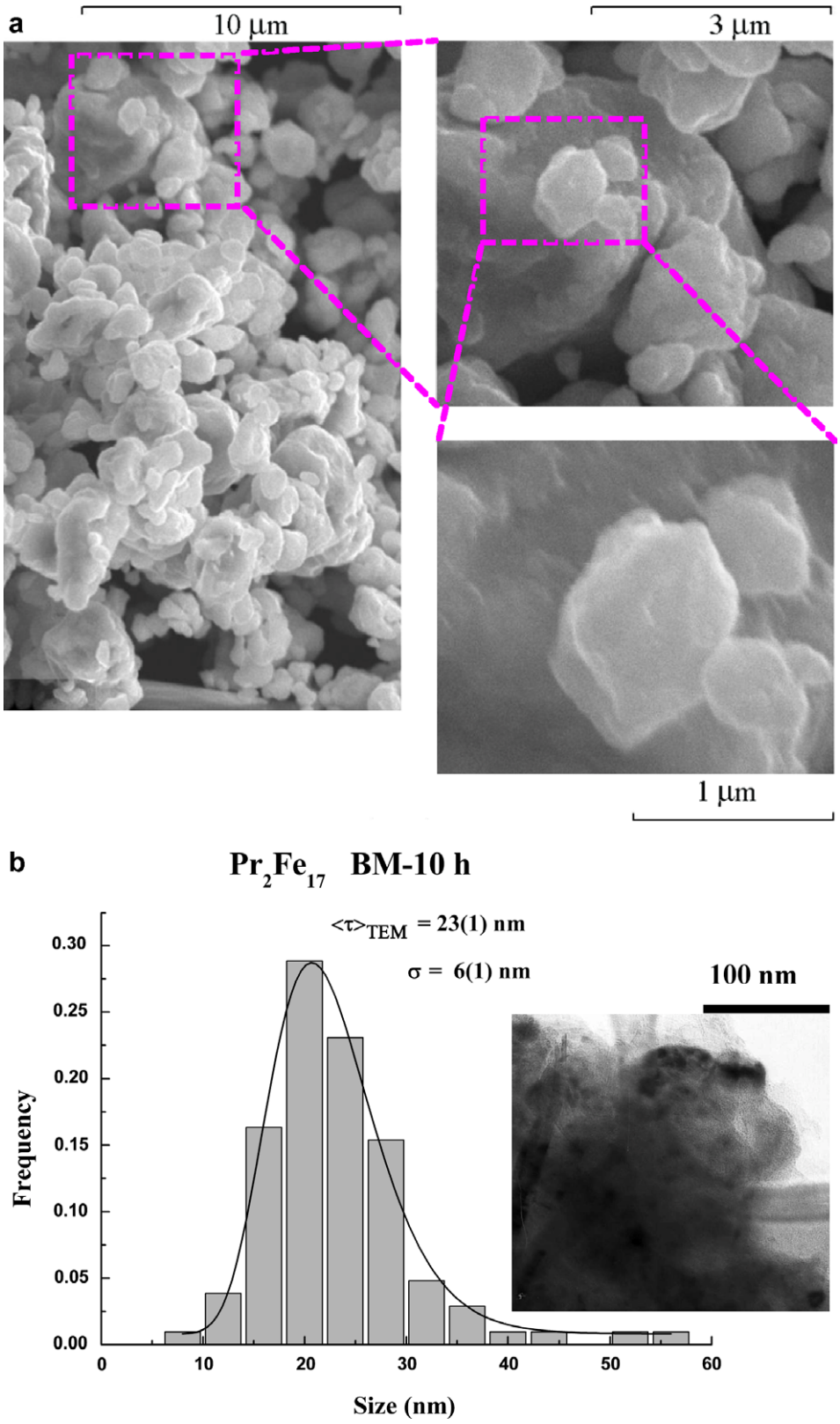

Fig. 1. (a) Scanning (SEM) and (b) transmission (TEM) electron microscopy images showing the microstructure and morphology of the BM-10 h Pr_2Fe_{17} powders. Grain size histogram together with the fit (solid line) to a log-normal distribution is presented in (b).

coincides rather well with that estimated from TEM images; (ii) a nearly vanishing induced microstrain, $\varepsilon \approx 0.03(2)\%$, thus suggesting that the ball-milling process mainly produces a progressive fracturing of the brittle Pr_2Fe_{17} crystals down to the nanometer length-scale. Furthermore, the values of the crystal unit cell parameters

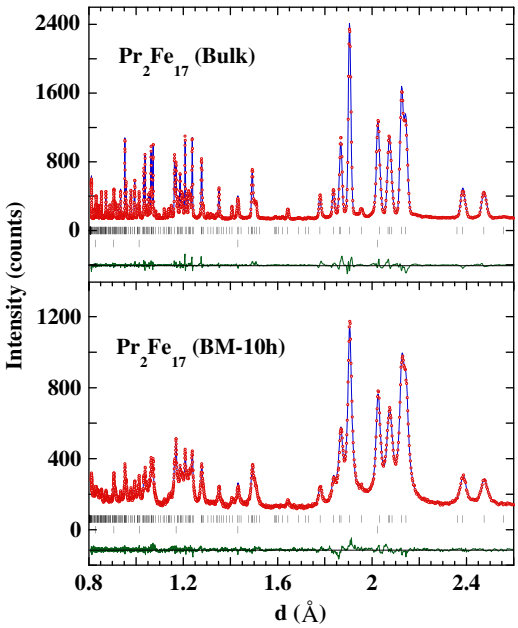

Fig. 2. Observed (dots) and calculated (solid line) high-resolution neutron powder diffraction patterns for Bulk and BM-10 h Pr_2Fe_{17} alloys at $T = 300$ K. Data were collected on the D2B diffractometer. Note the different y-scales used. Positions of the Bragg reflections (in terms of the interplanar distance, d, are represented by vertical bars: the first row corresponds to the Pr_2Fe_{17} phase while the second one is associated with α-Fe impurity. The observed – calculated difference is depicted at the bottom of each pattern.

Table 1
Structural data of both Bulk and BM-10 h Pr_2Fe_{17} ($R\bar{3}m$) compounds at $T = 300$ K obtained from the neutron powder diffraction patterns shown in Fig. 2. Data for single crystal [13] is also shown for comparison.

Compounds	Pr_2Fe_{17} (single crystal)	Pr_2Fe_{17} (Bulk)	Pr_2Fe_{17} (BM-10 h)
a (Å)	8.585(5)	8.5849	8.5880
c (Å)	12.464(8)	12.4659	12.4699
c/a	1.452	1.452	1.452
V (Å^3)	795.55	795.66	796.48
Pr (6c)			
z	0.3436(1)	0.3443(3)	0.3425(7)
B (Å^2)	0.54(12)	0.65(6)	0.91(9)
Fe1 (6c)			
z	0.0960(4)	0.0967(1)	0.0970(3)
B (Å^2)	0.55(15)	0.39(3)	1.43(7)
Fe2 (9d)			
B (Å^2)	0.47(12)	0.29(2)	0.91(5)
Fe3 (18f)			
x	0.2868(3)	0.2877(1)	0.2874(2)
B (Å^2)	0.66(12)	0.35(2)	1.09(4)
Fe4 (6c)			
x	0.1696(2)	0.1690(1)	0.1691(2)
y	0.8304	0.8310	0.8309
z	0.4897(2)	0.4896(1)	0.4891(2)
B (Å^2)	0.68(13)	0.35(2)	0.97(4)
R_B	3.9	3.3	2.5
R_P	–	3.2	2.7
R_{wp}	–	4.3	3.5
R_F	–	2.1	1.5
χ^2 (%)		7.0	1.5

exhibit a slight increase, and accordingly a cell volume enlargement, although the c/a ratio remains constant with a value of 1.452. The atomic positions undergo only subtle changes (see Table 1), the most striking feature after milling being a small increase in Fe1(6c)–Fe1(6c) interatomic distances (from 2.41 to 2.42 Å).

The observed increase in the value of the Debye–Waller temperature factor for all the atomic positions in the BM-10 h Pr_2Fe_{17} sample also suggests that the severe mechanical treatment generates a certain amount of structural disorder as a consequence of the large number of defects created in the crystalline domains, giving rise to grain fracturing followed by a drastic reduction in the average grain size. In this situation, a substantial increase in the percentage of atoms at the surface and/or grain boundaries begins to play a role that cannot be discarded. These atoms exhibit different physical–chemical behavior compared to those in the bulk, thus resulting in measured values of physical quantities which differ from those expected in bulk alloys [47].

3.3. Temperature and magnetic field dependencies of the magnetization

The value of T_C has been estimated from the minimum in the temperature derivative of the magnetization, dM/dT, vs. temperature curve (see Fig. 3). In the inset of Fig. 3 the normalized magnetization, $M/M_{250K}(T)$ curves, for the two samples measured in the Faraday balance (under a low applied magnetic field, $\mu_0 H = 20$ mT) are shown. It is worth noting that while M rapidly goes down in the bulk sample for temperatures above 280 K, the milled sample exhibits a much slower decrease. In our case, the bulk sample exhibits a sharp and well-defined minimum, giving a value of $T_C = 286 \pm 1$ K. However, a precise estimation of T_C is difficult for the milled sample because the dM/dT vs. T curve displays a broad and asymmetric minimum (see Fig. 3). Nevertheless, we could give an approximate

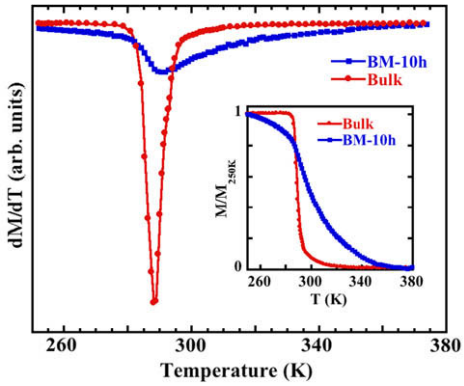

Fig. 3. Temperature derivative of the magnetization vs. temperature, from which the values of the Curie temperature have been determined. The inset shows the temperature dependence of the normalized magnetization, M/M_{250K}, under an applied magnetic field of $\mu_0 H = 20$ mT for both Bulk and BM-10 h Pr_2Fe_{17} alloys.

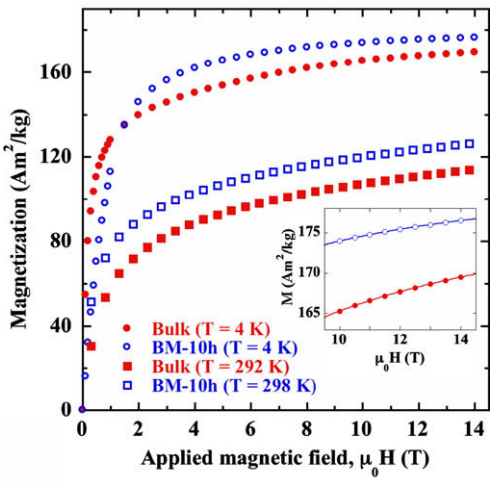

Fig. 4. Isothermal magnetization curves measured at 4 K and at a temperature slightly above T_C (292 and 298 K for Bulk and BM-10 h Pr_2Fe_{17} samples, respectively). In the inset the measured magnetization (points) and the fit (solid line) to an approach-to-saturation law (see text) are shown.

value of $T_C \approx 292 \pm 10$ K for the milled sample following this criterion. Moreover, the trend exhibited by both M/M_{250K} and dM/dT vs. T curves around T_C in the BM-10 h Pr_2Fe_{17} sample suggests a picture in which a broad distribution of T_C values should be considered instead of a unique and well-defined one. This fact can be a direct consequence of the induced structural disorder and the slightly different local environments of the atoms at the grain boundaries, giving rise to modification in their magnetic behavior, as has been observed in other Fe-based nanostructured magnetic materials [47].

In Fig. 4 the magnetization curves, $M(H)$, for Bulk and BM-10 h Pr_2Fe_{17} samples measured at 4 K and just above T_C are shown. Three features are worth noting relative to these $M(H)$ curves: (i) the high values of the magnetization (around 2/3 of the value at 4 K) that can be induced just above the magnetic ordering temperature if a high magnetic field is applied; (ii) the increase of ~6% in the value of the saturation magnetization, M_s, at low temperature for the BM-10 h sample; and (iii) the large increase in the magnetic anisotropy in the BM-10 h alloy, clearly seen in the $M(H)$ curves measured at $T = 4$ K, due to the drastic decrease in the mean crystalline size down to the nanometer length-scale [3].

The value of M_s at $T = 4$ K has been estimated from the fit to the corresponding $M(H)$ curves using a typical approach-to-saturation law [48] in the high magnetic field range (10–14 T):

$$M = M_S\left(1 - \frac{b}{H^2}\right) + \chi_0 H. \quad (1)$$

The fit (see inset in Fig. 4) gives values of $M_s = 162 \pm 5$ Am^2/kg for the Bulk Pr_2Fe_{17} sample and $M_s = 172 \pm 5$ Am^2/kg for BM-10 h, corresponding to 35.7 ± 0.1 μ_B/f.u. and 37.9 ± 0.1 μ_B/f.u., respectively.

3.4. Magnetocaloric effect

Taking into account the abrupt decrease in the magnetization near T_C in the bulk alloy (see Fig. 3), we can expect a remarkable change in its magnetic entropy, while for the milled alloy this change could be largely modified due to the very different M/M_{250K} vs. T behavior exhibited around T_C. In order to evaluate the magnetic entropy change,

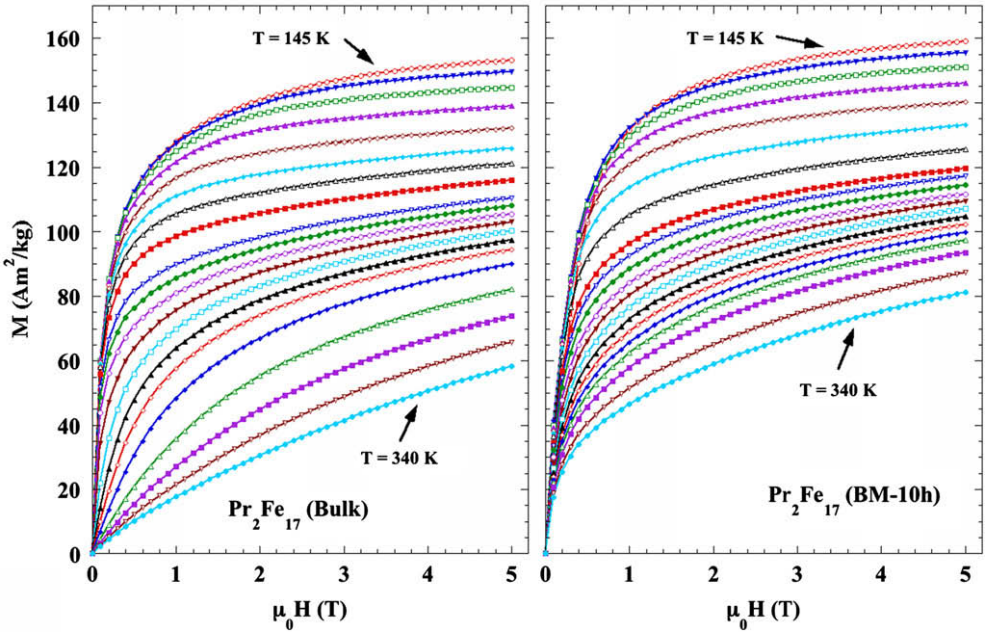

Fig. 5. Isothermal magnetization curves measured under applied magnetic fields up to $\mu_0 H = 5$ T, with $\mu_0 \Delta H = 0.1$ T. The ΔT between consecutive curves varies from 10 K (far from T_C) to 2 K (in the immediate vicinity of T_C).

ΔS_M, in both samples, isothermal magnetization curves have been collected for both Bulk and milled Pr_2Fe_{17} samples over a wide temperature range (some measured isothermal $M(H)$ curves are shown in Fig. 5).

Because the Curie temperature of the impurity phase (α-Fe) is very high ($T_C = 1044$ K), no contribution to MCE is expected from this phase at room temperature. It is well known that, for an isothermal process, ΔS_M can be evaluated by integrating the relevant Maxwell relation [23]:

$$\Delta S_M(T,H) = S_M(T,H) - S_M(T,0) = \int_0^H \left(\frac{\partial M}{\partial T}\right)_H dH, \quad (2)$$

where at a fixed temperature T, $S_M(T,H)$ and $S_M(T,0)$ are the magnetic entropy under an applied magnetic field H and in the absence of the magnetic field, respectively. In fact, in order to calculate ΔS_M at a given temperature, a numerical integration of two consecutive $M(H)$ isotherms around such temperature and the numerical derivative with temperature is performed. The results obtained from these calculations allow us to envisage the evolution of ΔS_M with temperature and/or applied magnetic field. In Fig. 6 we present the $|\Delta S_M|(T)$ curves ($\Delta S_M < 0$) at five different values for the applied magnetic field (upper (bottom) panel for the Bulk (BM-10 h) Pr_2Fe_{17} sample). It can clearly be seen that there is a well-defined maximum for the bulk sample at $T \approx T_C$ (286 K), reaching a value of $|\Delta S_M| = 6.3$ J kg^{-1} K^{-1} at 5 T. For the BM-10 h sample the $|\Delta S_M|(T)$ curve is broader, as could be expected from the slow decrease in M in this temperature range (see Fig. 3), the maximum value is one-third lower ($|\Delta S_M| = 4.5$ J kg^{-1} K^{-1}) under the same applied magnetic field and is scarcely shifted to higher temperatures (~300 K). It is also worth noting the asymmetric form of the $|\Delta S_M|(T)$ peak exhibited by the milled sample with a long tail after the maximum, which is undoubtedly correlated with that of the temperature derivative of the magnetization (see Fig. 3).

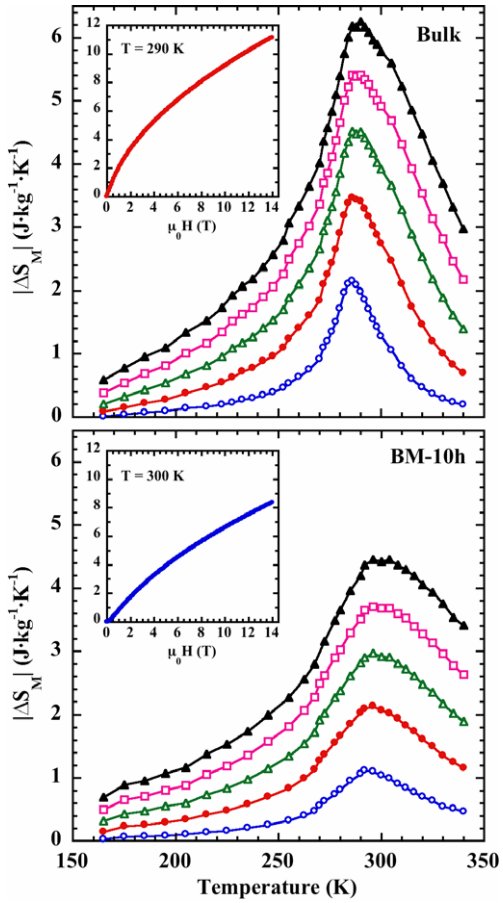

Fig. 6. Magnetic entropy change $|\Delta S_M|$ of Bulk (upper panel) and BM-10 h (lower panel) Pr_2Fe_{17} samples under applied magnetic fields of 1 T (open circles), 2 T (solid circles), 3 T (open triangles), 4 T (open squares) and 5 T (solid triangles). The insets show $|\Delta S_M|^{max}$ vs. $\mu_0 H$ up to 14 T for each material.

Additionally, the applied magnetic field dependence of the maximum value for $|\Delta S_M|$, up to $\mu_0 H = 14$ T, is shown in the insets of Fig. 6 for both samples. The $|\Delta S_M|^{max}(H)$ curve exhibits a larger slope at low magnetic fields for the Bulk sample, following a similar trend for magnetic field values above 8 T. In terms of the potential interest for application in magnetic refrigeration, the maximum $|\Delta S_M|$ value is not the only parameter to be taken into account when considering a material attractive. The temperature at which MCE occurs defines the technological field, and the temperature range in which it can operate is also of great importance. Hence, the parameter commonly used to characterize the magnetocaloric properties of a material, and its potential suitability as a magnetic refrigerant, is the relative cooling power (RCP). This parameter takes into account not only the maximum value of the MCE, but also the width of the $|\Delta S_M|(T)$ curve, which is calculated from the product of the maximum $|\Delta S_M|$ peak value and the full width at half maximum, δT_{FWHM}:

$$RCP(S) = |\Delta S_M|^{\max} \times \delta T_{FWHM}. \quad (3)$$

In other words, the higher the δT_{FWHM} value is, the larger temperature difference between the hot and cool ends of the cycle that can be used for operation. In our samples, the value for δT_{FWHM} increases greatly with milling, being at least 50% higher than that of the starting Bulk Pr_2Fe_{17} alloy, giving rise to an increase in the RCP value (reaching around 83% that of gadolinium) and largely extending (up to 125 K) the temperature difference between the hot and cold ends of the refrigeration cycle [30].

3.5. Magnetovolume anomalies

We have already mentioned that R_2Fe_{17} ferromagnetic compounds exhibit magnetovolume anomalies below T_C. This behavior, inherent to the Fe sublattice in these materials, can be explained in terms of the strong dependence of magnetic coupling on Fe–Fe distances [15–17]. The cell volume at low temperatures is higher than that expected for a non-magnetic system because it stabilizes a ferromagnetic coupling between the Fe magnetic moments [16]. As the temperature is increased, the Fe magnetic moment begins to decrease and the magnetovolume coupling loses strength

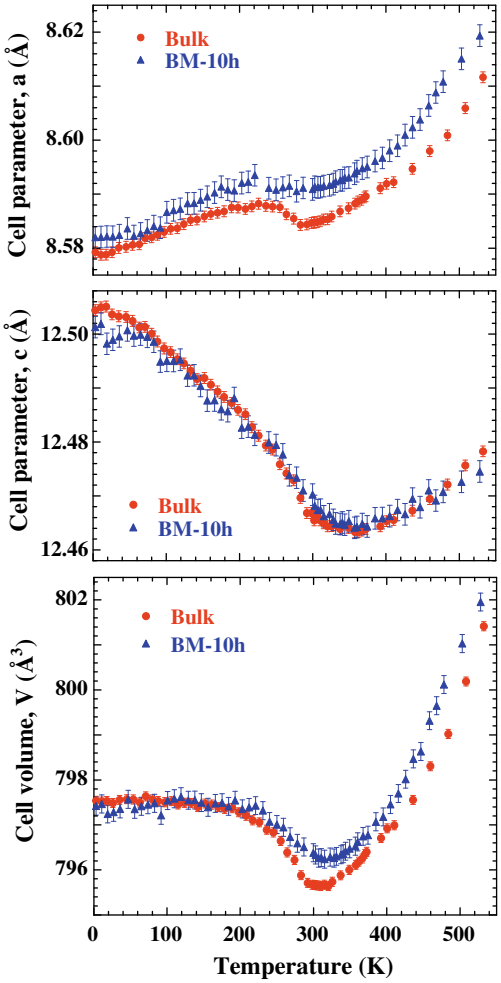

Fig. 7. Temperature dependences of the unit cell parameters, a and c, and the unit cell volume, V, for Bulk and BM-10 h Pr_2Fe_{17} samples as deduced from neutron thermodiffraction experiments.

progressively, giving rise to a lattice contraction. The volume goes down to the corresponding equilibrium value in the absence of ferromagnetic order, which is reached above the magnetic ordering temperature. Although this behavior is well known for other R_2Fe_{17} compounds (R = Y, Nd, Lu, etc.) [16,17,49,50] and a similar trend in Pr_2Fe_{17} alloys can be expected, the direct measurement of the volume contraction below T_C has not yet been reported.

We show in Fig. 7 the temperature dependences of the unit cell parameters, $a(T)$ and $c(T)$, together with that of the unit cell volume, $V(T)$, in the temperature range between 5 and 550 K for both Bulk and BM-10 h Pr_2Fe_{17} samples, obtained from the analysis of the neutron powder diffraction patterns collected on the D1B diffractometer. Three different regions can be appreciated for the temperature dependence of the cell parameter a, associated with the basal plane of the conventional hexagonal unit cell. At low temperature, a slight increase up to around 250 K is followed by a small minimum around $T = T_C$, and for temperatures above 400 K an almost linear Grüneissen-like increase, typical of metallic compounds, is observed.

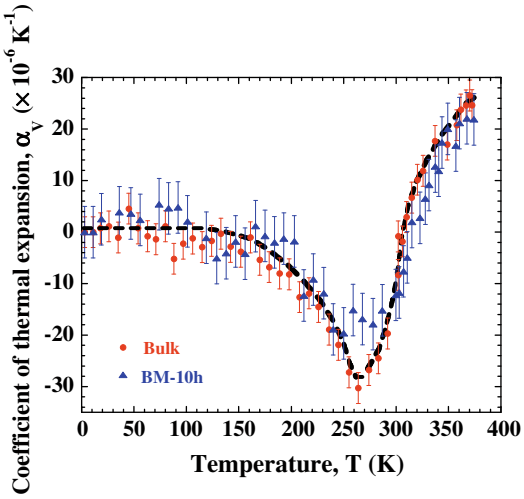

Fig. 8. Temperature dependence of the coefficient of thermal expansion, $\alpha_V = \frac{1}{V}\left(\frac{\partial V}{\partial T}\right)_P$, for Bulk and BM-10 h Pr_2Fe_{17} samples, as deduced from neutron thermodiffraction experiments (see Fig. 7). A five-point linear regression has been used to calculate the derivative. The line showing the tendency of $\alpha_V(T)$ is a visual guide.

However, the cell parameter c displays a continuous and pronounced decrease in its value on heating from 5 K to approximately 300 K, showing a well-defined minimum at around 350 K. It is worth noting that relative variation of the cell parameters between 5 and 300 K is unlikely: while a increases less than 0.07%, c decreases more than 0.3%. The latter can be appreciated clearly in Fig. 8, where a reduced d-space range of the neutron powder diffraction patterns for both Bulk and BM-10 h samples is shown. On heating from 5 to 300 K the position of the (220) reflection does not vary, while that of the (006) reflection moves towards lower d-values, thus demonstrating the lattice contraction along the c-axis. These features are also present in the BM-10 h sample, although the minimum of the $a(T)$ curve is poorly defined and that of the $c(T)$ curve seems to be broader and slightly shifted to higher temperatures.

The different temperature dependence of the cell parameters results in an almost constant value for the cell volume and a vanishing coefficient of thermal expansion, $\alpha_V = \frac{1}{V}\left(\frac{\partial V}{\partial T}\right)_P$, indicating the invar character of these compounds [16,17] below 150 K. At higher temperatures, the cell volume exhibits a clear minimum at around 300 K, giving rise to an anomalous temperature dependence of $\alpha_V(T)$, which exhibits negative values between 200 and 310 K (see Fig. 9), and a minimum in the immediacy of the magnetic ordering temperature, T_C. The large contribution of $c(T)$ to the negative thermal expansion in these compounds has been attributed to the dumb-bell pairs of Fe atoms, which are aligned along the c-axis. Furthermore, the existence of the anomaly in the $c(T)$ even above T_C and up to 350 K is due to a large short-range magnetic coupling between dumb-bell Fe atoms [17].

The same trend for the cell volume is still present in the mechanically processed sample, and two remarkable features are worth noting when comparing the $V(T)$ curves

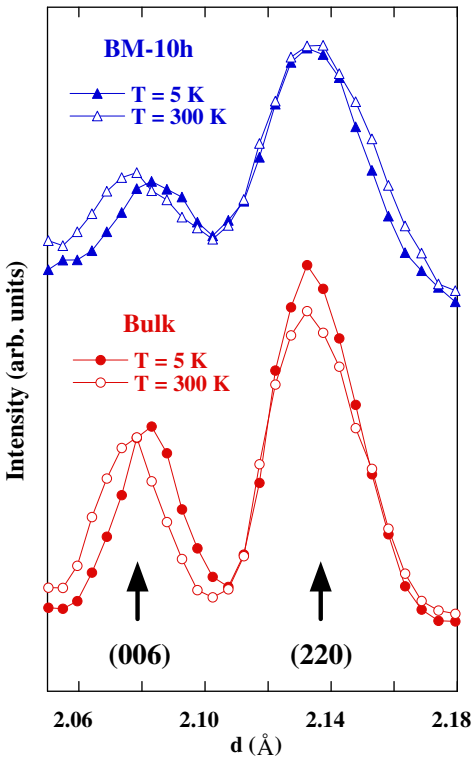

Fig. 9. Detail of the neutron powder diffraction patterns collected at 5 and 300 K for the (220) and (006) Bragg diffraction reflections as a function of the interplanar distance, d, showing the different temperature dependencies of the cell parameters a and c, respectively.

for both samples. Firstly, the milled sample depicts a broader and less profound minimum, slightly shifted to higher temperatures compared with that of the Bulk alloy. This behavior is analogous to that observed for $dM/dT(T)$ and $|\Delta S_M|(T)$ curves, giving rise to a broadening, and therefore a loss of definition of both the Curie temperature and magnetic entropy maximum (see Figs. 3 and 6). Secondly, and although the cell volume at low temperature is almost the same, at 300 K (the temperature at which the milling process takes place) it is somewhat higher for the BM-10 h sample. In addition, the slight increase observed in the Fe1(6c)–Fe1(6c) interatomic distances (from 2.41 to 2.42 Å) favours the ferromagnetism in the milled sample, and provokes a small shift in the value of T_C to higher temperatures. As a result, both magnetocaloric and magnetovolume effects are strongly correlated in this Pr_2Fe_{17} intermetallic compound. In fact, these effects can be largely modified provided that subtle modifications in the Fe–Fe interatomic distances are induced in the samples, through negative pressure or mechanical stress treatments.

4. Summary and conclusions

Nanostructured intermetallic Pr_2Fe_{17} powders have been obtained using mechanical processing from the as-cast alloys by means of high-energy ball milling for 10 h. A decrease in the mean crystalline size down to ~20 nm, with almost vanishing induced microstrain and a slight increase of 0.1% in the cell volume at $T = 300$ K, is observed. The Th_2Zn_{17}-type crystal structure, as well as the atomic positions in the unit cell, is not altered, thus suggesting a modification of the microstructure mainly due to progressive grain fracturing. The most characteristic features of this material, namely the magneto-caloric effect and magnetovolume anomalies, such as the invar character below 200 K and the negative thermal expansion in the vicinity of T_C, are still present after the milling procedure. Apart from that, the magnetic moment exhibits a slight increase of around 2 μ_B/f.u. after milling. Moreover, in the mechanically stressed sample, the magnetization vs. temperature curve shows a slow decrease around room temperature, suggesting that the nanostructured powders do not have a unique and well-defined value of T_C. The latter gives rise to a reduction in the maximum value of the magnetic entropy change together with the broadening of the $|\Delta S_M|(T)$. Nevertheless, these facts lead to an enhancement of at least 10% in the relative cooling power with respect to that of the parent Bulk alloy, and additionally, the working temperature difference between the hot and cold ends of the refrigeration cycle can be as larger as 125 K, making these nanostructured materials interesting for potential applications in magnetic refrigeration around room temperature. However, it must be pointed out that although nanostructured materials offer considerable promise because of their large surface area to volume ratios for heat transfer, the heat transfer fluid must flow around the particles. Therefore, if the pore size is very small in a packed regenerator bed, the pressure to pump the heat transfer fluid will rise exponentially, approaching infinity at nanosize pores. Finally, it must be taken into account that in ferromagnetic R_2Fe_{17} compounds, the sign of the magnetic interactions depends essentially on distances between nearest-neighbor Fe atoms. Hence, the counterbalancing between magnetic and elastic energies, below the magnetic ordering temperature, gives rise to the observed anomalies, such as an almost zero volume expansion below 200 K and a negative thermal expansion coefficient between 200 and 300 K.

Acknowledgements

Financial support from FEDER and Spanish MICINN (NAN2004-09203-C04-03 & MAT2008-06542-C04-03) is acknowledged. We thank ILL and Spanish CRG-D1B for allocating neutron beam time; and also SCT's (Univ. Oviedo) for assisting in SEM, TEM, XRD and magnetic measurements. P.A. (Ph.D. grant) and J.L.S.L. (research contract COF07-013) are grateful to FICyT.

References

[1] Gleiter H. Acta Mater 2000;48:1.
[2] Ma E. Prog Mater Sci 2005;50:413.
[3] Hadjipanayis GC. J Magn Magn Magn 1999;200:373.

[4] McHenry ME, Laughlin DE. Acta Mater 2000;48:223.
[5] Inoue A, Shen BL, Koshiba H, Kato H, Yavari AR. Nat Mater 2003;2:661.
[6] Kuz'min MD, Tishin AM. In: Buschow KHJ, editor. Handbook of magnetic materials, vol. 17. Amsterdam: North Holland; 2007. p. 149.
[7] Piqué C, Blanco JA, Burriel R, Abad E, Artigas M, Fernández-Díaz MT. Phys Rev B 2007;75:224424.
[8] Skomski R, Coey JMD. Phys Rev B 1993;48:15812.
[9] Tishin AM. In: Buschow KHJ, editor. Handbook of magnetic materials, vol. 12. Amsterdam: North Holland; 1999. p. 395.
[10] Gschneidner KA, Pecharsky VK, Tsokol AO. Rep Prog Phys 2005;68:1479.
[11] Buschow KHJ. Rep Prog Phys 1977;40:1179.
[12] Weitzer F, Hiebl K, Rogl PJ. Appl Phys 1989;65:4963.
[13] Johnson Q, Wood DH, Smith GS. Acta Cryst 1968;B24:274.
[14] Álvarez P, Sánchez Llamazares JL, Pérez MJ, Hernando B, Santos JD, Sánchez-Marcos J, et al. J Non-Cryst Solids 2008;354:5172.
[15] Buschow KHJ. J Less-Comm Metals 1975;43:55.
[16] Givord G, Lemaire R, James WJ, Moreau J-M, Shah JS. IEEE Trans Mag 1971;MAG-7:657.
[17] Givord G, Lemaire R. IEEE Trans Mag 1974;MAG-10:109.
[18] Long GJ, Pringle OA, Grandjean F, Yelon WB, Buschow KHJ. J Appl Phys 1993;74:504.
[19] Li ZW, Zhou XZ, Morrish AH. Phys Rev B 1995;51:2891.
[20] Isnard O, Miraglia S, Soubeyroux JL, Fruchart D, Pannetier J. Phys Rev B 1992;45:2920.
[21] Arnold Z, Kamarád J, Morellón L, Ibarra MR. J Appl Phys 1997;81:5693.
[22] Brouha M, Buschow KHJ, Miedema AR. IEEE Trans Mag 1974;MAG-10:182.
[23] Tishin AM, Spichkin YI. The magnetocaloric effect and its applications. Bristol: IOP Publishing; 2003.
[24] Dan'kov S Yu, Ivtchenko VV, Tishin AM, Gschneidner Jr KA, Pecharsky VK. Adv Cryog Eng 2000;46:397.
[25] Mandal K, Yan A, Kerschl P, Handstein A, Gutfleisch O, Müller K-H. J Phys D 2004;37:2628.
[26] Morellon L, Blasco J, Algarabel PA, Ibarra MR. Phys Rev B 2000;62:1022.
[27] Tegus O, Bruck E, Buschow KHJ, de Boer FR. Nature 2002;415:150.
[28] Provenzano V, Shapiro AJ, Shull RD. Nature 2004;429:853.
[29] Fujita A, Fujieda S, Hasegawa Y, Fukamichi K. Phys Rev B 2003;67:104416.
[30] Gorria P, Sánchez Llamazares JL, Álvarez P, Pérez MJ, Sánchez Marcos J, Blanco JA. J Phys D: Appl Phys 2008;41:192003.
[31] Suryanarayana C. Prog Mater Sci 2001;46:1.
[32] Yavari AR, Desré PJ, Benameur T. Phys Rev Lett 1992;68:2235.
[33] Gorria P, Garitaonandia JS, Pérez MJ, Blanco JA, Campo J. Phys Status Solidi (RRL) 2009;3:28.
[34] Gorria P, Martinez-Blanco D, Blanco JA, Hernando A, Garitaonandia JS, Férnandez Barquín L, et al. Phys Rev B 2004;69:214421.
[35] Gorria P, Martinez-Blanco D, Blanco JA, Pérez MJ, Hernando A, Férnandez Barquín L, et al. Phys Rev B 2005;72:014401.
[36] Gorria P, Martinez-Blanco D, Pérez MJ, Blanco JA, Smith RI. J Magn Magn Mater 2005;294:159.
[37] Chevalier B, Bobet J-L, Sánchez Marcos J, Rodríguez Fernández J, Gómez Sal JC. Appl Phys A 2005;80:601.
[38] Fang YK, Chang CW, Yeh CC, Chang HW, Li W, Chang WC. J Appl Phys 2008;103:07B302.
[39] Zhang T, Chen Y, Tang Y. J Phys D: Appl Phys 2007;40:5778.
[40] Gorsse S, Chevalier B, Orveillon G. Appl Phys Lett 2008;92:122501.
[41] Franco V, Borrego JM, Conde A, Roth S. Appl Phys Lett 2006;88:132509.
[42] Gschneidner Jr KA. J Alloys Comp 1993;193:1.
[43] Fernández-Martínez A, Gorria P, Cuello GJ, Santos JD, Pérez MJ. J Non-Cryst Solids 2007;353:855.
[44] Rodríguez Carvajal J. Physica B 1993;192:55.
[45] Hahn T, editor. International tables for crystallography. Vol. A. Space-group symmetry. 5th ed. Dordrecht: Kluwer; 2002.
[46] Martinez-Blanco D, Gorria P, Blanco JA, Pérez MJ, Campo J. J Phys: Condens Matter 2008;20:335213.
[47] Hernando A, Navarro I, Gorria P. Phys Rev B 1995;51:3281.
[48] Cullity BD. Introduction to magnetic materials. Reading, MA: Addison-Wesley; 1972.
[49] Zhang XD, Shumsky MG, James WJ, Yelon WB. IEEE Trans Mag 1995;31:3713.
[50] Girt E, Altounian Z, Swainson IP, Krishnan KM, Thomas GJ. Appl Phys 1999;85:4669.

J. Phys.: Condens. Matter **22** (2010) 216005 (8pp) doi:10.1088/0953-8984/22/21/216005

Nanocrystalline Nd_2Fe_{17} synthesized by high-energy ball milling: crystal structure, microstructure and magnetic properties

Pablo Álvarez[1], Pedro Gorria[1], Victorino Franco[2], Jorge Sánchez Marcos[3], María J Pérez[1], José L Sánchez Llamazares[1], Inés Puente Orench[4,5] and Jesús A Blanco[1]

[1] Departamento de Física, Universidad de Oviedo, Calvo Sotelo, s/n, 33007 Oviedo, Spain
[2] Departamento Física de la Materia Condensada, ICMSE-CSIC, Universidad de Sevilla, PO Box 1065, 41080 Sevilla, Spain
[3] Instituto de Ciencia de Materiales de Madrid, CSIC, Cantoblanco, 28049 Madrid, Spain
[4] Institute Laue-Langevin, BP 156, 6 rue Jules Horowitz, 38042 Grenoble Cedex 9, France
[5] Instituto de Ciencia de Materiales de Aragón, CSIC—Universidad de Zaragoza, 50009 Zaragoza, Spain

E-mail: alvarezpablo.uo@uniovi.es

Received 22 December 2009, in final form 23 March 2010
Published 5 May 2010
Online at stacks.iop.org/JPhysCM/22/216005

Abstract

Nanocrystalline Nd_2Fe_{17} powders have been obtained by means of high-energy ball milling from nearly single-phase bulk alloys produced by arc melting and high temperature homogenization annealing. The rhombohedral Th_2Zn_{17}-type crystal structure of the bulk alloy remains unaltered after the milling process, with almost unchanged values for the cell parameters. However, the severe mechanical processing induces drastic microstructural changes. A decrease of the mean crystalline size down to around 10 nm is observed, giving rise to a considerable augmentation of the disordered inter-grain boundaries. This modification of the microstructure affects the magnetic behaviour of the milled powders, although the magnetic structure remains collinear ferromagnetic. While a unique ferro-to-paramagnetic transition temperature, $T_C = 339 \pm 2$ K, is observed in the bulk alloy, the nanocrystalline samples exhibit a more likely distribution of T_C values. The latter seems to be responsible for the significant broadening of the temperature range in which magneto-caloric effect is observed, and the lowering of the maximum value of the magnetic entropy change.

(Some figures in this article are in colour only in the electronic version)

1. Introduction

High-energy ball milling (HEBM) is a widely used technique for the mechanical alloying or processing of a great variety of materials [1–3], and has opened exciting horizons in the production of materials with *sui-generis* and enhanced properties for different technological purposes. This technique allows the synthesis of diverse iron-based metallic metastable materials far from the thermodynamical equilibrium, such as amorphous metallic glasses [4–6] or disordered and supersaturated solid solutions [7–10]. Moreover, the microstructure of bulk alloys, obtained by other conventional fabrication routes, can be largely modified by means of severe mechanical processing using HEBM, giving rise in most cases to drastic changes in their physico-chemical behaviour [11–15]. In this way, HEBM permits obtaining nanocrystalline alloys with mean crystallite size even below 10 nm [16, 17].

R–Fe (R = rare earth) intermetallic compounds display a great variety of crystalline structures and different magnetic behaviours depending on the stoichiometry and the nature of the R ion [18, 19]. These alloys are therefore

attractive from a fundamental point of view, because they are well suited for the study of both 3d–3d and 3d–4f competing magnetic interactions [20, 21]. Moreover, these compounds are also interesting for applications in diverse technological fields including hard and soft magnets or magnetic refrigeration [22–26]. One subset of this family are the Fe-rich R_2Fe_{17} compounds, which crystallize in the rhombohedral Th_2Zn_{17}-type structure (space group $R\bar{3}m$) for the light rare earths, with four different crystallographic sites for the iron atoms, (6c, 9d, 18f and 18h in Wyckoff notation) and a unique 6c site for the rare earth [27–29]. The binary R_2Fe_{17} compounds with R = Pr or Nd are collinear ferromagnets with Curie temperatures, T_C, around room temperature (285 ± 5 and 335 ± 5 K respectively [25, 30–32]) and relatively high values ($\mu_{Fe} \approx 2\ \mu_B$) for the Fe magnetic moments [18–20, 30].

In this paper, and through the combination of x-ray and neutron powder diffraction with electron microscopy and magnetic measurements, we show the effect of HEBM on the morphology of Nd_2Fe_{17} powders, and how mechanically induced changes in the microstructure affect their magnetic behaviour and in particular the magneto-caloric effect (MCE).

2. Experimental methods and data analysis

As starting materials for preparing Nd_2Fe_{17}, as-cast pellets pieces of commercial (Goodfellow) pure elements (Fe 99.9% and Nd 99.98%, relative to the rare earth metal content [33]) were used. Pellets of around 2 g were prepared by arc melting under a controlled Ar atmosphere, followed by a homogenization annealing lasting one week at 1373 K in order to reach a single phase with a Th_2Zn_{17}-type structure (each pellet was wrapped in a tantalum foil and sealed under vacuum in a quartz ampoule to avoid oxidation). After annealing, the pellets were directly quenched in water. The milling was performed in a high-energy planetary ball mill (Retsch PM/400) using stainless steel vials and balls. Sieved powders of Nd_2Fe_{17} (maximum diameter of 106 μm), obtained by manual pulverization of the pellets, were sealed in the vials under an Ar atmosphere (see [34] for additional details) and milled for 10 or 20 h. From here onwards the samples will be labelled 'bulk', 'BM-10 h' and 'BM-20 h' Nd_2Fe_{17} for the bulk, the 10 h and the 20 h ball milled materials, respectively. Energy dispersive x-ray spectroscopy (EDS) was used for the analysis of the elemental distribution and composition of the powders. No remarkable deviation from the starting 2:17 stoichiometry was observed in the samples.

The powder morphology at the micrometre length scale and the statistical distribution of the nanocrystalline size have been visualized and evaluated from scanning (SEM) and transmission (TEM) electron microscopy images. The crystal structure of the samples was studied at room temperature by means of x-ray (XRPD) and neutron (NPD) powder diffraction. XRPD patterns in a *d-spacing* range between 0.8 and 3.4 Å (between 25° and 150° in 2θ with $\Delta\theta = 0.02°$, and counting times of 20 s per point) were collected in high-resolution mode (Seifert model XRD3000) using graphite-monochromated Cu Kα radiation ($\lambda = 1.5418$ Å). NPD experiments were carried out at the high-flux D1B two-axis diffractometer (ILL, Grenoble, France). The diffraction patterns were collected in a *d-spacing* range between 1.65 and 7.3 Å (between 20° and 100° in 2θ with $\Delta\theta = 0.2°$, and counting times of 1 h per pattern) using a neutron wavelength of $\lambda = 2.52$ Å selected from a pyrolytic graphite (002) monochromator. For each sample approximately 4 g in mass were introduced to a vanadium cylindrical sample-holder. The full-profile refinement of the patterns has been performed using the Fullprof suite package [35], based on the Rietveld method.

The temperature and applied magnetic field dependencies of the magnetization were measured in a vibrating sample magnetometer (Lakeshore VSM 7407). Around 45 isothermal magnetization versus applied magnetic field curves, $M(H)$, were measured in the temperature range 85–420 K, with ΔT steps of 10 or 5 K for temperatures far from or near to T_C, respectively. For each $M(H)$ curve the applied magnetic field was increased from 0 to a 15 kOe with field steps of 50, 100 or 250 Oe, thus measuring around 100 points per curve. The magnetic entropy change, $|\Delta S_M|$, was determined as a function of the temperature and the applied magnetic field through the numerical integration of the isothermally measured $M(H)$ curves. For an isothermal process, ΔS_M can be evaluated by integrating the following Maxwell relation [36]:

$$\Delta S_M(T, H) = S_M(T, H) - S_M(T, 0) = \int_0^H \left(\frac{\partial M}{\partial T}\right)_H \mathrm{d}H$$

where $S_M(T, H)$ and $S_M(T, 0)$ are the magnetic entropy under an applied magnetic field H and in the absence of the magnetic field, respectively, at a fixed temperature T. The calculation of ΔS_M at a given temperature is made by a numerical integration of two consecutive $M(H)$ isotherms around such a temperature followed by the numerical derivative with temperature.

3. Results and discussion

3.1. Powder morphology, microstructure and crystal structure

The SEM images displayed in figure 1 show very different morphologies at the micrometre length scale. While the sieved powders of the bulk sample exhibit a superposition of well-defined flaky sheets with sharp edges (see figure 1(a)), both BM-10 h and BM-20 h powders look like agglomerated micron size grains (0.5–10 μm) with irregular shapes and rounded borders (see figures 1(b) and (c)) due to the severe mechanical stressing procedure. However, a higher magnification is needed to appreciate the average size of the smaller particles forming the micrometre-sized grains. In figure 1(d) (inset) we show a TEM image, corresponding to the BM-20 h sample, where distinct particles within the nanometre length scale can be resolved. The histogram describing the mean particle size distribution over a large number of individual entities (>500) follows rather well a log-normal function (figure 1(d)), giving an average size for these nanocrystallites, $\langle\tau\rangle_{TEM} = 8(1)$ nm, with a standard deviation $\sigma = 3(1)$ nm for the BM-20 h powders. An average size of 17(1) nm with $\sigma = 4(1)$ nm, is calculated from the fit corresponding to the mean particle size distribution obtained from TEM images of the BM-10 h

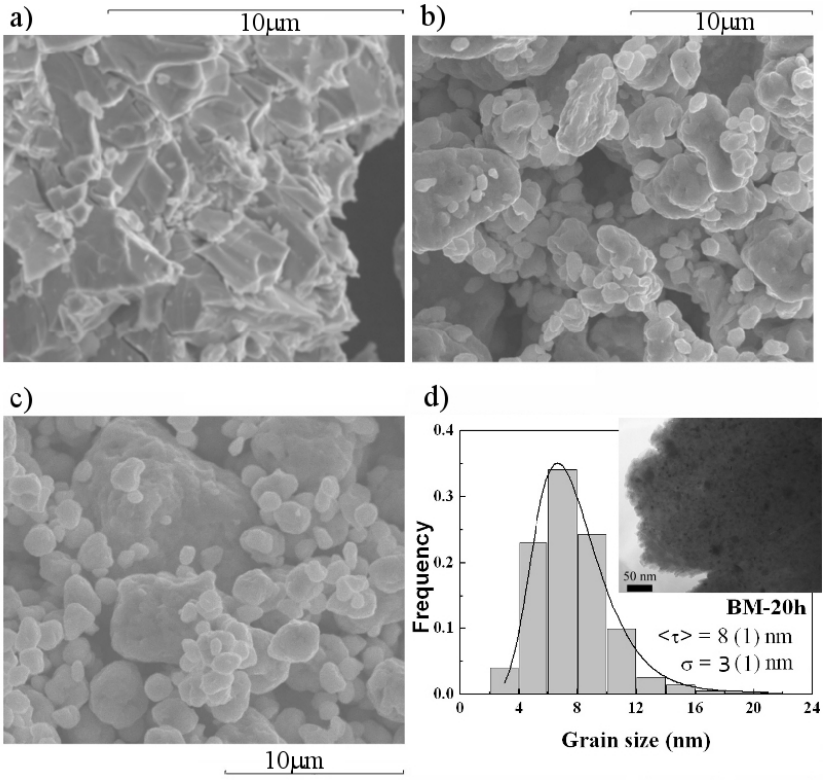

Figure 1. SEM images of bulk (a), BM-10 h (b) and BM-20 h (c) powders. (d) Particle size histogram and the fit (solid line) to a log-normal distribution, corresponding to the BM-20 h sample. The inset shows a typical TEM image.

sample. Hence, an increase of the milling time gives rise to further grain fracturing and to a considerable reduction in the nanocrystallite size.

In figure 2, the room temperature x-ray (left panel) and neutron (right panel) powder diffraction patterns for bulk, BM-10 h and BM-20 h Nd_2Fe_{17} samples are displayed. The patterns corresponding to the starting bulk alloy show peaks that can be indexed as the Bragg reflections belonging to the Nd_2Fe_{17} phase with $R\bar{3}m$ (#166) rhombohedral (Th_2Zn_{17}-type) crystal structure. We have obtained accurate values for the most important structural parameters associated with the atoms in the unit cell from the Rietveld refinement of the patterns. First we refined the non-structural parameters (scale factor, zero shift error and peak shape parameters for the pseudo-Voigt function), the cell parameters and a global isotropic temperature factor, B, for each atom. Then, the atomic coordinates of Nd [6c, $(00z)$] and Fe [6c, $(00z)$; 18f, $(x00)$; 18h, $(x\bar{x}z)$] were refined, those of 9d [$(\frac{1}{2}\,0\,\frac{1}{2})$] being fixed. Other attempts using [$(z\bar{z}x)$] coordinates for the 18h site crystallographic data [37] lead to similar results. Small profile differences, together with good agreement factors, were achieved from the final refinement (see figure 2). The values for the lattice parameters of the bulk sample (see table 1) are similar to those previously reported [38]. In addition, the position of the Bragg reflections in the diffraction patterns corresponding to BM-10 h and BM-20 h samples remain almost unaltered, thus indicating that the Th_2Zn_{17}-type crystal structure is maintained. The peak broadening indicates a drastic reduction of the grain size and therefore to the emergence of a considerable amount of disorder, mainly located at the increasing intergranular regions and/or grain boundaries [9, 16]. From the peak profile analysis (see [17] for more details), a mean crystalline size of $\langle\tau\rangle_{\mathrm{Diff}} = 24(3)$ and 14(5) nm for BM-10 h and BM-20 h samples, respectively, have been estimated, which are in reasonable agreement with those calculated from TEM histograms. The bulk polycrystalline sample does not show any broadening of the peaks with respect to the instrumental line width, thus indicating a minimum average grain size higher than 0.1 μm. However, the mechanically induced microstrain is very low, $\varepsilon \approx 0.04(2)\%$. The latter is a clear distinction with respect to the case of Fe or Fe–TM (TM = Cr, Ni, Cu, ...) ball milled powders in which the amount of induced microstrain can be over 1% [16, 17], hence, the milling process mainly produces a progressive breaking of the Nd_2Fe_{17} crystals down to the nanometre length scale. Additionally, small peaks corresponding to the reflections of a body centred cubic (bcc) crystal structure with a cell parameter $a \approx 2.87$ Å are detected in the diffraction patterns, which can be ascribed to α-Fe impurity. This impurity phase is around $3 \pm 2\%$ in the bulk sample while its amount increases up to around 8 ± 2 and $10 \pm 2\%$ in the BM-10 h and BM-20 h milled compounds, respectively.

It is worth noting that the contribution to the XRD peak width coming from induced strain is negligible (<0.1%). These findings suggest that the main process occurring during milling is a progressive grain breakage down to the nanometre length scale, concomitant with the emergence of structural

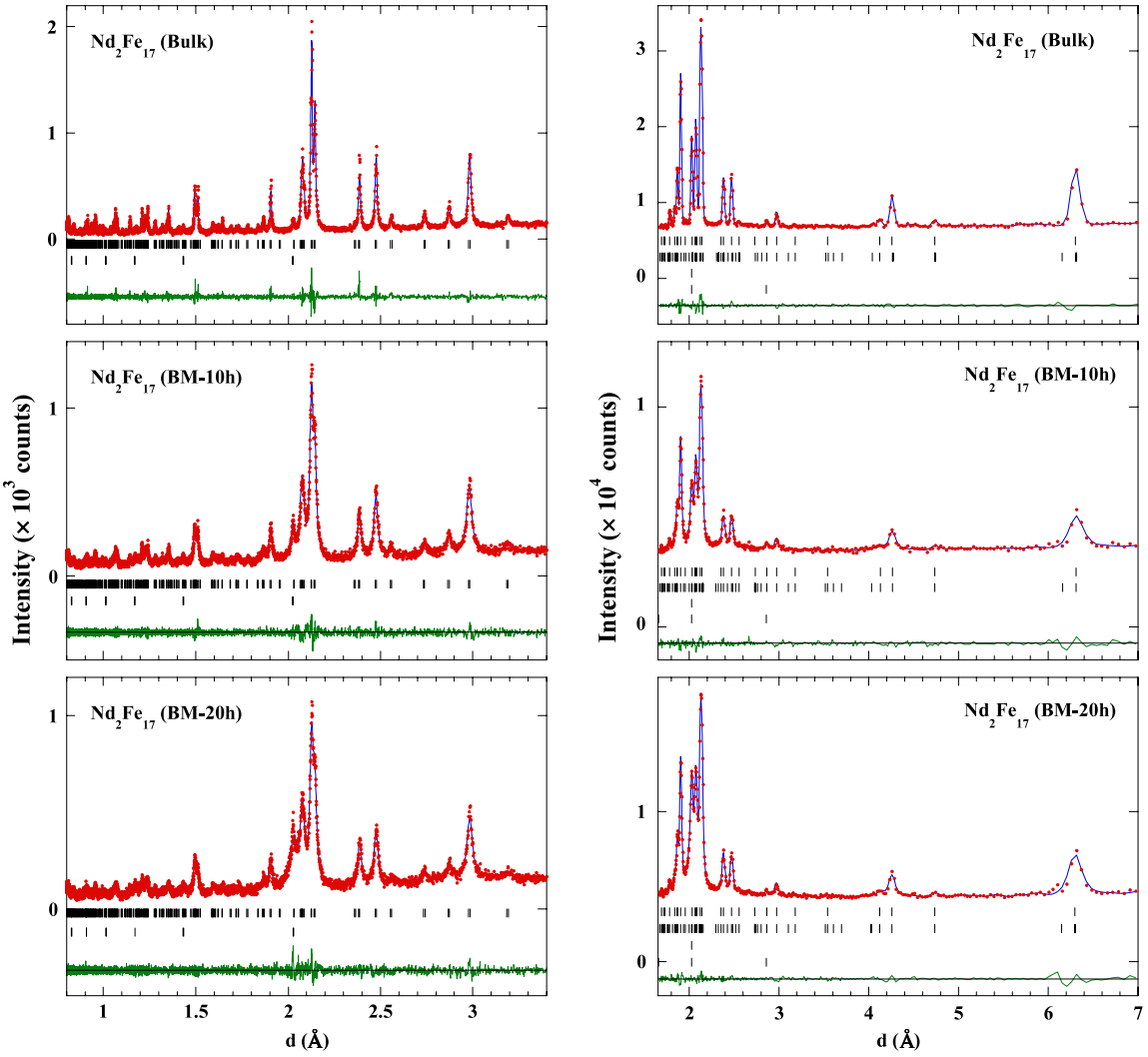

Figure 2. Observed (dots) and calculated (solid line) XRPD (left panel) and NPD (right panel) patterns for bulk, BM-10 h and BM-20 h Nd_2Fe_{17} alloys at $T = 300$ K. Positions of the Bragg reflections (in terms of the interplanar distance, d) are represented by vertical bars; the first row corresponds to the Nd_2Fe_{17} phase while the second one is associated with α-Fe impurity in the XRPD patterns. In the NPD patterns, the first two rows correspond to the Nd_2Fe_{17} phase (nuclear and magnetic) and those at the bottom are related to a α-Fe impurity (nuclear and magnetic). The observed–calculated difference is depicted at the bottom of each figure.

disorder in the material, as evidenced by the increase in the value of the Debye–Waller factor, B, (see table 1). Nevertheless, the lower resolution of the neutron diffraction pattern does not allow the estimation of reliable values for the average crystalline size and/or the induced strain. However, we have refined the nuclear as well as the magnetic structures, and the fit of the NPD patterns confirms that after the milling process the magnetic structure does not change, that is, it is still collinear ferromagnetic with parallel magnetic moments of both Nd and Fe sublattices lying along the basal plane. An accurate determination of the value of the magnetic moment, μ, in each of the five non-equivalent magnetic sites [Nd(6c), Fe1(6c), Fe2(9d), Fe3(18f) and Fe4(18h)] is not possible because there are no pure and well-separated magnetic reflections (at $T = 300$ K the expected values for μ are around 1 μ_B due to the proximity to T_C ($\approx$339 $\pm$ 5 K)), and the magnetic contribution to the intensity of the observed Bragg reflections is lower than 5%. Moreover, the broadening of these reflections due to grain size decrease adds an extra difficulty to achieve this task. In any case, the value obtained from the fit for the total magnetic moment of the Nd_2Fe_{17} phase is $\mu = 22 \pm 6$ μ_B/fu, in excellent agreement with previously reported values obtained from magnetization measurements in polycrystalline samples [39].

In table 1 the crystal unit cell parameters, atomic positions and Debye–Waller temperature factors are summarized. All these data are in reasonable agreement with previously reported data obtained from NPD on Nd_2Fe_{17} polycrystalline alloys [38]. The labelling for the Nd and Fe atomic coordinates is the same as that used in the International Tables for Crystallography [40] for the hexagonal setting of the rhombohedral space group $R\bar{3}m$ (#166).

3.2. Magnetic properties and magneto-caloric effect

Figure 3 shows the temperature and applied magnetic field dependence of magnetization for each sample. It can be seen

Table 1. Structural data (cell parameters a and c, unit cell volume, atomic positions and Debye–Waller temperature factor, B) for bulk, BM-10 h and BM-20 h Nd_2Fe_{17} ($R\bar{3}m$) compounds at $T = 300$ K obtained from the powder diffraction patterns shown in figure 2. The Bragg (R_B), profile (R_p), weighted profile (R_{wp}) and crystallographic (R_F) reliability factors are also reported (see text).

Compounds	Nd_2Fe_{17} (bulk)	Nd_2Fe_{17} (BM-10 h)	Nd_2Fe_{17} (BM-20 h)
a (Å)	8.582(1)	8.584(1)	8.582(1)
c (Å)	12.463(1)	12.463(1)	12.463(1)
V (Å^3)	795	795	795
Nd (6c)			
z	0.3448(2)	0.3440(4)	0.3427(5)
B (Å^3)	0.18(4)	1.2(1)	1.6(1)
Fe1 (6c)			
z	0.0941(4)	0.0947(6)	0.0959(8)
B (Å^3)	0.6(1)	2.1(3)	1.6(3)
Fe2 (9d)			
B (Å^3)	0.38(9)	0.8(2)	0.7(2)
Fe3 (18f)			
x	0.2873(4)	0.2876(5)	0.2861(6)
B (Å^3)	0.68(8)	1.6(2)	1.6(2)
Fe4 (18h)			
x	0.1694(3)	0.1682(4)	0.1687(5)
z	0.4899(3)	0.4912(5)	0.4894(7)
B (Å^3)	0.23(5)	1.3(1)	1.4(2)
R_B	5.8	3.4	3.4
R_p	8.5	7.6	7.6
R_{wp}	10.9	9.7	9.7
R_F	4.6	2.8	2.9
χ^2	1.3	1.1	1.1

in the low magnetic field range that while the ferromagnetic to paramagnetic transition is abrupt in the bulk sample, it becomes poorly defined as the milling time increases, starting at lower temperatures and finishing at higher temperatures than in the bulk one. The latter can be clearly observed in figure 4, where the normalized magnetization versus temperature curve in the immediate vicinity of the ferromagnetic to paramagnetic transition, measured under $H = 200$ Oe, is depicted. The value for the Curie temperature has been estimated from the minimum of the dM/dT versus T curve, using the data of figure 4. The bulk sample exhibits a sharp and well-defined minimum giving a value of $T_C = 339 \pm 5$ K, while the precise estimation of T_C is difficult for the milled samples, because the dM/dT versus T curves display broad and asymmetric minima located at around 340 ± 20 K. Therefore, a broad distribution of T_C values should be considered instead of a unique and well-defined one for the milled samples. This fact could be a direct consequence of the induced structural disorder and the slightly different local environments of the atoms at the grain boundaries, giving rise to a modification of their magnetic behaviour, as has been previously observed in other Fe-based nanostructured magnetic materials [31, 34, 41].

The saturation magnetization, M_s, at $T = 100$ K for the three samples was estimated from the fit of the $M(H)$ curves to an approach-to-saturation law:

$$M = M_s\left(1 - \frac{b}{H^2}\right) + \chi_0 H. \qquad (1)$$

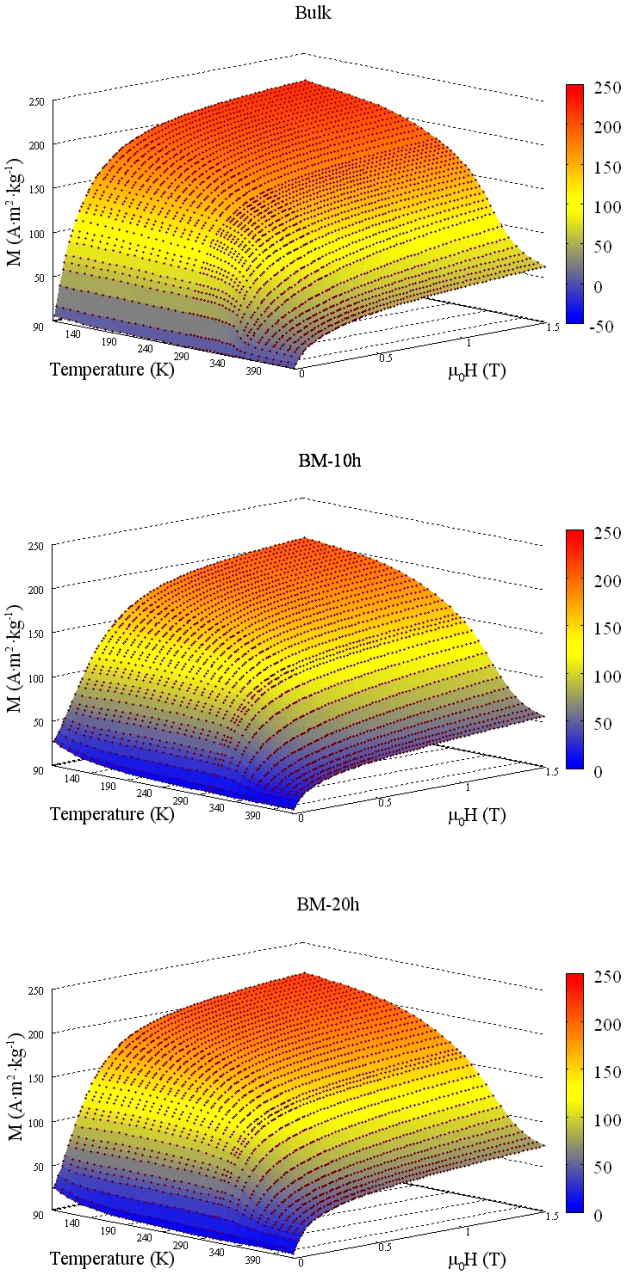

Figure 3. Temperature and applied magnetic field dependencies of the magnetization for the bulk and milled Nd_2Fe_{17} samples.

The fit gives values of 138 ± 5 A m^2 kg^{-1} (bulk), 128 ± 5 A m^2 kg^{-1} (BM-10 h) and 134 ± 5 A m^2 kg^{-1} (BM-20 h) for the M_s. However, these different values must be interpreted with care because the $M(H)$ curves corresponding to the milled samples show an increase of the magnetic anisotropy (which is reflected as a 30% increase in the values of b and χ_0 parameters, see equation (1)) and clearly the saturation regime is not reached under an applied magnetic field of 15 kOe. Moreover, both the coercivity and remanence increase in BM-10 h and BM-20 h samples with respect to those of the bulk alloy, giving rise to a non-zero magnetization value at low applied magnetic fields (see figure 3). We must point out that for every isothermal $M(H)$ curve, after measuring the last value of M ($H = 15$ kOe), H is removed

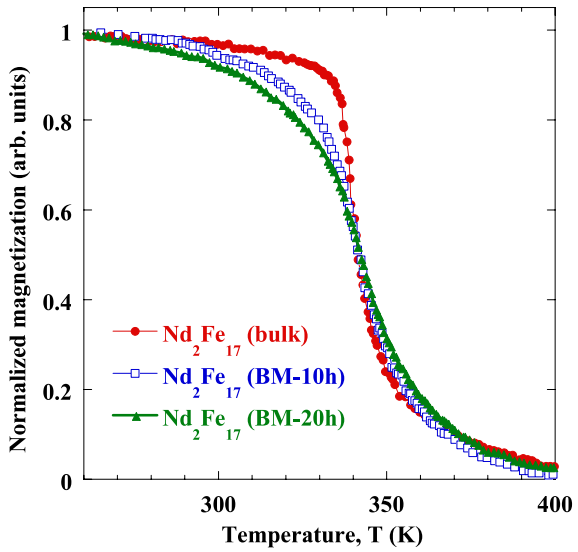

Figure 4. Temperature dependence of the magnetization (normalized to the value at $T = 260$ K) for the bulk and milled Nd_2Fe_{17} samples. Note that the contribution to the magnetization coming from the ferromagnetic α-Fe impurity has been subtracted for clarity.

and the temperature is changed to the next selected value in order to begin the measurement of the next isothermal $M(H)$ curve. In this situation, the first measured M value ($H = 50$ Oe) for each $M(H)$ isotherm is affected by the not-negligible values of coercivity and remanence of the sample. These facts have been previously observed in other milled materials [42], being a direct consequence of the increase of the magnetic anisotropy. Such magnetic anisotropy enhancement could be caused by the drastic decrease of the mean crystallite size down to the nanometre length scale, giving rise to complex magnetic interactions between the nanocrystals and/or nanograin boundaries [23, 35]. Besides that, it is observed that as the temperature is increased above the T_C of the Nd_2Fe_{17} phase, the magnetic field dependence of the magnetization does not resemble a linear trend, as could be expected for a paramagnetic system. The latter is due to both (i) the existence of the α-Fe impurity phase ($T_C = 1044$ K) contributing to the magnetization and (ii) the existence of short-range magnetic correlations that could extend even up to $T = 2T_C$.

In figure 5 a 3D view of the temperature and magnetic field dependence of the magnetic entropy change in the bulk and milled samples is depicted.

The abrupt decrease of the magnetization near T_C in the bulk alloy (see figure 3), gives rise to a remarkable change in its magnetic entropy, reaching a maximum value of $|\Delta S_M| \approx 2.6$ J kg^{-1} K^{-1} at 15 kOe (see figure 6). For both BM-10 h and BM-20 h samples the $|\Delta S_M|(T)$ curves exhibit an evident broadening, as could be expected from the slower decrease of M in this temperature range (see figures 3 and 4), the maximum value of $|\Delta S_M|$ (1.85 and 1.6 J kg^{-1} K^{-1} for BM-10 h and BM-20 h, respectively) is lower than that quoted above for the bulk sample (2.6 J kg^{-1} K^{-1}) under the same applied magnetic field. The temperature at which the maximum of $|\Delta S_M|(T)$ occurs (≈340 K) is nearly the same for the three samples and

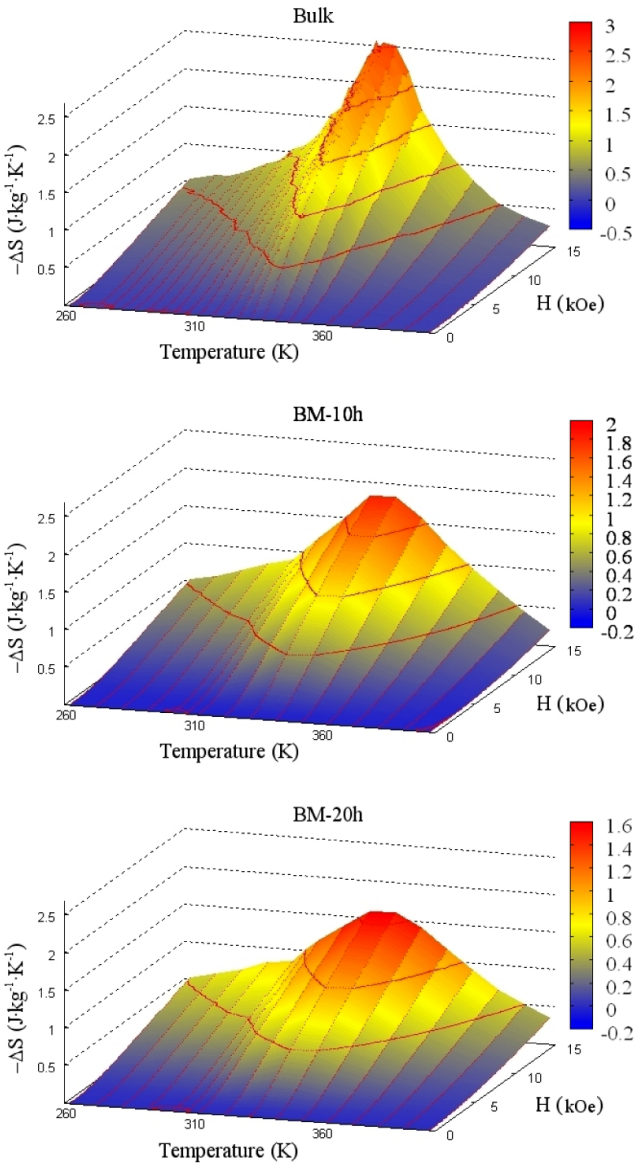

Figure 5. Temperature and applied magnetic field dependencies of the magnetic entropy change for the bulk and milled Nd_2Fe_{17} samples.

it almost coincides with the value of T_C in the bulk sample. It is also worth noting the asymmetric shape of the $|\Delta S_M|(T)$ peak exhibited by the milled sample, with a long tail after the maximum, which is undoubtedly correlated with that of the temperature dependence of magnetization.

Therefore, the ball milling process causes a decrease of the value of $|\Delta S_M|$, but at the same time, the MCE spreads out over a wider temperature range [12, 25, 26], as can be seen from the inset of figure 6, where the magnetic field dependence of the δT_{FWHM} parameter (defined as the full width at half maximum of $|\Delta S_M|(T)$ peak) is shown. The latter is an important parameter to be taken into account when the refrigerant capacity (RC) or relative cooling power (RCP) [25, 43, 44] of a material of potential interest in magnetic refrigeration has to be evaluated. An estimation of the refrigerant capacity ($RC = \delta T_{FWHM} \times |\Delta S_M|^{max}$) gives similar values for the three samples, 83, 87 and 87 J kg^{-1}

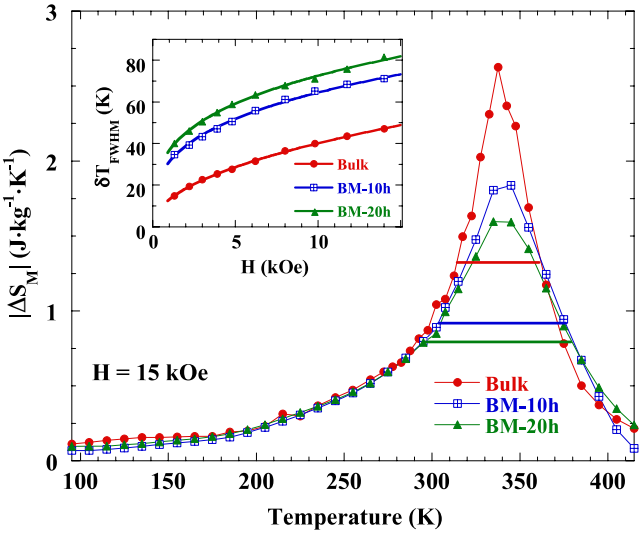

Figure 6. Temperature dependence of $|\Delta S_M|$ under $H = 15$ kOe for bulk and milled Nd_2Fe_{17} samples. The horizontal lines represent δT_{FWHM} for each sample. The inset shows the magnetic field dependence of δT_{FWHM} for all the samples (see text).

for bulk, BM-10 h and BM-20 h, respectively. Even though a slight increase (≈5%) in the value of RC is observed after milling, we cannot conclude that the mechanically induced microstructural changes improve the magneto-caloric effect in these compounds in the applied magnetic field range between 0 and 15 kOe.

4. Summary

Nanostructured Nd_2Fe_{17} powders have been obtained from the starting arc-melted massive compound by means of high-energy ball milling after milling times of 10 and 20 h. A reduction of the average crystallite size below 20 nm, with almost vanishing values for the mechanically induced microstrain ($\varepsilon < 0.1\%$) has been found. The Th_2Zn_{17}-type crystal structure, as well as the atomic positions in the unit cell, remain unaltered, thus suggesting a modification of the microstructure mainly due to progressive grain fracturing. The severe mechanical processing of the samples generates a high degree of disorder that should be mainly located at the grain boundaries, thus affecting the magnetic behaviour in two important aspects: (i) applied magnetic fields much higher than 15 kOe are needed to saturate the samples due to the increase of magnetic anisotropy; and (ii) the magnetization versus temperature curve shows a slow decrease around room temperature in the mechanically stressed sample, suggesting that the nanostructured powders do not have a unique and well-defined value of T_C. The latter gives rise to a reduction in the maximum value of the magnetic entropy change together with the broadening of the $|\Delta S_M|(T)$.

Acknowledgments

Financial support from FEDER and Spanish MICINN (Projects Nos MAT2008-06542-C04-03, MAT2007-65227 & NAN2004-09203-C04-03) and from the PAI of the Regional Government of Andalucia (Project No. P06-FQM-01823) is acknowledged. We thank ILL and CRG-D1B for allocating neutron beam time. PA and JSM are grateful for their research contracts to FICyT and MICINN respectively. The SCTs at the University of Oviedo are also acknowledged.

References

[1] Suryanarayana C 2001 *Prog. Mater. Sci.* **46** 1
[2] Zhang D L 2004 *Prog. Mater. Sci.* **49** 537
[3] Ma E 2005 *Prog. Mater. Sci.* **50** 413
[4] Randrianantoandro N, Cooper R J, Greneche J M and Cowlam N 2002 *J. Phys.: Condens. Matter* **14** 9713
[5] Mishra D, Srinivasan A and Perumal A 2008 *J. Phys. D: Appl. Phys.* **41** 215003
[6] Gorria P, Garitaonandia J S, Pérez M J, Blanco J A and Campo J 2009 *Phys. Status Solidi (RRL)* **3** 28
[7] Mishra D, Perumal A and Srinivasan A 2009 *J. Appl. Phys.* **105** 07A306
[8] Gorria P, Martinez-Blanco D, Blanco J A, Hernando A, Garitaonandia J S, Férnandez Barquín L, Campo J and Smith R I 2004 *Phys. Rev.* B **69** 214421
[9] Gorria P, Martinez-Blanco D, Pérez M J, Blanco J A and Smith R I 2005 *J. Magn. Magn. Mater.* **294** 159
[10] Valderruten J F, Pérez Alcázar G A and Grenèche J M 2008 *J. Phys.: Condens. Matter* **20** 485204
[11] Gorria P, Martinez-Blanco D, Blanco J A, Pérez M J, Hernando A, Férnandez Barquín L and Smith R I 2005 *Phys. Rev.* B **72** 014401
[12] Ipus J J, Blázquez J S, Franco V, Conde A and Kiss L F 2009 *J. Appl. Phys.* **105** 123922
[13] Gorria P *et al* 2009 *Phys. Status Solidi (RRL)* **3** 115
[14] Kalita M P C, Perumal A and Srinivasan A 2009 *J. Phys. D: Appl. Phys.* **42** 105001
[15] Gorria P *et al* 2009 *Phys. Rev.* B **80** 064421
[16] Martinez-Blanco D, Gorria P, Pérez M J, Blanco J A and Smith R I 2007 *J. Magn. Magn. Mater.* **316** 328
[17] Martinez-Blanco D, Gorria P, Blanco J A, Pérez M J and Campo J 2008 *J. Phys.: Condens. Matter* **20** 335213
[18] Buschow K H J 1977 *Rep. Prog. Phys.* 1977 **40** 1179
[19] Buschow K H J 1980 *Ferromagnetic Materials* vol 1, ed E P Wohlfarth (Amsterdam: North-Holland) p 297
[20] Givord D and Lemaire R 1974 *IEEE Trans. Magn.* **10** 109
[21] Piqué C, Blanco J A, Burriel R, Abad E, Artigas M and Fernández-D íaz M T 2007 *Phys. Rev.* B **75** 224424
[22] Hadjipanayis G C 1999 *J. Magn. Magn. Mater.* **200** 373
[23] Skomski R and Coey J M D 1993 *Phys. Rev.* B **48** 15812
[24] Gschneidner K A Jr, Pecharsky V K and Tsokol A O 2005 *Rep. Prog. Phys.* **68** 1479
[25] Gorria P, Sánchez Llamazares J L, Álvarez P, Pérez M J, Sánchez Marcos J and Blanco J A 2008 *J. Phys. D: Appl. Phys.* **41** 192003
[26] Sánchez Llamazares J L, Pérez M J, Álvarez P, Santos J D, Sánchez M L, Hernando B, Blanco J A, Sánchez Marcos J and Gorria P 2009 *J. Alloys Compounds* **483** 682
[27] Ray A E 1966 *Acta Crystallogr.* **21** 426
[28] Johnson Q, Wood D H and Smith G S 1968 *Acta Crystallogr.* B **24** 274
[29] Johnson Q, Smith G S and Wood D H 1969 *Acta Crystallogr.* B **25** 464
[30] Weitzer F, Hiebl K and Rogl P J 1989 *J. Appl. Phys.* **65** 4963
[31] Álvarez P, Sánchez Llamazares J L, Pérez M L, Hernando B, Santos J D, Sánchez-Marcos J, Blanco J A and Gorria P 2008 *J. Non-Cryst. Solids* **354** 5172
[32] Franse J J M and Radwanski R J 1993 *Handbook of Magnetic Materials* vol 7, ed K H J Buschow (Amsterdam: Elsevier) p 307

[33] Gschneidner K A Jr 1993 *J. Alloys Compounds* **193** 1
[34] Gorria P, Álvarez P, Sánchez Marcos J, Sánchez Llamazares J L, Pérez M J and Blanco J A 2009 *Acta Mater.* **57** 1724
[35] Rodríguez Carvajal J 1993 *Physica* B **192** 55
[36] Tishin A M and Spichkin Y I 2003 *The Magnetocaloric Effect and its Applications* (Bristol: Institute of Physics Publishing)
[37] Girt E, Altounian Z, Swainson I P, Krishnan K M and Thomas G 1999 *J. Appl. Phys.* **85** 4669
[38] Long G J, Marasinghe G K, Mishra S, Pringle O A, Hu Z, Yelon W B, Middleton D P, Buschow K H J and Grandjean F 1994 *J. Appl. Phys.* **76** 5383
[39] Girt E, Guillot M, Swainson I P, Krishnan K M, Altounian Z and Thomas G 2000 *J. Appl. Phys.* **87** 5323
[40] International Tables for Crystallography 2002 *Space-Group Symmetry* vol A, ed T Hahn (Dordrecht: Kluwer)
[41] Hernando A, Navarro I and Gorria P 1995 *Phys. Rev.* B **51** 3281
[42] Blázquez J S, Franco V, Conde A and Roth S 2006 *Phil. Mag.* **86** 2271
[43] Franco V, Borrego J M, Conde A and Roth S 2006 *Appl. Phys. Lett.* **88** 132509
[44] Franco V, Conde C F, Conde A and Kiss L F 2007 *Appl. Phys. Lett.* **90** 052509

MAGNETIC AND CRYSTAL STRUCTURE, MAGNETOCALORIC EFFECT AND MAGNETOVOLUME ANOMALIES IN THE Er_2Fe_{17} COMPOUND

Pablo Álvarez[a,1], Pedro Gorria[a], Jorge Sánchez Marcos[b], Gabriel Cuello[c], Inés Puente Orench[c], Jose Alberto Rodriguez Velamazán[c], Gastón Garbarino[d], Imanol de Pedro[e], José L. Sánchez Llamazares[f] and Jesús Angel Blanco[a].

[a] *Departamento de Física, Universidad de Oviedo, Calvo Sotelo, s/n, 33007 Oviedo, Spain*
[b] *Instituto de Ciencia de Materiales de Madrid, CSIC, Cantoblanco, 28049 Madrid, Spain*
[c] *Institute Laue Langevin, 6 rue Jules Horowitz, 38042 Grenoble, France*
[d] *European Synchrotron Radiation Facility (ESRF), BP 220, 6 rue Jules Horowitz, 38043 Grenoble Cedex, France*
[e] *Departamento CITIMAC, Universidad de Cantabria, Santander 39005, Spain*
[e] *Instituto Potosino de Investigación Científica y Tecnológica, Camino a la Presa San José 2055 Col. Lomas 4ª, San Luis Potosí, S.L.P. 78216, Mexico*

Abstract

Interest in the magnetic properties on R_2Fe_{17} (R = rare earth) has been recently renewed by the observation of a moderate magnetocaloric effect ($\Delta S_M \sim$ -6 J·kg^{-1}·K^{-1} for 50 kOe) at the Curie temperature for light-R Pr_2Fe_{17} and Nd_2Fe_{17} ferromagnetic compounds. Combining different experimental techniques investigations on ferrimagnetic heavy-R E_2Fe_{17} lead to the conclusion that the interplay between magnetocaloric and magnetovolume effects is fundamental to understand the physical properties of this material: the existence of short-range ordering effects, reflected in the spontaneous magnetostriction, which falls down to zero well above the Curie Temperature; a non-excessively large magnetocaloric response ($\Delta S_M \sim$ -5 J·kg^{-1}·K^{-1} for 80 kOe) near the ordering temperature for high applied magnetic fields; and the existence of an inverse magnetocaloric effect ($\Delta S_M \sim$ 1.5 J·kg^{-1}·K^{-1} for 80 kOe) at 40 K. This last feature seems to be related with a crystalline electric field-level crossover in the Er-sublattice. The main trends found experimentally are qualitatively well described considering a mean field Hamiltonian that incorporates both crystalline electric field and exchange interactions.

PACS numbers: 75.30.Sg, 61.05.C-, 61.05.F-,75.10.Hk, 75.30.Kz.

I Introduction

R-Fe (R = rare earth) intermetallic compounds may display a great variety of crystalline structures and different magnetic behaviors depending on the stoichiometry and the nature of the R ion involved, which makes these alloys very interesting for the study of both 3d-3d and 3d-4f competing magnetic interactions[1,2]. At the same time, their potential applications explain the important attention paid to these materials, from hard and soft magnets to magnetic refrigeration[1,3,4]. One subset of this family is the Fe-rich R_2Fe_{17} compounds, which are the highest Fe-content binary intermetallics within the R-Fe phase diagram[5]. In the 90´s they were a subject of considerable attention after it was discovered that interstitial C and N atoms increase their Curie temperature (T_C) and modify the character of magnetocrystalline anisotropy making some of them, namely $Sm_2Fe_{17}X_y$ (X = C, N), suitable for being used as permanent magnets[6]. R_2Fe_{17} compounds crystallize into the Th_2Zn_{17}-type rhombohedral crystal structure ($R\bar{3}m$) when R is one of the light-R, and into the hexagonal Th_2Ni_{17}-type ($P6_3/mmc$ space group) one for those compounds with rare earth heavier than Tb. Those compounds with R = Y, Gd and Tb can crystallize in either hexagonal or rhombohedral structures, depending on the annealing treatment[7,8]. In the rhombohedral crystal structure the crystallo-

1 Alvarezpablo.uo@uniovi.es

graphic sites for iron atoms are 6c, 9d, 18f and 18h (in Wyckoff notation) and a unique 6c site for the rare earth, whereas for the hexagonal structure Fe atoms occupy the 4f, 6g, 12j and 12k sites and two nonequivalent positions for the R element, 2b and 2d; in the latter case the structure can be a disordered variant which includes the 2c site for the R-element and the 4e for iron atoms[9-15]. The coordination numbers for Fe(4f), Fe(6g), Fe(12j) and Fe(12k) in the hexagonal structure are 13, 10, 10 and 10, respectively, and for Fe(6c), Fe(9d), Fe(18f) and Fe(18h) in the rhombohedral structure are 13, 10, 10 and 9, respectively. Fe(6c) and the Fe(4f), the so-called "dumbbell sites", possess the largest coordination numbers in their respective crystal structure[11], which is likely related to their largest magnetic moments in the whole structure. Magnetic character of these alloys is connected to the local environment of these Fe atoms, i.e., the sign and the magnitude of the magnetic interactions depends on the number of Fe nearest neighbors and especially on the Fe–Fe interatomic distances. The binary rhombohedral R_2Fe_{17} compounds with R = Pr or Nd are collinear ferromagnets with Curie temperatures (T_C) around room temperature (285 ± 5 and 335 ± 5 K respectively) and the Fe magnetic moments exhibit relatively high values ($\mu_{Fe} \sim 2\ \mu_B$)[9,10], whereas the hexagonal compounds are mostly ferrimagnetics with the ordering temperature located close to RT. According to the Slater–Neel curve, positive or negative Fe–Fe exchange interactions prevail when the interatomic distances are larger or lower than a critical distance of 2.4 Å, respectively[16]. In particular, when the distance between the dumbbell Fe atoms (located along the *c*-axis) is lower than this critical distance, a negative local magnetic interaction is induced and therefore, the negative exchange-coupling is favored. The rest of the iron magnetic moments are parallel due to Fe-Fe positive interactions, which implies that the magnetic energy is stored around the shortest interatomic distances where negative interactions exist. The strong dependence of the magnetic behavior on the Fe–Fe distances gives rise to magnetovolume anomalies below T_C, being a large and negative of both thermal expansion along the *c*-axis and pressure dependence of T_C the most representative signatures[9].

The magnetic behavior on R_2Fe_{17} compounds can be explained by a local moment two-sublattice model. It is generally accepted that in the R–T compounds the overall anisotropy is determined by the interplay of the R-sublattice and T-sublattice anisotropies. According to crystal field theory of rare earth-transition metal intermetallic compounds, a positive second-order Stevens coefficient α_J of Er ion combined with a negative second-order crystal field coefficient V_2^0 results in an uniaxial anisotropy of the Er sublattice, whereas the anisotropy of the Fe sublattice is planar[1,2,17,18]. However in this material the magnitude of the B_2^0 coefficient is quite small compared to that of the Fe-sublattice, leading to the fact that this latter anisotropy dominates over the whole temperature range below the Curie temperature (T_C), therefore the easy magnetization direction of Er_2Fe_{17} lies on the basal plane.

On the other hand, the family of R_2Fe_{17} compounds have attracted interest because several members have shown a moderate magnetocaloric effect (i.e., the temperature change of a magnetic material upon the application of a magnetic field), around room temperature, the magnetic isothermal entropy change for a magnetic field variation from 0 to 5 T being $\Delta S_M \approx -6\ J \cdot kg^{-1} \cdot K^{-1}$ in the case of R = Pr or Nd[3,19]. These R_2Fe_{17} alloys are of low-cost compared with Gd-based alloys, which are the archetypal alloys used in the current room temperature magnetic refrigeration prototypes. The most challenging purpose for magnetic refrigeration technology is the optimization of the engine efficiency minimizing both the powder consumption as well as the environmental impact compared with those on the existing vapor-cycle technology. Therefore, the search for new materials displaying significant magneto-caloric effect (*MCE*) is nowadays a very active field of research.

In this paper we report on both the crystal and magnetic structure in the Er_2Fe_{17} compound by means of both x-ray and neutron diffraction. Also, both the *MCE* and magnetovolume effects present in this alloy are studied using x-ray diffraction with pressure, dc magnetization and specific-heat measurements. Our article is organized as follows: Section 2 contains details about the experimental and the analysis procedures used. Section 2 is devoted to give the information on the Hamil-

tonian and main interactions considered in Er_2Fe_{17}. The Results and Discussion of the physical properties are presented in Section 4, while the section 5 concludes the article.

II Experimental Section and Analysis Details

Synthesis of material

As starting materials for preparing Er_2Fe_{17} as-cast pellets, pieces of commercial (Goodfellow) 99.9% pure elements have been mixed in the nominal molar ratio 2:17. Pellets of 4 g have been prepared by the common arc melting technique under controlled Ar atmosphere, being re-melted at least three times to ensure their homogeneity. An excess of 5% Er has been added to compensate the evaporation losses during melting. Each specimen has been wrapped in a tantalum foil and sealed under vacuum in a quartz ampoule and annealed during one week at 1373 K. The annealing has been followed by water quenching of the quartz ampoules directly from the furnace. Part of the resulting samples has been cut into pieces for magnetic measurements and the rest has been manually pulverized and sieved for diffraction experiments.

Structural characterization

The crystal structure, lattice parameters and atomic positions have been studied by means of both x-ray (XRD) and neutron powder diffraction (ND). XRD studies have been performed to check the crystal structure in a high resolution powder diffractometer (Seifert model XRD3000) operating in Bragg-Bentano geometry, with scans in 2θ taken between 30 and 50º with $\Delta 2\theta = 0.025^{\circ}$ steps and counting times of 2s per point using Cu *Kα* radiation ($\lambda = 1.542$ Å). ND patterns have been collected on the high resolution two-axis diffractometer D2B ($\lambda = 1.59$ Å) from T = 2 K to 325 K. Thermo-neutron powder diffraction (TND) patterns have been obtained on the high-flux D1B two-axis power diffractometer ($\lambda = 2.52$ Å) from $T = 5$ to 850 K. Neutron experiments have been performed at the ILL (Grenoble, France). Pressure dependence synchrotron powder diffraction (SPD) experiments have been carried out in the instrument ID27 at the ESRF (Grenoble, France). The Er_2Fe_{17} powders have been pressurized in a diamond anvil cell at room temperature. Neon has been used as pressure-transmitting medium. A small ruby chip has been loaded in the sample chamber for pressure calibration. The collecting time of each pattern was ~1 min. Experimental raw data have been integrated using the FIT2D program in order to obtain one-dimensional diffraction pattern. The compressive process has been recorded. Analyzes of the diffraction patterns based on both the Le Bail and Rietveld methods have been carried out with the Fullprof suite package[20].

Magnetic characterization

The temperature and applied magnetic field dependencies of the magnetization have been performed using a Quantum Design PPMS-9 T platform with the vibrating sample magnetometer (VSM) option. The temperature dependence of the magnetization, $M(T)$, has been registered at different applied magnetic fields, $H = 50$ Oe, 1 and 10 kOe. Isothermal magnetization vs. applied magnetic field curves, $M(H)$, have been measured in the temperature range 2 – 350 K with T-steps of 10 K or 5 K for temperatures far from or near T_C, respectively. For each $M(H)$ curve the applied magnetic field has been increased from 0 Oe up to 8 kOe with field steps of 0.5, 1 or 2 kOe, measuring around 60 points per curve. From $M(H,T)$ measurements the magnetic isothermal entropy variation ($\Delta S_M(T,H)$) due to a change of the applied magnetic field from an initial value $H = 0$ to a final value H is calculated using the well-known Maxwell relation[3]:

$$\Delta S_M(T,H) = S_M(T,H) - S_M(T,0) = \int_0^H \left(\frac{\partial M(T',H')}{\partial T'} \right)_{T'=T} dH' \qquad (1),$$

where $S_M(T,0)$ and $S_M(T,H)$ are the magnetic entropy at zero and H applied magnetic field respectively. Actually, the calculation of ΔS_M at a given temperature is done by a numerical approximation of (1) replacing the partial derivative by finite differences and calculating the integral by numerical methods . The Specific heat, $C_P(T)$, has been measured in the temperature range 3 – 355 K at zero applied magnetic field. The entropy at zero-field has been calculated from $C_P(T)$ measurements:

$$S_{tot}(T,H=0)=\int_{T_1\to 0}^{T}\frac{C_P(T',H=0)}{T'}dT' \qquad (2).$$

The entropy at a temperature T and under a magnetic field H is:

$$S_{tot}(T,H)=S_{tot}(T,H=0)-\Delta S_M(T,H) \qquad (3).$$

The adiabatic temperature change, $\Delta T_{ad}(T,H)$, has been obtained from the entropy–temperature diagram as the isentropic distance between the entropy curves at zero-field and H [21].

III Theory

The temperature dependence of the 3d (Fe) and 4f (Er^{3+}) magnetic moments, M_{3d} and M_{4f}, respectively, can be calculated as follows: first, the M_{3d} has been obtained from a Heisenberg Hamiltonian within the mean field approximation considering a spin angular momentum S = 1 for the Fe. Second, the M_{4f} has been calculated from the Hund's rule ground state $^4I_{15/2}$ with total angular momentum J = 15/2. Under the influence of a hexagonal crystalline electric field (CEF) with local symmetry D_{4h} (z-quantization axis along the c-axis) the Hamiltonian is given by:

$$H_{CEF}=B_2^0O_2^0+B_4^0O_4^0+B_6^0O_6^0+B_6^6O_6^6 \qquad (4)$$

where the O_l^m and B_l^m are the Stevens operators and CEF parameters, respectively[22]. The sixteenfold degenerate Hund's rule ground state is splitted into eight doublets, with CEF parameters $B_2^0=-1.65$ K, $B_4^0=-8.66\cdot10^{-3}$ K, $B_6^0=-3.44\cdot10^{-5}$ K and $B_6^6=-1.65\cdot10^{-5}$ K. The CEF parameters have been taken from reference[23]. The ordered magnetic moments M_{4f} in Er_2Fe_{17} is induced by 3d-4f exchange interactions. We model this by combining the CEF Hamiltonian (4) with a mean field Hamiltonian describing the 3d-4f exchange coupling (the 4f-4f exchange interaction is expected to be negligible compared to the 3d-4f one)

$$H=H_{CEF}-H_{3d-4f}M_{4f} \qquad (5)$$

where $H_{3d-4f}=\lambda_{3d-4f}M_{3d}$ is the molecular field due to the 3d-4f exchange interaction, with $\lambda_{3d-4f}=-560\ kOe/\mu_B$. After diagonalization of the Hamiltonian (4) the temperature dependence of M_{4f} can be calculated as explained in reference[24].

IV Results and Discussion

Crystal and magnetic structure

Fig. 1 depicts high-resolution ND patterns for the Er_2Fe_{17} compound measured on D2B at 2 K and 320 K (below and over the Curie temperature, $T_C\sim$ 303 K) respectively. Diffraction pattern collected in the paramagnetic phase shows only peaks that can be indexed as corresponding to the Bragg reflections associated with the hexagonal Th_2Ni_{17}-type crystal structure, which was previously determined by x-ray diffraction. The diffraction pattern in the paramagnetic state (320 K) has been fitted in order to reduce the number of refining parameters (such as the scale factor, the zero-shift of the goniometer, the profile parameters and the atomic coordinates) for describing the pattern corresponding to the magnetic ordering phase. Afterward, the cell parameters, the atomic coordinates and the isotropic temperature factor, for each ion of Er [2b (00 1/4), 2d (1/3 2/3 3/4)] and Fe [4f (1/3 2/3

z); 6g (1/2 00); 12j (x y1/4); 12k (x 2x z)], have been refined. In particular, the atomic coordinates are in good agreement with those previously reported. The most important structural parameters have been obtained from the Rietveld analysis (see Table I). The labeling for the Er and Fe atomic coordinates is the same as that used in the International Tables for Crystallography[25]. It is worth noting that several attempts using the disordered Th_2Ni_{17}-types structure (which is presented in other hexagonal R_2Fe_{17} compounds[7,14,26,27]) have been carried out, but they lead to fits of worse quality.

Once the structural and instrumental parameters have been established, the Fe-sublattice magnetic moments have been refined using as initial information the Fe magnetic moments for the different sublattices obtained for the Y_2Fe_{17} compound. The resulting magnetic structure is collinear ferrimagnetic with the magnetic moments lying in the basal plane, being the Er sublattice magnetic moments antiparallel to those of the Fe sublattice. It is worth noting that the components of the magnetic moments within the plane perpendicular to the unique-six fold axis of the hexagonal crystal structure cannot be determined from powder neutron diffraction experiments due to symmetry considerations[28].

The analysis of the TND patterns obtained on D1B for the Er_2Fe_{17} alloy using as starting information the Fe sublattice magnetic moments of Y_2Fe_{17} alloy has allowed us to obtain the temperature dependence of the magnetic moments at each non-equivalent atomic site (see Fig. 2a). To accomplish this task, we have taken in account that both 2b and 2d Er crystal sites have quite similar environment, therefore we have constrained both magnetic moments to have the same value and temperature dependence. It is clearly shown that the Er moments decrease monotonously, whereas Fe moments remain almost constant at low temperature, with a more abrupt decrease near T_C. Due to the ferrimagnetic behavior, the spontaneous magnetization of the Er_2Fe_{17} compound is expressed by subtracting the contribution of both sublattices[29]:

$$\mu_{Fe+Er}^{Total}=\mu_{Fe}^{Total}+\mu_{Er}^{Total}=\sum \mu_{Fe}^{i}-\sum |\mu_{Er}^{j}| \qquad (6).$$

Using eq. 6 the spontaneous magnetization is obtained and depicted in Fig. 2b, together with the reduced temperature dependence of the total magnetic moment for each sublattice. The temperature dependence of μ_{Fe+Er}^{Total} presents a maximum at $T \sim 0.3\ T_C$. This behavior occurs when μ_{Er}^{Total} decreases more rapidly with temperature than μ_{Fe}^{Total} , and therefore the spontaneous magnetization increases[30].

This kind of behavior has been predicted by Neel[31].

Magnetovolume anomalies

From the TND patterns the temperature dependencies of the cell parameters and volume are obtained and plotted in Fig. 3a. As well as for other R_2Fe_{17} compounds, Er_2Fe_{17} exhibits magnetovolume anomalies up to the Curie temperature, by a decrease of the crystalline cell along the *c*-axis up to $T \sim 410$ K, whereas the basal plane-cell parameters remains almost unchanged (less than 0.2% relative change for the *a* parameter) in the same temperature range. The magnetovolume effects are evidenced in the $V(T)$ curve through several features: i) $V(T)$ is almost constant from 0 up to 60 K; ii) a slight decrease of $V(T)$ with temperature is seen above 60 K up to 110 K; iii) then an almost constant volume in the temperature interval (110 K, 250 K) is observed again; and iv) a minimum at 360 K is found before reaching the linear variation characteristic of the Grüneissen dependence found at high temperatures in intermetallic materials. Moreover, the cell parameters *a* and $c(T)$, and therefore $V(T)$, do not follow this "Grüneisen-like" behavior until temperatures well above T_C. This is a consequence of the strong dependence of magnetic coupling with the Fe-Fe distances[2,9,11,32]. The cell volume at low temperatures is higher than that expected for a non-magnetic system. As the temperature is increased, the Fe magnetic moments decrease and the magnetovolume coupling progressively loses strength, giving rise to a lattice contraction. The volume goes down to the corresponding equilibrium value in the absence of magnetic order, which is reached above the ferrimagnetic ordering temperature.

On the other hand, the pressure dependence of the crystal cell parameters and volume has been also investigated (see low-left inset in Fig. 4 where PSD plots are gathered for several applied pressures). The form of the Bragg diffraction peaks is flatter and the intensity decreases when the pressure increases. Patterns have been analyzed using the LeBail method due to the extremely difficulty of performing a Rietveld's analysis. A continuous shift of the diffraction peaks to higher angles when increasing the pressure is observed, which is related to a decrease of the cell parameters. The normalized unit cell parameters of Er_2Fe_{17} as a function of pressure are also shown in Fig. 4. In both cases there is a continuous decrease, which allows concluding that no structural transformation occurs up to 15 GPa. The contraction along the *c*-axis and in the basal plane seems to be isotropic, as those two curves match. Data corresponding to the unit cell volume are fitted to the Birch–Murnaghan equation of state[33] considering the values of the Bulk modulus, B, as a fitting parameter. This value is estimated to be B = 143 GPa, in good agreement with the values reported in the literature[34].

Through the Grüneisen relation[35,36], the extrapolation of the paramagnetic behavior of $V(T)$ down to the low temperature range is done. For this purpose, as well as the value of the bulk modulus, we have used the Debye temperature $\theta_D \sim 450$ K, as for other R_2Fe_{17} compounds[37]. Fig. 3b shows the temperature dependence of both the experimental and extrapolated non-magnetic cell volume. As the extrapolated volume is lower than the experimental, the spontaneous magnetostriction, $\omega_S(T)$, is negative throughout the range from 0 K to above the Curie temperature T_C. In R_2Fe_{17} compounds, ω_S could be correlated to the square of the total Fe-sublattice magnetic moment, μ^2_{Fe}[38,39]. Fig. 5 shows the reduced volume effect $\omega_S(T)/\omega_S(5\text{ K})$ on the reduced temperature, T/T_C. The spontaneous magnetostriction depends quadratically on the magnetic moment up to the temperatures $T \sim 0.8\ T_C$. At high temperatures, the $\omega_S(T)$ curve deviates from $\mu^2_{Fe}(T)$, and at T_C about 40% of $\omega_S(5\text{ K})$ still remains, which apparently reflect the presence of short-range magnetic correlations which disappears at about 120 K above T_C[40].

Magnetic properties

The temperature dependence of the magnetization, $M(T)$ curves, at different applied magnetic fields are shown in Fig. 6. From the low applied magnetic field measurement (see inset in Fig. 6) the Curie temperature is estimated as the temperature where the minimum of $dM/dT(T)$ is achieved, giving the value of $T_C = 303 \pm 1$ K, in agreement with those previously reported [34,41]. It is worth underlying that M goes to zero after T_C and that no abrupt change below that temperature is present. When the applied magnetic field increases up to 10 kOe, a maximum of the magnetization located at $T \sim 140$ K becomes well defined. Also, the minimum in the temperature evolution of dM/dT becomes broader as the magnetic field increase, indicating that the ferri-to-paramagnetic transition becomes less defined.

The temperature and applied magnetic field dependence of the magnetization is plotted in Fig. 7. A linear trend for the magnetic field dependence of the magnetization is observed for temperatures over T_C, as it could be expected for a paramagnetic system. Below T_C no abrupt changes of the magnetization with the applied magnetic field is observed. It is known that in Er_2Fe_{17} single-crystals there is a first-order field-induced spin-reorientation transition[42], which is reflected in an abrupt change of the $M(H)$ curves, depending in the orientation of the single crystal with regard to the applied field. In the present case, such a transition is not observable because of the polycrystalline nature of the sample. The saturation magnetization, M_S, at $T = 2$ K has been estimated from the fit of the $M(H)$ curve to the approach-to-saturation law[43]:

$$M = M_S\left(1-\frac{b}{H^2}\right)+\chi_0 H \qquad (7).$$

The M_S value obtained is 72.5 ± 0.7 A·m^2·kg^{-1} (16 ± 1 μ_B), which agrees with the value of μ^{Total}_{Fe+Er} obtained from neutron diffraction and[44].

Magnetocaloric Effect

In Fig. 8a the temperature dependence of the magnetic entropy change for the Er_2Fe_{17} alloy is plotted for different magnetic fields. The peaks situated at T = 300 K correspond to a direct magnetocaloric effect due to the magnetic transition from the ferrimagnetic to paramagnetic state. The maximum of $|\Delta S_M|(T)$ at H = 50 kOe is 3.6 $J \cdot K^{-1} \cdot kg^{-1}$, in quite good agreement with the value reported in [45]. At H = 80 kOe the maximum reaches the value 4.7 $J \cdot K^{-1} \cdot kg^{-1}$. The Relative Cooling Power (*RCP*), is defined as follows:

$$RCP(H) = |\Delta S(T,H)|^{Max} \times \delta T(H)_{FWHM} \quad (9).$$

Due to experimental temperature limitations, the full width at half maximum is not achieved for applied fields higher than 40 kOe. Nevertheless, for that applied magnetic field the *RCP* is 222 $J \cdot kg^{-1}$, which is lower than that of the Gadolinium. In spite of this, Er_2Fe_{17} is interesting because also exhibits an inverse *MCE* with its maximum located at $T \sim 40$ K. The existence of this inverse magnetocaloric effect is due to both the ferrimagnetic character of the magnetic structure, as von[30], as well as the particular CEF level scheme of Er^{3+}. In the inset of Fig. 8a, the magnetic entropy change as a function of temperature, obtained considering a mean field Hamiltonian with CEF effects (see section III), is plotted. The prediction of a direct and inverse magnetocaloric effect is qualitatively well accounted for the theoretical model. Important differences are seen in the temperature range 100-200 K. These discrepancies seem to suggest that the role of other interactions could be important for describing the experimental behavior observed. The fact that the volume dependence has several features in the above temperature range could be due to the magnetoelastic coupling. The calculated *RCP* for the inverse *MCE* is 103 $J \cdot kg^{-1}$ at H = 80 kOe, with a maximum value of ΔS_M = 1.3 $J \cdot K^{-1} \cdot kg^{-1}$.

Taking into account eq. (2) and (3) the adiabatic temperature change has been obtained from the specific heat and magnetic entropy change (see Fig. 8b). Here also the existence of both effects is highlighted by the presence of a maximum and a minimum. The maximum values of $|\Delta T_{ad}|$ for the inverse and direct effects are 0.6 and 2.5 K respectively. These main experimental features are captured by the theoretical calculation obtained considering the contributions of the Fe sublattice due to Heisenberg exchange interactions, and CEF and Heisenberg exchange interactions for the Hamiltonian related to the Er-sublattice (see inset Fig. 8 b). Further investigations will be needed to elucidate the discrepancies with the experimental $|\Delta T_{ad}|$.

Summary and conclusions

In conclusion, the Er_2Fe_{17} intermetallic compound crystallizes, like other members of the R_2Fe_{17} family, in the hexagonal Th_2Ni_{17}-type crystal structure, as determined from high-resolution powder neutron diffraction studies. The magnetic structure has been found to be ferrimagnetic with two ferromagnetic sublattices, with the rare-earth magnetic moments antiparallel to those of the Fe-sublattice. The temperature dependence of Er magnetic moments has been found to be almost linear, while for the Fe-sublattice moments the main variation is located near T_C, being almost constant in the low temperature range. The magnetic measurements reveal that the magnetocaloric response ($\Delta S_M \sim$ -5 $J \cdot kg^{-1} \cdot K^{-1}$ for 80 kOe) is moderate near the ordering temperature for high applied magnetic fields; the existence of short-range ordering effect that are observed in the spontaneous magnetostriction, having; a maximum (~1.6 %) at 5 K but falling down to zero well above the Curie temperature; and the existence of an inverse magnetocaloric effect ($\Delta S_M \sim$ 1.5 $J \cdot kg^{-1} \cdot K^{-1}$ for 80 kOe) at 40 K. These main trends found experimentally are qualitatively well described considering a mean field Hamiltonian that includes both crystalline electric field and exchange interactions, and the present results seems to suggest that the magnetocaloric response is also governed by the magnetoelastic coupling in this material.

Acknowledgments

Financial support from Spanish MICINN through research project MAT2008-06542-C04-03 is acknowledged. P.A. (Ph.D. grant) is grateful to FICyT and JSM is grateful to MICINN (JdlC program). The SCTs at the University of Oviedo are also acknowledged. We thank ILL and CRG-D1B for allocating neutron beam-time, and ESRF for synchrotron beam time.

References

[1] K.H.J. Buschow, Rep. Prog. Phys. **40**, 1179-1256 (1977).
[2] D. Givord, R. Lemaire, IEEE Trans. Magn. **10**, 109-113 (1974).
[3] P. Gorria, J.L. Sánchez Llamazares, P. Álvarez, M.J. Pérez, J. Sánchez Marcos, J.A. Blanco, J. Phys. D: Appl. Phys. **41**, 192003 (2008).
[4] K.A. GschneidnerJr, V.K. Pecharsky, A.O. Tsokol, Rep. Prog. Phys. **68**, 1479-1539 (2005).
[5] T. Massalski, ASM International., *Binary Alloy Phase Diagrams*, 2nd ed. (ASM International, Materials Park Ohio, 1990).
[6] J.M.D. Coey, *Rare-earth Iron Permanent Magnets*, 1st ed. (Oxford University Press, 1996).
[7] Z. Arnold, J. Kamarad, P.A. Algarabel, B. Garcialanda, M.R. Ibarra, IEEE Trans. Magn. **30**, 619-621 (1994).
[8] Y. Xiao, G. Rao, Q. Zhang, G. Liu, Y. Zhang, J. Liang, J. Alloys Compd. **419**, 15-20 (2006).
[9] P. Gorria, P. Álvarez, J.S. Marcos, J.L. Sánchez Llamazares, M.J. Pérez, J.A. Blanco, Acta Mater. **57**, 1724-1733 (2009).
[10] P. Alvarez, J. Llamazares, M. Perez, B. Hernando, J. Santos, J. Sanchez Marcos, J. Blanco, P. Gorria, J. Non-Cryst. Solids **354**, 5172-5174 (2008).
[11] N. Yang, K.W. Dennis, R.W. McCallum, M.J. Kramer, Y. Zhang, P.L. Lee, J. Magn. Magn. Mater. **311**, 630-638 (2007).
[12] J.L. Sánchez Ll., M.J. Pérez, P. Álvarez, J.D. Santos, M.L. Sánchez, B. Hernando, J.A. Blanco, J. Sánchez-Marcos, P. Gorria, J. Alloys Compd. **483**, 682-685 (2009).
[13] I. Tereshina, S. Nikitin, W. Suski, J. Stepien-Damm, W. Iwasieczko, H. Drulis, K. Skokov, J. Alloys Compd. **404-406**, 172-175 (2005).
[14] I.S. Tereshina, S.A. Nikitin, J. Stepien-Damm, L.D. Gulay, N.Y. Pankratov, A.A. Salamova, V.N. Verbetsky, W. Suski, J. Alloys Compd. **329**, 31-36 (2001).
[15] R. Kumar, W.B. Yelon, J. Appl. Phys. **67**, 4641-4643 (1990).
[16] W. Iwasieczko, A.G. Kuchin, H. Drulis, J. Alloys Compd. **392**, 44-49 (2005).
[17] A.V. Andreev, F.R. de Boer, T.H. Jacobs, K.H.J. Buschow, J. Magn. Magn. Mater. **104-107**, 1305-1307 (1992).
[18] J.L. Wang, M.R. Ibarra, C. Marquina, B. García-Landa, W.X. Li, N. Tang, W.Q. Wang, F.M. Yang, G.H. Wu, J. Appl. Phys. **92**, 1453 (2002).
[19] P. Álvarez, P. Gorria, V. Franco, J. Sánchez Marcos, M.J. Pérez, J.L. Sánchez Ll., I. Puente Orench, J.A. Blanco, J. Phys.-Condes. Matter **22**, 216005 (8pp) (2010).
[20] J. Rodríguez-Carvajal, Physica B **192**, 55-69 (1993).
[21] A.R. Dinesen, S. Linderoth, S. Morup, J. Phys.-Condes. Matter **17**, 6257-6269 (2005).
[22] M. Hutchings, en *Solid State Physics* (Elsevier, 1964), págs. 227-273.
[23] K. Clausen, B. Lebech, J. Phys. C: Solid State Phys. **15**, 5095-5112 (1982).
[24] J. Blanco, D. Gignoux, J. Gomez-Sal, D. Schmitt, J. Magn. Magn. Mater. **104-107**, 1273-1274 (1992).
[25] T. Hahn, H. Fuess, T. Hahn, H. Wondratschek, U. Müller, U. Shmueli, E. Prince, A. Authier, V. Kopský, D.B. Litvin, M.G. Rossmann, E. Arnold, S. Hall, B. McMahon, editores, *International Ta-*

bles for Crystallography, 1st ed. (International Union of Crystallography, Chester, England, 2006).
[26] V.I. Voronin, I.F. Berger, A.G. Kuchin, D.V. Sheptyakov, A.M. Balagurov, J. Alloys Compd. **315**, 82-89 (2001).
[27] A.N. Christensen, R.G. Hazell, Acta Chem. Scand. Ser. A- Phys. Inorg. Chem. **34**, 455-459 (1980).
[28] C. Piqué, J. Blanco, R. Burriel, E. Abad, M. Artigas, M. Fernández-Díaz, Phys. Rev. B **75**, (2007).
[29] Z. Cheng, B. Shen, Q. Yan, H. Guo, D. Chen, C. Gou, K. Sun, F.R. de Boer, K.H.J. Buschow, Phys. Rev. B **57**, 14299 (1998).
[30] P.J. von Ranke, N.A. de Oliveira, B.P. Alho, E.J.R. Plaza, V.S.R. de Sousa, L. Caron, M.S. Reis, J. Phys.: Condens. Matter **21**, 056004 (2009).
[31] A. Herpin, *Theorie Du Magnetisme*, 1st ed. (Presses Universitaires de France, Paris, 1968).
[32] E. Girt, Z. Altounian, I.P. Swainson, K.M. Krishnan, G. Thomas, J. Appl. Phys. **85**, 4669-4671 (1998).
[33] H. Zhang, X. Wu, K.G. Nickel, J. Chen, V. Presser, J. Appl. Phys. **106**, 013519 (2009).
[34] M. Brouha, K. Buschow, A. Miedema, IEEE Trans. Magn. **10**, 182-185 (1974).
[35] K.H.J. Buschow, *Handbook of Magnetic Materials*, vol. 14 (Elsevier, Amsterdam, 2002).
[36] K.H.J. Buschow, *Handbook of Magnetic Materials*, vol. 16 (Elsevier, Amsterdam; Oxford, 2006).
[37] K.H.J. Buschow, *Handbook of Magnetic Materials*, vol. 8 (Elsevier, Amsterdam; London; New-York, 1995).
[38] A.V. Andreev, A. Lindbaum, J. Alloys Compd. **297**, 43-45 (2000).
[39] A.V. Andreev, F.R. de Boer, T.H. Jacobs, K.H.J. Buschow, Physica B **175**, 361-369 (1991).
[40] E.A. Tereshina, A.V. Andreev, Intermetallics **18**, 1205-1210 (2010).
[41] J. Kamarad, O. Mikulina, Z. Arnold, B. Garcia-Landa, M.R. Ibarra, J. Appl. Phys. **85**, 4874-4876 (1999).
[42] M.D. Kuz'min, Y. Skourski, K.P. Skokov, K.H. Muller, Phys. Rev. B **75**, (2007).
[43] B.D. Cullity, *Introduction to Magnetic Materials* (Addison-Wesley Publishing Company, 1972).
[44] E.E. Alp, A.M. Umarji, S.K. Malik, G.K. Shenoy, M.Q. Huang, E.B. Boltich, W.E. Wallace, J. Magn. Magn. Mater. **68**, 305-308 (1987).
[45] H. Chen, Y. Zhang, J. Han, H. Du, C. Wang, Y. Yang, J. Magn. Magn. Mater. **320**, 1382-1384 (2007).

Table captions

Table I. Cell parameters and volume at $T = 320$ K and atomic coordinates and Debye-Waller temperature factor of each crystallographic site of the studied Er_2Fe_{17} ($P6_3/mmc$) compound obtained from D2B ND pattern.

Table 2. Magnetic moments at $T = 5$ K for the Er_2Fe_{17} alloy gotten from the D1B ND pattern. Values are compared with those obtained from the theoretical model.

Table 3. Magnetic (Curie temperature, spontaneous magnetization, critical exponents) and magnetocaloric parameters (direct and inverse magnetic entropy change, relative cooling power) for the Er_2Fe_{17} compound.

Figure captions

Fig. 1 Observed (dots) and calculated (solid line) ND patterns from D2B at a) $T = 2$ K and b) $T = 310$ K temperature for Er_2Fe_{17} alloy. Positions of the Bragg reflections are represented by vertical bars; the first row corresponds to the Th_2Ni_{17} phase while the second one corresponds with the magnetic structure. The observed–calculated difference is depicted at the bottom of each figure.

Fig. 2 a) Magnetic atomic moments of the two in-equivalent crystallographic Er sites and the four in-equivalent crystallographic Fe sites vs. T/T_C. b) Fe and Er sublattice magnetic moments, together with the total magnetic moment as a function of T/T_C. Dashed lines are the result of the calculated temperature dependence of the magnetic moments (see text for more details).

Fig. 3 a) Temperature dependence of the cell parameters of the Er_2Fe_{17} compound. b) Temperature dependence of experimental volume and its extrapolation to low temperature.

Fig. 4 Fit of the $P(V)$ curve using the Birch–Murnaghan equation of state. Inset (up-right): pressure dependence of the cell parameters normalized to the value at $P = 0$ GPa of the Th_2Ni_{17} phase in the Er_2Fe_{17} compound at room temperature. Inset (down-left): observed (dots) and calculated (solid line) SPD patterns for Er_2Fe_{17} alloy collected at a) $P = 0$ GPa and b) $P = 15$ GPa. The observed–calculated difference is depicted at the bottom of each figure.

Fig. 5 Reduced volume effect $\omega_s(T)/\omega_s(5\ \mathrm{K})$ on the reduced temperature T/T_C compared with the temperature dependence of the square of the magnetic moment of Er_2Fe_{17}.

Fig. 6 Temperature dependence of magnetization for $H = 1$ and 10 kOe applied magnetic fields. Inset: $M(T)$ at 50 Oe

Fig. 7 Applied magnetic field dependence of magnetization isothermally measured.

Fig. 8 a) Magnetic entropy change vs. temperature for different applied magnetic fields up to 80 kOe for Er_2Fe_{17} compound. Temperature dependence of the heat capacity is shown as an inset. b) Adiabatic temperature change for different applied magnetic fields vs. temperature.

Table I. Cell parameters and volume at $T = 320$ K and atomic coordinates and Debye-Waller temperature factor of each crystallographic site of the studied Er_2Fe_{17} ($P6_3/mmc$) compound obtained from D2B ND pattern.

a (Å)	8.451 (1)
c (Å)	8.264 (1)
V (Å^3)	511.27 (1)
Er (2b)-B(Å^2)	1.2 (1)
Er (2d)-B(Å^2)	0.19 (8)
Fe (4f)-B(Å^2)	0.43 (5)
z	0.106 (1)
Fe (6g)-B(Å^2)	0.34 (5)
Fe (12j)-B(Å^2)	0.59 (3)
x	0.329 (3)
y	0.958 (1)
Fe (12k)-B(Å^2)	0.17 (2)
x	0.166 (1)
y	0.983 (1)
R_B	7.6
R_P	6.4
R_{WP}	8.9
R_F	6.0
χ^2(%)	10.5

Table 2. Magnetic moments at $T = 5$ K for the Er_2Fe_{17} alloy gotten from the D1B ND pattern. Values are compared with those obtained from the theoretical model.

Site	Measured (μ_B)
Er (2b;2d)	9.03 (1)
Fe (4f)	2.23 (1)
Fe (6g)	2.04 (1)
Fe (12j)	1.98 (1)
Fe (12k)	1.73 (1)
Er-Sublattice	18.06 (2)
Fe-Sublattice	32.8 (2)
Total	14.8 (2)
R_B	1.7
R_F	0.9
χ^2(%)	15.1

Table 3. Magnetic (Curie temperature, spontaneous magnetization, critical exponents) and magnetocaloric parameters (direct and inverse magnetic entropy change, relative cooling power) for the Er_2Fe_{17} compound.

T_C (K)	M_S (μ_B)	Direct $\lvert\Delta S_M\rvert$ (J·kg^{-1}·K^{-1})	Inverse $\lvert\Delta S_M\rvert$ (J·kg^{-1}·K^{-1})	ω_S 5K	B_0 (GPa)
303 (1)	16 (1)	4.7	1.03	1.6	143

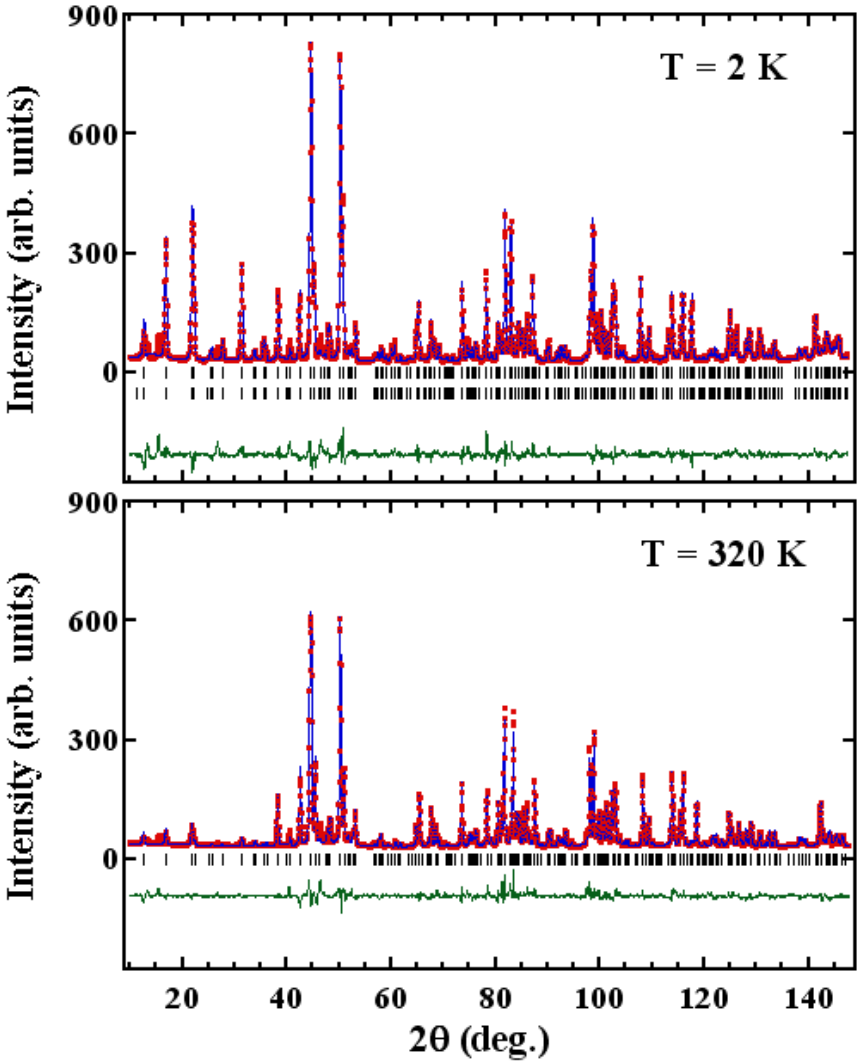

Fig. 1 Observed (dots) and calculated (solid line) ND patterns from D2B at a) $T = 2$ K and b) $T = 310$ K temperature for Er_2Fe_{17} alloy. Positions of the Bragg reflections are represented by vertical bars; the first row corresponds to the Th_2Ni_{17} phase while the second one corresponds with the magnetic structure. The observed–calculated difference is depicted at the bottom of each figure.

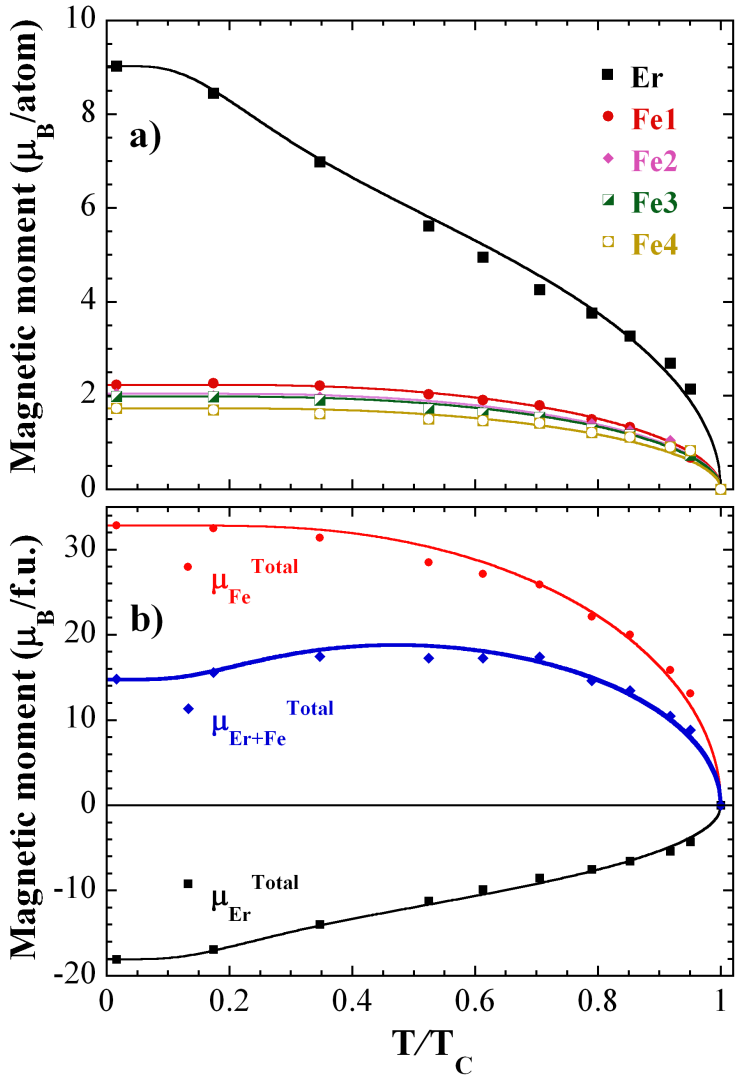

Fig. 2 a) Magnetic atomic moments of the two in-equivalent crystallographic Er sites and the four in-equivalent crystallographic Fe sites vs. T/T_C. b) Fe and Er sublattice magnetic moments, together with the total magnetic moment as a function of T/T_C. Dashed lines are the result of the calculated temperature dependence of the magnetic moments (see text for more details).

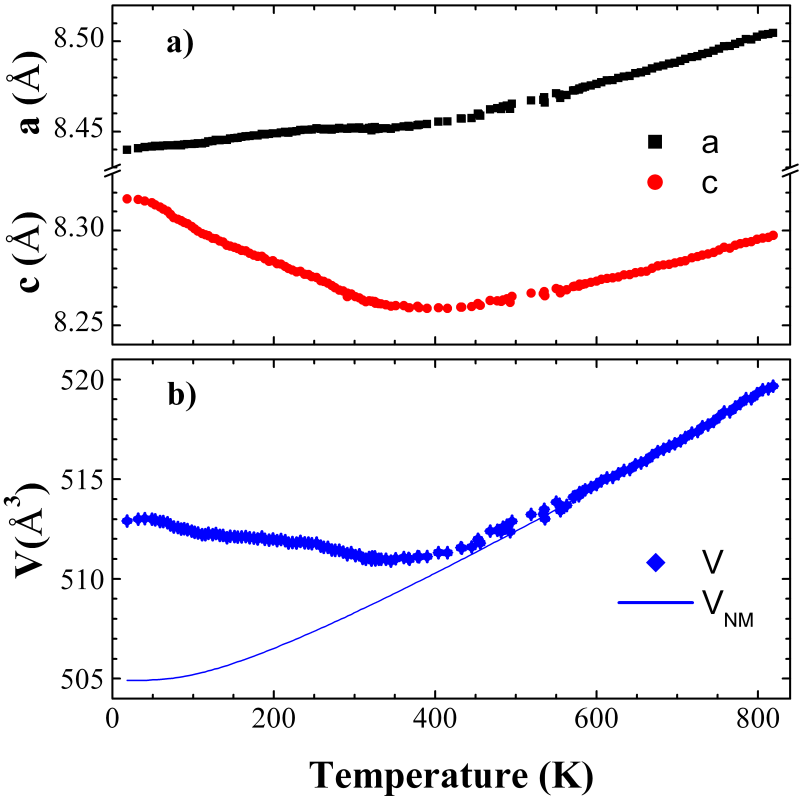

Fig. 3 a) Temperature dependence of the cell parameters of the Er_2Fe_{17} compound. b) Temperature dependence of experimental volume and its extrapolation to low temperature.

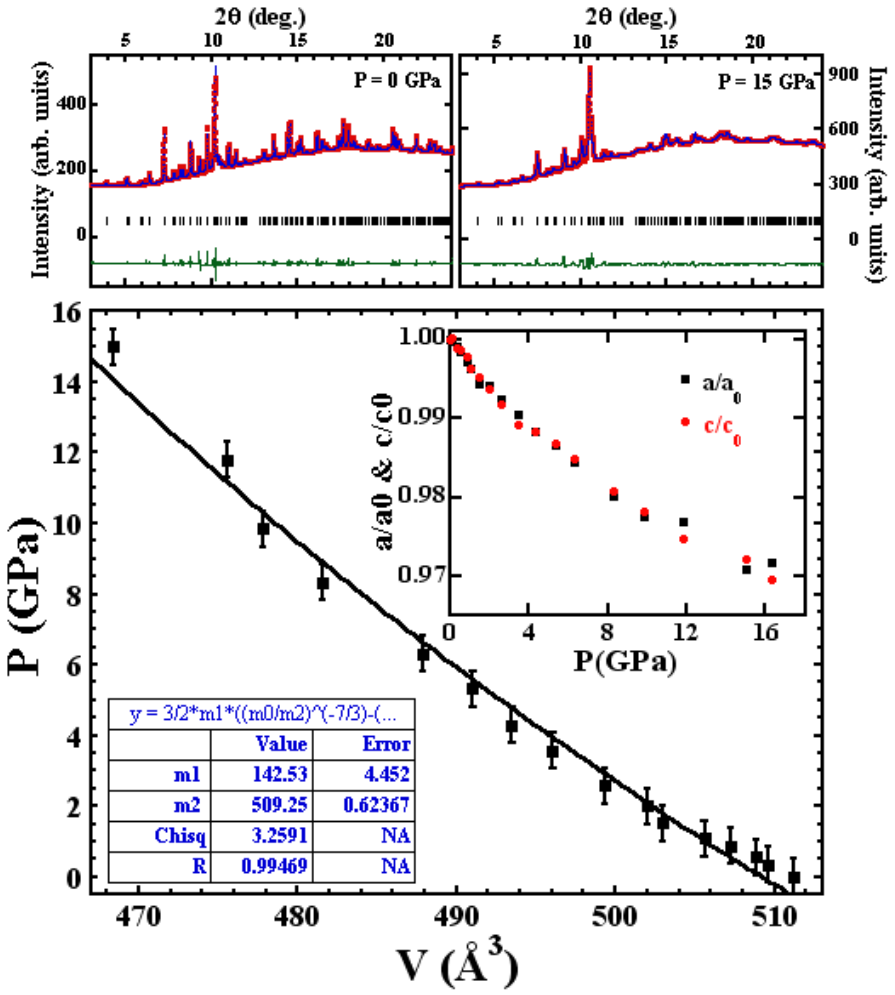

Fig. 4 Fit of the $P(V)$ curve using the Birch–Murnaghan equation of state. Inset (up-right): pressure dependence of the cell parameters normalized to the value at $P = 0$ GPa of the Th_2Ni_{17} phase in the Er_2Fe_{17} compound at room temperature. Inset (down-left): observed (dots) and calculated (solid line) SPD patterns for Er_2Fe_{17} alloy collected at a) $P = 0$ GPa and b) $P = 15$ GPa. The observed–calculated difference is depicted at the bottom of each figure.

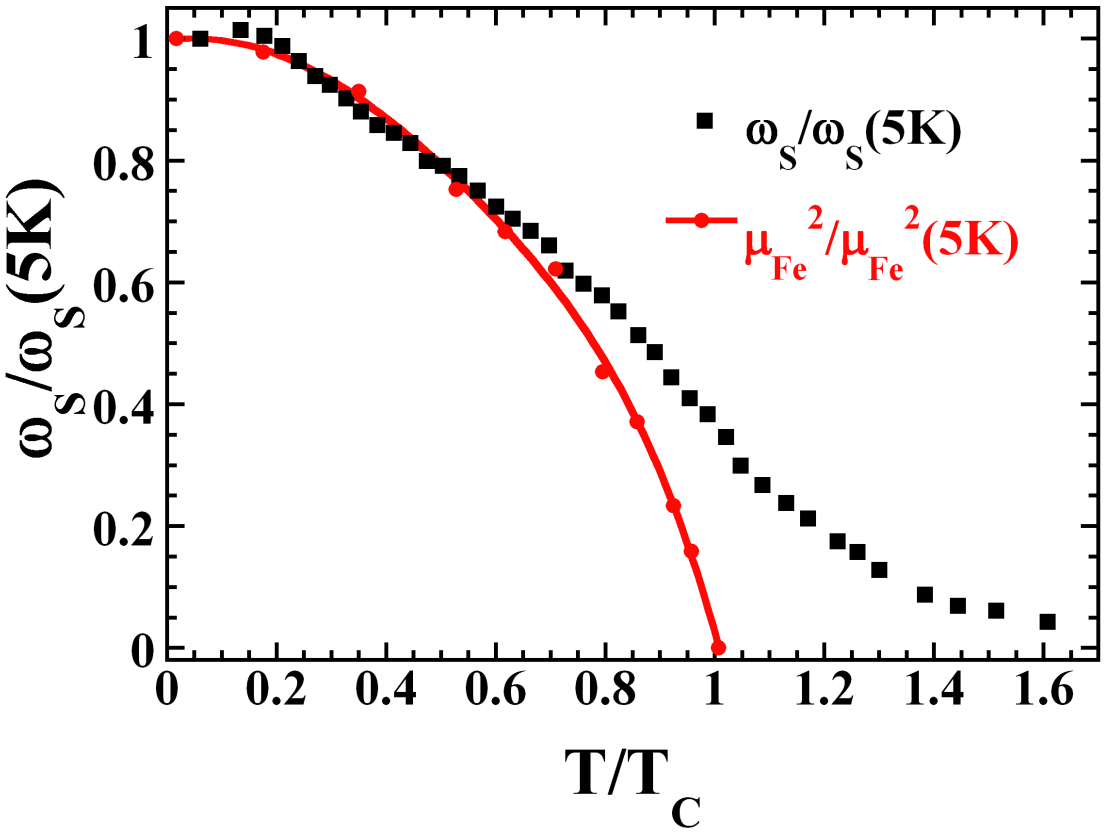

Fig. 5
Reduced volume effect $\omega_s(T)/\omega_s(5\ \mathrm{K})$ on the reduced temperature T/T_C compared with the temperature dependence of the square of the magnetic moment of Er_2Fe_{17}.

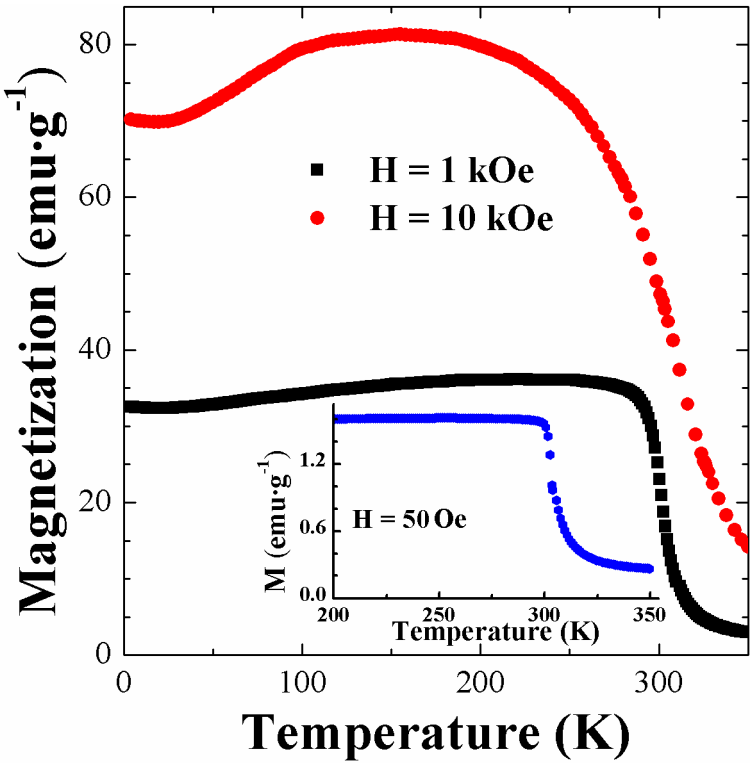

Fig. 6 Temperature dependence of magnetization for H = 1 and 10 kOe applied magnetic fields. Inset: $M(T)$ at 50 Oe.

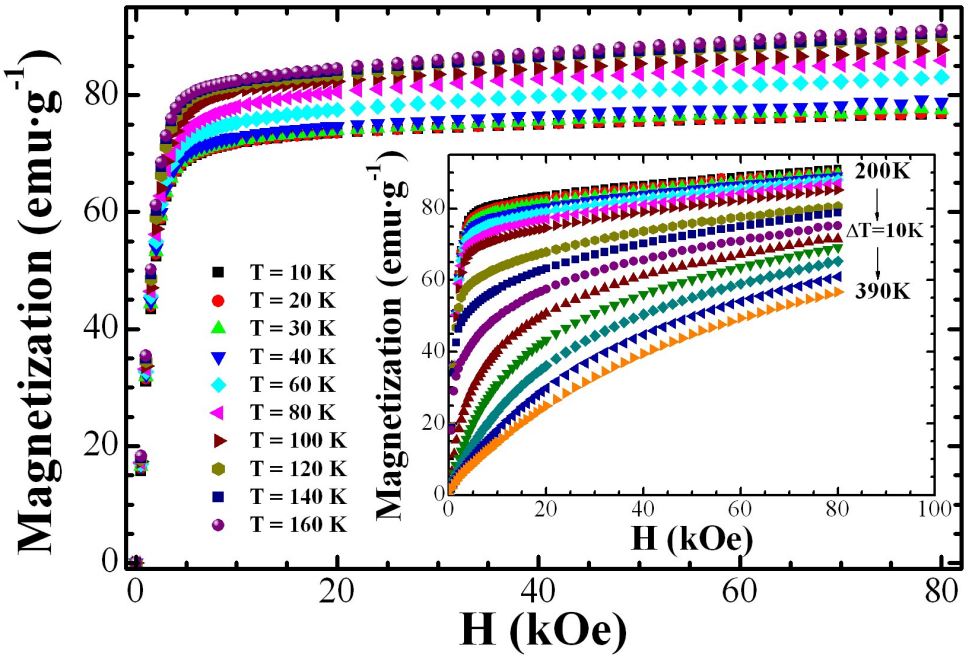

Fig. 7 Applied magnetic field dependence of magnetization isothermally measured.

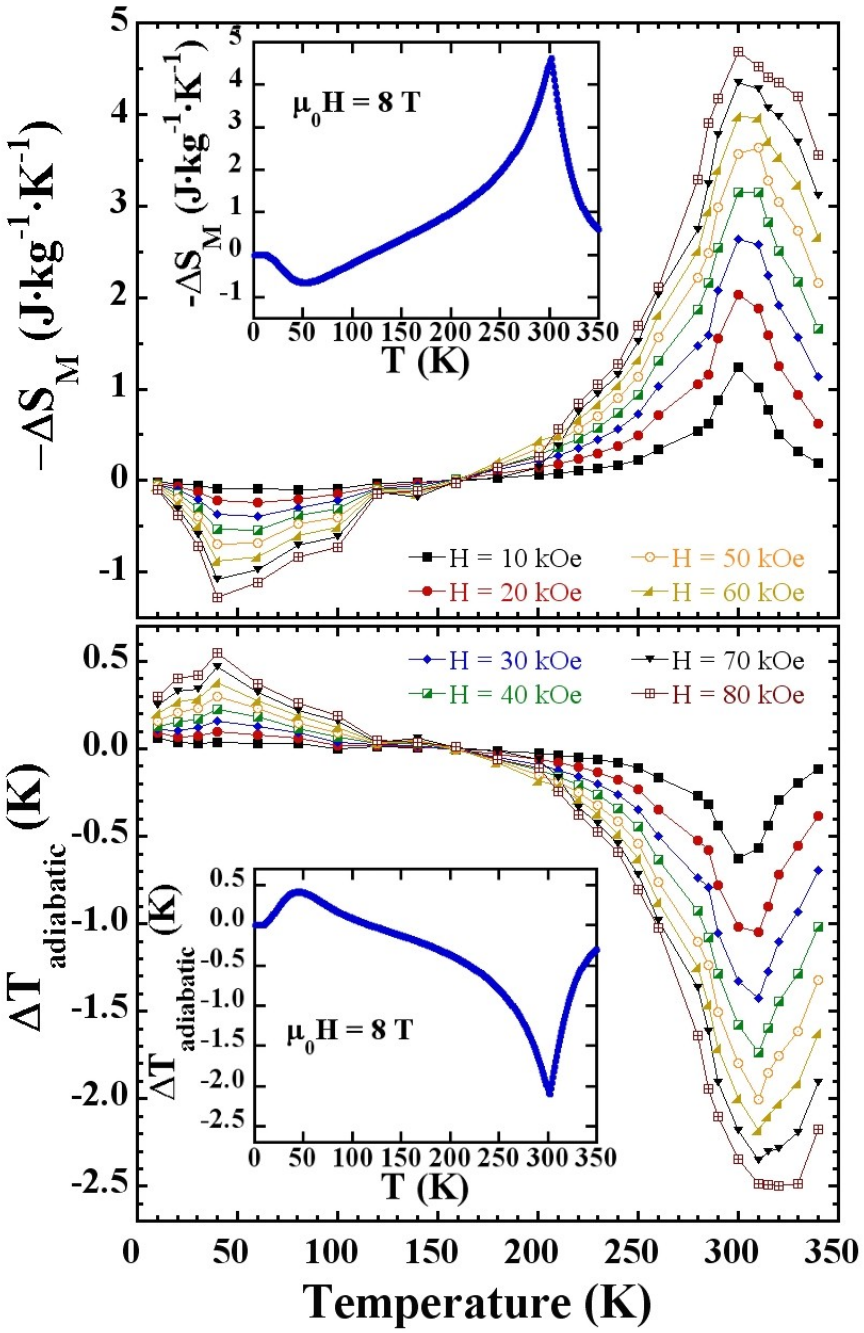

Fig. 8 a) Magnetic entropy change vs. temperature for different applied magnetic fields up to 80 kOe for Er_2Fe_{17} compound. Temperature dependence of the heat capacity is shown as an inset. b) Adiabatic temperature change for different applied magnetic fields vs. temperature.

IOP PUBLISHING
IOP FTC
JOURNAL OF PHYSICS D: APPLIED PHYSICS
J. Phys. D: Appl. Phys. **41** (2008) 192003 (5pp)
doi:10.1088/0022-3727/41/19/192003

FAST TRACK COMMUNICATION

Relative cooling power enhancement in magneto-caloric nanostructured Pr_2Fe_{17}

Pedro Gorria[1], José L Sánchez Llamazares[1], Pablo Álvarez[1], María José Pérez[1], Jorge Sánchez Marcos[2,3] and Jesús A Blanco[1]

[1] Departamento de Física, Universidad de Oviedo, Calvo Sotelo, s/n, 33007 Oviedo, Spain
[2] Institute Laue-Langevin, BP 156, 6 rue Jules Horowitz, 38042 Grenoble Cedex 9, France

E-mail: pgorria@uniovi.es

Received 18 June 2008
Published 5 September 2008
Online at stacks.iop.org/JPhysD/41/192003

Abstract

The magneto-caloric effect (MCE) of arc-melted bulk and 10 h ball-milled nanostructured Pr_2Fe_{17} powders has been investigated. The maximum value for the magnetic entropy change, $|\Delta S_M|$, in the milled alloy is 4.5 J kg^{-1} K^{-1} for $\mu_0 H = 5$ T, at around room temperature. The full width at half maximum, δT_{FWHM}, of $|\Delta S_M|(T)$ for the nanostructured powders is about 60% greater than that of the starting bulk alloy, thus giving rise to large relative cooling power values of 573 J kg^{-1} (4.5 J cm^{-3}) for $\mu_0 H = 5$ T estimated from the product of $|\Delta S_M|^{max} \times \delta T_{FWHM}$. These results have been compared with those of well-known magnetic materials that exhibit a large or giant MCE effect. The potential for using these low-cost iron based nanostructured Pr_2Fe_{17} powders in magnetic refrigeration at room temperature is also discussed.

(Some figures in this article are in colour only in the electronic version)

During the last decade, one of the most exciting, and at the same time, challenging endeavours in applied materials science and/or engineering has been the search for new materials or the processing of existing ones, modifying the microstructure and/or the size with the aim of tailoring and controlling their physical–chemical properties in such a way that functionality could be enhanced [1, 2]. Over the last decades, R_2Fe_{17} intermetallic compounds and their nitrides, carbides, etc have received considerable attention due to a wealth of interesting behaviours [3–5], being regarded as suitable candidates for high-performance permanent magnets [6]. Recently, a moderate magneto-caloric effect (MCE) [7] with values of the magnetic entropy change at about room temperature (for R = Nd, Pr) of $|\Delta S_M| \sim 6$ J kg^{-1} K^{-1} (for $\mu_0 H = 5$ T) [8, 9] has been reported for these materials. These values are lower than those measured in other well-known families of magneto-caloric materials, such as $Gd_5(Si_{1-x}Ge_x)_4$ or $MnFeP_{0.45}As_{0.55}$ [10–13], $La(Fe_xSi_{1-x})_{13}$ [14] or NiMn(Ga,In) [15, 16]; however, Pr_2Fe_{17} and Nd_2Fe_{17} compounds have some advantages, such as low fabrication costs, room-temperature $|\Delta S_M|$ maxima and broader $|\Delta S_M|$ peaks.

High-energy ball milling (HEBM) is a widely used technique for synthesizing new metastable alloys out from the thermo-dynamical equilibrium [17, 18]. HEBM is also employed in the mechanical processing of massive stable compounds with the aim of altering their microstructure and, therefore, modifying the physical properties [19, 20]. On the other hand, the search for MCE in new disordered, nanostructured and/or metastable phases out from the thermodynamic equilibrium is currently a growing field of research. In this way, some studies have recently been done in milled GdNiAl compounds [21], melt-spun Y_2Fe_{17} [22] and Gd-based [23] alloys or Fe-rich [24] metallic glasses. However, the production of nanostructured R_2Fe_{17} alloys with rhombohedral crystal structure has not been reported yet, and we present in this paper the fabrication route via

[3] Also at: Instituto de Ciencia de Materiales de Madrid, CSIC, Cantoblanco, 28049 Madrid, Spain.

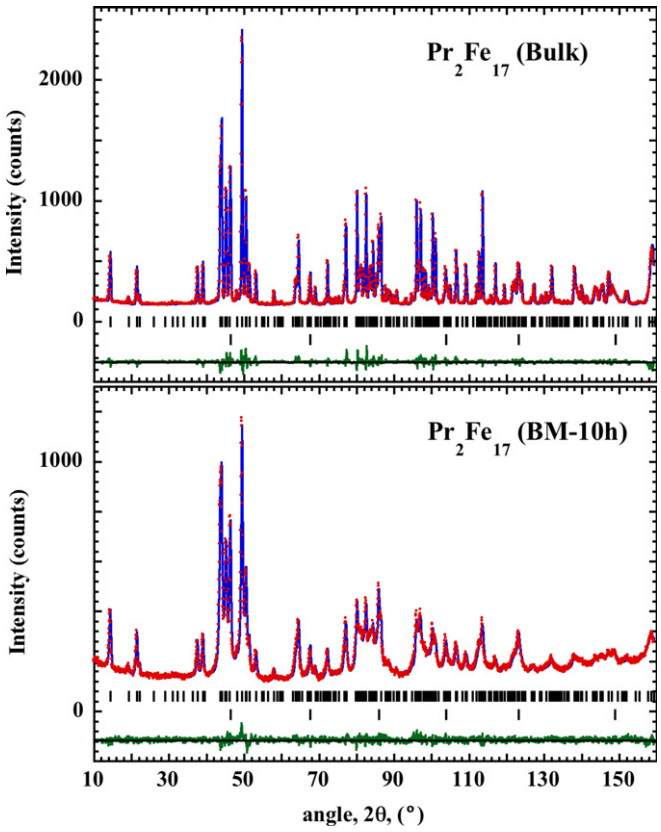

Figure 1. Observed (dots) and calculated (solid line) high-resolution neutron powder diffraction patterns of bulk and BM-10 h Pr_2Fe_{17} alloys collected at $T = 300$ K on D2B diffractometer ($\lambda = 1.594$ Å). Note the different y-scale used. Positions of the Bragg reflections are represented by vertical bars, the first row corresponds to the Pr_2Fe_{17} phase while the second one is associated with α-Fe impurity. The observed–calculated difference is depicted at the bottom of each figure.

mechanical processing from the starting Pr_2Fe_{17} bulk alloy by means of HEBM for 10 h, which gives rise to such a peculiar microstructural configuration. In the following the samples will be named 'bulk' and 'BM-10 h' for the as-cast material and the one ball milled (or mechanically stressed) for 10 h, respectively.

In figure 1, neutron powder diffraction patterns collected at room temperature on the high-resolution D2B two-axis diffractometer (Institute Laue-Langevin, Grenoble, France) for both bulk and BM-10 h Pr_2Fe_{17} samples are displayed. The patterns were measured in the 2θ range between 10° and 160° using a neutron wavelength of $\lambda = 1.594$ Å. The peaks observed in the pattern corresponding to the starting Bulk alloy can be indexed as the Bragg reflections belonging to two different phases with $R\bar{3}m$ rhombohedral and $Im\bar{3}m$ body centred cubic crystal structures. The former is a Pr_2Fe_{17} phase (Th_2Zn_{17}-type crystal structure) while the latter is an α-Fe impurity phase (about 8%). From the Rietveld refinement [25] of the pattern we have obtained accurate values for the important structural parameters associated with atoms in the unit cell, which are in good agreement with previously reported data on single crystal [26]. The pattern corresponding to the milled sample (see figure 1, bottom panel) shows an overall decrease in the peak intensities and a considerable broadening

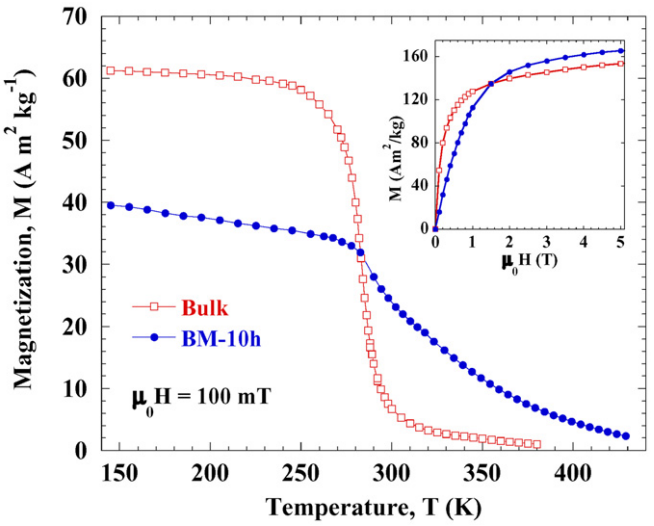

Figure 2. Temperature dependence of the magnetization for both bulk and BM-10 h Pr_2Fe_{17} alloys under an applied magnetic field of $\mu_0 H = 100$ mT. The inset shows the magnetization versus applied magnetic field curves at $T = 4$ K.

of the Bragg reflections. However, the Th_2Zn_{17}-type crystal structure is maintained, and the amount of the impurity phase does not change within the experimental error. The peak profile analysis performed [27] gives two important results: first of all, an average apparent size of the nanocrystals, $\langle\tau\rangle_{\mathrm{Diff}} = 20(2)$ nm, which coincides rather well with that estimated from TEM images, $\langle\tau\rangle_{\mathrm{TEM}} = 23(1)$ nm, and secondly, a nearly vanishing induced microstrain, $\varepsilon \approx 0.03(2)\%$, thus suggesting that the ball milling process mainly produces a progressive fracturing of the Pr_2Fe_{17} brittle intermetallic crystals down to the nanometre length scale.

In figure 2 the temperature dependence of the magnetization, $M(T)$ curves, for the two samples measured in a VSM magnetometer under $\mu_0 H = 100$ mT applied magnetic field is shown. The Curie temperature, T_C, has been estimated as the minimum value of the temperature derivative of the magnetization, $\mathrm{d}M/\mathrm{d}T$. It is worth noting that while M rapidly goes down in the bulk sample for temperatures above 280 K, the milled sample exhibits a much slower decrease. In our case, the bulk sample exhibits a sharp and well-defined minimum giving a value of $T_C = 286 \pm 1$ K. On the contrary, a precise estimation of T_C is difficult for the milled sample because the $\mathrm{d}M/\mathrm{d}T$ versus T curve (not shown) displays a broad and asymmetric minimum; in spite of this, we could give an approximate value of $T_C \approx 292 \pm 10$ K for the milled sample following this criterion. Moreover, the trend exhibited by the $M(T)$ curve in the milled sample suggests us a picture in which a broad distribution of T_C values should be considered, being a direct consequence of the induced structural disorder and the slightly different local environments of the atoms at the grain boundaries. Taking into account the abrupt decrease of the magnetization near T_C in the Bulk alloy (see figure 2), we can expect a remarkable change in its magnetic entropy, while for the milled alloy this change could be largely modified due to the very different M versus T behaviour exhibited around T_C. It is also worth noting that although the magnetization value

of the bulk sample at $T = 150$ K is 50% larger than that of the BM-10 h one (see figure 2), under high applied magnetic field values the situation is much different (see inset of figure 2). The low-temperature ($T = 4$ K) magnetization versus applied magnetic field curves, $M(H)$, measured up to $\mu_0 H = 5$ T, shows a slight increase in the saturation magnetization and, most importantly, a significant enlargement of the magnetic anisotropy in the BM-10 h powders. These findings can be understood on the basis of the magnetic coupling between the nanocrystals and the grain boundaries [28] that can induce the variation of intrinsic magnetic properties such as saturation magnetization, Curie temperature and/or magnetic anisotropy, already observed in a number of *R*–Fe-based nanostructured materials [29].

The MCE was determined as a function of the temperature and the applied magnetic field through the numerical integration of the isothermally measured magnetization versus applied magnetic field curves, $M(H)$, and using the appropriate Maxwell's thermodynamic relations [7]. Because the Curie temperature of the impurity phase (α-Fe) is very high ($T_C = 1044$ K), no contribution to MCE is expected from this phase at room temperature. More than 40 $M(H)$ curves were measured in the temperature range from 150 to 420 K using the VSM magnetometer. The temperature steps between consecutive isothermal $M(H)$ curves were 2 K near T_C, and 5 or 10 K far from the magnetic ordering temperature. At each temperature the data were collected using constant dc applied magnetic field steps of $\mu_0 \Delta H = 0.1$ T in the magnetic field range between 0 and 5 T. Taking into account that 50 field values were measured for each $M(H)$ curve, experimental errors have been largely minimized. The results obtained from these calculations allow us to envisage the evolution of ΔS_M with temperature. In figure 3 we present the $|\Delta S_M|(T)$ curves ($\Delta S_M < 0$) measured under applied magnetic fields $\mu_0 H = 5$ T for bulk and BM-10 h Pr_2Fe_{17} compared with that of pure gadolinium, which exhibits a caret-like shape [30]. A well-defined maximum for the bulk sample is clearly observed at $T \approx T_C$ (286 K), reaching a value of $|\Delta S_M| = 6.4\,\mathrm{J\,kg^{-1}\,K^{-1}}$ for $\mu_0 H = 5$ T. For the BM-10 h sample, the $|\Delta S_M|(T)$ curve is broader, as could be expected from the slow decrease in M in this temperature range (see figure 2), the maximum value is around one-third lower [$|\Delta S_M| = 4.5\,\mathrm{J\,kg^{-1}\,K^{-1}}$ for $\mu_0 H = 5$ T] and it is scarcely shifted to higher temperatures (~296 K). Also worth noting is the asymmetric form of the $|\Delta S_M|(T)$ peak exhibited by the milled sample with a long tail after the maximum, which is undoubtedly correlated with the slow fall over of the magnetization for $T > 280$ K (see figure 2). In terms of the potential interest for application in magnetic refrigeration, the maximum $|\Delta S_M|$ value is not the exclusive parameter to be taken into account for considering a material attractive. The temperature at which MCE occurs defines the technological field, and the temperature range in which it can operate is also of much importance [31]. Several attempts have been considered to estimate the so-called refrigerant capacity or relative cooling power (RCP), which indicates how much heat can be transferred from the cold end to the hot end of a refrigerator describing a thermodynamic cycle. A first attempt consists in using not only the maximum value

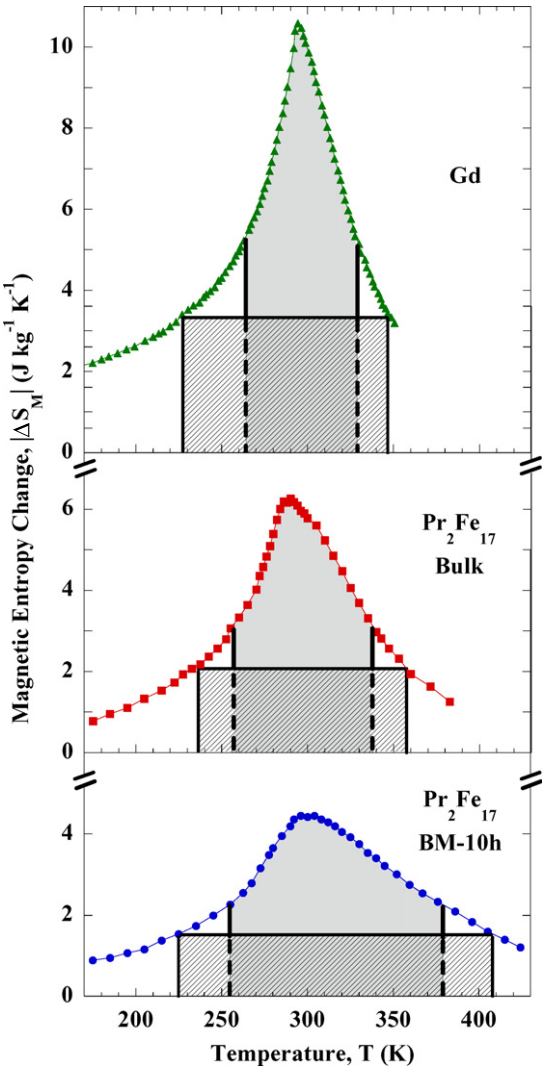

Figure 3. Temperature dependence of calculated $|\Delta S_M|(T)$ and RCP values under an applied magnetic field, $\mu_0 H = 5$ T, for pure Gd, bulk Pr_2Fe_{17} and BM-10 h Pr_2Fe_{17}. The RCP values (see table 1), estimated using three different methods, as is explained in the text, are also shown as the shaded areas (RCP-2) and striped rectangles (RCP-3) for each material.

of the MCE but also the width of the $|\Delta S_M|(T)$ curve, which is calculated from the product of the maximum $|\Delta S_M|$ peak value and the full width at half maximum, δT_{FWHM}, RCP-1 $(S) = |\Delta S_M|^{max} \times \delta T_{FWHM}$ [7]. The higher the δT_{FWHM} value is, the larger the temperature difference between the hot and the cool ends of the cycle that can be used for operation. In our samples, the value for δT_{FWHM} largely expands with milling, and provokes an RCP increase reaching values close to or even higher than those reported for $Gd_5(Si_{1-x}Ge_x)_4$ alloys at room temperature [7, 11, 13]. This method leads to values for bulk (506 J kg^{-1}) and BM-10 h (573 J kg^{-1}) of 74% and 83%, respectively, with regard to that of gadolinium. The fact that the δT_{FWHM} is 60% higher for the BM-10 h material than for the bulk one will allow the ambient temperature of the room where a refrigerator-appliance operates to fluctuate up to higher temperatures (see figure 3 and table 1).

The RCP values of the second method, RCP-2, were obtained from numerical integration of the area (dashed in

Table 1. RCP data estimated under an applied magnetic field of $\mu_0 H = 5$ T obtained from three different methods (see text) for both bulk and BM-10 h Pr_2Fe_{17} compounds (RCP-1 from δT_{FWHM} [7], RCP-2 from integration of $|\Delta S_M|$ [32] and RCP-3 from maximizing the product $|\Delta S_M| \times \Delta T$ [33]). Data for various representative magneto-caloric materials are also shown for comparison.

Material	RCP-1 J kg^{-1} (J cm^{-3})	RCP-2 J kg^{-1} (J cm^{-3})	RCP-3 J kg^{-1} (J cm^{-3})	Reference
Pr_2Fe_{17} bulk	506 (3.9)	385 (3.0)	256 (2.0)	This work
Pr_2Fe_{17} BM-10 h	573 (4.5)	430 (3.3)	283 (2.2)	This work
Gd	687 (5.6)	503 (4.0)	402 (3.3)	[30]
$Gd_5Ge_2Si_2$	—	240 (1.8)	200 (1.5)	[13]
$Gd_5Ge_{1.9}Si_2Fe_{0.1}$	—	355 (2.7)	235 (1.8)	[13]
$Ni_{50}Mn_{34}In_{16}$	—	103.8	—	[16]
$Gd_5Si_{1.8}Ge_{1.8}Sn_{0.4}$ (as-cast)	—	366 (2.8)	—	[23]
$Gd_5Si_{1.8}Ge_{1.8}Sn_{0.4}$ (ribbons)	—	335 (2.5)	—	[23]

figure 3) under $|\Delta S_M|(T)$ using T_{FWHM} as the integration limits [13, 32]. This method leads to values for bulk (385 J kg^{-1}) and BM-10 h (430 J kg^{-1}) of 77% and 85%, respectively, with regard to that of gadolinium. Finally, the last method used to estimate the RCP value, RCP-3, maximizes the product $|\Delta S_M| \times \Delta T$ below the $|\Delta S_M|(T)$ curve [13, 33]. The estimated values for Bulk (256 J kg^{-1}) and BM-10 h (283 J kg^{-1}), computed using this procedure, are 64% and 70%, respectively, with regard to that of gadolinium, and are represented in figure 3 as the striped-rectangular areas extending outside the shaded areas. In table 1, we compare the values of RCP calculated with the three different methods explained just above for both bulk and BM-10 h Pr_2Fe_{17} samples together with those for other representative materials displaying MCE, such as Gd, $Gd_5Ge_2Si_2$, $Gd_5Ge_{1.9}Si_2Fe_{0.1}$, $Ni_{50}Mn_{34}In_{16}$ or $Gd_5Si_{1.8}Ge_{1.8}Sn_{0.4}$. In final, using different methods to estimate the RCP magnitude for bulk and BM-10 h Pr_2Fe_{17} leads us to conclude that the magnetic refrigerant cooling power is improved in the BM material.

In summary, large values of the RCP are found in nanostructured Pr_2Fe_{17} powders, which exhibit moderate MCE after the milling procedure. There are several reasons for considering these nanostructured materials interesting for potential applications in magnetic refrigeration. Firstly, the maximum of $|\Delta S_M|(T)$ is shifted towards room temperature after milling. Secondly, we have reported a reduction of one-third in the value for the magnetic entropy change compared with that of the starting bulk alloy, but at the same time, the $|\Delta S_M|(T)$ peak width is enlarged by a factor close to 2, leading to an increase in the RCP value from 506 to 573 J kg^{-1} (3.9 to 4.5 J cm^{-3}) for $\mu_0 H = 5$ T, and thirdly, a working temperature difference of at least 125 K between the hot and the cold ends of the cycle is observed.

Acknowledgments

Financial support from MEC through research projects (NAN2004-09203-C04-03, MAT2005-06806-C04-01 and MAT2006-13925-C02-01) is acknowledged. We thank ILL and Spanish CRG-D1B for allocating neutron beam time. SCTs (Univ. Oviedo) are acknowledged for assisting in SEM, TEM, XRD and magnetic measurements. Finally, JLSL and PA are grateful to FICyT for their research contract (COF07-013) and PhD grant, respectively.

References

[1] Gleiter H 2000 *Acta Mater.* **48** 1
[2] Ma E 2005 *Prog. Mater. Sci.* **50** 413
[3] Givord D and Lemaire R 1974 *IEEE Trans. Magn.* **10** 109
[4] Arnold Z, Kamarád J, Morellón L and Ibarra M R 1997 *J. Appl. Phys.* **81** 5693
[5] Banerjee D, Kumar P, Suresh K G and Nigam A K 2007 *J. Phys. D: Appl. Phys.* **40** 2691
[6] Buschow K H J 1991 *Rep. Prog. Phys.* **54** 1123
[7] Tishin A M and Spichkin Y I 2003 *The Magnetocaloric Effect and its Applications* (Bristol: Institute of Physics Publishing)
[8] Dan'kov S Yu, Ivtchenko V V, Tishin A M, Gschneidner K A Jr and Pecharsky V K 2000 *Adv. Cryog. Eng.* **46** 397
[9] Mandal K, Yan A, Kerschl P, Handstein A, Gutfleisch O and Müller K-H 2004 *J. Phys. D: Appl. Phys.* **37** 2628
[10] Morellón L, Blasco J, Algarabel P and Ibarra M R 2000 *Phys. Rev.* B **62** 1022
[11] Tegus O, Bruck E, Buschow K H J and de Boer F R 2002 *Nature* **415** 150
[12] Manivel Raja M, Gopalan R, Rajkumar D M, Balamuralikrishnan R, Chandrasekaran V, Suresh K G and Hono K 2008 *J. Phys. D: Appl. Phys.* **41** 055008
[13] Provenzano V, Shapiro A J and Shull R D 2004 *Nature* **429** 853
[14] Fujita A, Fujieda S, Hasegawa Y and Fukamichi K 2003 *Phys. Rev.* B **67** 104416
[15] Krenke T, Duman E, Acet M, Wassermann E F, Moya X, Mañosa L and Planes A 2005 *Nature Mater.* **4** 450
[16] Sharma V K, Chattopadhyay M K and Roy S B 2007 *J. Phys. D: Appl. Phys.* **40** 1869
[17] Suryanarayana C 2001 *Prog. Mater. Sci.* **46** 1
[18] Gorria P, Martínez-Blanco D, Blanco J A, Hernando A, Garitaonandia J S, Fernández Barquín L, Campo J and Smith R I 2004 *Phys. Rev.* B **69** 214421
[19] Gorria P, Martínez-Blanco D, Blanco J A, Pérez M J, Hernando A, Fernández Barquín L and Smith R I 2005 *Phys. Rev.* B **72** 014401
[20] Gorria P, Martínez-Blanco D, Pérez M J, Blanco J A and Smith R I 2005 *J. Magn. Magn. Mater.* **294** 159
[21] Chevalier B, Bobet J-L, Sánchez Marcos J, Rodríguez Fernández J and Gómez Sal J C 2005 *Appl. Phys.* A **80** 601
[22] Fang Y K, Chang C W Yeh C C, Chang H W, Li W and Chang W C 2008 *J. Appl. Phys.* **103** 07B302
[23] Zhang T, Chen Y and Tang Y 2007 *J. Phys. D: Appl. Phys.* **40** 5778
[24] Franco V, Borrego J M, Conde A and Roth S 2006 *Appl. Phys. Lett.* **88** 132509
[25] Rodríguez Carvajal J 1993 *Physica* B **192** 55

[26] Johnson Q, Wood D H and Smith G S 1968 *Acta Crystallogr.* B **24** 274
[27] Martínez-Blanco D, Gorria P, Blanco J A, Pérez M J and Campo J 2008 *J. Phys.: Condens. Matter* **20** 335213
[28] Hernando A, Navarro I and Gorria P 1995 *Phys. Rev.* B **51** 3281
[29] Hadjipanayis G C 1999 *J. Magn. Magn. Mater.* **200** 373
[30] Dan'kov S Yu, Tishin A M, Pecharsky V K and Gschneidner K A Jr 1998 *Phys. Rev.* B **57** 3478
[31] Gschneidner K A Jr, Pecharsky V K and Tsokol A O 2005 *Rep. Prog. Phys.* **68** 1479
[32] Gschneidner K A Jr, Pecharsky V K, Pecharsky A O and Zimm C B 1999 *Mater. Sci. Forum* **315–317** 69
[33] Wood M E and Potter W H 1985 *Cryogenics* **25** 667

Journal of Alloys and Compounds 483 (2009) 682–685

Contents lists available at ScienceDirect

Journal of Alloys and Compounds

journal homepage: www.elsevier.com/locate/jallcom

The effect of ball milling in the microstructure and magnetic properties of Pr_2Fe_{17} compound

J.L. Sánchez Llamazares[a], M.J. Pérez[a], P. Álvarez[a], J.D. Santos[a], M.L. Sánchez[a], B. Hernando[a], J.A. Blanco[a], J. Sánchez Marcos[b,c], P. Gorria[a,*]

[a] Departamento de Física, Universidad de Oviedo, Calvo Sotelo, s/n, 33007 Oviedo, Spain
[b] Institute Laue-Langevin, BP 156, 6 rue Jules Horowitz, 33042, Grenoble Cedex 9, France
[c] Instituto de Ciencia de Materiales de Madrid, CSIC, Cantoblanco, 28049 Madrid, Spain

ARTICLE INFO

Article history:
Received 30 August 2007
Received in revised form 4 July 2008
Accepted 22 July 2008
Available online 17 December 2008

Keywords:
Rare earth alloys and compounds
Mechanical alloying
Magnetocaloric effect

ABSTRACT

The effect of a severe mechanical milling treatment on the microstructure, magnetic and magneto-caloric properties of Pr_2Fe_{17} powders is reported. Bulk alloys showing a rhombohedral Th_2Zn_{17}-type crystal structure were mechanically ball milled under Ar atmosphere. After 10 h of milling this crystal structure persists and the mean values of the lattice parameters remain almost unchanged. Average grain sizes around 27 nm were estimated by both, transmission electron microscopy and neutron powder diffraction measurements. While for the starting bulk alloys the low field temperature of the magnetization, $M(T)$, shows a well-defined and sharp decrease at the Curie temperature, $T_C = 285(2)$ K, in ball milled samples the transition becomes broad not allowing an accurate determination of Curie point; in addition, this intrinsic parameter seems to be shifted toward a higher temperature [292(10) K]. The magnetocaloric effect at $\mu_o H_{max} = 5$ T was evaluated from the temperature dependence of magnetic entropy change, through the variation of $M(H,T)$ curves. A decrease in the peak value of magnetic entropy change, $|\Delta S_M^{max}|$, from 5.7 to 3.7 J kg^{-1} K^{-1}, and the broadening of the maximum is observed for the milled sample respect to the bulk alloy.

Pr_2Fe_{17} is a ferromagnetic compound that crystallizes in the rhombohedral Th_2Zn_{17}–type crystal structure ($R\bar{3}m$), exhibiting high values of the spontaneous magnetisation and a Curie point, T_C, of 283 K [1]. Recently, this material has attracted a renewed interest because combines a significant magneto-caloric effect close to room temperature with low potential production cost due to its high Fe content. A magnetic entropy change value, $|\Delta S_M|$, around 6 J kg^{-1} K^{-1} at $\mu_o H_{max} = 5$ T has been reported, while the related adiabatic temperature change, ΔT_{ad}, was roughly estimated in 4.1 K [2–4]. Ball milling has been widely used as a technique for producing nanostructured or new metastable phases from pure elements [5] or bulk stable compounds, exhibiting a rich variety of novel physical properties compared with those of bulk starting material [6–8].

In this report we describe the effect of a severe ball milling treatment on structural, magnetic and magnetocaloric properties of Pr_2Fe_{17} powders. Nearly single-phase Pr_2Fe_{17} alloys were processed by high-energy ball milling during 10 h. A comparative study, by means of neutron powder diffraction (NPD), scanning (SEM) and transmission (TEM) electron microscopy, and magnetization vs. temperature and applied magnetic field measurements, of both, the starting and ball milled (BM) alloy is presented.

As-cast pellets of nominal composition Pr_2Fe_{17} were prepared by Ar arc melting from 99.9% pure Pr and 99.98% pure Fe. To produce a highly pure 2:17 phase alloys were wrapped in tantalum foil, sealed under vacuum in quartz ampoules, and homogenised during one week at 1373 K; the thermal treatment was followed of water quenching. Annealed samples were broken into smaller pieces and manually pulverised using an agate mortar. The obtained powder was sieved using a 106 μm pore size metallic sieve to be sealed in a stainless steel vial under argon atmosphere. A ball-to-powder weight ratio of 8:1 was chosen. Powder was dry milled during 10 h using a high energy Retsch PM/400 planetary ball mill. The process was carried out in successive steps of 5 min of milling followed of 5 min of break, in order to keep low the temperature to favour progressive grain size diminution.

Room temperature NPD patterns were collected on the D1B two-axis neutron diffractometer (ILL, Grenoble, France) using a neutron wavelength of $\lambda = 2.52$ Å. The Rietveld analysis of the diffraction patterns has been performed using the Fullprof package [9], in order to make a quantitative determination of structural parameters and phase composition. Powder morphology was characterised with

* Corresponding author. Tel.: +34 985102899; fax: +34 985103324.
E-mail address: pgorria@uniovi.es (P. Gorria).

0925-8388/$ – see front matter © 2008 Elsevier B.V. All rights reserved.
doi:10.1016/j.jallcom.2008.07.210

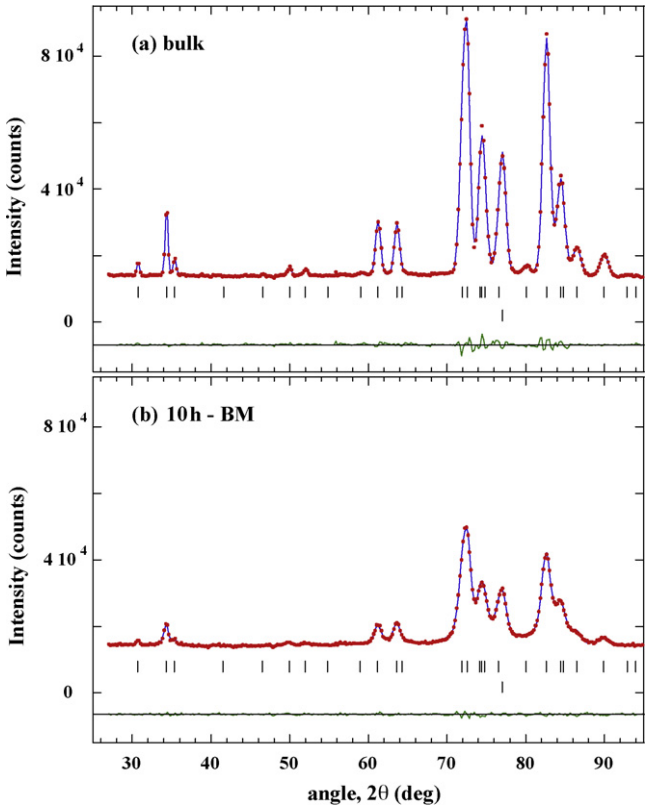

Fig. 1. Experimental (dots) and calculated (solid line) neutron powder diffraction patterns of Pr_2Fe_{17} alloys: (a) starting bulk alloy, (b) after 10 h of milling. Positions of the Bragg reflections are represented by vertical bars (the first vertical row corresponds to the crystal structure of Pr_2Fe_{17} (see text), while the second one is associated with α-Fe). The observed–calculated difference is depicted at the bottom of the patterns.

a Jeol model JSM-6100 scanning electron microscope (SEM), while the microstructure of milled particles was investigated by means of a Jeol 2000 EXII high resolution transmission electron microscope (TEM). Magnetization measurements were performed in the temperature interval of 5–350 K, using a Quantum Design PPMS-14T platform with the vibrating sample (VSM) magnetometer module. For the characterisation of bulk alloy a bar-shaped sample of around 1 mm × 1 mm × 5 mm, was prepared. The low field $M(T)$ curves were recorded at $\mu_o H_{ext} = 5$ mT with a temperature heating rate of 2 K/min. The measurements were done on thermally demagnetized samples. Curie points were inferred from the minimum in the dM/dT vs. T curves. For the determination of the magnetic entropy change, $|\Delta S_M|$, a set of $M(H)$ curves was measured from 0 to 5 T in 0.1 T steps from 260 to 340 K. The magnetic entropy change was calculated by using the well-known relation:

$$\Delta S_M(T, \Delta B) = \int_{B_1}^{B_2} \left(\frac{\partial M(T, B)}{\partial T} \right)_B dB.$$

Fig. 1 compares the NPD patterns of homogenized bulk and as-milled (10 h-BM) Pr_2Fe_{17} samples. The patterns have been refined considering two crystalline phases: the first one is a Th_2Zn_{17}–type rhombohedral crystal structure associated with the Pr_2Fe_{17} phase and the second one is related to a small amount of α-Fe impurity phase. The diffraction pattern for the starting bulk alloy is characterized by high intensity and sharp reflections. As shown in Fig. 1(b), milling leads to the significant broadening, overlapping, and reduction in the intensity of diffraction peaks; in addition, a perceptible increase in the background baseline of the diffraction pattern occurs. These effects reflect the disordering introduced during the milling process, which is usually expressed as vacancies, dislocations, grain boundaries and chemical disorder [6,10].

In Table 1 we report the mean cell parameters deduced from the profile refinement of whole diffraction pattern, accompanied by a summary of magnetic data. The values obtained are in perfect agreement with those reported in [1,11]. The R-factors obtained for the analysis reflects its satisfactory truthfulness (around 2% for both bulk and milled samples). It must be noted that mean cell volume has not been altered by milling. The amount of Fe in the samples was estimated in 7(2)%wt., for bulk and 10 h-BM samples.

A view to the powder morphology at mesoscopic scale is given in the SEM images of Fig. 2(a). Powder is composed of irregularly shaped micronic particles with a broad size distribution showing a slight tendency to agglomeration. Most of particles seem to be in the range of 0.5–5.0 μm. The higher magnification micrograph of the inset reveals that particles are in fact closed packed assemblies of smaller flaky, or laminar-like, particles whose real size is difficult to establish due to the poor definition of inter-particle boundaries, but it can be roughly estimate as 100–400 nm. Accordingly, in this case the construction of a particle size distribution is nor simple, nor a reliable task. Thus, a further study of the internal structure of such micronic particles was carried out by TEM. The inset of Fig. 2(b) is a typical micrograph of the nanostructure of individual particles. The grain size distribution is typified by the histogram presented in Fig. 2(b). The average crystalline grain size, $\langle\tau\rangle_{TEM}$, is 27(1) nm, in admirable agreement with the $\langle\tau\rangle_{NPD}$ value of 24(5) nm, deduced from the Rietveld refinement [12]. As Pr_2Fe_{17} is a brittle intermetallic, the reduction in grain size is a natural consequence of progressive fracturing produced during milling process.

Fig. 3 shows the low-field $M(T)$ curve of both samples. When temperature goes through the magnetic transition region a well defined and narrow drop in $M(T)$ is exhibited by the bulk alloy leading to a T_C value of 285(2) K in reasonable accordance with the reported value. Despite of its iron content, M seeks close to zero value. In contrast, the milled sample is characterised by a decrease in $M(T)$ values and a substantial broadening in the transition. The onset in the decrease of $M(T)$ starts before, the inflexion is now obtained at 292(10) K, and the magnetisation over the transition region remains relatively far from zero. In the inset of Fig. 3, the normalised dM/d$T(T)$ curves are plotted. While the bulk alloy exhibits a narrow minimum in the temperature evolution of the dM/dT, for the milled alloy this minimum is largely broadened, indicating that the ferro-to-paramagnetic transition is not well defined, probably due to the milling-induced disorder that gives rise to a distribution of Fe–Fe interatomic distances, and then spreading out the values for the T_C.

Table 1
Structural and magnetic data of the Pr_2Fe_{17} alloys studied.

Sample	a (Å)	c (Å)	T_C (K)	$\lvert\Delta S_M\rvert$ (J kg^{-1} K^{-1})	T @ ΔS_M^{max} (K)	$\langle\tau\rangle_{TEM}$ (nm)	$\langle\tau\rangle_{NPD}$ (nm)
Bulk alloy	8.583(2)	12.465(2)	285(2)	5.7(1)	289(2)	–	–
10 h - BM	8.585(2)	12.465(2)	292(10)	3.7(1)	303(6)	27(1)	24(5)

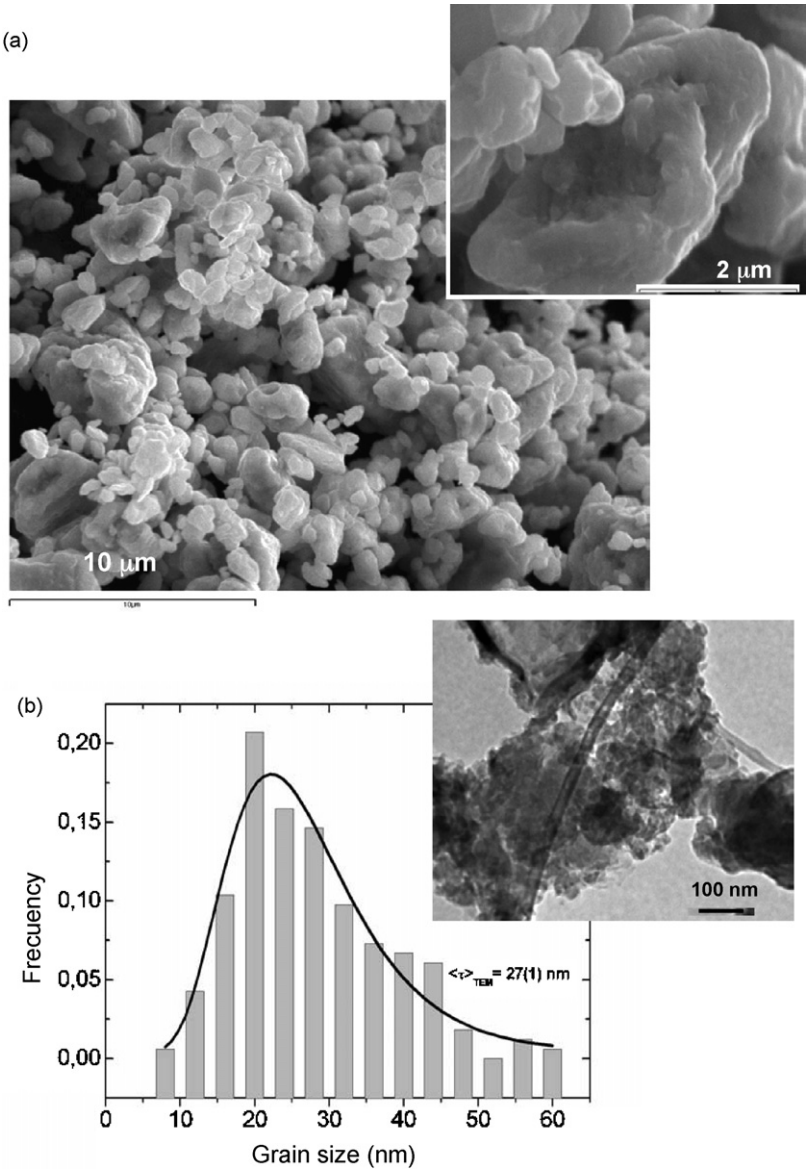

Fig. 2. (a) SEM micrograph of Pr_2Fe_{17} powders milled during 10 h (10 h-BM). Inset: higher magnification micrograph. (b) Histogram of the grain sizes. Inset: typical TEM micrograph showing the nanograined structure exhibited by powder particles.

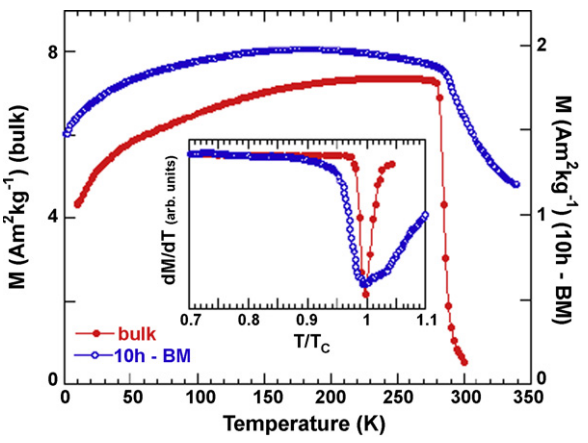

Fig. 3. Temperature dependence of magnetization at $\mu_o H_{ext} = 5$ mT for bulk and as-milled (10 h-BM) Pr_2Fe_{17} alloys. The dM/dT curve is shown in the inset.

In Fig. 4 we plot the temperature dependence of the magnetic entropy change, $|\Delta S_M|$ at $\mu_o H = 5$ T obtained from a series of $M(H)$ curves measured between 260 and 340 K. The maximum value achieved for the bulk sample, 5.7(1) J kg^{-1} K^{-1}, is in good agreement with previously reported data [2,4]. The maximum is well defined and approximately coincides with the value of T_C (see Table 1). Furthermore, the milling process leads to a reduction of the maximum value for $|\Delta S_M|$ (3.7 J kg^{-1} K^{-1}), undergoing a small shift to higher temperature and a broadening in the whole temperature range (see the inset of Fig. 4, where $\Delta S_M/\Delta S_M^{max}$ vs. T/T_C curve is represented). Hence, the latter must be a direct consequence of the lack of definition in the value of the T_C, shown in Fig. 3, due to a broad minimum in the dM/dT vs. T curve. Finally, it is worth to note that even the maximum value for the magnetic entropy change decreases around 40% after milling, the temperature range in which ΔS_M remains with more than the 90% of its maximum value is around 40 K (20 K in the case of bulk alloy). This large temperature interval with almost constant value of ΔS_M could be interesting for magnetic refrigeration appli-

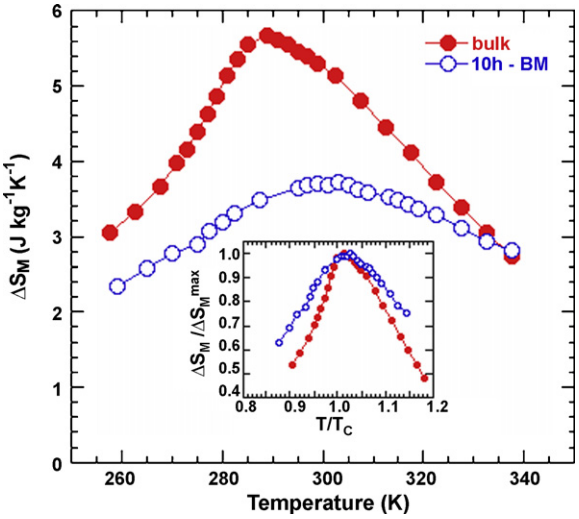

Fig. 4. Temperature dependence of the magnetic entropy change $|\Delta S_M|$ at $\mu_o H_{max} = 5$ T for bulk and as-milled Pr_2Fe_{17} alloys. The inset shows the curve normalized to ΔS_M^{max} and T_C.

cations at room temperature using these low-cost intermetallic compounds.

Finally we can summarize the following points: (a) powders show a non homogeneous microstructure formed by flaky particles of around 100–400 nm that agglomerate forming what at a lower magnification look like larger particles, irregular in shape, showing as well a moderate tendency to agglomeration; (b) internally particles are nanostructured with a mean grain size of around 27 nm; (c) disorder is macroscopically expressed from the magnetic point of view in the broadening of the ferro-to-paramagnetic transition, a shifting of the magnetic phase ordering temperature to higher temperatures, the reduction in the maximum magnetic entropy change and the broadening of the $\Delta S_M(T)$ dependence.

Acknowledgements

This work was supported by Spanish MEC, (NAN2004-09203-C04-03). J.L. S. Ll and P.A. are grateful to FICyT for financial support. We thank ILL and Spanish CRG-D1B for allocating neutron beam time. SCT's (Univ. Oviedo) are also acknowledged.

References

[1] K.H.J. Buschow, Rep. Prog. Phys. 40 (1977) 1179.
[2] K. Mandal, et al., J. Phys. D: Appl. Phys. 37 (2004) 2628.
[3] K. Pawlik, et al., J. Magn. Magn. Mater. 304 (2006) e510.
[4] P. Gorria, et al., J. Phys. D: Appl. Phys. 41 (2008) 192003.
[5] P. Gorria, et al., Phys. Status Solidi (RRL) 3 (2009) 28.
[6] C. Suryanarayana, Prog. Mater. Sci. 46 (2001) 1.
[7] E. Ma, M. Atzmon, Mater. Chem. Phys. 39 (1995) 249.
[8] P. Gorria, et al., Phys. Rev. B 72 (2005) 014401.
[9] J. Rodríguez Carvajal, Physica B 192 (1993) 55.
[10] D.L. Zhang, Prog. Mater. Sci. 49 (2004) 537.
[11] Q. Johnson, et al., Acta Cryst. B24 (1968) 274.
[12] D. Martínez-Blanco, et al., J. Phys.: Condens. Matter. 20 (2008) 335213.

Journal of Non-Crystalline Solids 354 (2008) 5172–5174

Contents lists available at ScienceDirect

Journal of Non-Crystalline Solids

journal homepage: www.elsevier.com/locate/jnoncrysol

Microstructural and magnetic characterization of Nd_2Fe_{17} ball milled alloys

P. Álvarez [a], J.L. Sánchez Llamazares [a], M.J. Pérez [a], B. Hernando [a], J.D. Santos [a], J. Sánchez-Marcos [b,c], J.A. Blanco [a], P. Gorria [a,*]

[a] Departamento de Física, Universidad de Oviedo, Calvo Sotelo, s/n, 33007 Oviedo, Spain
[b] Institut Laue-Langevin, BP 156, 6, rue Jules Horowitz, 38042 Grenoble cedex 9, France
[c] Instituto de Ciencia de Materiales de Madrid, CSIC, Cantoblanco, 28049 Madrid, Spain

ARTICLE INFO

Article history:
Available online 24 October 2008

PACS:
61.05.cp
61.05.fm
75.50.Bb
81.20.Ev

Keywords:
Mechanical alloying
Nanocrystals
Neutron diffraction/scattering
X-ray diffraction
Magnetic properties
Powders

ABSTRACT

Microstructural and magnetic changes induced by ball milling in Nd_2Fe_{17} alloy have been investigated. X-ray and neutron powder diffraction studies have shown that the main crystalline phase present in the as-cast Nd_2Fe_{17} compound is the rhombohedral Th_2Zn_{17}-type crystal structure. Contrary to other materials, the crystal structure does not change after milling, and the crystal lattice parameters slightly increases while the induced strain is less than 0.1%. It has been observed from SEM and TEM images that the microstructure consists of agglomerates of nanoparticles with a mean size around 20 nm, and from magnetic measurements a broadening of the temperature range in which ferromagnetic to paramagnetic transition takes place.

The intermetallic Nd_2Fe_{17} binary compound exhibits ferromagnetic order at room temperature with a Curie temperature, $T_C = 335$ K, and a relatively high value for the saturation magnetization at low temperatures, reaching values close to 200 Am^2/kg [1]. Nd_2Fe_{17} crystallizes in the rhombohedral Th_2Zn_{17}-type crystal structure (space group $R\bar{3}m$) with Fe atoms occupying four different sites (6c, 9d, 18f and 18h) while a unique 6c site is occupied by Nd atoms [2]. Moreover, the strong dependence of the magnetic behavior on the Fe–Fe interatomic distances gives rise to magneto-volume anomalies below T_C [3], likewise other R_2Fe_{17} (R = rare earth) ferromagnetic compounds [4]. Recently, the discover of a moderate magneto-caloric effect in some R_2Fe_{17} alloys around room temperature [5,6], and its comparatively low-cost processing compared with Gd-based alloys has renewed the interest in these compounds. However, it has not previously reported how can affect a crystalline size reduction, down to the nanometer length scale, to the magnetic behavior of these alloys, or even if it is possible to obtain R_2Fe_{17} nanostructured compounds maintaining the initial Th_2Zn_{17}-type crystal structure.

We report here the structural, morphological and magnetic changes induced in arc-melted Nd_2Fe_{17} ingots by a severe mechanical treatment, performed by means of high-energy ball milling, and using different characterization techniques. This fabrication route allows synthesizing a diverse kind of nanostructured materials with a rich variety of magnetic responses [7,8].

As-cast Nd_2Fe_{17} ingots were prepared from commercial pure elements (Fe 99.98% and Nd 99.9%) by arc melting under Ar atmosphere. In order to homogenize the samples, the ingots were annealed during 1 week at 1373 K followed by a water quenching. Afterwards, the samples were pulverized and the resulting powders together with stainless steel balls were sealed in a stainless steel vial under argon atmosphere. The milling has been carried out in a high-energy Retsch PM/400 planetary ball mill for 10 h. In the following, "Bulk" and "BM-10 h" will be used as the labels to identify the as-cast and the ball milled Nd_2Fe_{17} samples, respectively. High resolution X-ray diffraction patterns at room temperature have been obtained using monochromatic Cu K_α radiation ($\lambda = 1.5418$ Å). Neutron diffraction experiments at room temperature have been carried out at the D1B two-axis powder diffractometer (Institute Laue–Langevin, Grenoble, France), using a wavelength of $\lambda = 2.52$ Å. The Rietveld analysis of diffraction patterns has been performed using the Fullprof package [9]. Powder morphology has been characterized by scanning electron microscopy (SEM), while several images obtained with a transmission electron microscope (TEM) have been used in order to estimate

* Corresponding author. Tel.: +34 985102899; fax: +34 985103324.
E-mail address: pgorria@uniovi.es (P. Gorria).

0022-3093/$ - see front matter © 2008 Elsevier B.V. All rights reserved.
doi:10.1016/j.jnoncrysol.2008.08.020

the average grain size in the nanostructured powder. With the aim of accurately estimate the value of T_C, the temperature dependence of the magnetization, $M(T)$ curves, at low applied magnetic field ($\mu_0 H = 30$ mT) has been measured using a Faraday susceptometer in the temperature range between 250 K and 425 K.

The SEM micrographs (not shown) suggest that the powder morphology of the BM-10 h sample consists of agglomerated and irregularly shaped macroscopic grains with sizes in between 1 μm and 10 μm. In Fig. 1 the histogram corresponding to the nanoparticle size distribution obtained after counting a large number of particles from different TEM images (a typical one is shown in the inset) is represented. The fit of the histogram to a log-normal distribution gives an average grain size for the individual particles of $\langle\tau\rangle_{TEM} = 17(2)$ nm, with a standard deviation, $\sigma = 6(1)$ nm, thus confirming the mechanically-driven nanostructure formation after 10 h of milling.

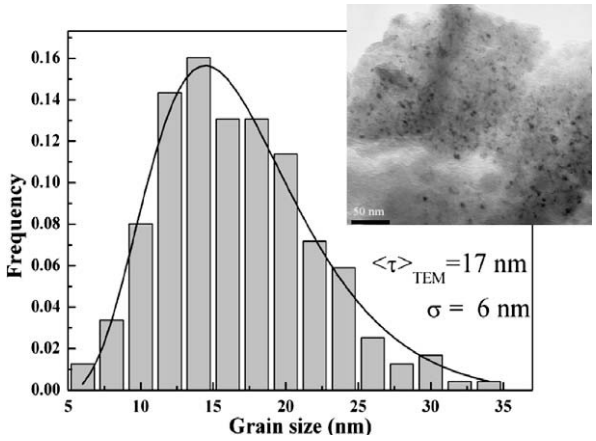

Fig. 1. TEM image and histogram of nanoparticle size distribution with the log-normal fit for the BM-10 h sample.

In Fig. 2, the X-ray (left) and neutron (right) powder diffraction patterns for both Nd_2Fe_{17} Bulk (upper panels) and Nd_2Fe_{17} BM-10 h (bottom panels) samples collected at room temperature are shown. The patterns have been fitted with two crystalline phases, one with a Th_2Zn_{17}-type crystal structure and the other with a body centered cubic (BCC) one, the former corresponds to the Nd_2Fe_{17} phase, while the latter is attributed to an impurity (less than 5%) α-Fe phase. First we refined the non-structural parameters (scale factor, zero shift error and peak shape parameters for the pseudo-Voigt function), the cell parameters and a global isotropic temperature factor, B, for each atom. Then, the atomic coordinates of Nd [6c, $(00z)$] and Fe [6c, $(00z)$; 18f, $(x00)$; 18h, $(x\bar{x}z)$; being fixed those of 9d, $(1/2\,0\,1/2)$] were refined. Other attempts using $[(z\bar{z}x)]$ coordinates for the 18h site crystallographic data lead to similar results [10]. Final refinement yielded good agreement factors and small profile differences (see Fig. 2). The values for the lattice parameters of the Bulk sample (see table 1) are in good agreement with previously reported data [11]. Besides that, it is clearly evidenced a peak broadening in the patterns corresponding to the BM-10h sample. The profile analysis of the XRD pattern [12] gives an average grain size of 24 ± 3 nm, in reasonable agreement with those estimated from TEM images, while Bulk polycrystalline sample does not show any broadening of the peaks respect to the instrumental line width, thus indicating a minimum average grain size of at least 0.1 μm.

It is worth noting that the contribution to the XRD peak width coming from induced strain is negligible (<0.1%). In addition, a slight increase in the value of the cell parameters is observed (see Table 1). These findings suggest that the main process occurring during milling is a progressive grain breakage down to the nanometer length scale, concomitant to the emergence of structural disorder in the material, as evidenced by the increase in the value of B parameter (see table 1). On the other hand, the lower resolution of the neutron diffraction pattern does not allow to give reliable values for the average crystalline size and/or the induced strain. However, we have refined the nuclear as well as the

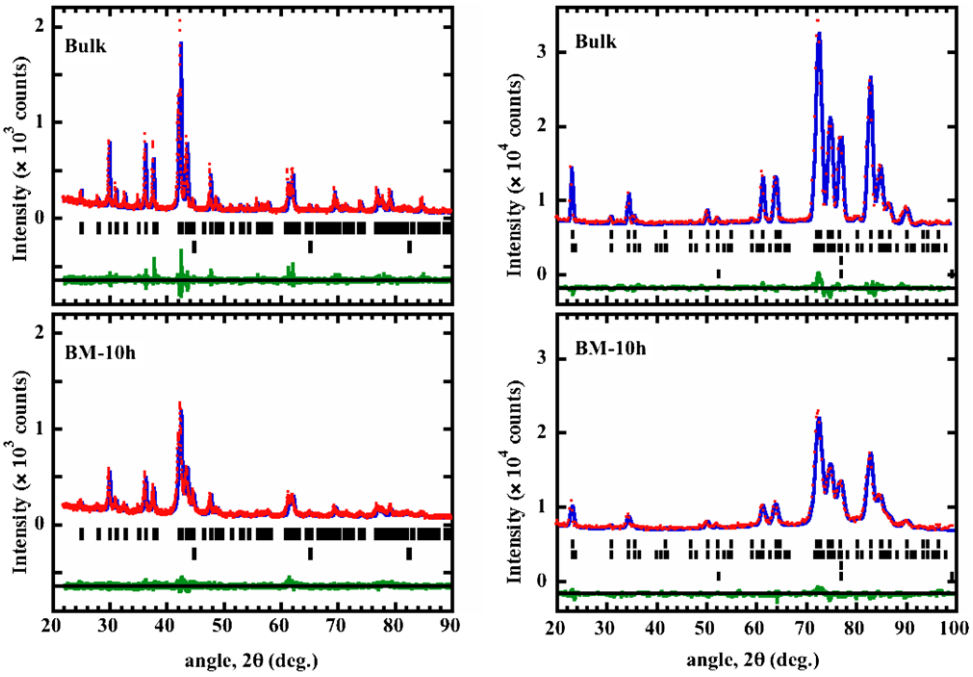

Fig. 2. Room temperature X-ray (left panels) and neutron (right panels) powder diffraction patterns corresponding to the Nd_2Fe_{17} Bulk (upper panels) and Nd_2Fe_{17} BM-10 h (bottom panels) samples. Dots are experimental data, solid lines show the calculated and difference patterns. In the left panels the first and second series of tick marks correspond to the allowed Bragg reflections of the crystal structure of Nd_2Fe_{17} and Fe impurity, while in the right panels, the first and second (third and fourth) series of tick marks correspond to the nuclear and magnetic structure of Nd_2Fe_{17} (Fe impurity).

Table 1
Structural data of Nd_2Fe_{17} ($R\bar{3}m$) at room temperature for Bulk and BM-10 h samples obtained from the analysis of powder diffraction patterns

Sample	Bulk	BM-10h
a (Å)	8.5820(1)	8.5862(2)
c (Å)	12.4618(2)	12.4625(5)
(Nd) 6c, z	0.3446(3)	0.3445(4)
(Fe) 6c, z	0.0933(5)	0.0923(7)
(Fe) 18f, x	0.2866(4)	0.2864(5)
(Fe) 18h, x	0.1699(3)	0.1691(4)
(Fe) 18h, z	0.4899(4)	0.4924(5)
B_{Nd} (Å^2)	0.80(7)	1.6(3)
B_{Fe} (Å^2)	0.60(7)	1.8(3)
$\langle\tau\rangle_{XRD}$ (nm)	–	24(3)
$\langle\tau\rangle_{TEM}$ (nm)	–	17(6)
R_B/χ^2 XRD	8.7%/1.8	6.5%
ND	4.0%/5.0	3.4%

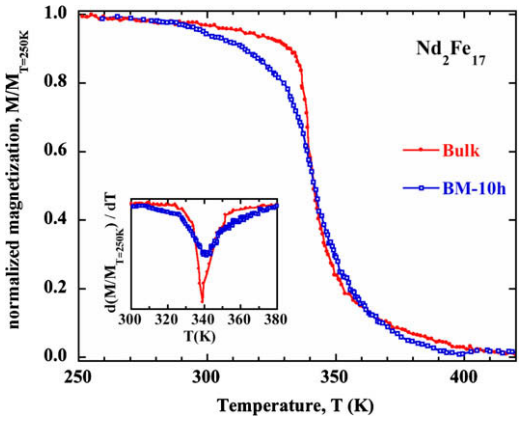

Fig. 3. Normalized magnetization vs. temperature curves for Bulk and BM-10 h samples. In the inset dM/dT vs. T is shown.

magnetic structures, taking into account that the measuring temperature is below the T_C of both Nd_2Fe_{17} and Fe impurity phase. The obtained value for the magnetic moment of the Nd_2Fe_{17} phase is $\mu = 22 \pm 6\mu_B$/f.u., in excellent agreement with previously reported values [13]. An increase of 1–2μ_B/f.u. in this value is obtained for the BM-10 h sample, which could be due to the slight increase in the value of T_C (see below), and/or the possible electronic structure modifications.

The temperature dependence of the magnetization at low applied magnetic field provides information on the alteration of the magnetic behavior due to the microstructural changes induced by milling. In Fig. 3 the normalized magnetization, $M/M_{T=250K}(T)$, after subtracting the contribution of the Fe impurity phase (almost constant in this temperature range, 217 Am^2/kg) is represented. The value of the T_C has been taken as that of the minimum in the dM/dT vs. T curve (see inset). For the bulk alloy, a value of $T_C = 339 \pm 2$ K is obtained, whereas the BM-10 h sample exhibits a broader minimum which makes difficult a precise estimation of T_C. The same trends have been observed in Pr_2Fe_{17} ball milled alloys [14]. This behavior is typical of amorphous and nanocrystalline ferromagnetic materials with a high degree of structural and/or chemical disorder, thus giving rise to a not well-defined magnetic transition from ferromagnetic to paramagnetic state [15]. Furthermore, the decrease of the crystalline grain size gives rise to the enhancement of the ratio between surface and bulk atoms together with an increase of disorder at the ground boundaries, which could be the ultimate responsible for the broader ferro-to-paramagnetic transition.

In summary, high-energy ball milling is an effective processing route to produce nanostructured Nd_2Fe_{17} intermetallic compounds without modifying the crystal structure. The average grain size decreases down to ca 20 nm while the lattice parameters remain almost unchanged and a negligible microstrain is induced. Further research relative to the effect of milling in the magneto-volume anomalies and magneto-caloric effect and its potential suitability for application purposes is under progress.

We are grateful to Spanish MEC for financial support under Projects NAN2004-09203-C04-03 and MAT2005-06806-C04-01. P.A. and J.L.S.-Ll. thank FCIyT for the PhD grant and research contract COF07-013, respectively. SCT's (Univ. Oviedo) are acknowledged for assistance in SEM, TEM and XRD measurements. We thank ILL and Spanish CRG-D1B for neutron beam time allocation.

References

[1] F. Weitzer, K. Hiebl, P. Rogi, J. Appl. Phys. 65 (1989) 4963.
[2] Q. Johnson, G.S. Smith, D.H. Wood, Acta Cryst. B 25 (1969) 464.
[3] Z. Arnold et al., IEEE Trans. Mag. 30 (1994) 619.
[4] D. Givord, R. Lemaire, IEEE Trans. Mag. 10 (1974) 109.
[5] S. Yu Dan'kov et al., Adv. Cryog. Eng. 46 (2000) 397.
[6] K. Mandal et al., J. Phys. D: Appl. Phys. 37 (2004) 2628.
[7] P. Gorria et al., Phys. Rev. B 69 (2004) 214421.
[8] P. Gorria et al., Phys. Rev. B 72 (2005) 014401.
[9] J. Rodríguez Carvajal, Phys. B 192 (1993) 55–69.
[10] E. Girt et al., J. Appl. Phys. 85 (1999) 4669.
[11] G.J. Long et al., J. Appl. Phys. 76 (1994) 5383.
[12] D. Martinez-Blanco et al., J. Phys.: Condens. Matter 20 (2008) 335213.
[13] E. Girt et al., J. Appl. Phys. 87 (2000) 5323.
[14] P. Gorria et al., J. Phys. D: Appl. Phys. 41 (2008) 192003.
[15] P. Gorria et al., Phys. B 299 (2001) 215.

Chapter 4

Magnetocaloric effect in pseudobinary $A_xB_{2-x}Fe_{17}$ alloys

4.1 Summary

With the aim of determining the role of the rare-earth in the MCE, we extended the study to several pseudobinary $A_xB_{2-x}Fe_{17}$ intermetallic alloys. Even more, it is known that the the Curie temperature of the R_2Fe_{17} can be modified by mixing different rare-earth [63, 119–122]. T_C control is interesting from the point of view of magnetic refrigeration, mainly because this temperature must be in the working temperature range.

When mixing two rare-earths in the form $A_xB_{2-x}Fe_{17}$ (with A $\neq$ B) the alloy can crystallize with only one crystal structure, or is possible that both crystal structures coexists, depending on the A_2Fe_{17} and B_2Fe_{17} crystal structures [119, 121]. In both cases it has been reported that the rare-earths share the crystallographic sites ($6c$ for rhombohedral or $2b$-$2d$ for hexagonal crystal structures) [122]. Therefore, mixing rare-earth is an interesting way of synthesize compounds in a single phase in which it can be a tricky task, like the Y_2Fe_{17} alloy.

We mixed Y, Ce, Pr and Dy with two goals: synthesize alloys with Curie temperatures in the interval (RT−20, RT+20) K (see table 4.1), and with the rhombohedral crystal structure for Dy (because Dy_2Fe_{17} usually crystallizes into the hexagonal phase) and Y (we were not able to obtain Y_2Fe_{17} in single phase). XRD shown that the studied compounds crystallize in the rhombohedral Th_2Zn_{17}-type structure, with no presence of the hexagonal Th_2Ni_{17}-type one. An α-Fe ($Im\bar{3}m$ crystal structure) impurity phase was present in less than 4 wt.% in all pseudobinary compounds.

The temperature dependence of M_S is depicted in fig. 4.1. It is expected that the Pr-based pseudobinary intermetallics would exhibit the largest magnetic entropy change because of their higher magnetization and the quick fall in the immediacy of the ferro-to-paramagnetic phase transition. Furthermore, values of M_S at $T = 5\,\mathrm{K}$ (see table 4.1) can be understood if it is assumed that the magnetic structure is close to those of the parent R_2Fe_{17} intermetallics. In the

Table 4.1: Main magnetic and magnetocaloric characteristics of $A_xB_{2-x}Fe_{17}$ intermetallics. M_S values were estimated from the isotherms at $T = 5\,K$ using the approach-to-saturation law (see eq. 3.3). Magnetocaloric data corresponds with a magnetic field change $\mu_0\Delta H = 1.5\,T$.

Composition	T_C (K)	M_S (Am^2kg^{-1})	$(-\Delta S_M)^{Peak}$ ($Jkg^{-1}K^{-1}$)	δT_{FWHM} (K)	RCP_1 (Jkg^{-1})	RCP_2 (Jkg^{-1})	RCP_3 (Jkg^{-1})
$Y_{1.2}Ce_{0.8}Fe_{17}$	253(5)	144	1.6	92	70	46	57
$Pr_{1.5}Ce_{0.5}Fe_{17}$	264(5)	152	2.4	103	78	54	42
$Dy_{1.15}Ce_{0.85}Fe_{17}$	273(5)	101	1.3	83	64	41	65
$YPrFe_{17}$	290(2)	-	2.3	98	75	51	42

pure Ce_2Fe_{17}, Cerium has a weak magnetic moment because it is in a Ce^{3+}-Ce^{4+} intermediate valence state [123, 124]. Thus the antiparallel coupling between the Dy^{3+} magnetic moments and those of the Fe sublattice can explain the low value exhibited by the Dy-containing alloy. Moreover, $Y_{1.2}Ce_{0.8Fe17}Fe_{17}$ has a lower M_S value than $Pr_{1.5}Ce_{0.5}Fe_{17}$, because Y has no magnetic moment and Pr magnetic moment is expected to be collinear with those of the Fe. Also, although there is not available data at 5 K, it would be expected a value close to $155\,Am^2Kg^{-1}$, which is the average value between those of Pr_2Fe_{17} and Y_2Fe_{17}.

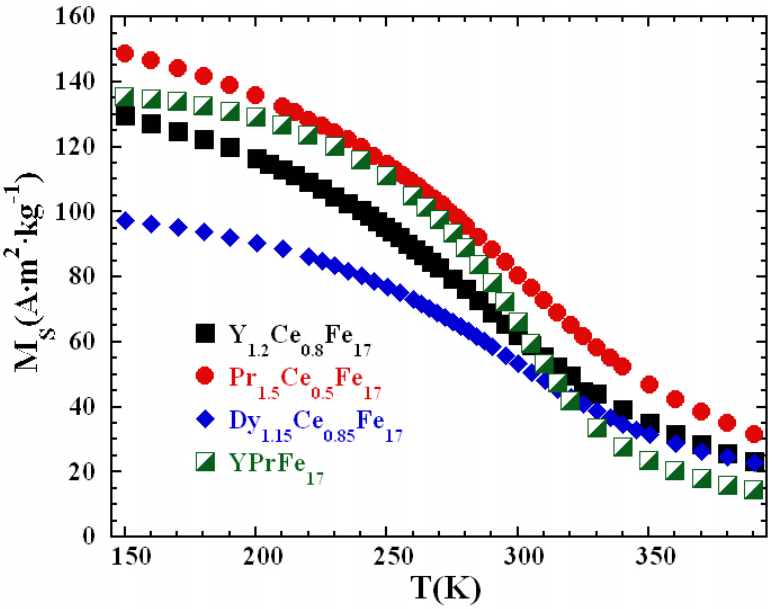

Figure 4.1: Temperature dependence of the saturation magnetization for $A_xB_{2-x}Fe_{17}$ alloys, obtained from the approach-to-saturation law (see eq. 3.3).

The temperature dependence of the magnetic entropy change (see fig. 4.2) agrees with what it would be expected regarding the temperature dependence of M_S. $\Delta S_M(T)$ curves are broad (δT_{FWHM} is over 80 K at $\mu_0\Delta H = 1.5\,T$), the highest peak values are for the Pr-containing pseudobinary alloys, and the temperature at which the peak is obtained coincides with T_C. When compared with the binary alloys, $|\Delta S_M|^{Peak}$ values are found to be around 10% lower. Furhter-

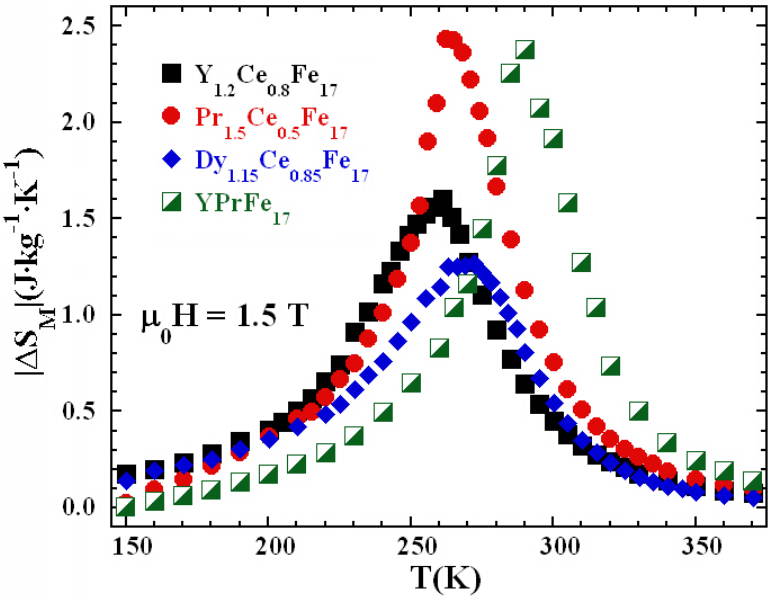

Figure 4.2: Temperature dependence of the magnetic entropy change for $A_xB_{2-x}Fe_{17}$ alloys under $\mu_0\Delta H = 1.5\,\mathrm{T}$.

more, it must be noticed that $Dy_{1.15}Ce_{0.85}Fe_{17}$ alloy does not presents an indirect effect as the pure Dy_2Fe_{17} does (see fig. 3.9).

It is interesting to note that the $|\Delta S_M(T)|$ curves exhibit a similar caret-like behavior, suggesting that the magnetocaloric effect in these intermetallic compounds is mainly governed by the Fe-sublattice. It has been shown, both theoretically and phenomenologically, that exists a master curve for the $\Delta S_{M,\Delta H}(T)$ curves in magnetic materials with a second-order phase transition [125, 126]. This master curve implies the collapse of the properly rescaled $\Delta S_M(T)$ curves at different applied magnetic field changes. This curve has been proposed to be useful to predict the magnetic field and temperature dependences of the magnetic entropy change in those materials which do not follow a mean field approach [91]. It is theoretically derived from the knowledge of the magnetic equation of state, whereas, phenomenologically, it is obtained from the $\Delta S_M(T)$ curves themselves.

We will focus in the second procedure. Firstly, each $\Delta S_M(T)$ curve is normalized to the value of the corresponding ΔS_M^{Peak}. Secondly, the temperature axis is rescaled imposing that a reference point in the $\Delta S_M(T)$ curve corresponding to a previously selected fraction of ΔS_M^{Peak}, makes the rescaled temperature, θ, to be equal 1 ($\theta = -1$) when the temperature at which the reference point, T_r, is chosen is $T_r > T_C$ ($T_r \leq T_C$) in the following way [127]:

$$\theta = (T - T_C)/(T_r - T_C) \tag{4.1}$$

[(or in the case of $T_r \leq T_C$, $\theta = -(T - T_C)/(T_r - T_C)$]. This procedure has been successfully tested in several amorphous and single phase and polycrystalline magnetic solids [126, 128]. However, if a secondary magnetic phase is present in the material, the temperature axis is rescaled in the

form [127]

$$\theta = \begin{cases} (T - T_C)/(T_{r_1} - T_C) & T \leq T_C \\ (T - T_C)(T_{r_2} - T_C) & T > T_C \end{cases} \tag{4.2}$$

where T_{r_1} and T_{r_2} are the temperatures, below and above T_C respectively, of the two reference points of each curve that correspond to $a \times \Delta S_M^{Peak}$, with a in between 0 and 1. In this work $a = 0.5$ because, for this value, the reference point corresponds with the half maximum of the $\Delta S_M(T)$ curve.
Due to the presence of a secondary magnetic phase, even though the Curie temperature is far from room temperature ($T_C = 1044\,\mathrm{K}$), the phenomenological $\Delta S_M(T)/\Delta S_M^{Peak}$ curves were obtained using two reference temperatures. These curves for different fields collapse into the same curve for each sample in the paramagnetic zone. Nevertheless, when comparing these master curves for different alloys, there are slight differences in the ordered magnetic phase (i.e. $\theta < 0$), as it can be observed in article I. This indicates the different magnetic behavior in the low temperature range, which can be due to the reminiscence of the magnetic behavior of the binary R_2Fe_{17} counterparts, where the ferrimagnetism and the antiferromagnetism do not allows to obtain the master curve.

The field dependence of the relative cooling power was obtained (see fig. 4.3). As a general remark, these values are lower than those of the parent Pr_2Fe_{17} and Y_2Fe_{17} alloys, as a direct consequence of the reduction of the M_S value. Nevertheless, the Dy-containing pseudobinary increased their RCP values with respect to the pure Dy_2Fe_{17}. It is worth to note that Ce_2Fe_{17} has two direct effects that do not allow to properly calculate the RCP for this compound.

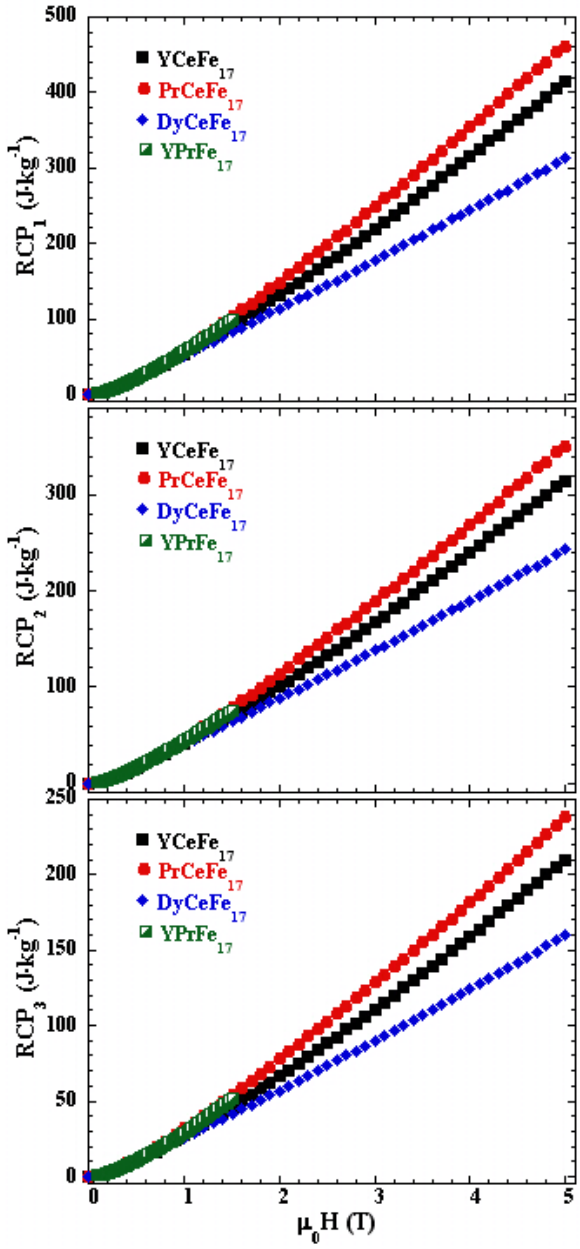

Figure 4.3: The three relative cooling power (RCP) of $A_xB_{2-x}Fe_{17}$ alloys as function of the magnetic field. In the case of $YPrFe_{17}$ no data above 1.5 T is available.

4.2 Article I: Magnetic properties and Magnetocaloric effect in several Ce-based R_2Fe_{17} alloys

4.3 Article II: Magneto-caloric effect in the pseudo-binary $YPrFe_{17}$ alloy

Intermetallics 19 (2011) 982–987

Contents lists available at ScienceDirect

Intermetallics

journal homepage: www.elsevier.com/locate/intermet

Magnetic properties and magneto-caloric effect in pseudo-binary intermetallic $(Ce,R)_2Fe_{17}$ compounds (R = Y, Pr and Dy)

Pablo Álvarez [a], Pedro Gorria [a,*], José L. Sánchez Llamazares [b], María J. Pérez [a], Victorino Franco [c], Marian Reiffers [d], Ivan Čurlik [d], Emil Gažo [d], Jozef Kováč [d], Jesús A. Blanco [a]

[a] Departamento de Física, Universidad de Oviedo, Calvo Sotelo s/n, 33007 Oviedo, Asturias, Spain
[b] División de Materiales Avanzados, Instituto Potosino de Investigación Científica y Tecnológica, Camino a la presa San José 2055, CP 78216, San Luis Potosí, Mexico
[c] Departamento de Física de la Materia Condensada, ICMSE-CSIC, Universidad de Sevilla, P.O. Box 1065, 41080 Sevilla, Spain
[d] Institute of Experimental Physics, Watsonova 47, SK-04001 Košice, Slovakia

ARTICLE INFO

Article history:
Received 7 January 2011
Received in revised form
24 February 2011
Accepted 25 February 2011
Available online 31 March 2011

Keywords:
A. Magnetic intermetallics
A. Rare-earth intermetallics
B. Magnetic properties
G. Ambient-temperature uses

ABSTRACT

We have synthesized three pseudo-binary $(Ce,R)_2Fe_{17}$ intermetallic alloys, where cerium has been partially substituted by R = Y, Pr and Dy, with the aim of tuning the Curie temperature (between 253 and 273 K) for obtaining the maximum magneto-caloric response of the alloys just below room temperature. The analysis of the x-ray powder diffraction patterns show that the three samples crystallize in the rhombohedral Th_2Zn_{17}-type crystal structure (space group $R\bar{3}m$). We report the temperature dependence of the isothermal magnetic entropy change, $|\Delta S_M|(T)$, the magnetic field dependence of its maximum value, $|\Delta S_M{}^{max}|(H)$, and the relative cooling power around the second-order magnetic transition for magnetic field changes $\mu_0\Delta H_{max} = 5$ T. The collapse of the normalized $\Delta S_M(\theta)/\Delta S_M{}^{max}$ vs. temperature (where θ is a rescaled temperature) into a single master curve allows the extrapolation of $|\Delta S_M|(T)$ curves for higher magnetic field changes, and/or the estimation of the temperature dependence of the magnetic entropy for other 2:17 pseudo-binary compounds. The lower values of $|\Delta S_M{}^{max}|$ compared with those of the R_2Fe_{17} compounds with R = Pr or Nd are explained in terms of the decrease of the saturation magnetization. The magnetic field dependence of the $|\Delta S_M{}^{max}|$ indicates that only $Pr_{1.5}Ce_{0.5}Fe_{17}$ alloy roughly follows a mean-field behaviour.

1. Introduction

The binary R_2Fe_{17} intermetallic compounds (R = rare earth element) are, within the R–Fe phase diagram, those with the highest iron content [1]. These alloys attracted considerable attention in the 90's because it was discovered that the addition of interstitial C and/or N atoms results in significant enhancements of the Curie temperature, T_C, and the crystal-field magnetic anisotropy [2]. Therefore, $R_2Fe_{17}N_xC_y$ compounds turned out to be suitable for being used in technological applications as permanent magnets [3–5]. More recently R_2Fe_{17} compounds with R = Pr, Nd, have drawn attention as promising materials for room temperature magnetic refrigeration technology [6,7]. They are characterized by a remarkable magneto-caloric effect (MCE), with moderate values for the maximum magnetic entropy change, $|\Delta S_M{}^{max}|$, reaching 6.3 J kg^{-1} K^{-1} under a magnetic field change from 0 to 5 T in the case of Pr_2Fe_{17}, and broad $\Delta S_M(T)$ curves, giving rise to large refrigerant capacity around the second-order ferromagnetic transition of the 2:17 phase [7,8]. However, those alloys with heavy rare earths display smaller MCE (under a magnetic field change from 0 to 5 T $|\Delta S_M{}^{max}| \approx 3.7$ J kg^{-1} K^{-1} and 4.1 J kg^{-1} K^{-1} for R = Er [9] and Lu [10], respectively) due to the lower saturation magnetization values.

These R_2Fe_{17} compounds crystallize in the rhombohedral Th_2Zn_{17}-type (space group $R\bar{3}m$) structure for the light rare earths (R = Ce, Pr, Nd, Sm,), with a unique crystallographic site for the rare earth and four inequivalent sites for the Fe atoms [1]. The hexagonal Th_2Ni_{17}-type is the stable structure (space group $P6_3/mmc$) in those compounds with heavy rare earths, occupying the R element two different sites in this case, while also four crystallographic sites are found for the Fe atoms [1]. Both structures are possible for R = Gd and Tb [11]. This family of intermetallic compounds has been extensively studied since the 70's because depending on the rare earth element the competition between the 3d and 4f magnetism originates different types of magnetic orderings, including ferro- or ferrimagnetic behaviours, and more complex fan or helical magnetic structures [12]. Moreover, slight variations of the interatomic distances between neighbouring Fe atoms strongly affect the magnetic interactions, leading to remarkable magneto-volume effects, such as negative thermal expansion below the

* Corresponding author. Tel.: +34 985102899; fax: +34 985103324.
E-mail address: pgorria@uniovi.es (P. Gorria).

0966-9795/$ – see front matter © 2011 Elsevier Ltd. All rights reserved.
doi:10.1016/j.intermet.2011.02.020

magnetic ordering temperature or a large spontaneous positive magnetostriction [12–15]. Ce_2Fe_{17} can yield to a complex magnetic phase diagram, since antiferromagnetic, ferromagnetic non-collinear and helimagnetic magnetic structures are possible [12,16,17]. Moreover, a metamagnetic transition from a modified helix structure to a ferromagnetic one or between helimagnetic phases can be caused either by an external magnetic field or under high pressures [18]. Apart from that, the magnetic state of Ce_2Fe_{17} is unstable and sample dependent at low temperatures, even though in this compound Cerium has no magnetic moment because of its Ce^{3+}–Ce^{4+} intermediate valence state [19,20]. Therefore, the magnetic properties arise from the competing exchange interactions between the Fe sublattices. On the other hand, Y_2Fe_{17}, and Pr_2Fe_{17} exhibit ferromagnetic order, but while Y does not carry any magnetic moment, the Pr^{3+} magnetic moments are parallel to those of Fe atoms. However, Dy_2Fe_{17} is ferromagnetic, with the magnetization of the Dy and Fe sublattices being antiparallel to each other [13,21,22].

Furtheremore, it is possible to modify the Curie temperature (T_C) of R_2Fe_{17} intermetallics by mixing different rare earth elements [23–25]. In this way, the combination of two R elements can facilitate the synthesis of single-phase materials with one of the two possible crystal structures, which is sometimes difficult; such is the case of Y and Gd [26]. Having that in mind, we have mixed Ce with Y, Pr and Dy with the aim of synthesizing three pseudo-binary compounds with different values of T_C just below room temperature, and looked at the possible changes in the magneto-caloric effect. In this contribution we report on the synthesis, the crystal structure, the magnetic properties and the magneto-caloric response of three pseudo-binary Ce-based alloys: $Y_{1.2}Ce_{0.8}Fe_{17}$, $Pr_{1.5}Ce_{0.5}Fe_{17}$ and $Dy_{1.15}Ce_{0.85}Fe_{17}$. The compositions have been selected for having the Curie temperature higher by about 10 K.

2. Experimental methods and data analysis

Polycrystalline as-cast ingots of nominal composition $Y_{1.2}Ce_{0.8}Fe_{17}$, $Pr_{1.5}Ce_{0.5}Fe_{17}$ and $Dy_{1.15}Ce_{0.85}Fe_{17}$ were prepared by the standard arc-melting technique. The purity of the starting elements was 99.99% for Fe and 99.9% in the case of Ce, Y, Pr and Dy (relative to rare earth content). For each alloy the evaporation loss of the R elements was studied for each alloy and carefully compensated by adding the adequate rare earth amount excess. Samples were wrapped in tantalum foil, sealed under vacuum in quartz ampoules and annealed at 1263 K during 12 days for phase homogenization purposes. The annealing finished by water quenching of the quartz ampoules. Crystal structure of each compound was checked by means of high-resolution x-ray powder diffraction (XRD) at room temperature using a Seifert XDR 3000 T/T diffractometer. The scans in 2θ were performed between 2 and 160° with $\Delta\theta = 0.02°$ steps and counting times of 20s per point using monochromatic Cu $K\alpha$ radiation ($\lambda = 1.5418$ Å). The full-profile analyses of the diffraction patterns were carried out with the FullProf suite package refining the crystallographic parameters by the Rietveld method [27].

The saturation magnetization has been estimated from the magnetization vs applied magnetic field curve, $M(H)$, measured at $T = 5$ K on a Quantum Design PPMS-5 SQUID magnetometer. For the measurement of the $M(H)$ curve the applied magnetic field was varied in fixed increments of 0.1 T between 0 and $\mu_0 H_{max} = 5$ T. In addition, several isothermal $M(H)$ curves were measured at selected temperatures between 100 and 390 K (on heating), following the same conditions, in order to obtain the temperature and magnetic field dependences of the magnetic entropy change, $|\Delta S_M|(H,T)$. There is no observable hysteresis for field up versus field down in these $(Ce,R)_2Fe_{17}$ intermetallic alloys undergoing a second-order magnetic phase transition, contrary to that occurring in those materials displaying MCE around a first order one [28]. The value of T_C for each sample was taken as the minimum of the temperature derivative of the magnetization vs temperature, $dM/dT(T)$, after measuring the $M(T)$ curve under a low applied magnetic field $\mu_0 H = 5$ mT and at a heating rate of 1.5 K/min.

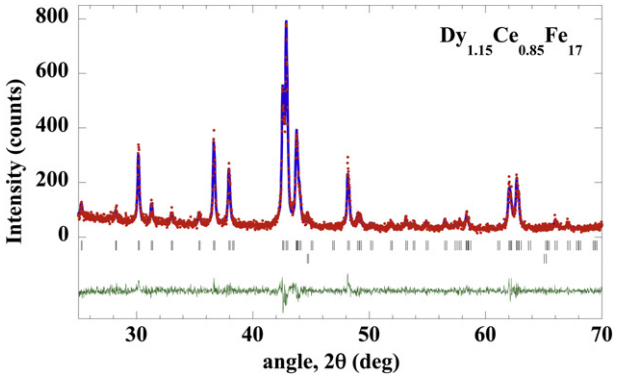

Fig. 1. Observed (dots) and calculated (solid line) XRD patterns at $T = 300$ K for the $Dy_{1.15}Ce_{0.85}Fe_{17}$ alloy. Vertical bars represent the positions of the Bragg reflections; the upper and lower row marks correspond to the Th_2Zn_{17}-type phase and α-Fe impurity, respectively. The observed–calculated difference is depicted at the bottom of the figure.

The isothermal magnetic entropy change $|\Delta S_M|$ due to a change of the applied magnetic field from an initial value $H = 0$ to a final value H is obtained by numerical approximation of the Maxwell relation [7]:

$$\Delta S_M(T,H) = S_M(T,H) - S_M(T,0) = \int_0^H \left(\frac{\partial M(T',H')}{\partial T'}\right)_{T'=T} dH' \qquad (1)$$

where T is the temperature at which each $M(H)$ curve is measured. After applying this calculation procedure to the whole set of $M(H)$ curves we obtain the temperature and applied magnetic field dependences of the magnetic entropy change, $|\Delta S_M(H,T)|$. For these calculations we have considered the nominal value of the applied magnetic field, H_{app}, instead of the effective (internal) magnetic field on the sample, H_{eff}, being $H_{eff} = H_{app} - NM_s$, and N the demagnetizing factor. However, and in order to discard large errors following this procedure [29], N has been estimated from the linear fit of the low-field part of the $M(H)$ curves measured at $T = 5$ K,

Table 1
Cell parameters, atomic positions and percentage of R (Y, Pr, Dy) atoms at 6c positions of the studied compounds (with rhombohedral Th_2Zn_{17}-type crystal structure; space group $R\bar{3}m$) obtained from room temperature XRD patterns ($\lambda = 1.5418$ Å).

Sample	$Y_{1.2}Ce_{0.8}Fe_{17}$	$Pr_{1.5}Ce_{0.5}Fe_{17}$	$Dy_{1.15}Ce_{0.85}Fe_{17}$
a (Å)	8.490 (1)	8.565 (1)	8.487 (1)
c (Å)	12.394 (1)	12.487 (2)	12.417 (3)
c/a	1.460	1.455	1.461
V (Å^3)	774.1 (1)	790.2 (1)	773.5 (1)
Ce/R (6c)			
z	0.340 (1)	0.320 (1)	0.359 (2)
% R	58 (5)	76 (4)	64 (5)
Fe1 (6c)			
z	0.098 (2)	0.091 (3)	0.125 (6)
Fe3 (18f)			
x	0.281 (1)	0.287 (1)	0.291 (2)
Fe4 (18h)			
x	0.165 (1)	0.172 (1)	0.160 (2)
z	0.481 (2)	0.481 (2)	0.482 (2)
R_B	11.0	10.8	5.7
χ^2 (%)	1.5	3.0	1.2

Table 2
Values for magnetic and magneto-caloric parameters for the three studied compounds. M_S values were obtained from the approach-to-saturation law (see text). The $|\Delta S_M|$, δT_{FWHM} and *RCP* values correspond to a magnetic field change $\mu_0\Delta H = 5$ T.

Alloy	T_C (K)	M_S A m^2 kg^{-1}	M_S (μ_B/f.u.)	$\lvert\Delta S_M\rvert$ (J kg^{-1} K^{-1})	δT_{FWHM} (K)	*RCP*–1 (J kg^{-1})	*RCP*–2 (J kg^{-1})	*RCP*–3 (J kg^{-1})
$Y_{1.2}Ce_{0.8}Fe_{17}$	253 ± 5	125 ± 2	26	4.3	96 ± 5	414	315	210
$Pr_{1.5}Ce_{0.5}Fe_{17}$	264 ± 5	133 ± 2	29	5.3	87 ± 5	461	351	238
$Dy_{1.15}Ce_{0.85}Fe_{17}$	273 ± 5	93 ± 2	20	3.3	94 ± 5	313	243	160

being the slope of such fit equal to $1/N$. The values for N are around 0.2 for the three samples, thus implying that always $H_{eff} > 0.95\,H_{app}$, and therefore, the values of $|\Delta S_M|$ are underestimated by no more than 5% in all the cases.

The relative cooling power (*RCP*) is a parameter that takes into account the amount of heat that the magnetic material can absorb from the cold focus and deliver to the hot focus during an ideal refrigeration cycle. This parameter is commonly calculated using three different criteria [see reference 7 for details], and hereafter we shall call them *RCP*-1, *RCP*-2 and *RCP*-3. They are defined as: *RCP*-$1(H) = |\Delta S_M{}^{max}|(H) \times \delta T_{FWHM}(H)$, where δT_{FWHM} is the full width at half maximum of $|\Delta S_M|(T)$ curve; *RCP*-2 is the area below $|\Delta S_M|(T)$ curve in the temperature range between T-δT_{FWHM} and T+δT_{FWHM}; and *RCP*-3 is the maximum value of the product $|\Delta S_M| \times \Delta T$ below the $|\Delta S_M(T)|$ curve.

3. Results

Fig. 1 shows the room temperature XRD pattern corresponding to the $Dy_{1.15}Ce_{0.85}Fe_{17}$ compound together with its Rietveld refinement. The other two samples show similar powder diffraction patterns, because all of them have the rhombohedral ($R\bar{3}m$) Th_2Zn_{17}-type crystal structure. In that phase the rare earth occupy the 6c site for pure R_2Fe_{17} alloys [30,31], and when mixing two different rare earth elements both occupy the same 6c crystallographic site. Hence, Ce stabilizes the rhombohedral phase although the hexagonal structure is more stable for the Y_2Fe_{17} and Dy_2Fe_{17} binary intermetallic compounds. In addition, a minor impurity phase (<3 wt.%), identified as α-Fe, has been found in the three samples. Table 1 summarizes the values of the crystallographic parameters as well as the reliability factors of the refinements. The cell volume of the Pr containing compound shows an increase of around 2% respect to the other two alloys, due to the smaller atomic radii of Y and Dy compared with that of Pr.

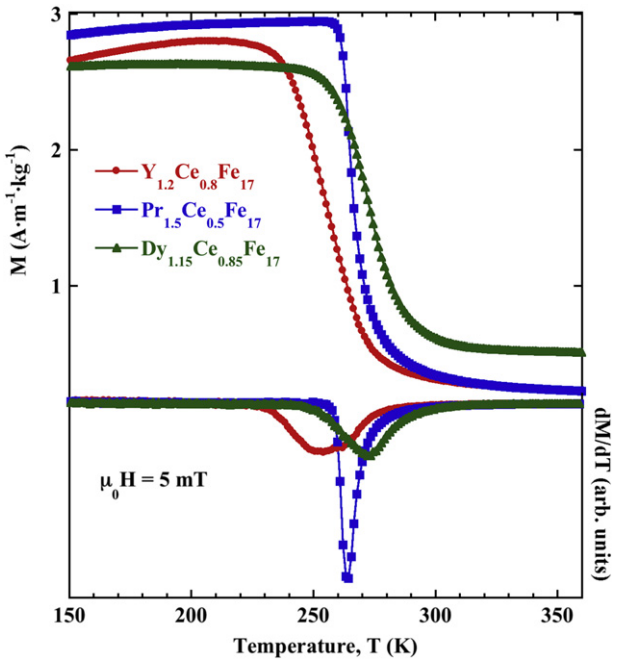

Fig. 2. Temperature dependence of the magnetization under an applied magnetic field $\mu_0 H = 5$ mT. The *dM/dT vs. T* curves are shown at the bottom of the figure.

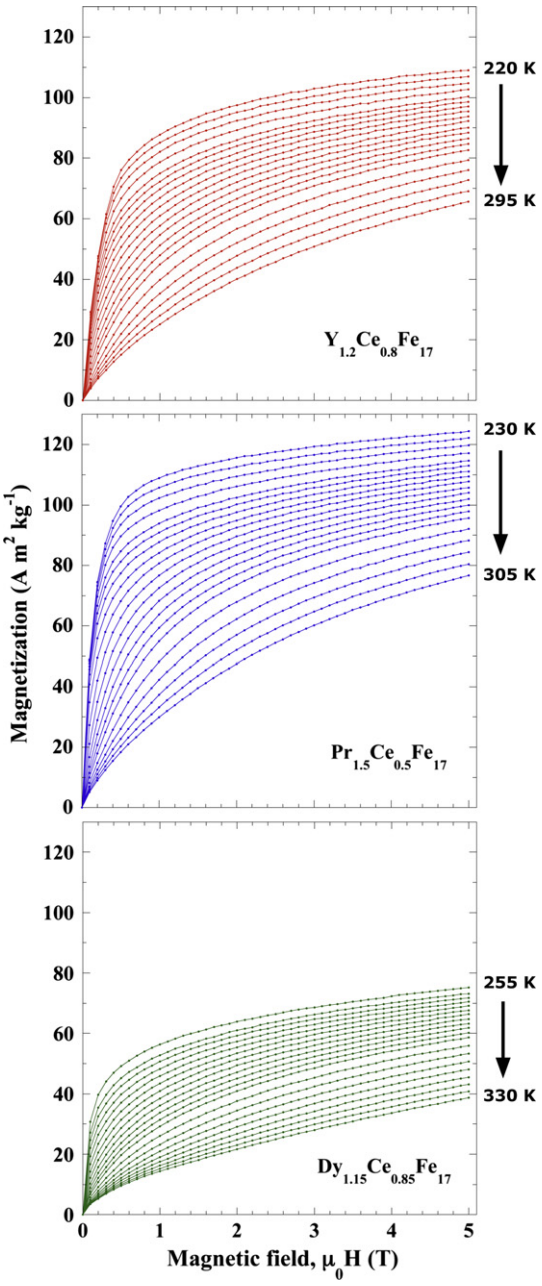

Fig. 3. Isothermal magnetization curves, *M(H)*, for the $Y_{1.2}Ce_{0.8}Fe_{17}$, $Pr_{1.5}Ce_{0.5}Fe_{17}$ and $Dy_{1.15}Ce_{0.85}Fe_{17}$ compounds around the second-order magnetic transition.

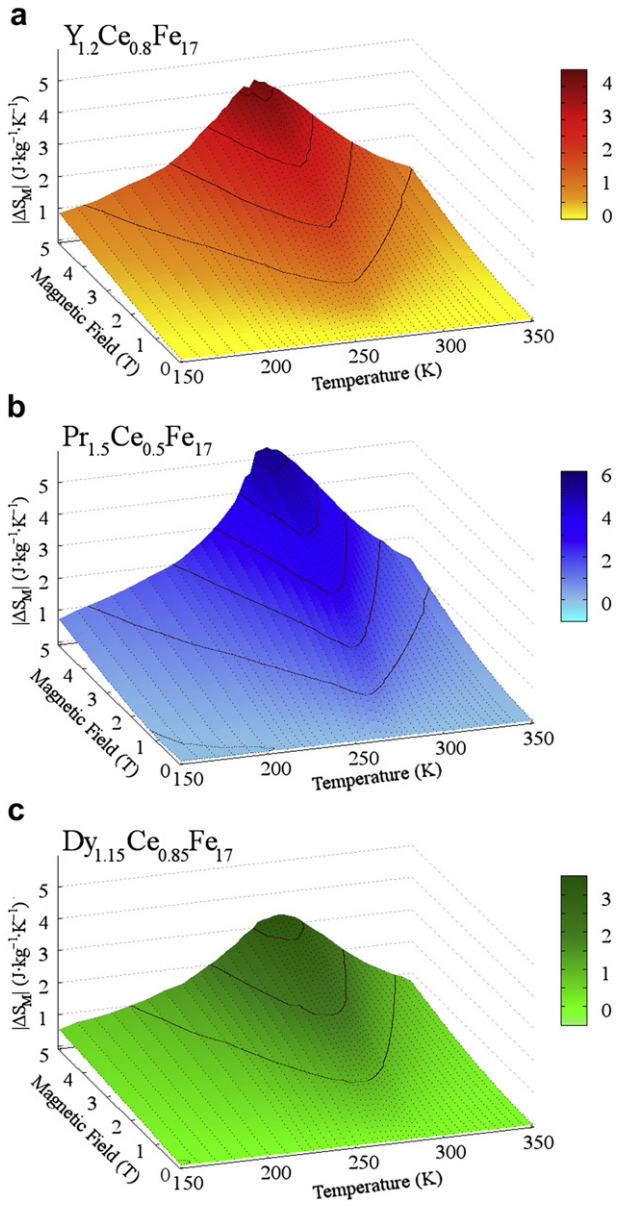

Fig. 4. 3D-surfaces showing the temperature and applied magnetic field dependences of the magnetic entropy change $|\Delta S_M(H,T)|$, for the $Y_{1.2}Ce_{0.8}Fe_{17}$ (a), $Pr_{1.5}Ce_{0.5}Fe_{17}$ (b), and $Dy_{1.15}Ce_{0.85}Fe_{17}$ (c) alloys.

The temperature dependence of the magnetization (Fig. 2), *M(T)* curves, measured under a low applied magnetic field ($\mu_0 H = 5$ mT), together with the corresponding temperature derivatives of the magnetization as a function of the temperature, *dM/dT vs. T* curves, for the three samples are shown. The different trend of the *M*(*T*) curves observed below $T = 200$ K is due to the fact that the samples are far away from being magnetically saturated (note that the three samples show similar magnetization values, all of them below 3 A m^2 kg^{-1}, which is between 2 and 4% of the respective saturation magnetization values, see Table 2), because the low applied magnetic field only provokes a slight rotation of the magnetic domains. Therefore, different configurations of the magnetic domains in each sample could conduct to different temperature dependences of the low-field magnetization. As it has been mentioned above, the values of T_C (see Table 2) are chosen as those corresponding to the minima of the *dM/dT*(*T*) curves. The fact that magnetization does not drop to zero for temperatures well above T_C

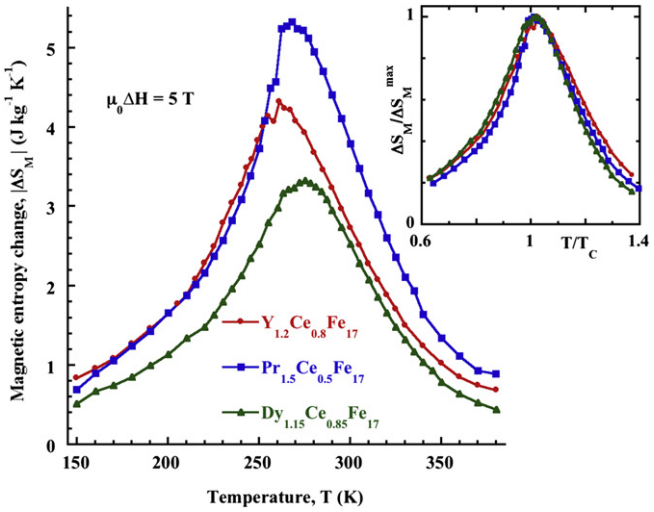

Fig. 5. Temperature dependence of the magnetic entropy change for the maximum applied magnetic field change $\mu_0\Delta H = 5$ T. The inset shows the normalized $|\Delta S_M|$ vs T/T_C curves.

is a direct consequence of the existence of a low amount of α-Fe impurity with a much higher value of T_C (1043 K). A kink in the magnetization vs. temperature curve is observed as *T* increases, and following the method based in the variation of the magnetization kink with the applied magnetic field, and explained by Tanaka et al. in Ref. [32], we have estimated the value of T_C in the three compounds, being almost the same (±5 K) to those obtained from the *dM/dT*(*T*) curves.

The magnetization vs. applied magnetic field, *M*(*H*) curves, show a similar trend for the three compounds although the magnetization values are different. The value for the saturation magnetization, M_S, has been estimated at $T = 5$ K (see Table 2) from the fit of the *M*(*H*) curves in the high applied magnetic field range (2–5 T) using a common approach-to-saturation law [33], $M = M_S(1\text{-}b/H^2)+\chi_0 H$. These values are within the range that could be expected assuming that the magnetic moments of the rare earths are arranged in the

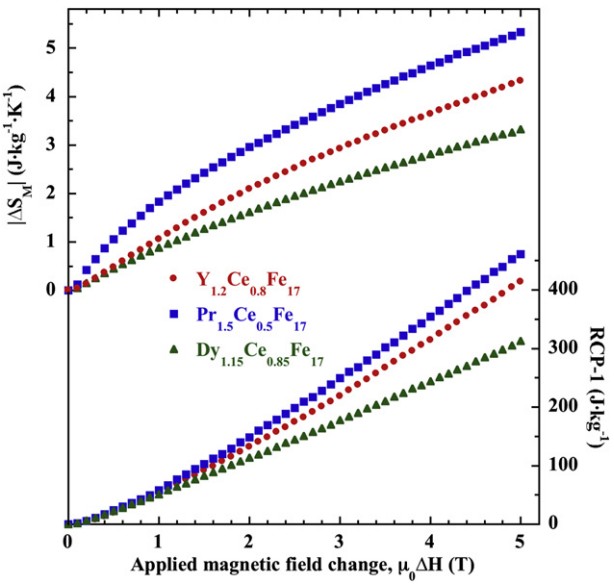

Fig. 6. Magnetic field dependences of the maximum magnetic entropy change, $|\Delta S_M^{max}|$, (upper curves) and the Relative Cooling Power, *RCP-1* (bottom curves) for $Y_{1.2}Ce_{0.8}Fe_{17}$ $Pr_{1.5}Ce_{0.5}Fe_{17}$ and $Dy_{1.15}Ce_{0.85}Fe_{17}$ samples.

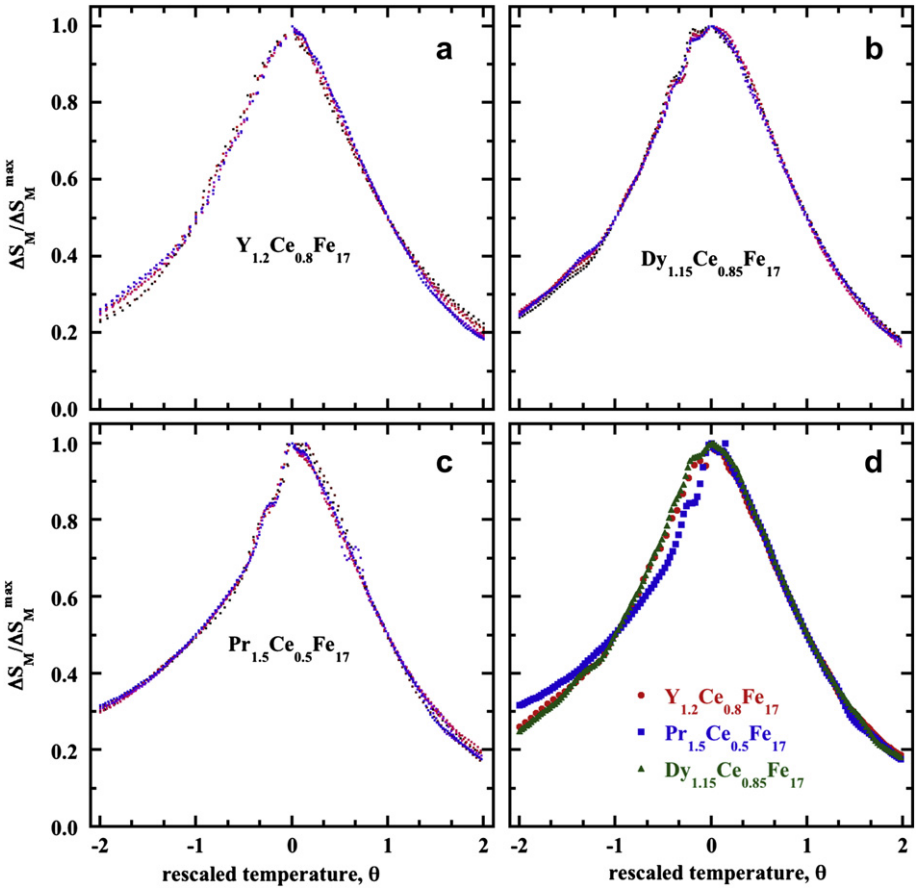

Fig. 7. Master curves for the three compounds obtained using two temperatures of reference (see text for details).

same way as in pure R_2Fe_{17} compounds. The antiparallel coupling between the Dy^{+3} magnetic moments and those of the Fe sublattice can explain the low M_S value exhibited by the Dy-containing alloy. Moreover, it is understandable that $Y_{1.2}Ce_{0.8}Fe_{17}$ has a lower M_S value than $Pr_{1.5}Ce_{0.5}Fe_{17}$, because Y has no magnetic moment and Pr magnetic moment (around 3 μ_B/Pr atom) are expected to be collinear with those of the Fe. From the M_S value and the quick fall of the magnetization around T_C it can be anticipated that the Pr containing alloy will display a higher magneto-caloric effect.

The value of $|\Delta S_M|$ at each temperature has been calculated from the isothermal $M(H)$ curves (see Fig. 3) by using the eq. (1).

We show in Fig. 4 the 3-D surfaces corresponding to the temperature and applied magnetic field dependencies of the magnetic entropy change, $|\Delta S_M|(H,T)$, for the $Y_{1.2}Ce_{0.8}Fe_{17}$ (a), $Pr_{1.5}Ce_{0.5}Fe_{17}$ (b) and $Dy_{1.15}Ce_{0.85}Fe_{17}$ (c) intermetallic alloys. In addition, the temperature dependence of the isothermal magnetic entropy change for an applied magnetic field change, $\mu_0\Delta H$, from 0 to $\mu_0 H_{max} = 5$ T, $|\Delta S_M|(T)$ curves, are compared in Fig. 5 for the three compounds.

It is interesting to note that even though somewhat different $|\Delta S_M{}^{max}|$ values are obtained, 4.3 (Y), 5.3 (Pr) and 3.3 J K^{-1} kg^{-1}(Dy), the normalized $|\Delta S_M|/|\Delta S_M{}^{max}|$ vs T/T_C curves (see inset of Fig. 5) exhibit a similar "caret-like" behaviour, suggesting that the magneto-caloric effect in these intermetallic compounds is mainly governed by the Fe sublattice. Moreover, $|\Delta S_M{}^{max}|$ values are found to be around 10% lower than those previously reported for the corresponding pure binary alloys [6,7,9], except in the case of Y_2Fe_{17} for which values between 3.2 and 5 J K^{-1} kg^{-1} (depending on the sample treatment) have been reported [10]. Therefore, we can assume that Ce atoms do not contribute to the spontaneous magnetization of the studied pseudo-binary alloys for explaining the reduction of the $|\Delta S_M{}^{max}|$ values, since the magneto-caloric effect in these compounds is proportional to the magnetization change in the vicinity of the second-order magnetic phase transition [7,34].

The relative cooling power has been calculated by using the three different methods previously mentioned in section 2 and the maximum values are given in Table 2. In the case of the Pr-based alloy *RCP* values are lower (10% for *RCP*-1 and *RCP*-2, 17% for *RCP*-3) than those for the Pr_2Fe_{17} binary alloy [7], although a similar δT_{FWHM} value is observed. Hence, the reduction of about 15% in the value of $|\Delta S_M{}^{max}|$ is the main responsible for the decrease in the relative cooling power. For the other two binary compounds, Y_2Fe_{17} and Dy_2Fe_{17}, *RCP* data has not previously been reported. Fig. 6 displays the applied magnetic field dependence of the $|\Delta S_M|$ peak value and that of the *RCP*-1. It is observed that the $|\Delta S_M|(H)$ curves follow a power low dependence on the applied magnetic field ($|\Delta S_M| \propto H^n$). For the Pr containing alloy, with collinear ferromagnetic order, the exponent n has a value close to that expected from a mean-field theory ($n_{mf} = 2/3$), while for the other two alloys $n > n_{mf}$ ($n \approx 0.8$), thus suggesting a more complex magnetic scenario. The *RCP-1* vs H curves also follow a power-like dependence on the applied magnetic field, being the exponent close to 5/4 in the case of Pr and Y compounds with almost parallel trends for $\mu_0 H > 2$ T, and close to 1 for Dy alloy.

Moreover, it has been proposed that in ferromagnetic materials exhibiting a second-order magnetic transition, the $|\Delta S_M|(T)$ curves for different magnetic field changes collapse into a single master

curve if a proper normalization is carried out [35,36]. Such a master curve is useful if the extrapolation of the $|\Delta S_M|(H,T)$ curves for temperature and/or applied magnetic field values out from those available in the laboratory is pursued, and also to avoid the spurious contribution to the magnetic entropy change coming from ferromagnetic impurity phases [37]. The master curve is obtained as follow: firstly, the $|\Delta S_M|(T)$ curves are normalized to its maximum value $|\Delta S_M{}^{max}|$ for each value of the applied magnetic field change. Secondly, the temperature axis is rescaled using two different reference temperatures:

$$\theta = -(T - T_C)/(T_{r1} - T_C) \quad T < T_C \tag{2}$$

$$\theta = -(T - T_C)/(T_{r2} - T_C) \quad T > T_C \tag{3}$$

where T_{r1} and T_{r2} are the temperatures at which $|\Delta S_M| = a \times |\Delta S_M{}^{max}|$, with $0 \leq a \leq 1$. In our case we have chosen $a = 0.5$ (this value makes T_{r1} and T_{r2} coincident with those temperatures at which $|\Delta S_M| = |\Delta S_M{}^{max}|/2$ [37]). The master curves for the three compounds are plotted in Fig. 7 (a, b and c), and it can be observed how the $\Delta S_M/\Delta S_M{}^{max}$ vs. θ curves for different magnetic field changes almost collapse into a unique one for each compound.

Moreover, it can be shown that if the curves corresponding to the three alloys are plotted altogether (see Fig. 7d) they overlap for positive values of the rescaled temperature θ, i.e. in the paramagnetic phase ($T > T_C$), while slight differences are observed for $\theta < 0$, i.e. within their ordered magnetic phases ($T < T_C$).

4. Summary and conclusions

The crystal structure of the $Y_{1.2}Ce_{0.8}Fe_{17}$, $Pr_{1.5}Ce_{0.5}Fe_{17}$ and $Dy_{1.15}Ce_{0.85}Fe_{17}$ pseudo-binary intermetallic compounds is rhombohedral with a space group $R\bar{3}m$. The values of the Curie temperature are between 253 and 273 K, and can be tuned by small changes in the composition, therefore, it is possible to select the temperature for the maximum of $|\Delta S_M|$ as well. The Pr containing compound exhibits the higher magnetization value due to the collinear parallel configuration of both Fe and Pr sublattice magnetic moments, while the lower magnetization value measured in the other two alloys is attributed to the zero contribution of Y to the net magnetization and the collinear antiparallel (ferrimagnetic) configuration of Dy and Fe sublattices, respectively. The latter explains the observed differences in the value of the maximum magnetic entropy change, although the temperature dependence of the $|\Delta S_M|$ is analogous in the three compounds. In addition, the use of the rescaled temperature gives rise to a master curve for the magnetic entropy and allows the extrapolation of the $|\Delta S_M|$ (T) curves for different values of the applied magnetic field change, as well as for the estimation of $|\Delta S_M|$ (T) curves in other intermetallic compounds with related compositions, in which the rare earth metal and/or the relative amount is varied.

Acknowledgments

We thank Spanish MICINN and FEDER programme for financial support through the research project MAT2008-06542-C04-03 and the Slovak grant agency VEGA 2/0007/09. P.A. is grateful to FICyT for Ph.D. contract. The Slovak Research and Development Agency under the contract No. VVCE-0058-07, the CLTP as the Centre of Excellence SAS and P.J. Šafárik University, the CEX Nanofluid as the Centre of Excelence SAS, the 7.FP EU—MICROKELVIN and the SCTs at the University of Oviedo are also acknowledged. The liquid nitrogen for the experiment has been sponsored by the U.S. Steel Kosice, s.r.o.

References

[1] Buschow KHJ. Rep Prog Phys 1977;40:1179.
[2] Buschow KHJ. Rep Prog Phys 1991;54:1123.
[3] Isnard O, Miraglia S, Soubeyroux JL, Fruchart D, Stergiou A. J Less-Comm Met 1990;162:273.
[4] Isnard O, Miraglia S, Kolbeck C, Tomey E, Soubeyroux JL, Fruchart D, et al. J Alloys Comp 1992;178:15.
[5] Coey JMD. Rare-Earth iron permanent magnets. Oxford University Press; 1996.
[6] Mandal K, Yan A, Kerschl P, Handstein A, Gutfleisch O, Muller K. J Phys D Appl Phys 2004;37:2628.
[7] Gorria P, Sánchez Llamazares JL, Álvarez P, Sánchez Marcos J, Pérez MJ, Blanco JA. J Phys D Appl Phys 2008;41:192003.
[8] Álvarez P, Gorria P, Franco V, Sánchez Marcos J, Pérez MJ, Sánchez Llamazares JL, et al. J Phys Condens Matter 2010;22:216005.
[9] Chen H, Zhang Y, Han J, Du H, Wang C, Yang Y. J Magn Magn Mater 2008;320:1382.
[10] Tishin AM, Spichkin YI. The Magnetocaloric effect and its applications. Bristol: IoP; 2003.
[11] Arnold Z, Kamarad J, Algarabel PA, Garcia-Landa B, Ibarra MR. IEEE Trans Mag 1994;30:619.
[12] Givord D, Lemaire R. IEEE Trans Mag 1974;10:109.
[13] Gorria P, Álvarez P, Sánchez Marcos J, Sánchez Llamazares JL, Pérez MJ, Blanco JA. Acta Mater 2009;57:1724.
[14] Andreev AV, Lindbaum A. J Alloys Compd 2000;297:43.
[15] Iwasieczko W, Kuchin AG, Drulis H. J Alloys Comp 2005;392:44.
[16] Prokhnenko O, Ritter C, Arnold Z, Isnard O, Kamarád J, Pirogov A, et al. J Appl Phys 2002;92:385.
[17] Janssen Y, Chang S, Kreyssig A, Kracher A, Mozharivskyj Y, Misra S, et al. Phys Rev B 2007;76:054420.
[18] Janssen Y, Fujii H, Ekino T, Izawa K, Suzuki T, Fujita T, et al. Phys Rev B 1997;56:13716.
[19] Isnard O, Miraglia S, Giorgetti C, Dartyge E, Krill G, Fruchart D. J Alloys Comp 1997;262:198.
[20] Coey JMD, Allan JEM, Minakov AA, Bugaslavsky YV. J Appl Phys 1993;73:5430.
[21] Tereshina I, Nikitin S, Suski W, Stepien-Damm J, Iwasieczko W, Drulis H, et al. J Alloys Comp 2005;404-406:172.
[22] Kajitani T, Morii Y, Iriyama T, Kato H. Physica B 1994;213:294.
[23] Kamaraju K, Yang JB, Yelon WB, Pringle OA, James WJ, Cai Q, et al. J Appl Phys 2003;93:6936.
[24] Ben Kraiem MS, Ellouze M, Cheikhrouhou A, L'Heritier P. J Magn Magn Mater 2003;256:262.
[25] Jin S, Liu L, Wang Y, Chen B. J Appl Phys 1991;70:6275.
[26] Xiao Y, Rao G, Zhang Q, Liu G, Zhang Y, Liang J. J Alloys Comp 2006;419:15.
[27] Rodríguez-Carvajal J. Physica B 1992;192:55.
[28] Gschneidner KA, Pecharsky VK, Tsokol AO. Rep Prog Phts 2005;68:1479.
[29] Lyubina J, Kuz'min MD, Nenkov K, Gutfleisch O, Richter M, Schlagel DL, et al. Phys Rev B 2011;83:012403.
[30] Johnson Q, Wood DH, Smith GS, Ray AE. Acta Cryst 1968;B24:274.
[31] Buschow KHJ, van Wieringen JS. Phys Stat Sol 1970;42:231.
[32] Tanaka T, Miyatani K. J Appl Phys 1997;82:5658.
[33] Cullity BD. Introduction to magnetic materials. Reading, MA: Addison-Wesley; 1972.
[34] Álvarez P, Gorria P, Sánchez Marcos J, Fernández Barquín L, Blanco JA. Intermetallics 2010;18:2464.
[35] Franco V, Conde A, Provenzano V, Shull R. J Magn Magn Mater 2010;322:218.
[36] Franco V, Caballero-Flores R, Conde A, Dong Q, Zhang H. J Magn Magn Mater 2009;321:1115.
[37] Álvarez P, Sánchez Marcos J, Gorria P, Fernández Barquín L, Blanco JA. J Alloys Comp 2010;504S:S150.

Magneto-caloric effect in the pseudo-binary intermetallic $YPrFe_{17}$ compound

Pablo Álvarez[a], Pedro Gorria[a,*], José L. Sánchez Llamazares[b], María J. Pérez[a], Victorino Franco[c], Marian Reiffers[d], Jozef Kováč[d], Inés Puente-Orench[e], Jesús A. Blanco[a].

[a]*Departamento de Física, Universidad de Oviedo, Calvo Sotelo, s/n, 33007 Oviedo, Spain*

[b]*División de Materiales Avanzados, Instituto Potosino de Investigación Científica y Tecnológica, Camino a la presa San José 2055, CP 78216, San Luis Potosí, Mexico.*

[c]*Departamento de Física de la Materia Condensada, ICMSE-CSIC, Universidad de Sevilla, P.O. Box 1065, 41080 Sevilla, Spain*

[d]*Institute of Experimental Physics, Watsonova 47, SK-04001 Košice, Slovakia.*

[e]*Institute Laue Langevin, 6 rue Jules Horowitz, 38042 Grenoble, France*

*E-mail: pgorria@uniovi.es

Abstract. We have synthesized the intermetallic $YPrFe_{17}$ compound by arc-melting. X-ray and neutron powder diffraction show that the crystal structure is rhombohedral with space group $R\bar{3}m$ (Th_2Zn_{17}-type). The investigated compound exhibits a broad magnetic entropy change $\Delta S_M(T)$ associated with the ferro-to-paramagnetic phase transition ($T_C \approx 290$ K). The isothermal $|\Delta S_M|$ (≈ 2.3 J kg^{-1} K^{-1}) and the relative cooling power (≈ 100 J kg^{-1}) have been calculated for applied magnetic field changes up to 1.5 T. A single master curve for ΔS_M under different values of the magnetic field change can be obtained by a rescaling of the temperature axis. The results are compared and discussed in terms of the magneto-caloric effect in the isostructural R_2Fe_{17} (R = Y, Pr and Nd) binary intermetallic alloys.

Keywords: A. Magnetically ordered materials; C. Crystal structure and symmetry; D. Magneto-caloric effect; E. Magnetic measurements

1. Introduction

The magneto-caloric effect (MCE) is nowadays a subject of considerable current research interest [1-3] motivated by the enhanced performance (efficiency, mechanical vibration, size, etc) and reduced environmental impact of refrigeration systems based on this effect compared with those of the existing vapour-compression gas technology [4]. In this way, diverse types of compounds have been investigated until now with the aim of scrutinizing both the intensity and the temperature range for the MCE [3, 5-7]. A magnetic material must exhibit a large magnetization change, ΔM, around its magnetic phase transition in order to display a large MCE response. From the point of view of the implementation of these materials in magnetic refrigeration systems, another important parameter is the relative cooling power (*RCP*) [8,9], which gives a figure of merit of how much heat could be transferred between the hot and cold reservoirs by the magnetic refrigerant in an ideal thermodynamic cycle. For materials with second-order phase transition the peak value of the magnetic entropy change $\left|\Delta S_M^{peak}\right|$ is smaller than that observed in materials with first-order magnetic phase transitions [1,2]. Nevertheless the lack of magnetic field hysteresis and the larger operation temperature range in materials displaying a second-order magnetic phase transition give commonly rise to higher *RCP* values [9-11]. Therefore, a compromise between the magnitude of the magnetic entropy change and the *RCP* is mandatory for employing a magnetic material in magnetic refrigeration applications. Mostly of the current prototypes for room temperature magnetic refrigeration employ rare-earth-based materials (with the rare-earth being mainly Gd)

[2,12]. However, some Fe-rich R_2Fe_{17} (R = Rare Earth) compounds have shown values of *RCP* comparable with those of Gd-based magnetic materials together with a lower cost of the main component (Fe), easy fabrication procedures and absence of disadvantageous hysteresis effects [13,14]. Within the whole R_2Fe_{17} series the alloys with R = Y, Pr or Nd have the largest magnetic moment per formula unit, and therefore the higher $|\Delta S_M^{peak}|$ value [15], due to the collinear ferromagnetic order, and also magnetic ordering temperatures, T_C, around 300 K. These facts make them suitable for their use in magnetic refrigeration as active magnetic regenerative systems operating around room temperature [16]. Moreover, the value of T_C in this 2:17 type of compounds can be tuned by mixing two rare earth elements (i.e. in the form $R_{2-x}R'_xFe_{17}$) [17], or by partial substitution of Fe other 3d-atom [18]. The crystal structure of the binary intermetallic R_2Fe_{17} compounds can be either of Th_2Zn_{17}-type (rhombohedral $R\bar{3}m$ space group) for light rare-earths, or Th_2Ni_{17}-type (hexagonal $P6_3mmc$ space group) for heavy rare-earths [19,20]. In the case of R = Y, Gd and Tb or in pseudo-binary intermetallic $R_{2-x}R'_xFe_{17}$ alloys with a mixture of two different R atoms, both crystal structures can coexist, with the rare-earths sharing the crystallographic sites [21-24].

In the present work we have studied the crystal structure of a new pseudo-binary intermetallic $YPrFe_{17}$ alloy by means of neutron and x-ray powder diffraction, together with its magnetic properties and the magneto-caloric effect up to a maximum applied magnetic field change of $\mu_0\Delta H$ = 1.5 T. The experimental results are compared with those measured in binary Y_2Fe_{17}, Pr_2Fe_{17} and Nd_2Fe_{17}.

2. Experimental details and data analysis

As-cast ingots with $YPrFe_{17}$ nominal composition were prepared from 99.99% pure elements (relative to rare earth content in the case of Pr) by standard arc-melting technique under a controlled Ar atmosphere. The polycrystalline as-cast pellets were sealed under vacuum in quartz ampoules and further annealed during one week at 1263 K. After finishing the heat treatment the samples were quenched directly in water. Crystal structure was determined at room temperature (T = 290 K) by both x-ray (XRD) and neutron powder diffraction (ND). XRD studies were performed in a high-resolution x-ray powder diffractometer (Seifert model XRD3000) operating in Bragg-Bentano geometry. The scans in 2θ were performed between 2 and 160º with 0.02º steps and counting times of 20 s per point using $Cu\ K_\alpha$ radiation (λ = 1.5418 Å). The ND pattern was collected on the high-intensity D1B two-axis powder diffractometer at the ILL (Grenoble) with a neutron wavelength of λ = 2.52 Å, 2 hours of acquisition time and an angular range of 80º in 2θ (in steps of 0.2º). The full-profile analysis of the diffraction patterns was carried out with the FullProf suite package [25], and no peak broadening due to small crystal and/or microstrain effects [26] were detected.

The low-magnetic field magnetization as a function of temperature $M(T)$ curves were recorded in a Faraday susceptometer under a heating rate of 2 K/min. Isothermal magnetization curves, $M(H)$, were measured with a Lakeshore model 7407 VSM vibrating sample magnetometer in the temperature range between 90 and 450 K with a maximum applied magnetic field of 1.5 T, and in a Quantum Design MPMS-5T magnetometer in the temperature range 90 – 390 K with applied magnetic fields up to 5 T. At each temperature the magnetization was measured for a large number selected values of the applied magnetic field (≈ 150 for the VSM measurements and 50 for the MPMS) with the aim of gaining accuracy in the estimation of the isothermal magnetic entropy change, $|\Delta S_M|$. The value of $|\Delta S_M|$ at each temperature T due to a change of the applied magnetic field from H = 0 to $H = H_{max}$ were calculated using the Maxwell relation [8]:

$$\Delta S_M(T,H) = S_M(T,H) - S_M(T,0) = \int_0^H \left(\frac{\partial M(T',H')}{\partial T'}\right)_{T'=T} dH' \quad (1)$$

After applying this procedure to the whole set of $M(H)$ curves the value of $|\Delta S_M|$ for a given applied magnetic field change and at a selected temperature is obtained by numerical approximation of eq. 1, where the partial derivative is replaced by finite differences and then the integral is calculated by means of numerical methods [6,9]. In addition, the relative cooling power (*RCP*) has been calculated using three different criteria (see reference [9] for details): *RCP*-1(H) = $|\Delta S_M^{max}|(H) \times \delta T_{FWHM}(H)$, where δT_{FWHM} is the full width at half maximum of $|\Delta S_M|(T)$ curve; *RCP*-2 is the area below $|\Delta S_M|(T)$ curve in the temperature range between T-δT_{FWHM} and T+δT_{FWHM}; and *RCP*-3 is the maximum value of the product $|\Delta S_M| \times \Delta T$ below the $|\Delta S_M(T)|$ curve.

3. Results and discussion

In Fig. 1 the room temperature x-ray (upper panel) and neutron (bottom panel) powder diffraction patterns of the $YPrFe_{17}$ sample are shown.

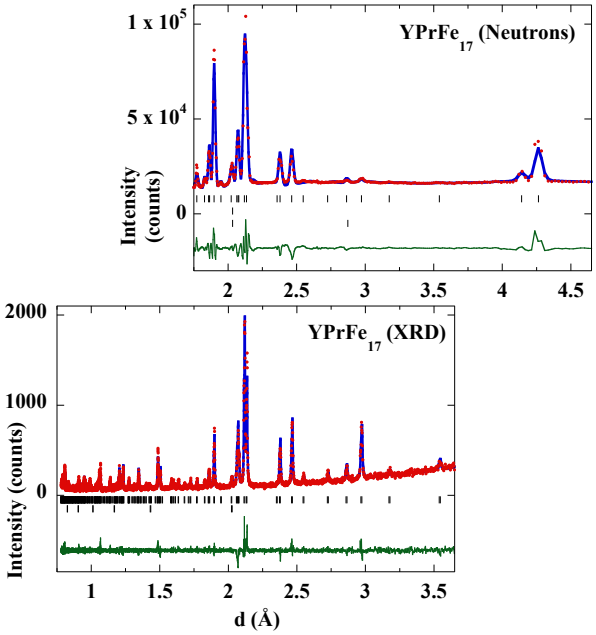

Fig. 1. Observed (dots) and calculated (solid line) powder diffraction patterns for $YPrFe_{17}$ alloy collected at T = 300 K. Positions of the Bragg reflections are represented by vertical bars; the first row corresponds to the rhombohedral Th_2Zn_{17}–type phase while the second one is associated with an α-Fe impurity (< 3%). The observed–calculated difference is depicted at the bottom of each figure.

Both XRD and neutron diffraction patterns have been refined by using the Rietveld method in multi-pattern mode (see [25] for further technical details). The observed intensity peaks can be indexed as the Bragg reflections corresponding to a rhombohedral Th_2Zn_{17}-type crystal structure with $R\bar{3}m$ space group (#164), and if the hexagonal setting is chosen the lattice parameters are: a = 8.540 (1) Å and c = 12.419 (1) Å. No traces of the hexagonal Th_2Ni_{17}-type crystal structure have been found, as confirmed by neutron diffraction from which information of the whole sample is attained, in contrast with XRD. Whereas in other 2:17 pseudo-binary alloys of this family a disordered rhombohedral structure has been proposed in order to explain the strong intensity reduction observed for many reflexions [27,28], in the present case there is no such a reduction, even though when compared with the diffraction patterns of the binary Y_2Fe_{17}, Pr_2Fe_{17} or Nd_2Fe_{17} alloys [13,29]. From the fit of the diffraction patterns it is evident that the 6c site corresponding to the R atoms is equally shared between Y and Pr with the same atomic coordinates. The values for the

main crystallographic parameters are given in Table I. The values for the cell parameters are, as it could be expected, between those of the Y_2Fe_{17} and Pr_2Fe_{17} (a = 8.46 Å, c = 12.39 Å and a = 8.585 Å; c = 12.464 Å, respectively) [13,20,30]. The ratio c/a ~ 1.54 is in good agreement with those reported for the rhombohedral crystal structure in these 2:17-type alloys [13,29,30].

In order to estimate the Curie temperature of the sample, the magnetization vs. temperature, $M(T)$, curve under a low applied magnetic field $\mu_0 H$ = 5 mT (not shown) has been measured. Thereafter, the value of T_C has been taken as the minimum of the dM/dT vs. T curve, which is a commonly adopted criterion [13,24,29]. In this way, T_C = 291 ± 5 K for $YPrFe_{17}$, which is in between those reported values for Pr_2Fe_{17} (T_C = 286 ± 2 K [13]), and for Y_2Fe_{17} (T_C = 301 ± 4 K [15]). Therefore, it seems that by mixing Y and Pr the Curie temperature of the resulting pseudo-binary alloy can be tuned between those values of the pure binary compounds.

Fig. 2 shows a 3D surface plot representing simultaneously the temperature and magnetic field dependences of the magnetization, $M(H,T)$ for $YPrFe_{17}$ alloy.

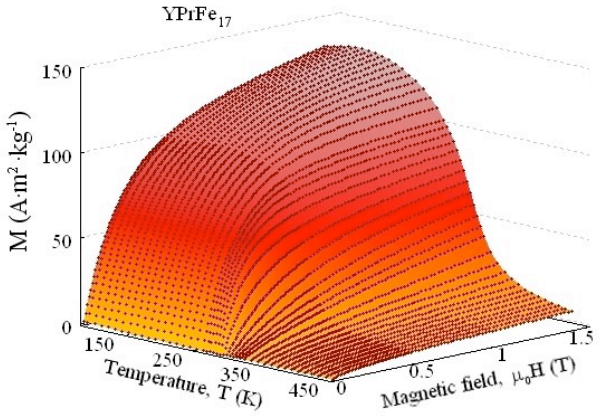

Fig. 2. 3D surface corresponding to the temperature and applied magnetic field dependences for the magnetization of the $YPrFe_{17}$ compound.

The isothermal magnetic entropy change, $|\Delta S_M|$ has been calculated from the set of isothermal magnetization vs. applied magnetic field, $M(H)$, curves depicted in Fig. 2 and following the procedure explained in the previous section. In Fig. 3 the temperature dependence of $|\Delta S_M|$ for the maximum applied magnetic field change, from 0 to $\mu_0 H_{max}$ = 1.5 T is shown. In addition, data for Y_2Fe_{17}, Pr_2Fe_{17} and Nd_2Fe_{17} binary intermetallic compounds with the same rhombohedral Th_2Zn_{17}-type crystal structure are also shown for comparison. The maximum value for the magnetic entropy change, $\left|\Delta S_M^{peak}\right|$, for the $YPrFe_{17}$ compound is 2.3 J kg^{-1} K^{-1}, which is just in between those values for the binary Pr_2Fe_{17} (2.6 J K^{-1} kg^{-1}) and Y_2Fe_{17} (1.9 J K^{-1} kg^{-1}) alloys. The latter can be understood taking into account that $\left|\Delta S_M^{peak}\right|$ is roughly proportional to the magnetization change of the alloy across the second order ferro- to paramagnetic phase transition. In the case of Pr_2Fe_{17}, the magnetic moments of Pr and Fe sublattices are parallel to each other, hence, the contribution of Pr atoms (≈ 3 μ_B/Pr atom [31]) to the net magnetization of the alloy is additive, while in the case of Y_2Fe_{17}, Yttrium atoms do not carry any magnetic moment, and the net magnetization of the alloys comes exclusively from the Fe sublattice. Assuming that: (i) the Fe atoms possess the same values for the magnetic moment in Pr_2Fe_{17}, $YPrFe_{17}$ and Y_2Fe_{17} alloys; (ii) the $M(T)$ curves show a very similar trend for the three alloys; and (iii) the Pr^{+3} ions in $YPrFe_{17}$ have their magnetic moments parallel to those of Fe atoms, we could expect that the substitution of half of the Pr^{+3} ions by Y ones should give rise to a decrease in the magnetic entropy change, respect to that of Pr_2Fe_{17}, down to an approximate value given by: $\left|\Delta S_M\right|_{Y\,Pr\,Fe_{17}} \approx \frac{1}{2}\left(\left|\Delta S_M\right|_{Pr_2\,Fe_{17}} + \left|\Delta S_M\right|_{Y_2Fe_{17}}\right)$.

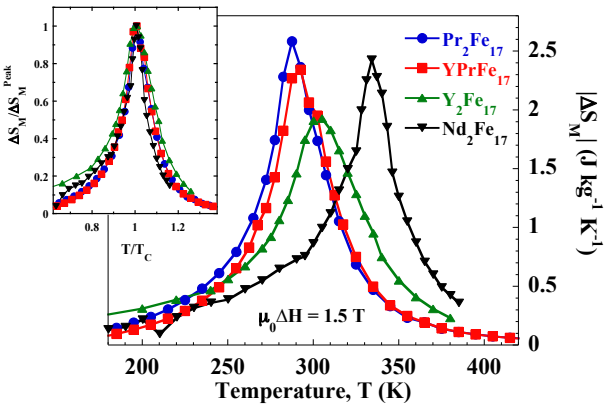

Fig. 3. Temperature dependence of the magnetic entropy change in the pseudo-binary $YPrFe_{17}$ compound around the $|\Delta S_M|$ peak for an applied magnetic field change $\mu_0\Delta H$ = 1.5 T. Data for binary R_2Fe_{17} (R = Y, Pr and Nd) are also shown for comparison. The lines connecting the calculated points are guides for the eyes. Inset: Normalized $\Delta S_M/\Delta S_M^{Peak}$ vs. T/T_C for the four intermetallic alloys.

We summarize in table 2 the values for T_C, $|\Delta S_M|$ (peak value for $\mu_0\Delta H$ = 1.5 T) together with the *RCP* estimated by using the three criteria previously defined. It is worth noting that although Y_2Fe_{17} exhibits the lowest $|\Delta S_M|$ the *RCP* -1 is the highest due to a broader $|\Delta S_M|(T)$ peak as it can be observed in the inset of Fig. 3, where $|\Delta S_M|$ vs. the reduced temperature T/T_C is plotted.

In Fig. 4 the magnetic field dependence of the *RCP* for $YPrFe_{17}$ is depicted. From a linear fit of the *RCP* (*H*) curves for $\mu_0 H > 1$ T, we have extrapolated the values for an applied magnetic field change of 2 T in order to compare with available date for Gd (see table 2), which is the archetypical magento-caloric material with second order magnetic phase transitions.

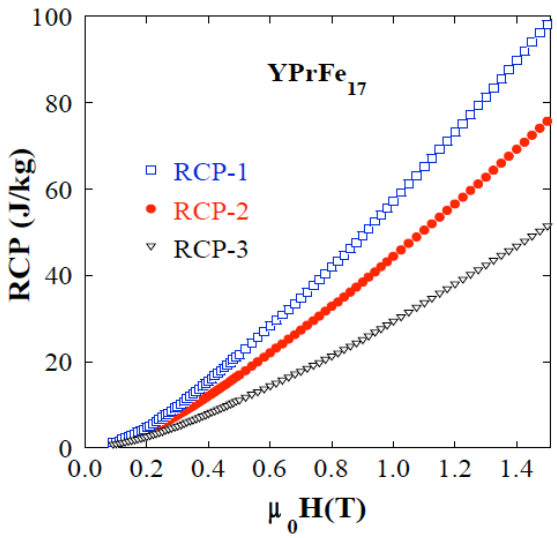

Figure 4. Magnetic field dependence of the Relative Cooling Power (*RCP*). See text for details.

The pseudo-binary $YPrFe_{17}$ alloy exhibits *RCP* values comparable to those of the R_2Fe_{17} compounds with R = Y, Pr or Nd), and both *RCP* -1 and *RCP* -2 are ca. 75 % of those for pure Gd [32].

Moreover, it has been proposed that $|\Delta S_M|(T)$ curves for different magnetic field changes can collapse into a single master curve, after an appropriate normalization, in ferromagnetic materials exhibiting a second order magnetic phase transition [33]. The master curve is obtained as follow [34]: firstly, the $|\Delta S_M|(T)$ curves are normalized to its maximum value $|\Delta S_M^{max}|$ for each value of the applied magnetic field change. Secondly, the temperature axis is rescaled

using two different reference temperatures:

$$\theta = -(T - T_C)/(T_{r1} - T_C) \qquad T < T_C \tag{2}$$

$$\theta = (T - T_C)/(T_{r2} - T_C) \qquad T > T_C \tag{3}$$

where T_{r1} and T_{r2} are the temperatures at which $|\Delta S_M| = a \times |\Delta S_M^{Peak}|$, with $0 \leq a \leq 1$. In our case we have chosen $a = 0.5$ (this value makes T_{r1} and T_{r2} coincident with those temperatures at which $|\Delta S_M| = |\Delta S_M^{Peak}|/2$ [34]). The master curves for the $YPrFe_{17}$ compounds are shown in Fig. 5, and it can be observed how the $\Delta S_M/\Delta S_M^{Peak}$ vs. θ curves for different magnetic field values almost collapse into a unique one for each compound.

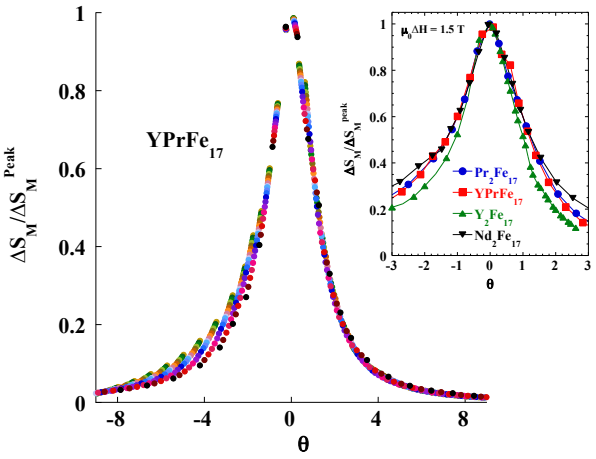

Fig. 5. Normalized $|\Delta S_M|$ vs. reduced temperature for the pseudo-binary $YPrFe_{17}$ compound. The inset shows the comparison with the curves for the binary Y_2Fe_{17}, Pr_2Fe_{17} and Nd_2Fe_{17} for an applied magnetic field $\mu_0 H = 1.5$ T.

Moreover, it can be shown that if the $\Delta S_M/\Delta S_M^{Peak}$ vs. θ curve for $YPrFe_{17}$ compound, corresponding to $\mu_0 \Delta H = 1.5$ T, is compared with those for the binary R_2Fe_{17} alloys (R = Y, Pr, Nd, see inset in Fig. 5), the curves almost overlap in the range $-1 \leq \theta \leq 1$ (for temperatures between T_{r1} and T_{r2}), thus suggesting that in these compounds the temperature dependence of the magnetic entropy change exhibits a similar trend [35]. From a practical point of view, the building of such a master curve can be considered as an useful tool for extrapolating the $|\Delta S_M|(H,T)$ curves for temperature and/or applied magnetic field values different from those available in the laboratory [36]. On the other hand, it also could help in detecting and studying, from a more fundamental viewpoint, different co-existing magnetic phenomena [37].

Summary and conclusions

The magnetic properties and the magneto-caloric effect in the pseudo-binary $YPrFe_{17}$ alloy have been studied. Room temperature x-ray and neutron powder diffraction confirm that the compound crystallizes into the ordered Th_2Zn_{17}-type rhombohedral crystal structure. The magnetic entropy change has been obtained by the isothermal magnetic measurements, showing that the introduction of the non-magnetic Y atoms leads to a shift of the temperature where the maximum of $|\Delta S_M|$ is obtained with a small reduction of the peak value. The calculated values for the *RCP* in $YPrFe_{17}$ can reach 75 % of the pure Gd, Therefore, we could expect that an adequate mixture of Pr or Nd with Y in R_2Fe_{17} compounds allows us tuning the Curie temperature around room temperature (between 285 and 340 K) with almost similar values for the *RCP*. Therefore, $(YPrNd)_2Fe_{17}$ compounds are potential candidates for its use in magnetic refrigeration. Finally, the magnetic entropy change for several magnetic fields can be represented using a master curve representation for all these alloys.

Acknowledgments

We thank Spanish MICINN and FEDER programme for financial support through the research project MAT2008-06542-C04-03 and the Slovak grant agency VEGA 2/0007/09. P.A. is grateful to FICyT for Ph.D. contract. The Slovak Research and Development Agency (contract No. VVCE-0058-07), the CLTP as the Centre of Excellence SAS and P.J. Šafárik University, the CEX Nanofluid as the Centre of Excelence SAS, the 7.FP EU–MICROKELVIN and the SCT's at the University of Oviedo (XRD measurements) are also acknowledged. We also thank ILL and Spanish CRG-D1B for allocating neutron beam time.

References

[1] O. Tegus, E. Brück, K.H.J. Buschow, F.R. de Boer, Nature (London) 415 (2002) 150.
[2] K.A. Gschneidner Jr., V.K. Pecharsky, A.O. Tsokol, Rep. Prog. Phys. 68 (2005) 1479.
[3] E. Brück, J. Phys. D: Appl. Phys. 38 (2005) R381.
[4] V.K. Pecharsky, K.A. Gschneidner Jr., J. Magn. Magn. Mater. 200 (1999) 44.
[5] N. Kervan, S. Kervan, H. Sözeri, A. Gencer, Mater. Chem. Phys. 116 (2009) 586.
[6] P. Álvarez, P. Gorria, J. Sánchez Marcos, L. Fernández Barquín, J.A. Blanco, Intermetallics 18 (2010) 2464.
[7] Q.Y. Donga, B.G. Shen, J. Chen, J. Shen, J.R. Sun, Solid State Commun. 151 (2011) 112.
[8] M. Wood, W. Potter, Cryogenics, 25, (1985) 667.
[9] P. Gorria, J.L. Sánchez Llamazares, P. Álvarez, M.J. Pérez, J. Sánchez Marcos, J.A. Blanco, J. Phys. D: Appl. Phys. 41 (2008) 192003.
[10] R. Caballero-Flores, V. Franco, A. Conde, K.E. Knipling, M.A. Willard, Appl. Phys. Lett. 98 (2011) 102505.
[11] J.L. Zhao, J. Shen, B.G. Shen, F.X. Hu, J.R. Sun, Solid State Commun. 150 (2010) 2329.
[12] K.A. Gschneidner Jr., V.K. Pecharsky, A. Pecharsky, C. Zimm, Mater Sci Forum 315-317, (1999) 69.
[13] P. Gorria, P. Álvarez, J. Sánchez Marcos, J.L. Sánchez Llamazares, M.J. Pérez, J.A. Blanco, Acta Mater. 57, (2009) 1724.
[14] J.S. Llamazares, M. Pérez, P. Álvarez, J.D. Santos, M.L. Sánchez, B. Hernando, J.A. Blanco, J. Sánchez Marcos, P. Gorria, J. Alloys Compd. 483 (2009) 682.
[15] K. Mandal, A. Yan, P. Kerschl, A. Handstein, O. Gutfleisch, K-.H. Müller, J. Phys. D: Appl. Phys. 37 (2004) 2628.
[16] F. Shir, L. Yanik, L.H. Bennett, E. Della Torre, R.D. Shull, J. Appl. Phys. 93 (2003) 8295.
[17] M.B. Kraiem, A. Cheikhrouhou, J. Alloys Compd. 397 (2005) 37.
[18] A.G. Kuchin, W. Iwasieczko, Solid State Commun. 150 (2010) 1580.
[19] Q. Johnson, D.H. Wood, G.S. Smith, A.E. Ray, Acta Crystallogr. B24 (1968) 274.
[20] K.H.J. Buschow, Rep. Prog. Phys. 40 (1977) 1179.
[21] G. Marasinghe, W. Priyantha, K. Kamaraju, W. James, W. Yelon, I. Dubenko, P. Hill, N. Ali, M. Ellouze, P. l'Heritier, IEEE Trans. Magn. 37 (2001) 2599
[22] Y. Xiao, G. Rao, Q. Zhang, G. Liu, Y. Zhang, J. Liang, J. Alloys Compd. 407 (2006) 1.
[23] Y. Xiao, G. Rao, Q. Zhang, G. Liu, Y. Zhang, J. Liang, J. Alloys Compd. 419 (2006) 15.
[24] P. Álvarez, P. Gorria, J.L. Sánchez Llamazares, M.J. Pérez, V. Franco, M. Reiffers, I. Čurlik, E. Gažo, J. Kováč, J.A. Blanco, Intermetallics 19 (2011) (10.1016/j.intermet.2011.02.020).
[25] J. Rodríguez-Carvajal, Physica B 192 (1993) 55.
[26] D. Martínez-Blanco, P. Gorria, J.A. Blanco, M.J. Pérez, J. Campo, J. Phys.: Condens. Matter 20 (2008) 335313.
[27] W.B. Yelon, W. J. James, J.B. Yang, K. Kamaraju, Q. Cai, Z. Chu, S.K. Malik, J. Appl. Phys. 91 (2002) 8486.
[28] K. Kamaraju, J.B. Yang, W.B. Yelon, O.A. Pringle, W.J. James, Q. Cai, Z. Chu, P. I'Heritier, J. Appl. Phys. 93 (2003) 6936.
[29] P. Álvarez, P. Gorria, V. Franco, J. Sánchez Marcos, M.J. Pérez, J.L. Sánchez Llamazares, I. Puente Orench, J.A. Blanco, J. Phys.: Condens. Matter 22 (2010) 216005.
[30] Q. Johnson, G.S. Smith, D.H. Wood, Acta Crystallogr. B25, (1969) 464.
[31] O. Isnard, S. Miraglia, J.L. Soubeyroux, D. Fruchart, Solid State Commun. 81 (1992) 13.
[32] S.Y. Dan'kov, A.M. Tishin, V.K. Pecharsky, K.A. Gschneidner, Phys. Rev. B 57, 3478 (1998).
[33] V. Franco, J.S. Blázquez, A. Conde, Appl. Phys. Lett. 89 (2006) 222512.
[34] V. Franco, C.F. Conde, J.S. Blázquez, M. Millán, A. Conde, J. Appl. Phys. 102 (2007) 013908.
[35] V. Franco, A. Conde, International J. Refrig. 33 (2010) 465.
[36] V. Franco, J.S. Blázquez, M. Millán, J.M. Borrego, C.F. Conde, A. Conde, J. Appl. Phys. 101 (2007) 09C503.
[37] P. Álvarez, J.S. Marcos, P. Gorria, L. Fernández Barquín, J.A. Blanco, J. Alloys Compd. 504 (2010) S150.

Table 1. Table I. Crystallographic parameters, cell volume and atomic coordinates of the studied R_2Fe_{17} ($R\bar{3}m$) compounds obtained from the both NPD and XRD patterns in multi-pattern fit.

a (Å)	8.540 (1)
c (Å)	12.419 (1)
c/a	1.454
V (Å^3)	784.3 (2)
Pr/Y (6c)	
z	0.348 (3)
Fe1 (6c)	
z	0.092 (1)
Fe3 (18f)	
x	0.293 (1)
Fe4 (18h)	
x	0.169 (2)
z	0.489 (1)
R_B	5.7
χ^2 (%)	1.5

Table 2. Curie temperature, T_C, magnetic entropy change, $|\Delta S_M|$ and relative cooling power, *RCP*, obtained from the three methods (see text). Extrapolated values of *RCP* for a magnetic field change $\mu_0\Delta H$ = 2 T are compared with those for Gd taken from Ref. [32].

Alloy	$YPrFe_{17}$	Pr_2Fe_{17}	Y_2Fe_{17}	Nd_2Fe_{17}	Gd
$\boldsymbol{T_C}$ (K)	290(5)	286(2)	303(4)	339(2)	291(2)
$\boldsymbol{\lvert\Delta S_M\rvert}$ **(1.5 T)** (J·kg^{-1}·K^{-1})	2.3	2.6	1.9	2.5	---
T_{r1} (K)	269	268	278	314	---
T_{r2} (K)	312	308	334	349	---
RCP-1 **(1.5 T)** (J kg^{-1})	98	101	112	85	---
RCP-2 **(1.5 T)** (J kg^{-1})	75	78	86	64	---
RCP-3 **(1.5 T)** (J kg^{-1})	51	55	56	57	---
RCP-1 **(2 T)** (J kg^{-1})	145	156	155	133	200
RCP-2 **(2 T)** (J kg^{-1})	111	116	121	98	147
RCP-3 **(2 T)** (J kg^{-1})	77	81	82	81	135

Chapter 5

Magnetic properties and magnetocaloric effect of Fe-based amorphous alloys

5.1 Summary

In sake of completeness of the study of Fe-rich magnetic materials presenting a MCE close to room temperature, a series of FeZrBCu amorphous ribbons was studied. Those metallic glasses exhibit a ferro-to-paramagnetic phase transition in the vicinity of room temperature, which makes them interesting from the point of view of applications as magnetic refrigerators. Also their geometry is optimum for applications like AMR systems.

Seven different compositions with Curie temperatures ranging from 210 to 320 K were chosen (see table 5.1). Measurements were performed with two clear aims: the first one was to obtain general information about the magnetic properties and the MCE behavior with the applied magnetic field and the temperature, for both single ribbons and two-ribbon systems. The other main objective was to investigate the possible existence of common features in the $\Delta S_M\,(T, H)$ curves of these metallic glasses which would allows us to discuss the existence of a master curve behavior.

Curie temperature of these metallic glasses increases in the range 200-350 K almost linearly with the decrease of the Fe atomic percentage, being nearly independent of the relative amount of Zr and B (see article I). This is an interesting feature for refrigeration purposes at room temperature, as it has been pointed out in chapter 4. The temperature dependence of the $|\Delta S_M|$ under applied fields up to 8 T for all the samples are plotted in fig. 5.1. Peak values are low when compared with those of the ferromagnetic Pr_2Fe_{17} and Nd_2Fe_{17} bulk and ball-milled alloys. The reason is twofold: the low saturation magnetization together with a broad ferro-to-paramagnetic phase transition, as it has been pointed out in article I.
Nevertheless, the full width at half maximum spreads over 210 K (in the case of $Fe_{87}Zr_6B_6Cu_1$ it cannot be figured out because of the available measurement temperature regime, but it can be estimated to be at least 220 K). This huge spreading gives rise to large RCP values, which are

Table 5.1: Main magnetocaloric characteristics of FeZrBCu amorphous ribbons studied in the present work.

Composition	$T_C(K)$	$(-\Delta S_M)^{Peak}$ (Jkg^{-1}K^{-1})			RCP_1 (Jkg^{-1})		
		$\mu_0 H = 1.5\,\mathrm{T}$	$\mu_0 H = 5\,\mathrm{T}$	$\mu_0 H = 8\,\mathrm{T}$	$\mu_0 H = 1.5\,\mathrm{T}$	$\mu_0 H = 5\,\mathrm{T}$	$\mu_0 H = 8\,\mathrm{T}$
$Fe_{90}Zr_{10}$	230	1.0	2.7	3.9	142	497	801
$Fe_{90}Zr_9B_1$	209	1.0	2.7	3.8	145	492	795
$Fe_{91}Zr_7B_2$	216	0.9	2.5	3.6	132	462	755
$Fe_{90}Zr_8B_2$	240	1.0	2.6	3.7	156	514	830
$Fe_{88}Zr_8B_4$	280	1.1	2.8	4.0	148	551	905
$Fe_{86}Zr_7B_6Cu_1$	301	1.2	3.0	4.3	151	590	953
$Fe_{87}Zr_6B_6Cu_1$	321	1.3	3.0	4.4	143	572	-

comparable to or higher than those obtained in the Pr_2Fe_{17} and Nd_2Fe_{17} ball-milled alloys (it must be remembered from chapter 3 that the high-energy ball-milling produces an enhancement of the RCP values compared with the bulk precursors).

Fig. 5.2(a) depicts the composition dependence of both the peak of the magnetic entropy change for a maximum applied magnetic field change of 8 T and the temperature at which each peak occurs. Clearly the percentage of Fe determines the value of ΔS_M^{Peak}, which is also related with T^{Peak}. The field dependence of RCP_1 is depicted in fig. 5.2(b). The RCP for the sample $Fe_{87}Zr_6B_6Cu_1$ cannot be calculated for magnetic fields over 6 T due to limitations in the measurement temperature range available. One interesting result is that there is an almost linear dependence of the RCP with the applied fields exceeding 1 T. Even though a linear-like behavior were also shown in R_2Fe_{17} and $A_xB_{2-x}Fe_{17}$ alloys up to $\mu_0 H = 5\,\mathrm{T}$ (see figs. 5.2(b)), here such linear dependence is much more clear, and it is maintained up to 8 T. Also, it is remarkable the large RCP_1 values in spite of the low values of ΔS.

We also studied the master curve (for more details, see chapter 4) for each compound. These master curves, when using one reference temperature with $T_r > T_C$, do not collapse in the low reduced temperature range (see article II), which is attributed to the existence of ferromagnetic clusters inside a ferromagnetic matrix with different spin dynamics and competing interactions [82, 129]. Nevertheless, when using two reference temperatures the collapse is complete. The rescaled curves with two reference temperatures for an applied magnetic field change of $\mu_0 \Delta H = 8\,\mathrm{T}$ for the six compounds (sample $Fe_{87}Zr_6B_6Cu_1$ is not properly defined under this field because of the experimental temperature limitation) are plotted in fig. 5.3. Even when it is clear that in $Fe_{90}Zr_{10}$ and $Fe_{90}Zr_9B_1$ there are several points which are not well defined as a consequence of the experimental data, the match of all the curves over T_C is clear, but below it is not possible to speak of a real collapse. Therefore it is not possible to speak about a universal curve for this family of alloys. This could be expected because of their different critical exponents [130], and the relation between the universal curve and those exponents [131].

As we have already said in section 1.1.2, the maximum efficiency of a magnetic cooling system is attained when the refrigerant presents constant $\Delta S_M(T)$ curves in all the working temperature range. For this reason, we studied complex magnetic materials composed of mixtures of two ribbons of FeZrBCu metallic glasses with different transition temperatures. First of all, we

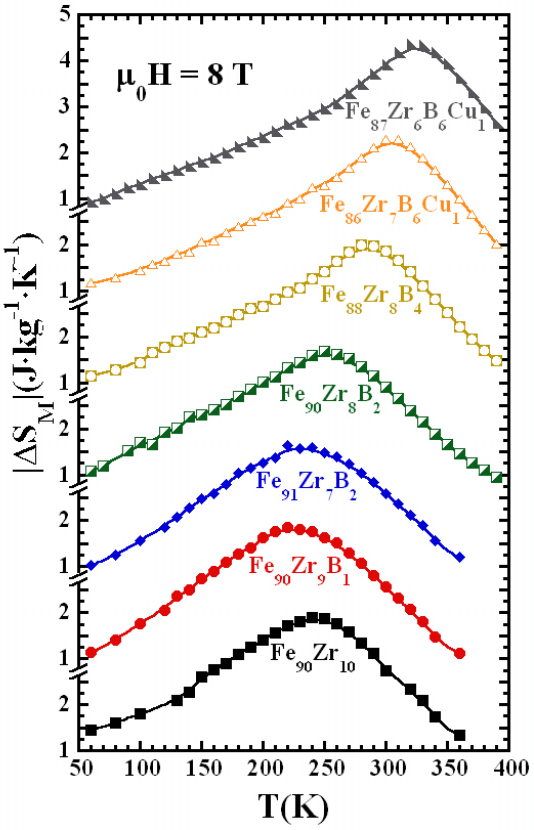

Figure 5.1: Temperature dependence of the magnetic entropy change for the different FeZrBCu amorphous ribbons under an applied magnetic field change of 8 T. Lines are guides for the eyes.

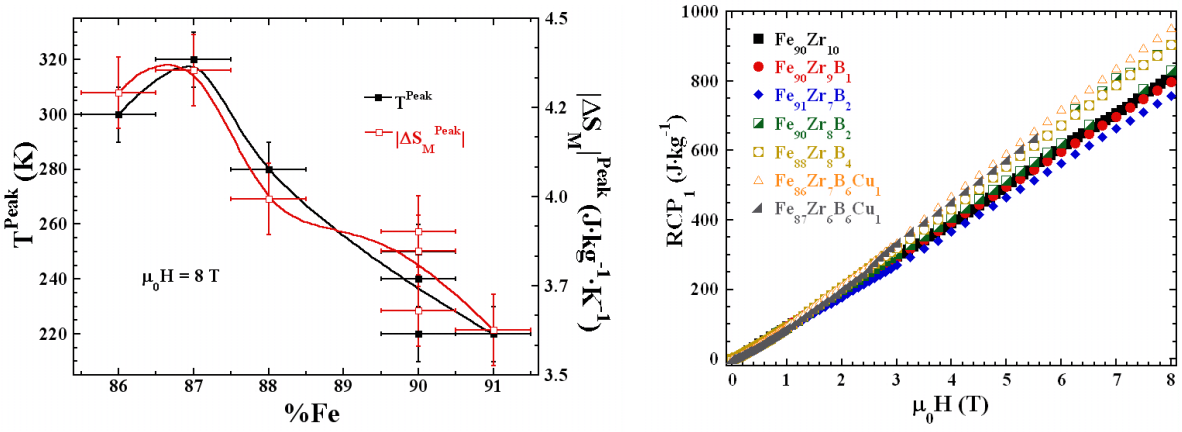

Figure 5.2: Left plot: Fe percentage dependence of the peak value of $|\Delta S_M(T)|$ and the temperatures at which these peaks are attained for the different FeZrBCu amorphous ribbons under an applied magnetic field change of 8 T. Lines are guides for the eyes. Right plot: Magnetic field dependence of the RCP for the studied FeZrBCu amorphous alloys. Data for $Fe_{87}Zr_6B_6Cu_1$ is not available above 5.5 T

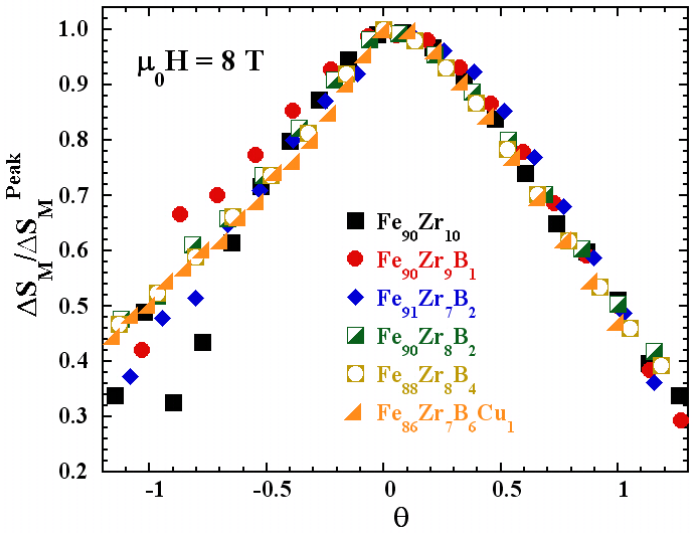

Figure 5.3: Comparison of the phenomenological master curve for the FeZrBCu alloys under a magnetic field change of $\mu_0 H = 8\,\mathrm{T}$.

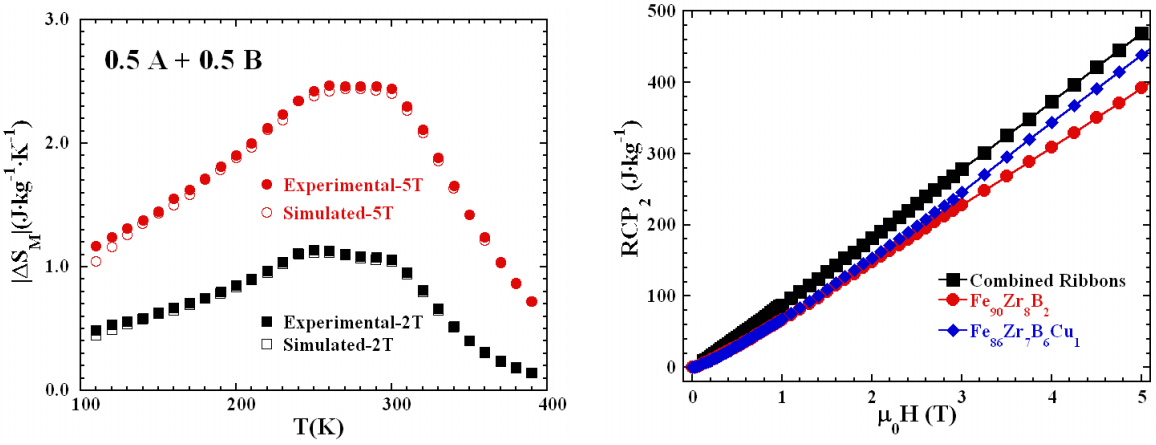

Figure 5.4: Left plot: Experimental and simulated $|\Delta S_M(T)|$ for the combined system 0.5 A + 0.5 B, with A = $Fe_{87}Zr_6B_6Cu_1$ and B = $Fe_{90}Zr_8B_2$. Magnetic entropy change for $H_{max} = 2.0\,\mathrm{T}$ (square symbols) and 5.0 T (circle symbols) obtained from the $M(H,T)$ curves measured for the combined system $0.5A+0.5B$ (full symbols) and the calculated from the independently measured samples A and B (open symbols). Right plot: Magnetic field dependence of the RCP_2 for a pair of FeZrBCu amorphous alloys, $Fe_{90}Zr_8B_2$ and $Fe_{86}Zr_7B_6Cu_1$, in the proportion 1:1. Data for $Fe_{90}Zr_8B_2$ and $Fe_{86}Zr_7B_6Cu_1$ are depicted for comparison.

estimated the magnetic entropy change that would have such a system by means of the weighted average of the magnetization of two ribbons. A set of scripts were prepared for this purpose (see appendix Scilab Functions). Secondly, we selected one of the possible pair of ribbons in the suitable mass proportion to obtain a constant $\Delta S_M(T)$ in the broad temperature range. Finally, the magnetization of the combined system was measured, showing a quite good agreement with the calculated curve (see fig. 5.4(a)). Moreover, we estimated the RCP_2 of the combined systems, which enhanced when compared to the individual ribbons (see fig. 5.4(b)) owing to a broadening of the $\Delta S_M(T)$ curves. It is worth to note that for either lower magnetic fields, other proportions of the studied pair of samples, or even more, for other pair of ribbons, $\Delta S_M(T)$ of such a system usually has a double-peak structure. For that reason, the RCP_2 can be only properly defined when the minimum between those peaks are higher than the half of the highest of those peaks.

5.2 Article I: The role of boron on the magneto-caloric effect of FeZrB metallic glasses

5.3 Article II: Magneto-caloric effect in FeZrB amorphous alloys near room temperature

Intermetallics 18 (2010) 2464–2467

Contents lists available at ScienceDirect

Intermetallics

journal homepage: www.elsevier.com/locate/intermet

Short communication

The role of boron on the magneto-caloric effect of FeZrB metallic glasses

Pablo Álvarez [a], Pedro Gorria [a,*], Jorge Sánchez Marcos [b], Luis Fernández Barquín [c], Jesús A. Blanco [a]

[a] Departamento de Física, Universidad de Oviedo, Calvo Sotelo, s/n, 33007 Oviedo, Asturias, Spain
[b] Instituto de Ciencia de Materiales de Madrid, CSIC, Cantoblanco, 28049 Madrid, Spain
[c] Departamento CITIMAC, F. Ciencias, Universidad de Cantabria, 39005 Santander, Spain

ARTICLE INFO

Article history:
Received 26 May 2010
Received in revised form
20 July 2010
Accepted 22 July 2010
Available online 21 August 2010

Keywords:
A. magnetic intermetallics
B. magnetic properties
G. ambient-temperature uses
G. magnetic applications

ABSTRACT

Fe-rich FeZrB metallic glasses exhibit magneto-caloric effect (MCE) around room temperature. Amorphous ribbons of two different compositions, $Fe_{91}Zr_7B_2$ and $Fe_{88}Zr_8B_4$, with respective Curie temperature values of 230 and 285 K have been studied. Although the maximum magnetic entropy change is relatively moderate ($|\Delta S_M|^{max} \sim 3$ J K^{-1} kg^{-1} under an applied magnetic field change from 0 to 50 kOe), the MCE spreads over a broad temperature interval ($\Delta T \sim 200$ K), giving rise to a large refrigerant capacity loss (RC $\sim$ 435 J kg^{-1}) without any hysteresis. The Curie temperature can be easily tuned between 200 and 350 K by changing the boron content. Therefore, the MCE can be controlled over a wide temperature interval, thus making these amorphous alloys promising candidates for magnetic refrigeration near room temperature.

1. Introduction

The search for new materials displaying magneto-caloric effect (MCE), for applications in magnetic refrigeration, is currently an active research field [1–5]. For applications near room temperature, a material with high or giant magnetic entropy change, $|\Delta S_M|$, inside a narrow temperature interval (as occurring around a first-order phase transition), is not well suited. It is needed a broad $|\Delta S_M|(T)$ peak because the operational temperature difference between the hot and cold reservoirs in the refrigerant engine usually expands more than 50 K. The latter condition is fulfilled by some ferromagnetic materials, which exhibit a moderate MCE over a wide temperature range associated to the second-order magnetic phase transition (SOMPT) [2,6]. Well-known examples of such materials are Gd, rare-earth intermetallic compounds or some manganites [2,3,7–9]. However, moderate MCE has been recently observed in disordered, nanostructured and amorphous magnetic materials displaying SOMPT [10–15]. Although the maximum of $|\Delta S_M|$ is relatively low compared to that of other crystalline compounds, the broad $|\Delta S_M|(T)$ peak gives rise to large values for the refrigerant capacity (RC) [6,13,16].

Fe-rich FeZrB metallic glasses offer several advantages as magnetic refrigerant materials around room temperature: (i) ultra-soft magnetic properties and absence of energy losses due to hysteresis effects, (ii) easily modifiable temperature range for the MCE by selecting the appropriate composition, and (iii) high electrical resistivity ($\rho \approx 130$ μΩ cm at 295 K), good mechanical behaviour and corrosion resistance [17,18]. In addition, FeZrB metallic glasses combine relatively high values for the saturation magnetization (above 1.5 μ_B/Fe at.) with tunable T_C values between 200 and 400 K [18,19].

Fe-rich FeZr metallic glasses are ferromagnetic below room temperature and possess crystallization temperatures above 750 K [20]. These alloys display striking magnetic behaviours including re-entrant spin-glass, exceptional magneto-volume effects or a reduction of T_C with increasing Fe content, due to the strong competition between Fe–Fe magnetic interactions [21–23]. The addition of boron up to 10% wt. gives rise to a large increase in T_C (up to around 400 K), without losing complexity in the magnetic behaviour [18,22,24]. Moreover, these alloys have attracted huge attention because after adequate heat treatments a stable nanocrystalline microstructure is reached, thus displaying ultra-soft magnetic properties [25,26] and allowing its use in a number of commercial applications [27]. In this letter we show that FeZrB amorphous alloys exhibit large RC values with an easy-to-control temperature range of operation between 100 and 450 K by small changes in the composition.

2. Materials and experimental details

$Fe_{91}Zr_7B_2$ (B2) and $Fe_{88}Zr_8B_4$ (B4) amorphous ribbons, with 1.5 mm × 20 μm cross sections, were fabricated by the melt-spinning method after preparing the master alloys (around 2 g of mass) in an

* Corresponding author.
E-mail address: pgorria@uniovi.es (P. Gorria).

0966-9795/$ – see front matter © 2010 Elsevier Ltd. All rights reserved.
doi:10.1016/j.intermet.2010.07.018

arc-melting furnace under Ar atmosphere. The melt spinner equipment was operated using a stain steel wheel (50 m/s linear speed) under a controlled Ar atmosphere. The X-ray diffraction patterns corresponding to either ribbon faces show only broad haloes, thus confirming a complete amorphous state and absence of crystallinity in the ribbons. Isothermal magnetization vs. applied magnetic field, $M(H)$ curves, were measured using an SQUID magnetometer in the temperature range between 50 and 370 K. At each temperature the data were collected under constant *dc* applied magnetic field steps of $H = 1$ kOe in the magnetic field range between 0 and 50 kOe.

3. Results and discussion

In Fig. 1 the temperature evolution of the $M(H)$ curves for both B2 and B4 samples are depicted. The values of T_C (230 ± 5 and 285 ± 5 K for B2 and B4, respectively) have been estimated from the low-field $M(T)$ curves, as the minimum of the dM/dT vs. T curves.

The MCE as a function of the magnetic field and the temperature has been obtained by integrating the adequate Maxwell relation [2]:

$$\Delta S_M(H,T) = S_M(H,T) - S_M(0,T) = \int_0^H \left(\frac{\partial M}{\partial T}\right)_H dH$$

where $S_M(H,T)$ and $S_M(0,T)$ are the magnetic entropy under an applied magnetic field H and in the absence of any magnetic field, respectively, and at a fixed temperature T. Hence, the results obtained after applying this procedure to the whole set of $M(H)$ curves provide the temperature and/or magnetic field dependences of the magnetic entropy, $\Delta S_M(T,H)$.

Both amorphous samples exhibit $\Delta S_M(T,H)$ surfaces with broad maxima around $T = T_C$, as it can be observed in the 3D view of Fig. 2, thus indicating that these materials exhibit MCE in a wide temperature range.

The calculated maximum values for $|\Delta S_M|$ are 2.8 and 3.3 J kg^{-1} K^{-1} for B2 and B4 alloys, respectively, under a magnetic field change between 0 and 50 kOe. In order to compare the MCE between different materials the refrigerant capacity (RC) is a very useful parameter, defined as the amount of heat that can be transferred between the cold and hot reservoirs in an ideal refrigeration cycle, at temperatures T_{cold} and T_{hot} respectively [28,29]. The T_{cold} and T_{hot} are commonly taken as those temperatures where

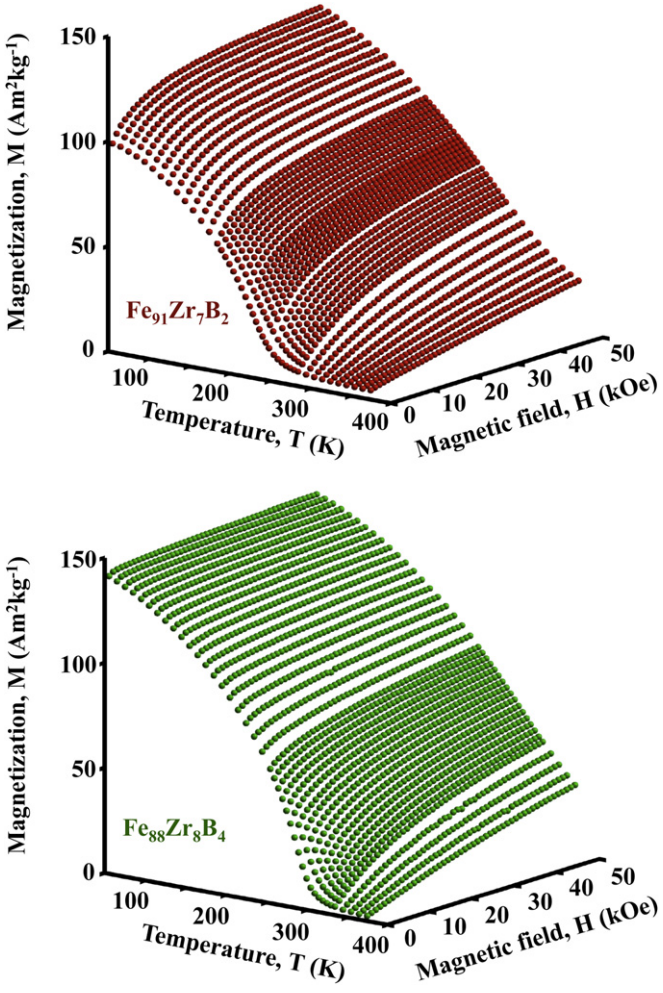

Fig. 1. Temperature and applied magnetic field dependences of the magnetization for both $Fe_{91}Zr_7B_2$ (upper panel, B2) and $Fe_{88}Zr_8B_4$ (bottom panel, B4) amorphous ribbons.

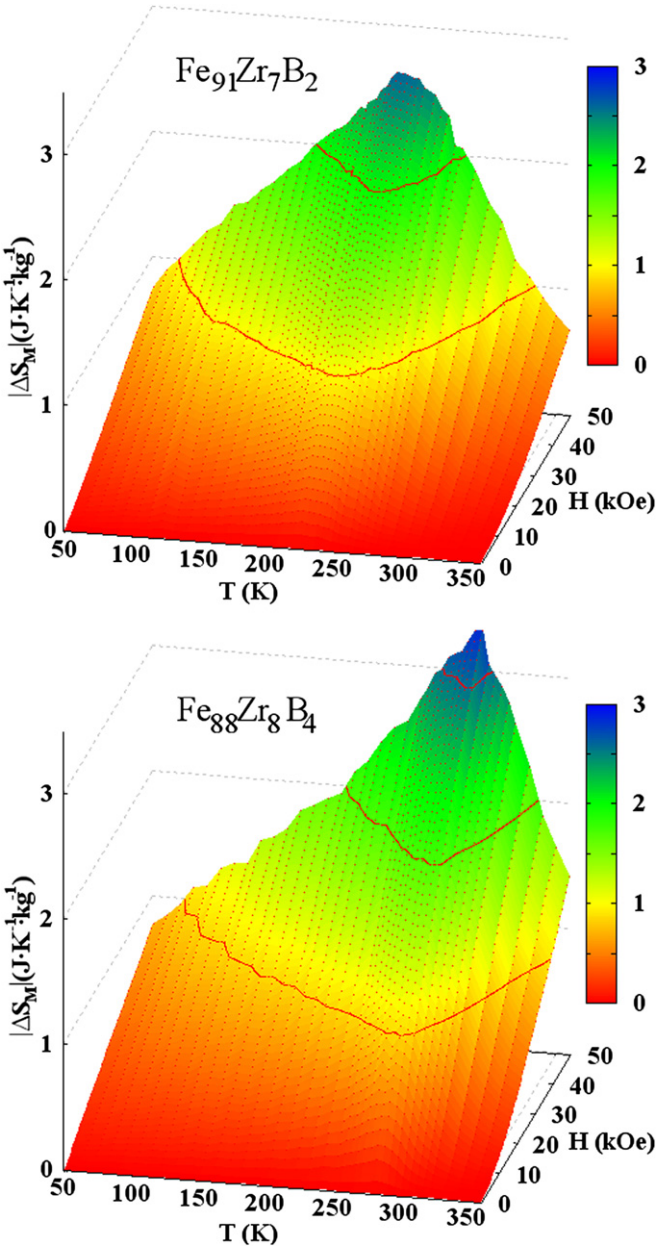

Fig. 2. Temperature and magnetic field dependences of $|\Delta S_M|$ for B2 and B4 samples.

$|\Delta S_M|$ is half of its maximum. We have estimated the RC values from numerical integration of the area under $|\Delta S_M|(T)$ curve by using T_{cold} and T_{hot} as the integration limits. The obtained RC values are clearly higher to those of GdSiGe compounds [30], reaching 435 J kg^{-1} ($\approx$3.5 $\pm$ 0.1 J cm^{-3}), which is ca 90% of that corresponding to pure gadolinium ($\approx$4 J cm^{-3}).

It must be pointed out that even though the maximum value of $|\Delta S_M|$ for the B2 sample is around 15% lower, due to its smaller magnetization (a reduction of 15% compared with that of B4 sample is observed at 5 K [17]), the smoother decrease of M around T_C for B2 compound results in a broader $|\Delta S_M|(T)$ curve, giving rise to roughly identical RC value for both samples.

In Fig. 3 we show the $|\Delta S_M|(T)$ curves for applied magnetic field change of $\Delta H = 20$ and 50 kOe, in these FeZrB amorphous alloys ΔT can reach 200 K under a magnetic field change of $\Delta H = 50$ kOe. If $\Delta H = 20$ kOe, which is a value that can be reached without using superconducting magnets, the RC and ΔT values for the B2(B4) sample are 148(159) J kg^{-1} and 163(150) K respectively.

Moreover, the compositional dependence of the Curie temperature in these alloys follows an almost linear tendency with a negative slope (see Fig. 4 for T_C vs. Fe content plot), being nearly independent of the relative amount of Zr and B. Hence, the temperature range for the refrigeration cycle can be tuned between 100 and 450 K, taking into account that the value of T_C can be straightforwardly adjusted between 200 and 350 K via small changes in the composition of FeZrB metallic glasses (a decrease of 1 at. % in the amount of Fe approximately equals to an increase of 20 K in the value of T_C, see Fig. 4).

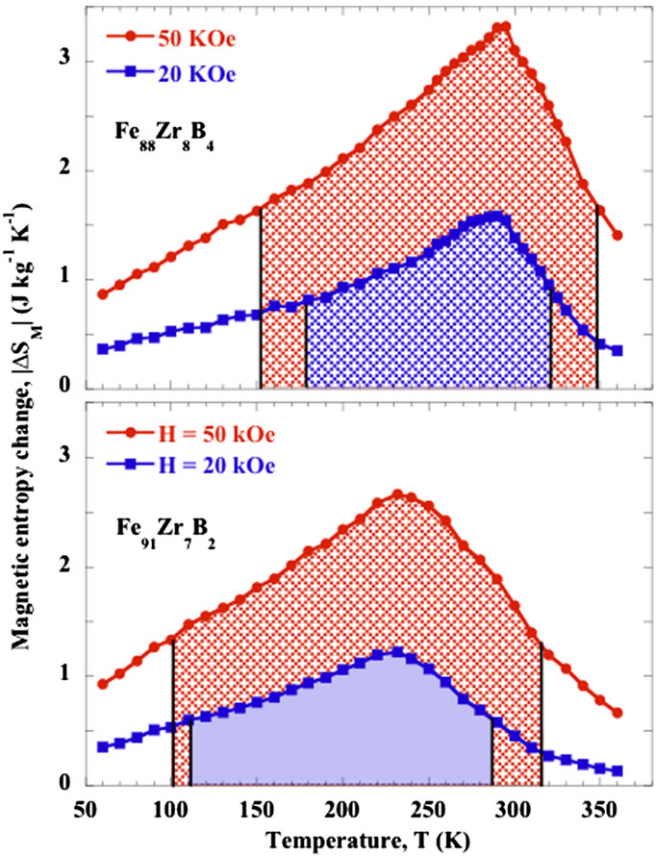

Fig. 3. Temperature dependence of $|\Delta S_M|$ for $\Delta H = 20$ kOe (blue squares) and $\Delta H = 50$ kOe (red circles) for $Fe_{91}Zr_7B_2$ and $Fe_{88}Zr_8B_4$ samples. The area of the dashed regions corresponds to the values of RC (see text). (For interpretation of references to colour this figure legend the reader is referred the web version of this article).

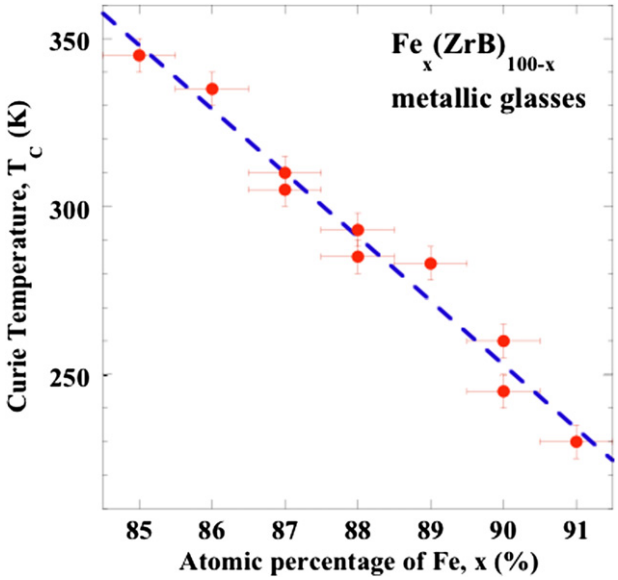

Fig. 4. Almost linear dependence of the Curie temperature with the percentage of Fe atoms in Fe-rich FeZrB alloys. Data are taken from Refs. [31–33].

4. Conclusions

In summary, FeZrB amorphous alloys exhibit low magnetic entropy change maxima (around 3 J kg^{-1} K^{-1} for $\Delta H = 50$ kOe), but expanded over wide temperature ranges, thus giving rise to large RC values, reaching 435 J kg^{-1} (3.5 J cm^{-3}) and without any hysteresis loses. Moreover, the Curie temperature can be easily controlled by small compositional changes in the range 200–350 K. Furthermore, the possibility of combination of two or more alloys by selecting the adequate T_C values could be a good option for a hypothetical near room temperature magnetic refrigerator operating in multistage mode. The latter could ensure a more or less constant value of $|\Delta S_M|$ between the hot and cold ends of the refrigeration cycle, which is the optimal condition for an ideal Ericsson refrigeration cycle. Therefore, these alloys are promising candidates for their potential application in magnetic refrigeration at about room temperature.

Acknowledgments

Financial support from FEDER and the Spanish MICINN through research projects NAN2004-09203-C04-03 and MAT2008-06542-C04 is acknowledged. Two of us (PA & JSM) thank FICyT and MICINN for PhD and “Juan de la Cierva” research contracts, respectively.

References

[1] Tegus O, Brück E, Buschow KHJ, de Boer FR. Nature (London) 2002;415:150.
[2] Gschneidner Jr KA, Pecharsky VK, Tsokol AO. Rep Prog Phys 2005;68:1479.
[3] Brück E. J Phys D: Appl Phys 2005;38:R381.
[4] Ipus JJ, Blázquez JS, Franco V, Conde A, Kiss LF. Intermetallics 2010;18:565.
[5] Chang J, Hui X, Xu ZY, Lu ZP, Chen GL. Intermetallics 2010;18:1132.
[6] Gorria P, Sánchez Llamazares JL, Álvarez P, Sánchez Marcos J, Pérez MJ, Blanco JA. J Phys D: Appl Phys 2008;41:192003.
[7] Tencé S, Gaudin E, Chevalier B. Intermetallics 2010;18:1216.
[8] Gorria P, Álvarez P, Sánchez Marcos J, Sánchez Llamazares JL, Pérez MJ, Blanco JA. Acta Mater; 2009:1724.
[9] Kallel S, Kallel N, Hagaza A, Peña O, Oumezzine M. J Alloys Comp 2010;492:241.
[10] Chevalier B, Bobet J-L, Sánchez Marcos J, Rodríguez Fernández J, Gómez Sal JC. Appl Phys A 2005;80:601.
[11] Skorvanek I, Kovac J. Czech J Phys 2004;54:D189.
[12] Franco V, Conde CF, Conde A, Kiss LF. Appl Phys Lett 2007;90:052509.
[13] Du J, Zheng Q, Brück E, Buschow KHJ, Cui WB, Feng WJ, et al. J Magn Magn Mater 2009;321:413.

[14] Dong QY, Shen BG, Chen J, Shen J, Wang F, Zhang HW, et al. Solid State Commun 2009;149:417.
[15] Álvarez P, Gorria P, Franco V, Sánchez Marcos J, Pérez MJ, Sánchez Llamazares JL, et al. J Phys Condens Matter 2010;22:216005.
[16] Franco V, Blázquez JS, Conde F, Conde A. Appl Phys Lett 2006;88:042505.
[17] Barandiarán JM, Fernández Barquín L, Gómez Sal JC, Gorria P, Hernando A. Solid State Commun 1993;88:75.
[18] Barandiarán JM, Gorria P, Orue I, Fdez-Gubieda ML, Plazaola F, Gómez Sal JC, et al. J Phys Condens Matter 1997;9:5671.
[19] Barandiarán JM, Gorria P, Gómez Sal JC, Fernández Barquín L, Kaul SN. IEEE Trans Magn 1994;30:4776.
[20] Gorria P, Garitaonandia JS, Pérez MJ, Blanco JA, Campo J. Phys Status Solidi (RRL) 2009;3:28.
[21] Kaul SN. Phys Rev B 1983;27:6923.
[22] Barandiarán JM, Gorria P, Orue I, Fdez-Gubieda ML, Plazaola F, Hernando A. Phys Rev B 1996;54:3026.
[23] García Calderón R, Fernández Barquín L, Kaul SN, Gómez Sal JC, Gorria P, Pedersen JS, et al. Phys Rev B 2005;71:134413.
[24] Fernández Barquín L, Gómez Sal JC, Gorria P, Garitaonandia JS, Barandiarán JM. Eur Phys J B 2003;35:3.
[25] Suzuki K, Kataoka N, Inoue A, Makino A, Masumoto T. Mater Trans JIM 1990;31:743.
[26] Gorria P, Orue I, Plazaola F, Fdez-Gubieda ML, Barandiarán JM. IEEE Trans Magn 1993;29:2682.
[27] McHenry ME, Willard MA, Laughlin DE. Prog Mater Sci 1999;44:291.
[28] Wood ME, Potter WH. Cryogenics 1985;25:667.
[29] Pecharsky VK, Gschneidner Jr KA. J Appl Phys 2001;90:4614.
[30] Provenzano V, Shapiro AJ, Shull RD. Nature (London) 2004;429:853.
[31] Slawska-Waniewska A, Nowicki P, Lachowicz HK, Gorria P, Barandiarán JM, Hernando A, et al. Phys Rev B 1994;50:6465.
[32] Slawska-Waniewska A, Zuberek R. J Magn Magn Mater 1996;160:253.
[33] Hernando A, Crespo P, Castaño FJ, Arcas J, Multigner M, Barandiarán JM, et al. Phys Rev B 2000;61:3219.

Journal of Alloys and Compounds 504S (2010) S150–S154

Contents lists available at ScienceDirect

Journal of Alloys and Compounds

journal homepage: www.elsevier.com/locate/jallcom

Magneto-caloric effect in FeZrB amorphous alloys near room temperature

Pablo Álvarez [a], Jorge Sánchez Marcos [b], Pedro Gorria [a,*], Luis Fernández Barquín [c], Jesús A. Blanco [a]

[a] Departamento de Física, Universidad de Oviedo, Avda. Calvo Sotelo, s/n, 33007 Oviedo, Spain
[b] Instituto de Ciencia de Materiales de Madrid, ICMM-CSIC, Cantoblanco, 28049 Madrid, Spain
[c] Departamento CITIMAC, Universidad de Cantabria, Avda. de los Castros, s/n, 39005 Santander, Spain

ARTICLE INFO

Article history:
Received 31 July 2009
Received in revised form 28 January 2010
Accepted 21 February 2010
Available online 3 March 2010

Keywords:
Metallic glasses
Fe-based alloys
Magneto-caloric effect

ABSTRACT

The magneto-caloric effect exhibited by three Fe-rich FeZrB amorphous alloys with different compositions and Curie temperatures between 230 and 300 K has been studied. Albeit the maximum entropy change is low ($|\Delta S_M|^{max} \sim 3\,J\,kg^{-1}\,K^{-1}$ under an applied magnetic field change from 0 to 50 kOe), the magneto-caloric effect (MCE) spreads out over a broad temperature interval ($\Delta T \sim 200$ K). The estimated values for the relative cooling power are close to that of pure Gd. From the applied magnetic field dependence of the magnetic entropy change a master curve valid for these Fe-rich FeZrB amorphous alloys has been found. However, two reference temperatures of the $|\Delta S_M|(T)$ are needed in order to get a collapsing curve for all the maximum applied magnetic field values. The latter suggests that the striking magnetic behaviour of these compounds below 200 K influences the MCE effect. Moreover, the collapse into the same curve for different rescaled temperature dependences of the magnetic entropy change in the three samples implies the existence of similar magnetic interactions in these compounds.

1. Introduction

The most challenging purpose for refrigeration technology is the optimization of the engine efficiency minimizing both the powder consumption as well as the environmental impact. The emerging technology based on magnetic refrigeration will probably be the most adequate way to fulfill these requirements [1–3]. Therefore, the search for new materials displaying significant magneto-caloric effect (MCE) is nowadays a very active field of research [4–8]. For applications near room temperature (where the temperature difference between the hot and cold reservoirs for a domestic refrigerator could be higher than 80 K), rather than a material with high or giant magnetic entropy change, $|\Delta S_M|$, inside a narrow temperature interval (as occurring around a first-order phase transition) [1,2], it is needed a broad $|\Delta S_M|(T)$ peak expanded over the temperature range where the refrigerant engine should operate. Some ferromagnetic materials exhibit moderate MCE over wide temperature ranges around their second-order (ferro-to-paramagnetic) phase transition (SOPT), such as it is the case of pure Gd [1], rare-earth intermetallic compounds [1,2,6–8] or some manganites [9]. Recently, disordered and non-crystalline magnetic materials displaying SOPT such as rare-earth-based amorphous ribbons [10,11] and bulk metallic glasses [12,13], ball milled amorphous alloys [14,15], as well as Fe-rich metallic glasses [16,17] have attracted emergent relevance in the field. The reason for that is the broad $|\Delta S_M|$ (T) peak exhibited, being even larger than 150 K under applied magnetic field changes of 50 kOe, although the maximum of $|\Delta S_M|$ is relatively low compared to that of other materials displaying MCE.

In the case of Fe-rich metallic glasses, the MCE is due to Fe atoms, and they present several advantages that must be pointed out, namely, (i) lower fabrication costs due the absence of rare-earth metals in the composition, (ii) the ultra-soft magnetic properties, with vanishing magnetocrystalline anisotropy and very low coercive fields, withdraw any energy losses due to hysteresis effects thus allowing higher operation frequencies and faster response, and (iii) the magnetic transition temperatures, and then the temperature ranges for the MCE, can be easily adjustable by selecting the appropriate composition. Upto now, the most studied compositions consist of around 70–80 at.% of Fe with upto 15–20 at.% of metalloid elements (B, Si, P, Ge, ...) and small amounts of one or more transition metal atoms (Nb, Mo, Co, Cr, Zr, Mn, ...) [18–22]. However, in almost all the cases the Curie temperatures, T_C, are above room temperature, therefore if the material should be used in a refrigerant engine for cooling from room to lower temperatures, the maximum of the MCE must occur just below room temperature. In this way, FeZrB metallic glasses are good candidates for fulfilling the latter requirements, since these alloys combine high values for the saturation magnetization (above 1.5 μ_B/Fe at.) with T_C values above 200 K.

Fe-rich FeZr metallic glasses are ferromagnetic below room temperature and possess crystallization temperatures above 750 K

* Corresponding author. Tel.: +34 985102899; fax: +34 985103324.
E-mail address: pgorria@uniovi.es (P. Gorria).

0925-8388/$ – see front matter © 2010 Elsevier B.V. All rights reserved.
doi:10.1016/j.jallcom.2010.02.149

[23]. These alloys display striking magnetic behaviours including re-entrant spin-glass, exceptional magneto-volume effects and a reduction of T_C with increasing Fe content, due to the strong competition between Fe–Fe magnetic interactions [24–26]. The addition of boron upto 10 wt%. gives rise to a large increase in T_C (upto around 400 K), without losing complexity in the magnetic behaviour [27,28]. Moreover, these alloys have attracted huge attention because after adequate heat treatments a stable nanocrystalline microstructure is reached, thus displaying ultrasoft magnetic properties [29] and allowing the study of magnetic interactions between the Fe nanocrystals and the remaining amorphous matrix [30,31]. In this article we show that although FeZrB amorphous alloys do not exhibit large MCE values, the estimated relative cooling power (RCP) or refrigerant capacity (RC) values are comparable with those of other reference materials such is the case of pure gadolinium. In addition, the dependencies of $|\Delta S_M|$ with both the temperature and the applied magnetic field have been studied in terms of a master curve via renormalization of temperature scale.

2. Experimental details and data analysis

The amorphous ribbons of compositions $Fe_{91}Zr_7B_2$ (B2), $Fe_{88}Zr_8B_4$ (B4) and $Fe_{87}Zr_6B_6Cu_1$ (B6) with 1.5 mm × 20 μm cross-sections were fabricated by melt-spinning under Ar atmosphere from the arc-melted master alloys. The absence of intense peaks in the X-ray diffraction patterns, in which only broad haloes are present, confirms the amorphous state of the ribbons. Around 40 isothermal magnetization vs applied magnetic field, $M(H)$ curves, were measured using a SQUID magnetometer in the temperature range between 50 and 370 K (see Fig. 1 right bottom panel for several $M(H)$ curves corresponding to B6 sample). The temperature steps between consecutive isothermal $M(H)$ curves were 4 K in the immediacy of the Curie temperature (between $T_C - 30$ K and $T_C + 30$ K) and 10 K out of this temperature region. At each temperature the data were collected under constant *dc* applied magnetic field steps of $H = 1$ kOe in the magnetic field range between 0 and 50 kOe.

The MCE as a function of the applied magnetic field and the temperature has been obtained from the magnetic entropy change, ΔS_M, taking into account that for an isothermal process, ΔS_M can be evaluated integrating the adequate Maxwell relation [32]:

$$\Delta S_M(H,T) = S_M(H,T) - S_M(0,T) = \int_0^H \left(\frac{\partial M}{\partial T}\right)_H dH \quad (1)$$

Note that at a fixed temperature T, the magnetic entropy under an applied magnetic field H and in the absence of the magnetic field are $S_M(H,T)$ and $S_M(0,T)$, respectively.

Essentially, the value for ΔS_M at a given temperature is obtained after a numerical integration of two consecutive $M(H)$ isotherms around such temperature, followed by the numerical derivative with temperature. The results obtained after applying this procedure to the whole set of $M(H)$ measured curves allow us to obtain the temperature and/or applied magnetic field dependences of the magnetic entropy, $|\Delta S_M|(H,T)$.

For applications in magnetic refrigeration at room temperature is important to take into account the amount of heat that the studied material can absorb during the refrigeration cycle from the cold focus. For that reason the most common parameter used to quantify this are either RCP or RC, that can be defined in several ways [6,32]; in this paper we have chosen the product of the maximum $|\Delta S_M|$ peak value and the full width at half maximum, δT_{FWHM},

$$RCP(S) = |\Delta S_M|^{max} \times \delta T_{FWHM} \quad (2)$$

The magnetic field dependence of $|\Delta S_M|$ is analytically calculated using the following expression:

$$n = \frac{d\left|\ln(\Delta S_M)\right|}{d\ln\ T} \quad (3)$$

In a material with second-order transition, the $\Delta S_M(T)$ curves for different maximum magnetic fields collapse into a single master curve [20]. That master curve is useful for predicting the field dependence of the magnetic entropy change and extrapolating it over both the experimental temperature and magnetic field range available in a laboratory. The master curve is obtained as follow: first, the $\Delta S_M(T)$ curves are normalized to its maximum value ΔS_M^{Peak} for each maximum applied magnetic field, and then, if there is no presence of a secondary magnetic phase, the temperature axis is rescaled as [33]:

$$\theta = \frac{(T - T_C)}{(T_r - T_C)} \quad (4)$$

where T_r is a reference point in the curve corresponding to a certain fraction of ΔS_M^{Peak}. If another magnetic phase exists or the material exhibits magnetic inhomogeneities is necessary the use of two different reference temperatures, which leads to:

$$\theta = -\frac{(T - T_C)}{(T_{r1} - T_C)} \quad T < T_C \quad (5)$$

$$\theta = \frac{(T - T_C)}{(T_{r2} - T_C)} \quad T > T_C \quad (6)$$

where T_{r1} and T_{r2} are the temperatures of the two reference points of each curve that correspond to $a\ \Delta S_M^{Peak}$, with a in between 0 and 1.

3. Results and discussion

In Fig. 1 the temperature dependence of the $|\Delta S(H)|$ curves for the $Fe_{91}Zr_7B_2$ (B2), $Fe_{88}Zr_8B_4$ (B4) and $Fe_{87}Zr_6B_6Cu_1$ (B6) studied

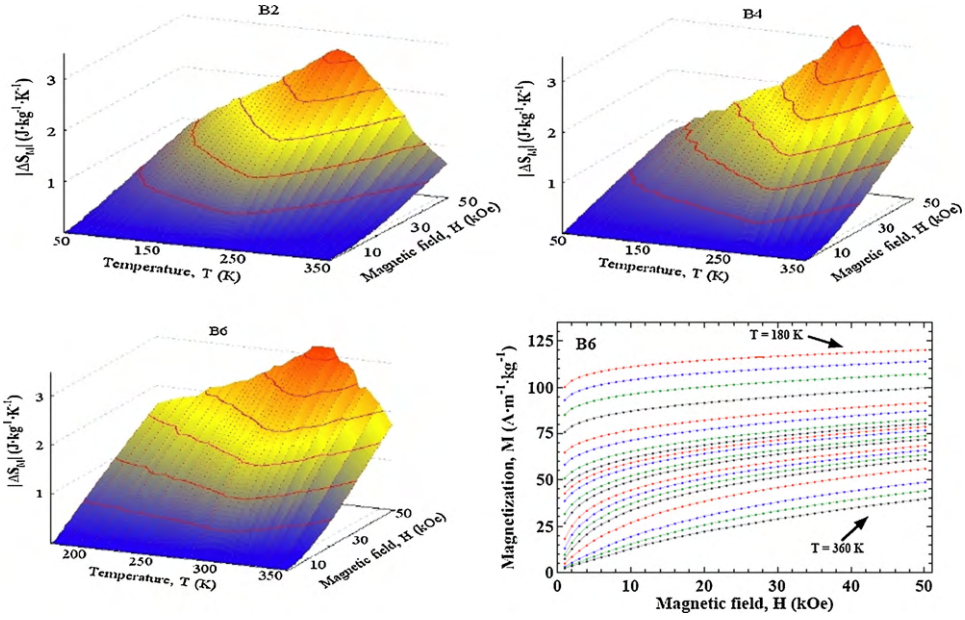

Fig. 1. Temperature and applied magnetic field dependencies of the magnetic entropy change, $|\Delta S_M|$, for B2, B4 and B6 samples. Right bottom panel displays some of the measured $M(H)$ isotherms for the B6 sample from which $|\Delta S_M|$ (T,H) surfaces have been obtained (see text).

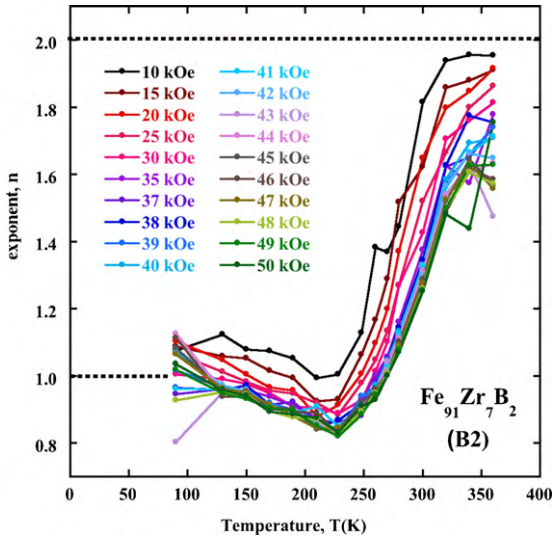

Fig. 2. Temperature dependence of the exponent of the magnetic entropy change under different applied magnetic field values for $Fe_{91}Zr_7B_2$. Lines are guides for the eyes. The dashed lines correspond to the paramagnetic $n = 2$ value and the low temperature (far fro $T = T_C$) ferromagnetic $n = 1$ value.

samples are shown. The maximum $|\Delta S_M|$ values for an applied magnetic field change from 0 to 50 kOe are 2.8, 3.3 and 3.2 J kg^{-1} K^{-1} for B2, B4 and B6 alloys, respectively. Those values correspond approximately to a quarter of the value for pure gadolinium under the same applied magnetic field change. The temperatures of the $|\Delta S_M|(T)$ peaks are around 250 (B2), 295 (B4) and 300 K (B6). The RCP values calculated as mentioned in the previous section, are 532 (B2), 649 (B4) and 577 J kg^{-1} (B6), which are around 80–90% of the value for pure Gd. This fact is due to a large temperature span of the $|\Delta S_M|(T)$ peak, which could reach $\delta T_{FWHM} \approx 150$–200 K. While the maximum values of $|\Delta S_M|$ are similar in B4 and B6 samples and higher than that calculated for B2, the $|\Delta S_M|(T)$ peak is broader (larger δT_{FWHM}) for B2 than for B4 and B6. These two features are closely related to a higher magnetic moment for the Fe atoms in both B4 and B6 ($\mu \approx 1.6\,\mu_B$) respect to B2 sample ($\mu \approx 1.4\,\mu_B$), and the slower drop of the magnetization with temperature of the B2 samples in de immediacy of T_C [34]. It is worth noting that in addition to both $\Delta S(H)$ and RCP values, also the temperature range in which the MCE occurs is important for practical applications. As it is well known, the maximum of the magnetic entropy change of a ferromagnetic material is achieved close to its Curie temperature, T_C. Hence, for refrigeration purposes at room temperature it is important the feasible control of the T_C value of the material via slight compositional changes. This requirement is fulfilled by FeZrB(Cu) metallic glasses, because T_C follows an almost linear dependence with the Fe atomic percentage (with a negative slope), being nearly independent of the relative amount of Zr and B [27,30,34]. Therefore, the temperature range for the refrigeration cycle can be tuned between 100 and 350 K.

On the other hand, the value of the magnetic entropy change depends on the measuring temperature, but also on the maximum magnetic field change. Then, for a material displaying a second-order ferromagnetic transition, it can be expected that such dependencies for each temperature follow a potential law, $\Delta S_M \alpha H^n$ [17]. We show in Fig. 2 the variation of the exponent n with temperature for different maximum magnetic field changes (from $\Delta H = 10$ kOe to $\Delta H = 50$ kOe).

The n values at each temperature have been obtained through the fit of the $|\Delta S_M|(H)$ curves using Eq. (3). As it can be observed, n depends on the magnetic state of the compound. While $n \approx 2$ for temperatures well above T_C, being a direct consequence of the Curie–Weiss law [35], its value goes to 1 in ferromagnetic state far enough from T_C. Moreover, $n(T)$ curves display a minimum at $T \approx T_C$ (see Fig. 2).

In the framework of the mean field theory (MFT), a minimum for the exponent n at $T = T_C$ with a constant value of $n = 2/3$ and being independent of the applied magnetic field is expected. In addition, n can be related to the critical exponents β and γ at the magnetic phase transition in the following way:

$$n = 1 + \frac{\beta - 1}{\beta + \gamma} \tag{7}$$

where $\beta = 0.5$ and $\gamma = 1$ in MFT. However, in FeZrB amorphous alloys n exhibits a clear dependence on the applied magnetic field, with diminishing values down to $n \approx 0.82$ for $H \geq 45$ kOe, as H is increased in B2 sample. The origin of this $n(H)$ dependence can be attributed to the fact that $Fe_{91}Zr_7B_2$ amorphous alloy is far from being magnetically saturated under an applied magnetic field $H = 10$ kOe, due to the complex competing magnetic interactions between Fe atoms [27,34]. For $H > 10$ kOe the $M(H)$ curve reduces gradually its slope, thus explaining the almost constant value of n for $H \geq 45$ kOe (see Fig. 2).

Although similar behaviour is observed for B4 and B6 samples, the H-dependence of n (not shown) is less pronounced because these compounds are closer to be magnetically saturated. Concerning the minimum values of n for these B4 and B6 samples, $n \approx 0.77$ in both cases under an applied magnetic field change from 0 to 50 kOe. Therefore, it can be concluded that the mean field model no longer applies to these compounds. Moreover, the change in the value of the exponent n as the boron content increases can be correlated with the magnetic state of the samples, and in particular with the compositional dependence of the exponent n, as follows. If the exponent β is estimated from the high field $M(H)$ curves by means of modified Arrott plots [$M^{1/\beta}$ vs $(H/M)^{1/\gamma}$], using a value of $\gamma = 1.38$ [34], β varies from 0.325 in B2 sample to 0.39 and 0.4 in B4 and B6 samples, respectively. β values lower than 0.5 indicate the existence of magnetic inhomogeneities in a ferromagnetic compound [36,37]. Hence, the compounds became magnetically more homogeneous as the boron content increases [34], thus exhibiting smaller and nearly magnetic field independent minimum values of the n exponents, as is the case of B4 and B6 alloys in comparison with B2 one.

As a consequence of the low temperature re-entrant spin-glass behaviour exhibited by these FeZrB compounds, already attributed to the existence of ferromagnetic clusters inside a ferromagnetic matrix with different spin dynamics and competing interactions [26,28], Eq. (2) lose its validity. On the other hand, Franco et al. proposed that the magnetic field dependence of n is due to the contribution coming from a second magnetic phase [33]. In our case, the $n(H)$ dependence cannot be attributed to any secondary magnetic phase, even though the effects are the same, with the difference that above certain applied magnetic field ($H \geq 45$ kOe for B2) n is almost constant.

With the aim of getting a more detailed knowledge of the temperature dependence of the magnetic entropy change in these alloys, we have normalized the $|\Delta S_M(T)|$ curves and rescaled the temperature axis in order to show if these curves collapse into a single master curve for different values of the applied magnetic field. In the case of B2 sample two different reference temperatures [see Eqs. (5) and (6)] are needed as it can be seen in Fig. 3 where the curves for $H \geq 20$ kOe scale into a master curve in the entire temperature range, which indicates that no other magnetic transition can be expected in the temperature interval of the measurements [35]. The use of only one reference temperature gives rise to non-collapsing curves in the low temperature range (not shown), being a clear signature of the magnetic inhomogeneous

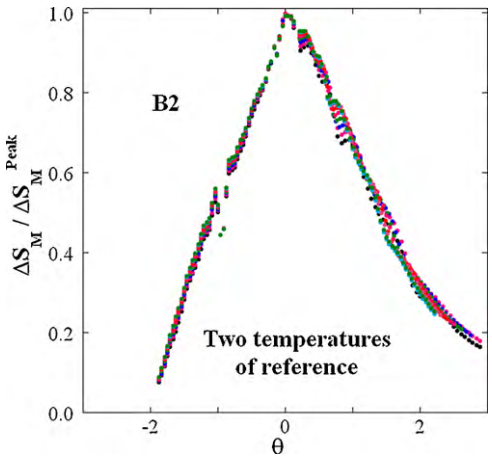

Fig. 3. Master curve of the magnetic entropy change for the $Fe_{91}Zr_7B_2$ amorphous alloy determined from different maximum applied fields, ranging from 20 to 50 kOe and using two reference temperatures.

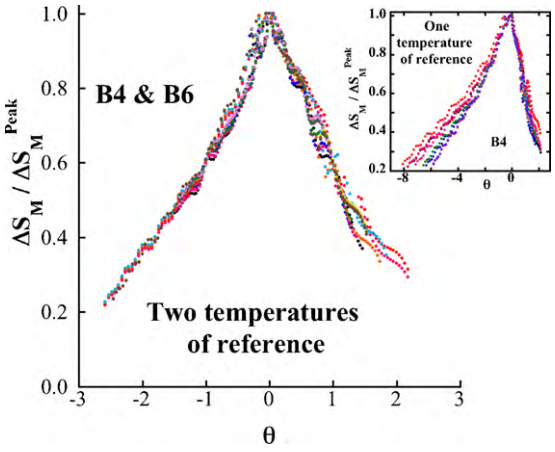

Fig. 4. Collapse into the same master curve of the rescaled temperature dependence of magnetic entropy change of $Fe_{88}Zr_8B_4$ and $Fe_{87}Zr_6B_6Cu_1$ obtained using two temperatures of reference.

state of the alloy, which exhibits re-entrant spin-glass behaviour below 100 K [26,28].

A similar trend is followed by B4 and B6 samples as it can be observed in Fig. 4, where two reference temperatures have been also considered. It is worth noting that the curves for both samples collapse into the same master curve, thus confirming a similar magnetic behaviour of these two compounds (we must remember that the values for T_C, β and n exponents are close in B4 and B6 amorphous alloys). The inset of Fig. 4 shows the normalized curve of the magnetic entropy change for several applied magnetic fields of B4 sample, when only one reference temperature is used. Obviously the different curves do not collapse into a single master curve in the low temperature range.

Taking into account that almost an identical curve is obtained for B6 sample, a similar inhomogeneous magnetic state could be expected for both B4 and B6 alloys at low temperature, as it was already probe by SQUID magnetometry and Mössbauer spectroscopy [34].

4. Summary and conclusions

We have studied the magneto-caloric effect on three FeZrB amorphous ribbons with different boron content and Curie temperatures ranging from 230 to 300 K. The maximum magnetic entropy change of the ribbons are low when compared with Gd-based alloys, but they exhibit a broad $|\Delta S_M(T)|$ peaks extending over 150–200 K under applied magnetic field changes from 0 to 50 kOe. The latter gives rise to elevated values for the relative cooling power or refrigerant capacity, which can be comparable to that of pure gadolinium. The applicability of these alloys in real refrigeration engines is today a matter of controversy. However, we have tried to find a relationship between the temperature and applied magnetic field dependencies of the magnetic entropy change with the complex and inhomogeneous magnetic state of these alloys. In order to get a single master curve resulting from a collapse of the normalized magnetic entropy curves, we have shown that two different temperatures of reference are needed instead of using only one reference temperature, like in conventional ferromagnetic alloys. The magnetic inhomogeneous state of these alloys, due to competing magnetic interactions between Fe atoms, is the most plausible scenario for explaining the magnetic behaviour in these Fe-rich FeZrB amorphous alloys including the magnetic field and temperature dependencies of the magneto-caloric effect.

Acknowledgements

Financial support from FEDER and the Spanish MICINN (NAN2004-09203-C04 and MAT2008-06542-C04) is acknowledged. Two of us (PA and JSM) thank FICyT and MICINN for PhD and "Juan de la Cierva" research contracts, respectively.

References

[1] A.M. Tishin, Y.I. Spichkin, The Magnetocaloric Effect and its Applications, IOP Publishing, Bristol, 2003.
[2] K.A. Gschneidner Jr., V.K. Pecharsky, A.O. Tsokol, Rep. Prog. Phys. 68 (2005) 1479.
[3] E. Brück, J. Phys. D: Appl. Phys. 38 (2005) R381.
[4] O. Tegus, E. Brück, K.H.J. Buschow, F.R. de Boer, Nature (Lond.) 415 (2002) 150.
[5] J. Lyubina, K. Nenkov, L. Schultz, O. Gutfleisch, Phys. Rev. Lett. 101 (2008) 177203.
[6] P. Gorria, J.L. Sánchez Llamazares, P. Álvarez, J. Sánchez Marcos, M.J. Pérez, J.A. Blanco, J. Phys. D: Appl. Phys. 41 (2008) 192003.
[7] Q. Zhang, J.H. Cho, J. Du, F. Yang, X.G. Liu, W.J. Feng, Y.J. Zhang, J. Li, Z.D. Zhang, Solid State Commun. 149 (2009) 396.
[8] P. Gorria, P. Álvarez, J. Sánchez Marcos, J.L. Sánchez Llamazares, M.J. Pérez, J.A. Blanco, Acta Mater. 57 (2009) 1724.
[9] M.-H. Phan, S.-C. Chu, J. Magn. Magn. Mater. 308 (2007) 325.
[10] S. Tencé, S. Gorsse, E. Gaudin, B. Chevalier, Intermetallics 17 (2009) 115.
[11] Q.Y. Dong, B.G. Shen, J. Chen, J. Shen, F. Wang, H.W. Zhang, J.R. Sun, Solid. State Commun. 149 (2009) 417.
[12] L. Liang, X. Hui, C.M. Zhang, G.L. Chen, J. Alloys Compd. 463 (2008) 30.
[13] J. Du, Q. Zheng, E. Brück, K.H.J. Buschow, W.B. Cui, W.J. Feng, Z.D. Zhang, J. Magn. Magn. Mater. 321 (2009) 413.
[14] B. Chevalier, J.-L. Bobet, J. Sánchez Marcos, J. Rodríguez Fernández, J.C. Gómez Sal, Appl. Phys. A 80 (2005) 601.
[15] J.J. Ipus, J.S. Blázquez, V. Franco, A. Conde, L.F. Kiss, J. Appl. Phys. 105 (2009) 123922.
[16] V. Franco, J.S. Blázquez, C.F. Conde, A. Conde, Appl. Phys. 88 (2006) 042505.
[17] V. Franco, J.S. Blázquez, A. Conde, J. Appl. Phys. 100 (2006) 064307.
[18] I. Skorvanek, J. Kovac, Czech. J. Phys. 54 (2004) D189.
[19] F. Johnson, R.D. Shull, J. Appl. Phys. 99 (2006) 08K909.
[20] V. Franco, J.S. Blázquez, A. Conde, Appl. Phys. Lett. 89 (2006) 222512.
[21] V. Franco, A. Conde, l.F. Kiss, J. Appl. Phys. 104 (2008) 033903.
[22] Y.K. Fang, C.C. Yeh, C.C. Hsieh, C.W. Chang, H.W. Chang, W.C. Chang, X.M. Li, W. Li, J. Appl. Phys. 105 (2009) 07A910.
[23] P. Gorria, J.S. Garitaonandia, M.J. Pérez, J.A. Blanco, J. Campo, Phys. Status Solidi (RRL) 3 (2009) 28.
[24] S.N. Kaul, Phys. Rev. B 27 (1983) 6923.
[25] J.M. Barandiarán, P. Gorria, I. Orue, M.L. Fdez-Gubieda, F. Plazaola, A. Hernando, Phys. Rev. B 54 (1996) 3026.
[26] R. García Calderón, L. Fernández Barquín, S.N. Kaul, J.C. Gómez Sal, P. Gorria, J.S. Pedersen, R.K. Heenan, Phys. Rev. B 71 (2005) 134413.
[27] J.M. Barandiarán, P. Gorria, J.C. Gómez Sal, L. Fernández Barquín, S.N. Kaul, IEEE Trans. Mag. 30 (1994) 4776.
[28] L. Fernández Barquín, J.C. Gómez Sal, P. Gorria, J.S. Garitaonandia, J.M. Barandiarán, Eur. Phys. J. B 35 (2003) 3.
[29] P. Gorria, I. Orue, F. Plazaola, M.L. Fernández-Gubieda, J.M. Barandiarán, IEEE Trans. Mag. 29 (1993) 2682.

[30] A. Slawska-Waniewska, P. Nowicki, H.K. Lachowicz, P. Gorria, J.M. Barandiarán, A. Hernando, Phys. Rev. B 50 (1994) 6465.
[31] J.S. Garitaonandia, P. Gorria, L. Fernández Barquín, J.M. Barandiarán, Phys. Rev. B 61 (2000) 6150.
[32] V.K. Pecharsky, K.A. Gschneidner Jr., J. Appl. Phys. 90 (2001) 4614.
[33] V. Franco, R. Caballero-Flores, A. Conde, Q.Y. Dong, H.W. Zhang, J. Magn. Magn. Mater. 321 (2009) 1115.
[34] J.M. Barandiarán, P. Gorria, I. Orúe, M.L. Fernández-Gubieda, F. Plazaola, J.C. Gómez Sal, L. Fernández Barquín, L. Fournes, J. Phys. : Condens. Matter. 9 (1997) 5671.
[35] V. Franco, A. Conde, V.K. Pecharsky, K.A. Gschneidner Jr., EPL 79 (2007) 47009.
[36] A. Aharoni, J. Appl. Phys. 56 (1984) 3479.
[37] A. Aharoni, J. Appl. Phys. 57 (1985) 648.

Chapter

6

Conclusions

The use of complementary experimental techniques to carefully characterize the morphology, crystal and magnetic structures of R_2Fe_{17} intermetallic compounds greatly helps in the understanding of their magnetic response. This magnetic behavior, and specially the magnetocaloric effect, in R_2Fe_{17} and FeZrBCu alloys exhibits common features, such as a broad $|\Delta S_M|(T)$ curve and a high value for the relative cooling power, together with outstanding magnetovolume anomalies. From this Thesis work, the following general conclusions can also be extracted:

- Magnetovolume anomalies are present in R_2Fe_{17} alloys independently of the crystal structure, showing indeed similar characteristics for both crystal structures. These anomalies consist mainly in an invariant temperature dependence of the in-plane unit cell parameters below T_C, whereas the c-axis exhibits a contraction on heating from low temperature with a minimum located around T_C, which implies an anomalous temperature dependence of the unit cell volume up to $\approx 1.5\,T_C$.
  Nevertheless, magnetocaloric effect is different depending on the magnetic order structure of the compound. In the case of those with ferromagnetic behavior, the magnetic entropy change presents a single peak, whereas in those ferrimagnetic compounds, two peaks with opposite sign can appear. Ce_2Fe_{17}, where the magnetic structure is much more complex, has also two peaks but with the same sign, associated with two different magnetic phase transitions.

- This is the first time, as far as we are aware, that Dy_2Fe_{17} is synthesized with the rhombohedral Th_2Zn_{17}-type structure. Its magnetic structure is ferrimagnetic with the Dy moments antiparallel to those of the Fe-sublattice. Its Curie temperature is slightly lower than that of the hexagonal phase ($T_C = 363\,\mathrm{K}$). The pressure dependence of M vs. T of Tm_2Fe_{17} has been also studied, which has shown an impressive change of T_C with pressure of $-100\,\mathrm{K}$ per GPa. Moreover, both spin-reorientation and ferro-paramagnetic transition tend to overlap with increasing pressure.

- The microstructure is largely modified in ferromagnetic collinear Pr_2Fe_{17} and Nd_2Fe_{17} alloys by means of high energy ball milling without substantial changes in the magnetic and

crystal structures. The grain breaking, down to nanosized scale, implies the appearance of a Curie temperature distribution, which also provokes a spreading of the $|\Delta S_M|(T)$ curve, together with a reduction of the peak value. Nevertheless, the relative cooling power slightly increases with the milling time up to 20 h. After that milling time, the reduction of the peak is uncompensated with the enlargement of the $|\Delta S_M|(T)$ width.

- By mixing two rare-earths in the form $A_xB_{2-x}Fe_{17}$ facilitates the synthesis of single-phase materials in those cases where both structures are possible, such is the case of Y, which has been mixed with Pr and Ce rare-earth obtaining the rhombohedral crystal structure. Also Dy and Ce rare-earths have been mixed, crystallizing in the rhombohedral crystal structure. Moreover, it has been shown that the values of the Curie temperature can be controlled by combining different rare-earths.

- For FeZrBCu alloys, the study of the magnetic properties up to high magnetic fields ($\mu_0\Delta H = 8$ T) has been carried out. The possibility of tunning the Curie temperature changing the %Fe, together with the spreading of the $|\Delta S_M|(T)$ in a wide range of temperatures (wider than 210 K), make them interesting candidates as magnetic refrigeration materials. Also, it has been shown that the $\Delta S_M/\Delta S_M^{Peak}(\theta)$ curves for different applied magnetic fields can collapse into the same master curve when two reference temperatures are employed.

- The combination of two FeZrBCu ribbons with different composition has shown that a flattening of the magnetic entropy change can be as large as 90 K for $\mu_0\Delta H = 5$ T, and that it is accompanied by an increase of the relative cooling power.

El uso de técnicas experimentales complementarias para realizar una cuidadosa caracterización de la morfología y de las estructuras cristalina y magnética de los compuestos intermetálicos R_2Fe_{17}, sirve para profundizar en comprensión de su propiedades magnéticas. El comportamiento magnético, y especialmente el efecto magnetocalórico, de las aleaciones R_2Fe_{17} y FeZrBCu exhiben características similares, tales como curvas anchas de $|\Delta S_M|(T)$ y un alto valor del poder relativo de refrigeración, junto con unas anomalías magnetovolúmicas destacadas. Del trabajo realizado en esta Tesis se pueden extraer las siguientes conclusiones generales:

- Las anomalías magnetovolúmicas estás presentes en las aleaciones R_2Fe_{17} independientemente de la estructura cristalina, mostrando además características similares para las dos estructuras. Estas anomalías consisten principalmente en una dependencia de los parámetros del plano de la celda unidad prácticamente nula por debajo de T_C, mientras que el parámetro en la dirección uniáxica se contrae al calentar desde baja temperatura hasta llegar a un mínimo situado en torno a T_C, lo cuál implica una dependencia anómala del volumen de la celda unidad con la temperatura hasta aproximadamente $\approx 1.5\,T_C$.
  Sinembargo, el efecto magnetocalórico es diferente dependiendo de la estructura del compuesto. En el caso de aquellos con comportamiento ferromagnético, la variación de la entropía magnética presenta un único pico, mientras que pueden aparecer dos picos en las aleaciones ferrimagnéticas. El Ce_2Fe_{17}, donde de hecho la estructura magnética es bastante compleja, tiene también dos picos, pero con el mismo signo, asociados con dos transiciones de fase magnéticas diferentes.

- Esta es la primera vez que el Dy_2Fe_{17} ha sido sintetizado con estrutura romboédrica tipo Th_2Zn_{17}. Su estructura magnética es ferrimagnética con los momentos de la subred del Dy antiparalelos a los de la subred del Fe. Su temperatura de Curie es ligeramente inferior a la correspondiente de la fase hexagonal ($T_C = 363\,\mathrm{K}$).
  También se ha estudiado el efecto de la presión sobre la dependencia de M vs. T del Tm_2Fe_{17}, que muestra un cambio de T_C con la presión de $-100\,\mathrm{K}$ per GPa. Más aún, la reorientación de espín y la transición desde el estado ferromagnético al paramagneético tienden a solaparse al aumentar la presión.

- Se ha modificado profundamente la microestructura de las aleaciones ferromagnéticas Pr_2Fe_{17} y Nd_2Fe_{17} mediante la molienda mecánica, pero sin producir cambios substanciales en las estructuras cristalina y magnética. La rotura de granos, por debajo de la escala nanoscópica, conlleva la existencia de una distribución de temperaturas de Curie, que a su vez provoca un ensanchamiento de la curva de $|\Delta S_M|(T)$ junto con una reducción del valor del pico. Sinembargo, el poder relativo de refrigeración aumenta ligeramente con el tiempo de molienda hasta 20 h. Después de este tiempo de molienda, la reducción del valor del pico no puede ser compensado con el aumento de la anchura de las curvas $|\Delta S_M|(T)$.

- Mezclando dos tierras raras en la forma $A_xB_{2-x}Fe_{17}$ se facilita la síntesis de materiales con úna única fase en aquellos casos en los que ambas estructuras son posibles, como en el caso del Y, que ha sido aleado junto con Pr y Ce, obteniendo la estructura cristalina romboédrica. Además se la aleado Dy con Ce, exhibiendo también estructura romboédrica. Más aún, se ha mostrado que el valor de la temperatura de Curie se puede controlar combinando diferentes tierras raras.

- Se ha llevado a cabo un estudio de las propiedades magnéticas de las aleaciones FeZrBCu para altos valores de campo ($\mu_0 \Delta H = 8\,\mathrm{T}$). La posibilidad de tunear la temperatura de Curie cambiando el porcentaje de Fe, junto con valores de $|\Delta S_M|(T)$ significativamente distintos de cero en un amplio rango de temperaturas (por encima de 210 K), las hacen muy interesantes como potenciales candidatos como materiales utilizables en refrigeración magnética. También se ha mostrado que las curvas $\Delta S_M/\Delta S_M^{Peak}(\theta)$ para diferentes valores de campo colapsan en la misma curva maestra cuando se utilizan dos temperaturas de referencia.

- Al combinar dos cintas de FeZrBCu con diferente composición se ha observado que se produce un aplanamiento de la variación de la entropía magnética que puede alcanzar 90 K para $\mu_0 \Delta H = 5\,\mathrm{T}$, y que viene acompañado por un aumento de la capacidad relativa de refrigeración.

Bibliography

[1] X.X. Zhang, G.H. Wen, F.W. Wang, W.H. Wang, C.H. Yu, and G.H. Wu. *Applied Physics Letters*, 77(19):3072–3074, 2000. 1, 1.1.2

[2] O. Tegus, E. Brück, K.H.J. Buschow, and F.R. de Boer. *Nature*, 415(6868):150–152, 2002. 1.1.2

[3] A. Yan. *Rare Metals*, 25(6, Supplement 1):544–549, 2006.

[4] V. Franco, J.M. Borrego, A. Conde, and S. Roth. *Applied Physics Letters*, 88(13):132509, 2006. 1

[5] B.F. Yu, Q. Gao, B. Zhang, X.Z. Meng, and Z. Chen. *International Journal of Refrigeration*, 26(6):622–636, 2003. 1, 1.1.2, 1.2, 1.1.2, 1.1.2

[6] E. Warburg. *Ann. Phys*, 13:141–164, 1881. 1.1

[7] A.M. Tishin and Y.I. Spichkin. *Magnetocaloric Effect and Its Applications*. Series in Condensed Matter Physics. Institute of Physics Publishing, London, 1 edition, 2003. 1.1, 1.1.2

[8] V.K. Pecharsky and K.A. Gschneidner Jr. *Journal of Magnetism and Magnetic Materials*, 200:44–56, 1999. 1.1, 1.1.1

[9] K.H.J. Buschow and F.R. Boer. *Physics of magnetism and magnetic materials*. Springer, New York, 1 edition, 2003. 1.1

[10] H.B. Callen. *Thermodynamics and an Introduction to Thermostatistics*. John Wiley & Sons, Inc., Republic of Singapore, 2 edition, 1985. 1.1.1

[11] K.H.J. Buschow, editor. *Handbook of Magnetic Materials*, volume 12. Elsevier, Amsterdam, 1 edition, 1999.

[12] V.K. Pecharsky, K.A. Gschneidner, Jr., A. Pecharsky, and A. Tishin. *Physical Review B*, 64(14):144406, 2001. 1.1

[13] A. Tishin, A. Derkach, Y. Spichkin, M. Kuzmin, A. Chernyshov, K.A. Gschneidner, Jr., and V.K. Pecharsky. *Journal of Magnetism and Magnetic Materials*, 310(2):2800–2804, 2007. 1.1.2, 1.1.2

[14] A. Planes, Ll. Mañosa, and M. Acet. *Journal of Physics: Condensed Matter*, 21(23):233201, 2009. 1.1.1

[15] E. Brück. *Journal of Physics D: Applied Physics*, 38(23):R381–R391, 2005. 1.1.1, 1.1.2

[16] A.R. Dinesen, S. Linderoth, and S. Morup. *Journal of Physics: Condensed Matter*, 17(39):6257–6269, 2005. 1.1.1, 1.1.1

[17] L. Tocado, E. Palacios, and R. Burriel. *Journal of Magnetism and Magnetic Materials*, 290-291:719–722, 2005. 1.1.1

[18] S.Y. Dan'kov, A.M. Tishin, V.K. Pecharsky, and K.A. Gschneidner Jr. *Physical Review B*, 57(6):3478, 1998. 1.1.1

[19] K.A. Gschneidner, Jr., V.K. Pecharsky, and A.O. Tsokol. *Reports on Progress in Physics*, 68(6):1479–1539, 2005. 1.1.1, 1.1.1

[20] V.K. Pecharsky and K.A. Gschneidner Jr. *Journal of Applied Physics*, 86(1):565–575, 1999. 1.1.1

[21] Ll. Mañosa, D. González-Alonso, A. Planes, E. Bonnot, M. Barrio, J.L. Tamarit, S. Aksoy, and M. Acet. *Nature Materials*, 9(6):478–481, 2010. 1.1.1

[22] P. Debye. *Annalen der Physik*, 386(25):1154–1160, 1926. 1.1.2

[23] W.F. Giauque. *Journal of the American Chemical Society*, 49(8):1864–1870, 1927. 1.1.2

[24] W.F. Giauque and D.P. MacDougall. *Physical Review*, 43(9):768, 1933. 1.1.2

[25] G.V. Brown. *Journal of Applied Physics*, 47:3673–3680, 1976. 1.1.2

[26] C. Zimm, A. Jastrab, A. Sternberg, V.K. Pecharsky, K.A. Gschneidner, Jr., M. Osborne, and I. Anderson. *Advances in cryogenic engineering*, 1998. 1.1.2

[27] V.K. Pecharsky and K.A. Gschneidner Jr. *International Journal of Refrigeration*, 29(8):1239–1249, 2006. 1.1.2

[28] V.K. Pecharsky and K.A. Gschneidner Jr. *Physical Review Letters*, 78(23):4494, 1997. 1.1.2

[29] K. Matsumoto, T. Kondo, S. Yoshioka, K. Kamiya, and T. Numazawa. *Journal of Physics: Conference Series*, 150(1):012028, 2009. 1.1.2

[30] S.F. Kral and J.A. Barclay. *Applications of Cryogenic Technology*, volume 10. Springer, New York, 1991. 1.1.2

[31] G. Green, J. Chafe, J. Stevens, and J. Humphrey. *Advances in Cryogenic Engineering*, 35:1165–1174, 1990. 1.1.2

[32] T. Hashimoto, T. Kuzuhara, M. Sahashi, K. Inomata, A. Tomokiyo, and H. Yayama. *Journal of Applied Physics*, 62(9):3873–3878, 1987. 1.1.2

[33] G. Brown. *IEEE Transactions on Magnetics*, 13(5):1146–1148, 1977.

[34] F. Shir, L. Yanik, L.H. Bennett, E. Della Torre, and R.D. Shull. *Journal of Applied Physics*, 93(10):8295, 2003. 1.1.2

[35] M.A. Richard, A.M. Rowe, and R. Chahine. *Journal of Applied Physics*, 95(4):2146–2150, 2004. 1.1.2, 1.1.2

[36] K.H.J. Buschow, editor. *Handbook of Magnetic Materials*, volume 17. Elsevier, Amsterdam, 1 edition, 2007. 1.3

[37] A. Rowe, A. Tura, J. Dikeos, and R. Chahine. In *Proceedings of the International Green Energy Conference*, volume 12, page 16, 2005. 1.4, 1.1.2

[38] K. Engelbrecht. *A Numerical Model of an Active Magnetic Regenerator Refrigeration System*. PhD thesis, University of Wosconsin-Madison, 2004. 1.1.2

[39] K. Engelbrecht, G.F. Nellis, and S.A. Klein. In *Proceedings of the 13th International Cryocooler Conference*. Springer, 2005. 1.1.2

[40] M.E. Wood and W.H. Potter. *Cryogenics*, 25(12):667–683, 1985. 1.1.2

[41] P. Gorria, J.L. Sánchez Llamazares, P. Alvarez, M.J. Pérez, J. Sánchez Marcos, and J.A. Blanco. *Journal of Physics D: Applied Physics*, 41(19):192003, 2008. 1.1.2

[42] J. Du, Q. Zheng, Y.B. Li, Q. Zhang, D. Li, and Z.D. Zhang. *Journal of Applied Physics*, 103(2):023918, 2008. 1.1.2

[43] C. Zimm, A. Jastrab, A. Strenberg, V.K. Pecharsky, K.A. Gschneidner, Jr., M. Osborne, and I. Anderson. *Journal of Alloys and Compounds*, 43:1759–1766, 1998. 1.1.2

[44] U. Lucia. *arXiv:1011.1684v1*, 2010. 1.1.2

[45] E. du Tremolet de Lacheisserie and D. Gignoux, editors. *Magnetism*, volume 1: Fundamentals. Springer, Boston, 2004. 1.5

[46] E.P. Wohlfarth and K.H.J. Buschow, editors. *Ferromagnetic Materials*, volume 5. Elsevier, Amsterdam-New York-Oxford, 1 edition, 1988. 1.2, 1.6

[47] A.V. Andreev and A. Lindbaum. *Journal of Alloys and Compounds*, 297(1-2):43–45, 2000. 1.2, 3.1

[48] A. Authier, H. Fuess, T. Hahn, H. Wondratschek, U. Müller, U. Shmueli, E. Prince, A. Authier, V. Kopský, D.B. Litvin, M.G. Rossmann, E. Arnold, S. Hall, and B. McMahon, editors. *International Tables for Crystallography*, volume D. Chester, England, 1 edition, 2006. 1.2

[49] K.H.J. Buschow, editor. *Handbook of Magnetic Materials*, volume 14. Elsevier, Amsterdam, 1 edition, 2002. 1.2

[50] K.H.J. Buschow, editor. *Handbook of Magnetic Materials*, volume 16. Elsevier, Amsterdam-Oxford, 1 edition, 2006. 1.2

[51] R.N. Singh, A.K. George, and S. Arafin. *Journal of Physics D: Applied Physics*, 39(6):1220–1225, 2006. 1.2

[52] J. Sánchez-Marcos. *Calor específico y efecto magnetocalórico en intermetálicos de Gd, hidruros de Ce y fosfatos de metales de transición*. PhD thesis, University of Cantabria, Facultad de Ciencias, 2004. 1.2

[53] K. Irisawa, A. Fujita, K. Fukamichi, M. Yamada, H. Mitamura, T. Goto, and K. Koyama. *Physical Review B*, 70(21), 2004. 1.2

[54] K.H.J. Buschow, editor. *Handbook of Magnetic Materials*, volume 8. Elsevier, Amsterdam-London-New York, 1 edition, 1995. 1.2

[55] E.P. Wohlfarth, editor. *Ferromagnetic Materials*, volume 1. North-Holland Publishing Company, Amsterdam-New York, 1 edition, 1980. 1.3

[56] H. Wondratschek, U. Müller, H. Fuess, Th. Hahn, H. Wondratschek, U. Müller, U. Shmueli, E. Prince, A. Authier, V. Kopský, D. B. Litvin, M. G. Rossmann, E. Arnold, S. Hall, and B. McMahon, editors. *International Tables for Crystallography*, volume A1. International Union of Crystallography, Chester, England, 1 edition, 2006. 1.3

[57] Q. Johnson, D.H. Wood, G.S. Smith, and A.E. Ray. *Acta Crystallographica Section B: Structural Crystallography and Crystal Chemistry*, 24(2):274–276, 1968. 1.3

[58] R. Kumar and W.B. Yelon. *Journal of Applied Physics*, 67(9):4641–4643, 1990. 1.3

[59] D. Givord, F. Givord, R. Lemaire, W.J. James, and J.S. Shah. *Journal of the Less Common Metals*, 29(4):389–396, 1972. 1.3, 1.3

[60] A.N. Christensen and R.G. Hazell. *Acta Chemica Scandinavica Series a-Physical and Inorganic Chemistry*, 34(6):455–459, 1980. 3.1

[61] J. Park, Y. Jo, J.G. Park, K. Prokes, S. Welzel, C.H. Lee, N. Kudrevatykh, E. Valiev, A. Pirogov, and D. Sheptyakov. *Journal of Magnetism and Magnetic Materials*, 237(2):158–168, 2001.

[62] I.S. Tereshina, S.A. Nikitin, J. Stepien-Damm, L.D. Gulay, N.Y. Pankratov, A.A. Salamova, V.N. Verbetsky, and W. Suski. *Journal of Alloys and Compounds*, 329(1-2):31–36, 2001. 1.3

[63] M.S. Ben Kraiem and A. Cheikhrouhou. *Journal of Alloys and Compounds*, 397(1-2):37–41, 2005. 1.3, 1.3, 4.1

[64] A. Lukoyanov, E. Kokorina, M. Medvedev, and I. Nekrasov. *Physical Review B*, 80(10), 2009. 1.7

[65] K.H.J. Buschow, editor. *Handbook of Magnetic Materials*, volume 6. Elsevier, Amsterdam-London-New York-Tokyo, 1 edition, 1991. 1.3, 1.4

[66] K. Koyama, T. Kajitani, Y. Morii, H. Fujii, and M. Akayama. *Physical Review B*, 55(17):11414, 1997. 1.3

[67] D. Givord, R. Lemaire, W. James, J.M. Moreau, and J. Shah. *IEEE Transactions on Magnetics*, 7(3):657–659, 1971. 1.3

[68] K.H.J. Buschow. *Reports on Progress in Physics*, 40(10):1179–1256, 1977. 1.3, 3.1

[69] Z. Arnold, J. Kamarad, P.A. Algarabel, B. Garcialanda, and M.R. Ibarra. *IEEE Transactions on Magnetics*, 30(2):619–621, 1994. 1.3, 3.1

[70] A.I. Gubanov. *Soviet Physics: Solid State*, 2:468–471, 1960. 1.4

[71] S. Mader, A.S. Nowick, and H. Widmer. *Acta Metallurgica*, 15(2):203–214, 1967.

[72] S. Kobe and A.R. Ferchmin. *Journal of Materials Science*, 12(9):1713–1749, 1977. 1.4

[73] A. Hernando. *Nuevos Materiales: Los Vidrios Metálicos*. Eudema, Madrid, 1987. 1.4

[74] T.M. Hayes, J.W. Allen, J.Tauc, B.C. Giessen, and J.J. Hauser. *Physical Review Letters*, 40(19):1282, 1978. 1.4

[75] H. Kronmüller, M. Fähnle, M. Domann, H. Grimm, R. Grimm, and B. Gröger. 13(1-2):53–70, 1979. 1.4

[76] J.M.D. Coey, J. Chappert, J.P. Rebouillat, and T.S. Wang. *Physical Review Letters*, 36(17):1061, 1976. 1.4

[77] J.M.D. Coey. *Journal of Applied Physics*, 49(3):1646, 1978. 1.4

[78] D.H. Ryan, J.M.D. Coey, E. Batalla, Z. Altounian, and J.O. Ström-Olsen. *Physical Review B*, 35(16):8630, 1987. 1.4

[79] C.L. Chien, D. Musser, E.M. Gyorgy, R.C. Sherwood, H.S. Chen, F.E. Luborsky, and J.L. Walter. *Physical Review B*, 20(1):283, 1979. 1.4

[80] H. Kronmüeller and S. Parkin, editors. *Handbook of Magnetism and Advanced Magnetic Materials*. Wiley-Interscience, New York, 1 edition, 2007. 1.4

[81] S.N. Kaul, V. Siruguri, and G. Chandra. *Physical Review B*, 45(21):12343, 1992. 1.4

[82] R. Garcia Calderon, L. Fernandez Barquin, S.N. Kaul, J. C. Gomez Sal, P. Gorria, J.S. Pedersen, and R.K. Heenan. *Physical Review B*, 71(13):134413, 2005. 1.4, 5.1

[83] S.Y. Dan'kov, V.V. Ivtchenko, A.M. Tishing, V.K. Pecharsky, and K.A. Gschneidner Jr. *Advances in Cryogenic Engineering (Materials)*, 46:397–404, 2000. 1.5

[84] K. Mandal, A. Yan, P. Kerschl, A. Handstein, O. Gutfleisch, and K.H. Muller. *Journal of Physics D: Applied Physics*, 37(19):2628–2631, 2004. 1.5

[85] I. Orue, M. L. Fdez-Gubieda, P. Gorria, S. Pizzini, and A. Fontaine. *Journal of Synchrotron Radiation*, 8(2):443–445, 2001. 1.5

[86] B. Hernando, P. Alvarez, J.D. Santos, P. Gorria, M.L. Sanchez, J. Olivera, M.J. Perez, and V.M. Prida. *Journal of Magnetism and Magnetic Materials*, 300(1):e59–e62, 2006.

[87] A. Fernandez-Martinez, P. Gorria, G.J. Cuello, J.D. Santos, and M.J. Perez. *Journal of Non-Crystalline Solids*, 353(8-10):855–858, 2007. 2.2.1

[88] J.M. Barandiarán, P. Gorria, I. Orúe, M. L. Fdez-Gubieda, F. Plazaola, and A. Hernando. *Physical Review B*, 54(5):3026, 1996.

[89] J.M. Barandiarn, P. Gorria, I. Orúe, M.L. Fernández-Gubieda, F. Plazaola, J.C. Gómez Sal, L. Fernández Barquín, and L. Fournes. *Journal of Physics: Condensed Matter*, 9(26):5671–5685, 1997. 1.5

[90] V. Franco, C. F. Conde, J. S. Blázquez, A. Conde, P. Švec, D. Janičkovič, and L. F. Kiss. *Journal of Applied Physics*, 101(9):093903, 2007. 1.5

[91] V. Franco and A. Conde. *International Journal of Refrigeration*, 33(3):465–473, 2010. 1.5, 4.1

[92] C.R. Brundle, C.A. Evans, Jr., and S. Wilson, editors. *Encyclopedia of materials characterization: surfaces, interfaces, thin films*. Materials characterization series. Manning Publications Co., United States of America, 1 edition, 1992. 2.2.1, 2.2.2, 2.2.2

[93] J. Baruchel, J.L. Hodeau, M.S. Lehmann, J.R. Regnard, and C. Schlenker, editors. *Neutron and synchrotron radiation for condensed matter studies.*, volume Volume I: Theory, instruments and methods. Springer-Verlag, France, 1 edition edition, 1993. 2.2.1, 2.2.1

[94] D. Martinez-Blanco, P. Gorria, J.A. Blanco, M.J. Perez, and J. Campo. *Journal of Physics: Condensed Matter*, 20(33):335213, 2008. 2.2.1, 3.1

[95] V.K. Pecharsky and P. Zavalij. *Fundamentals of powder diffraction and structural characterization of materials*. Springer, New York, 2005. 2.2.1, 2.2.2, 3.2

[96] J. Rodriguez-Carvajal. *Physica B: Condensed Matter*, 192(1-2):55–69, 1993. 2.2.1

[97] A.P. Hammersley. ESRF Internal Report, 1998. 2.2.1

[98] R. Erni, M.D. Rossell, C. Kisielowski, and U. Dahmen. *Physical Review Letters*, 102(9):096101, 2009. 2.2.2

[99] P.J. Goodhew, F.J. Humphreys, and R. Beanland. *Electron microscopy and analysis*. Taylor & Francis, London and New York, 3 edition, 2000. 2.2.2, 2.2.2, 2.2.2

[100] M. Tejedor, A. Fernandez, and B.Hernando. *Rev.Sci.Instrum.*, 57(7):1446–1447, 1986. 2.3.1

[101] M.J. Pérez. *Estructura e imanación de saturación en materiales magnéticos amorfos en función de la temperatura*. PhD thesis, University of Oviedo, 1995. 2.3.1

[102] N. Yang. *Synchrotron diffraction studies of spontaneous magnetostriction in rare earth transition metal compounds*. PhD thesis, Iowa State University, 2004. 3.1

[103] V.I. Voronin, V.V. Serikov, N.M. Kleinerman, and A.G. Kuchin. *Physica B: Condensed Matter*, 276-278:570–571, 2000. 3.1

[104] O. Isnard, D. Hautot, G. J. Long, and F. Grandjean. *Journal of Applied Physics*, 88(5):2750–2759, 2000. 3.1, 3.1

[105] D. Givord and R. Lemaire. *IEEE Transactions on Magnetics*, 10(2):109–113, 1974. 3.1

[106] Y. Janssen, S. Chang, A. Kreyssig, A. Kracher, Y. Mozharivskyj, S. Misra, and P.C. Canfield. *Physical Review B*, 76(5), 2007. 3.1, 3.1

[107] A.V. Andreev, F.R. de Boer, T.H. Jacobs, and K.H.J. Buschow. *Physica B: Condensed Matter*, 175(4):361–369, 1991. 3.1

[108] P. Gorria, R. Boada, A. Fernández-Martínez, G. Garbarino, R.I. Smith, J. Chaboy, J.I. García-Alonso, D. Martínez-Blanco, G.R. Castro, M. Mezouar, A. Hernando, and J.A. Blanco. *Physica Status Solidi-Rapid Research Letters*, 3(4):115–117, 2009. 3.1

[109] H. Zhang, X. Wu, K.G. Nickel, J. Chen, and V. Presser. *Journal of Applied Physics*, 106(1):013519, 2009. 3.1

[110] K. Koyama, H. Fujii, T. Goto, H. Fukuda, and Y. Janssen. *Physica B*, 294:168–171, 2001. 3.1

[111] P.C.M. Gubbens and K.H.J. Buschow. *Journal of Applied Physics*, 44(8):3739–3741, 1973. 3.1

[112] P.C.M. Gubbens, A.A. Moolenaar, T.H. Jacobs, and K.H.J. Buschow. *Journal of Alloys and Compounds*, 176(1):115–121, 1991. 3.1

[113] P.J. von Ranke, N.A. de Oliveira, B.P. Alho, E.J.R. Plaza, V.S.R. de Sousa, L. Caron, and M.S. Reis. *Journal of Physics: Condensed Matter*, 21(5):056004, 2009. 3.1

[114] P. Alvarez, P. Gorria, and J.A. Blanco. *Physical Review B*, Accepted, 2011. 3.1

[115] B.D. Cullity and C.D. Graham. *Introduction to Magnetic Materials*. Addison-Wesley Publishing Company, 2 edition, 2008. 3.1

[116] T.H. Jacobs, K.H.J. Buschow, G.F. Zhou, and F.R. de Boer. *Physica B: Condensed Matter*, 179(3):177–183, 1992. 3.1

[117] K. Ohno, K. Shimazawa, T. Urakabe, T. Saito, K. Shinagawa, and T. Tsushima. *Journal of Alloys and Compounds*, 222(1-2):78–81, 1995. 3.1

[118] A. Hernando, I. Navarro, and P. Gorria. *Physical Review B*, 51:3281, 1995. 3.1

[119] K. Kamaraju, J.B. Yang, W.B. Yelon, O.A. Pringle, W.J. James, and P. I'Heritier. *Journal of Applied Physics*, 91(10):7893, 2002. 4.1

[120] K. Kamaraju, J.B. Yang, W.B. Yelon, O.A. Pringle, W.J. James, Q. Cai, Z. Chu, and P. I'Heritier. *Journal of Applied Physics*, 93(10):6936, 2003.

[121] Y.G. Xiao, G.H. Rao, Q. Zhang, G.Y. Liu, Y. Zhang, and J.K. Liang. *Journal of Alloys and Compounds*, 419(1-2):15–20, 2006. 4.1

[122] Y.G. Xiao, G.H. Rao, Q. Zhang, G.Y. Liu, Y. Zhang, and J.K. Liang. *Journal of Alloys and Compounds*, 407(1-2):1–7, 2006. 4.1

[123] O. Isnard, S. Miraglia, C. Giorgetti, E. Dartyge, G. Krill, and D. Fruchart. *Journal of Alloys and Compounds*, 262:198–201, 1997. 4.1

[124] F. Grandjean, G.D. Waddill, T.R. Cummins, D.P. Moore, G.J. Long, and K.H.J. Buschow. *Solid State Communications*, 109(12):779–784, 1999. 4.1

[125] V. Franco, J.S. Blazquez, and A. Conde. *Applied Physics Letters*, 89(22):222512, 2006. 4.1

[126] V. Franco, A. Conde, V.K. Pecharsky, and K.A. Gschneidner Jr. *Europhysics Letters*, 79(4):5 pages, 2007. 4.1, 4.1

[127] V. Franco, R. Caballero-Flores, A. Conde, Q.Y. Dong, and H.W. Zhang. *Journal of Magnetism and Magnetic Materials*, 321(9):1115–1120, 2009. 4.1, 4.1

[128] V. Franco, J.S. Blazquez, M. Millan, J.M. Borrego, C.F. Conde, and A. Conde. *Journal of Applied Physics*, 101(9):09C503, 2007. 4.1

[129] L. Fernandez Barquin, P. Gorria, J.M. Barandiaran, J.C. Gomez Sal, and J. Rodriguez Carvajal. *Physica B: Condensed Matter*, 234-236:418–420, 1997. 5.1

[130] P. Gorria. *Estudio de las propiedades magnéticas de algunas aleaciones amorfas y nanocristalinas ricas en Hierro*. PhD thesis, University of Basque Country, 1996. 5.1

[131] V. Franco, A. Conde, J.M. Romero-Enrique, and J.S. Blázquez. *Journal of Physics: Condensed Matter*, 20(28):285207, 2008. 5.1

Appendix

Scilab Functions

In this appendix, some functions written in Scilab used to obtain the MCE properties from magnetization and heat capacity measurements are included. Each function is shortly described in the head of the function.

```
function  mce(X,s,ncampos,const,f,b,X0)
//This function obtains the magnetic entropy change and other magnitudes from the M(T,H)
//data, using the Maxwell relation.
//Input:
//X: it is the magnetization in emu/g, T in K and H in T
//s: # of points for the interpolation
//ncampos: # of fields for the universal curve
//const: Constant of reference for the universal curve
//f: # of fields for the fit to the approach to saturation law
//b: seed of the b parameter of the the approach to saturation
//X0: seed of the b parameter of the the approach to saturation

  n=size(X,1);
//It is necessary to know the number of temperatures of the sample
  l=2; t=1;
  while l<n do
    if abs(X(l,1)-X(l-1,1))>0.8  //Temperature values are in the first column of X
      t=t+1;
    end
    l=l+1;
  end
//Number of different fields
  h=n/t;
//Integration and we save the results in a auxiliary column
  for m=1:h:n-1                  //There are h fields for each temperature
    for i=1:h-1                  //We integrate M(H) for each temperature
      X(m+i,4)= intsplin(X(m:m+i,2),X(m:m+i,3));   //Integration of experimental data
    end
  end
//Now we derivate
```

```
  for m=1:h
    inte(1:t,m)=-X(m:h:$,4);
    T(1:t,m)=X(m:h:$,1);
    H(1:t,m)=X(m:h:$,2);
    M(1:t,m)=X(m:h:$,3);
    a=diff(inte(1:$,m));
    b=diff(T(1:$,m));
    dS(1:size(a,1),m)=-a./b;
  end
//RCP(H)
//First we obtain DSMax and the temperature at which appears for each magnetic field
  [dSMax,pos]=max(dS,'r');    //dS_Max and its position (pos) into the array for each field
  TMax=T(pos);                //Temperature of the maximum
//Secondly, we interpolate DS and T
  for j=1:h
    if pos(j)>1
      inter1=linspace(T(1,j),T(pos(j),j),s);
      inter2=linspace(T(pos(j),j),T($-1,j),s);
      T1inter(1:s,j)=interp1(T(1:pos(j),j),T(1:pos(j),j),inter1,'spline')';
      dS1inter(1:s,j)=interp1(T(1:pos(j),j),dS(1:pos(j),j),inter1,'spline')';
      T2inter(1:s,j)=interp1(T(pos(j):$-1,j),T(pos(j):$-1,j),inter2,'spline')';
      dS2inter(1:s,j)=interp1(T(pos(j):$-1,j),dS(pos(j):$,j),inter2,'spline')';
    end
  end
//Third, we locate the position of dSMax/2 and the temperature for each field
  for j=1:h
    [dif,T1pos]=min(abs(dS1inter(1:s,j)-dSMax(j)/2));
    T1Pos(j)=T1pos;
    T1(j)=T1inter(T1pos,j);
    [dif,T2pos]=min(abs(dS2inter(1:s,j)-dSMax(j)/2));
    if dSMax(j)>0
      percent(j)=dif/dSMax(j)*100;
    else
      percent(j)=0;
    end
    if percent(j)>1
      T2(j)=0;
    else
      T2Pos(j)=T2pos;
      T2(j)=T2inter(T2pos,j);
    end
  end
//RCP1 = DS*DT
  R1=dSMax'.*(T2-T1);
//RCP2 = area below the curve
  for j=2:h
    if T2(j)>0
   R2(j)=intsplin(T1inter(T1Pos(j):s,j),dS1inter(T1Pos(j):s,j))
         +intsplin(T2inter(1:T2Pos(j),j),dS2inter(1:T2Pos(j),j));
    else
      R2(j)=0;
    end
  end
//RCP3 = maximum DS*DT
  for j=2:h
```

```
    for i=1:s
      [dif(i),pos0(i)]=min(abs(dS2inter(i,j)-dS1inter(1:s,j)),'r');
    end
    [WPmaximo,WPpos]=max((T2inter(1:s,j)-T1inter(pos0(1:s),j)).*dS2inter(1:s,j));
    if WPpos<s then
      R3(j)=WPmaximo;
      TH(j)=T2inter(WPpos,j);
      TC(j)=T1inter(pos0(WPpos),j);
    else
      R3(j)=0;
      TH(j)=0;
      TC(j)=0;
    end
  end
//Universal Curve
  DOS=0;TR1=0;TR2=0;UNA=0;
  rep=2;  const=0.5; ncampos=10;
  while rep==2
    mess=messagebox("One or two Temperatures?", "modal", "info", ["Dos" "Una"]);
    if mess==2 then  //One Temperature
      mess=messagebox("Tr < Tc? ", "modal", "info", ["No" "Yes"]);
      if mess==1 then   //Tr > TC
        for j=ncampos:h
          [dSMax1,pos1]=max(dS1inter(1:s,j));
          [dSMax2,pos2]=max(dS2inter(1:s,j));
          dSNorm1(1:s,j)=dS1inter(1:s,j)/dSMax1;
          dSNorm2(1:s,j)=dS2inter(1:s,j)/dSMax2;
          [difconst,posconst]=min(abs(dSNorm2(1:s,j)-const));
          Theta11(1:s,j)=(T1inter(1:s,j)-T2inter(pos2,j))/(T2inter(posconst,j)-T2inter(pos2,j));
          Theta21(1:s,j)=(T2inter(1:s,j)-T2inter(pos2,j))/(T2inter(posconst,j)-T2inter(pos2,j));
        end
        TR2=1;
      else  //Tr < TC
        for j=ncampos:h
          [dSMax1,pos1]=max(dS1inter(1:s,j));
          [dSMax2,pos2]=max(dS2inter(1:s,j));
          dSNorm1(1:s,j)=dS1inter(1:s,j)/dSMax1;
          dSNorm2(1:s,j)=dS2inter(1:s,j)/dSMax2;
          [difconst,posconst]=min(abs(dSNorm1(1:s,j)-const));
          Theta12(1:s,j)=-(T1inter(1:s,j)-T1inter(pos1,j))/(T1inter(posconst,j)-T1inter(pos1,j));
          Theta22(1:s,j)=-(T2inter(1:s,j)-T1inter(pos1,j))/(T1inter(posconst,j)-T1inter(pos1,j));
        end
        TR1=1;
      end
    else            //Two Temperatures
      for j=ncampos:h
        [dSMax1,pos3]=max(dS1inter(1:s,j));
        [dSMax2,pos4]=max(dS2inter(1:s,j));
        dSNorm1(1:s,j)=dS1inter(1:s,j)/dSMax1;
        dSNorm2(1:s,j)=dS2inter(1:s,j)/dSMax2;
        [difconst,posconst1]=min(abs(dSNorm1(1:s,j)-const));
        Theta3(1:s,j)=-(T1inter(1:s,j)-T1inter(pos3,j))/(T1inter(posconst1,j)-T1inter(pos3,j));
        Theta4(1:s,j)=(T2inter(1:s,j)-T2inter(pos4,j))/(T2inter(posconst2,j)-T2inter(pos4,j));
      end
      DOS=1;
```

```
    end
   rep=messagebox("Do you repeat the calculation?", "modal", "info", ["No" "Yes"]);
  end
//Saturation magnetization
    rep=2; j=0;
    deff('y=MS(x)','y=a*(1-b/x^2)+c*x')
    deff('e=G(p,z)','a=p(1),b=p(2),c=p(3),x=z(1),y=z(2),e=y-MS(x)')
    Z=[H(1,h-f:$);M(1,h-f:$)];
    [p,err]=fit_dat(G,[max(Z);b;c],Z);
    a(1)=p(1);b(1)=p(2);c(1)=p(3);E(1)=err;
    for k=2:t
      Z=[H(k,h-f:$);M(k,h-f:$)];
      [p,err]=fit_dat(G,[max(Z);b(k-1);c(k-1)],Z);
    end
  end
//Exponent n (DS is proportional to H^n)
   for m=1:t-1
    c=diff(log(abs(dS(m,2:h))));
    d=diff(log(H(m,2:h)));
    nexp(m,1:size(c,2))=c./d;
  end
endfunction

-------------------------------------------------------------------------------

function  twosamples(X,Y,a)
//Determines the resultant DS of two combined samples by means of weighted averaging
//the magnetization of both samples.
//Input:
//X: it is the magnetization in emu/g, T in K and H in T, of the first sample
//Y: it is the magnetization in emu/g, T in K and H in T, of the second sample
//a: proportion of the first sample

  n=size(X,1);
  m=size(Y,1);
//It is necessary to know the number of temperatures of the first sample
  l=2; t1=1;
  while l<n do
    if abs(X(l,1)-X(l-1,1))>0.8
      t1=t1+1;
    end
    l=l+1;
  end
//We get the number of different fields for the first sample
  h1=n/t1;
//It is necessary to know the number of temperatures of the second sample
  l=2; t2=1;
  while l<m do
    if abs(Y(l,1)-Y(l-1,1))>0.8
      t2=t2+1;
    end
    l=l+1;
  end
//We get the number of different fields for the second sample
  h2=m/t2;
```

```
//We store field, temperature and magnetization in the following matrix for the first sample:
  for i=1:h1
    T1(1:t1,i)=X(i:h1:$,1);
    H1(1:t1,i)=X(i:h1:$,2);
    M1(1:t1,i)=X(i:h1:$,3);
  end
//We store field, temperature and magnetization in the following matrix for the second sample:
  for i=1:h2
    T2(1:t2,i)=Y(i:h2:$,1);
    H2(1:t2,i)=Y(i:h2:$,2);
    M2(1:t2,i)=Y(i:h2:$,3);
  end
//We interpolate M1 for the T2 and H2 values
  for i=1:h1
    Magn(1:t2,i)=interp1(T1(1:$,1),M1(1:$,i),T2(1:$,1),'spline');
  end
//We do the weighted average
  Z=a*Magn+(1-a)*M2;
//We call MCE function to obtain the MCE properties of the combined system
call mce(Z,s,ncampos,const,f,b,X0)
endfunction

-------------------------------------------------------------------------------

function adiabatica(X,Y)
//This function obtains the adiabatic entropy change from the temperature depence of the
//total entropy, and the DS(T,H) data, as the isentropic distance between two isofield
//curves for H=0 and H of the entropy-temperature diagram.
//Input:
//X: S(T) obtained from heat capacity measurements
//Y: DS(T,H1,H2,.....Hn) data

  n=size(Y,1);
  m=size(Y,2);
//We interpolate the entropy at zero field in the temperature range of DS
  Sinter(1:n,1)=interp1(X(1:$,1),X(1:$,2),Y(1:$,1)',spline')';
//Calculation of the total entropy (S(T,H=0)+DS) at the DS temperatures
  for j=2:m
    Stot(1:n,j)=Sinter(1:n,1)+Y(1:n,j);
  end
//Interpolation of the temperatures of the entropy at zero field for the values of the
//total entropy
  for j=1:m-1
    Tinter(1:n,j)=interp1(X(1:$,2),X(1:$,1),Stot(1:n,j+1)',spline')';
  end
//DT_adi is the difference between the temperatures at zero field and at field H for the
//same value of H
  for j=1:m-1
    DT(1:n,j)=Tinter(1:n,j)-Y(1:n,1);
  end
endfunction
```

Appendix

Publications

This thesis is presented in the form of compendium of scientific articles already published or under review, which summarizes the results obtained and conclusions reached in the development of this study. In order to give an overview of my research from the beginning, here a list of the published and submitted articles which resulted from this work is presented, together with other articles related to this topic. Also, other papers from the results of my other studies in several Material Science topics are summarized.

Published

I) P. Gorria, J.L. Sánchez Llamazares, P. Álvarez, M.J. Pérez, J. Sánchez Marcos, and J.A. Blanco, Relative cooling power enhancement in magneto-caloric nanostructured Pr_2Fe_{17}, *Journal of Physics D: Applied Physics*, 41: 192003, 2008.

II) P. Álvarez, J.L. Llamazares, M.J. Perez, B. Hernando, J.D. Santos, J. Sánchez Marcos, J.A. Blanco, and P. Gorria, Microstructural and magnetic characterization of Nd_2Fe_{17} ball milled alloys, *Journal of Non-Crystalline Solids*, 354: 5172-5174, 2008.

III) J.S. Llamazares, M.J. Pérez, P. Álvarez, J.D. Santos, M.L. Sánchez, B. Hernando, J.A. Blanco, J.S. Marcos, and P. Gorria, The effect of ball milling in the microstructure and magnetic properties of Pr_2Fe_{17} compound, *Journal of Alloys and Compounds*, 483: 682-685, 2009.

IV) P. Gorria, P. Álvarez, J.S. Marcos, J.L. Sánchez Llamazares, M.J. Pérez, and J.A. Blanco, Crystal structure, magnetocaloric effect and magnetovolume anomalies in nanostructured Pr_2Fe_{17}, *Acta Materialia*, 57:1724-1733, 2009.

V) P. Álvarez, P. Gorria, V. Franco, J. Sánchez Marcos, M.J. Pérez, J.L. Sánchez Llamazares, I. Puente Orench, and J.A. Blanco, Nanocrystalline Nd_2Fe_{17} synthesized by high-energy

ball milling: crystal structure, microstructure and magnetic properties, *Journal of Physics: Condensed Matter*, 22:216005 (8pp), 2010.

VI) P. Álvarez, M.J. Pérez, J.A. Blanco, P. Gorria, L.F. Barquín, and J. Sánchez-Marcos, Magneto-caloric effect in FeZrB amorphous alloys near room temperature, *Journal of Alloys and Compounds*, 504(1):S150-S154, 2010.

VII) P. Álvarez, P. Gorria, J. Sánchez Marcos, L. Fernández Barquín, and J.A. Blanco, The role of boron on the magneto-caloric effect of FeZrB metallic glasses, *Intermetallics*, 18:2464-2467, 2010.

VIII) P. Álvarez, P. Gorria, J.L. Sánchez Llamazares, M.J. Pérez, V. Franco, M. Reiffers, I. Curlik, E. Gazo, J. Kovác, and J.A. Blanco, Magnetic properties and magneto-caloric effect in pseudo-binary intermetallic $(CeR)_2Fe_{17}$ compounds (R = Y, Pr and Dy), *Intermetallics*, 19:982-987, 2011.

Submitted

I) P. Álvarez, P. Gorria, J. Sánchez Marcos, G. Cuello, I. Puente Orench, J.A. Rodríguez Velamazán, G. Garbarino, J.L. Sánchez Llamazares, and J.A. Blanco, Magnetic and crystal structure, magnetocaloric effect and magnetovolume anomalies in the Er_2Fe_{17} compound.

II) P. Álvarez, P. Gorria, J.L. Sánchez Llamazares, M.J. Pérez, V. Franco, M. Reiffers, J. Kovác, and J.A. Blanco, Magneto-caloric effect in the pseudo-binary $YPrFe_{17}$ alloy.

Related papers

I) B. Hernando, P. Alvarez, J.D. Santos, P. Gorria, M.L. Sánchez, J. Olivera, M.J. Pérez, and V.M. Prida, Magnetoimpedance effect in Nanoperm alloys, *Journal of Magnetism and Magnetic Materials*, 300(1):e59-e62, 2006.

II) J.D. Santos, T.Sánchez, P. Alvarez, M.L. Sánchez, J.L. Sánchez Llamazares, B. Hernando, Ll. Escoda, J.J. Suñol, and R. Varga, Microstructure and magnetic properties of $Ni_{50}Mn_{37}Sn_{13}$ Heusler alloy ribbons, *Journal of Applied Physics*, 103(7):07B326, 2008.

III) P. Gorria, P. Álvarez, J. Sánchez Marcos, J.L. Sánchez Llamazares, and J.A. Blanco, Nanocrystalline Pr_2Fe_{17} studied by neutron powder diffraction, *Journal of Physics: Conference Series*, 251:012012 (4pp), 2010.

IV) P. Álvarez, J. Sánchez Marcos, J.L. Sánchez Llamazares, V. Franco, M. Reiffers, J.A. Blanco, and P. Gorria, Magnetocaloric Effect in Nanostructured Pr_2Fe_{17} and Nd_2Fe_{17} Synthesized by High-Energy Ball-Milling, *Acta Physica Polonica A*, 118:867-869, 2010.

V) P. Álvarez, P. Gorria, G. Cuello, I. Puente Orench, J.A. Rodriguez Velamazán, J. Sánchez-Marcos, J.L. Sánchez Llamazares, and J.A. Blanco, Crystal and magnetic structures and magnetovolume anomalies in Er_2Fe_{17} compound, *Journal of Physics: Conference Series*, Accepted, 2011.

VI) P. Álvarez, P. Gorria, and J.A. Blanco, Influence of magnetic fluctuations in the magnetocaloric effect on Rare Earth intermetallic compounds, *Physical Review B*, Accepted, 2011.

Other papers

I) B. Hernando, J. Olivera, P. Alvarez, J.D. Santos, M.L. Sánchez, M.J. Prez, T Sánchez, and P. Gorria, The effect of different annealing treatments on magneto-impedance in Finemet wires, *Physica B*, 384(1-2):165-168, 2006.

II) T. Sánchez, P. Alvarez, J. Olivera, M.J. Prez, F.J. Belzunce, J.D. Santos, J.L. Sánchez Ll., M.L. Sánchez, P. Gorria, and B. Hernando, Torsion annealing influence on the impedance behaviour in amorphous FeSiB and CoSiB wires, *Journal of Non-Crystalline Solids*, 353(8-10):914-918, 2007.

III) J.D. Santos, J. Olivera, P. Alvarez, T. Sánchez, M.J. Pérez, M.L. Sánchez, P. Gorria, and B. Hernando, Torsion-induced magnetoimpedance in nanocrystalline Fe-based wires, *Journal of Magnetism and Magnetic Materials*, 316(2):e915-e918, 2007.

IV) M.L. Sánchez, J. Olivera, P. Alvarez, M.J. Pérez, P. Gorria, and B. Hernando, Fe-Rich Wires as Elements for Torsion Sensors Based in Torsion Impedance Effect, *Sensors Letters*, 5:89-92, 2007.

V) M.L. Sánchez, T. Sánchez, I. Ribot, M.J. Pérez, J.D. Santos, J.L. Sánchez-Llamazares, V.M. Prida, P. Alvarez, B. Hernando, Ll. Escoda, and J.J. Suñol, Off-diagonal magnetoimpedance effect in $Fe_{80}B_{20}$ amorphous ribbons, *Journal of Non-Cryst. Solids* 354(47-51):5147-5149, 2008.

VI) B. Hernando, V.M. Prida, M.L. Sanchez, J. Olivera, C. Garcia, J.D. Santos, P. Alvarez, J.L. Sánchez-Llamazares, and N. Perov, Thermal annealing dependence of high-frequency magnetoimpedance in amorphous and nanocrystalline FeSiBCuNb ribbons, *Journal of Nanoscience and Nanotechnology*, 8(6):2873-82, 2008.

VII) J.D. Santos, A.R. Ruiz, F. Cobos, I. Ribot, V. Vega, P. Álvarez, M.L. Sánchez, J.L. Sánchez Ll., V.M. de la Prida, and B. Hernando, Domain wall dynamics in Fe-rich glass covered amorphous microwires, *Physica Status Solidi (a)*, 206(4):618-621, 2009.